THE UNIVERSITY *of* EDINBURGH

Numerical Modelling of Superconducting Power Cables with Second Generation High Temperature Superconductors

A thesis submitted by Min Yao
for the degree of Doctor of Philosophy
School of Engineering

University of Edinburgh

2019

Declaration

1) I declare that this thesis has been composed solely by myself and that it has not been submitted, in whole or in part, in any previous application for a degree. Except where states otherwise by reference or acknowledgment, the work presented is entirely my own.

2) I confirm that this thesis presented for the degree of PhD in Energy Systems, has

   i) been composed entirely by myself

   ii) been solely the result of my own work

   iii) not been submitted for any other degree or professional qualification.

3) I declare that this thesis was composed by myself, that the work contained herein is my own except where explicitly stated otherwise in the text, and that this work has not been submitted for any other degree or processional qualification except as specified. Parts of this work have been published in the work stated in the list of publications.

Signature: _____ **Date:** _____

Table of Contents

List of figures

List of tables

Acknowledgements

The work presented in this thesis would not have been completed without the help and support of many people. To all who have contributed, either directly or indirectly, to the completion of this thesis I am deeply grateful.

Firstly I would like to express my most sincere gratitude to my supervisor, Dr Quan Li. Without his guidance and expert knowledge in superconductivity this project could not have been finished. The advice and professional criticism he provided throughout my PhD programme have helped me in an immeasurable way and ensured the completion of this project on time. I like to give my special thanks to Prof. David Ingram for his enlightening feedbacks throughout my study and his great insight for mathematical modelling.

I would also like to thank my colleagues at the University of Edinburgh, without their support and friendship this journey would have been much more difficult. I want to thank my colleagues from the applied superconductivity group, in no particular order, Kevin Kails, Philip Machura, Yvonne Baird, Hongyi Chen, Mbayer Abunku, Hongye Zhang. Working with you all is truly an enjoyable experience. I must also thank Dr Kenton D'Mellow of EPCC and Mr Michael Gordon of School of Engineering for their knowledge and help on coding and scientific computing.

Finally I must give my warmest thanks to my parents who have supported me wholeheartedly, and to my family and all my friends. Your emotional support has always been my source of courage to embark on new challenges.

Abstract

The advancements made in the manufacturing technology have made the second-generation high-temperature superconducting (2G HTS) applications increasingly appealing for the power transmission industry. The 2G HTS materials, with their inherent characteristics of extremely low resistance and immense power carrying capacity, now have the true potential of transforming the entire power network and bringing about an exponentially more powerful and virtually 'loss free' future for the power industry. The topic of numerical modelling of superconducting applications, being an effective method of understanding the electromagnetic properties of superconductors, has since received much attention from the research community. Amongst the broad range of existing utilities, the HTS power cable with 2G superconducting wires is one of the most attracting and widely adopted HTS applications. Over the years, the effort of developing comprehensive 3D numerical models for 2G HTS cables has yielded many outstanding research outcomes. However, with more advanced cable designs being developed and commercialised, their geometrical features are becoming increasingly complicated. This brings about a new challenge as the complex structure of HTS power cables significantly increases the computation power needed to perform simulations. This thesis aims to address this issue by adopting innovative approximation method to build a compact 3D numerical model for HTS cables designed with YBCO wires whilst maintaining good accuracy. In doing so, this project hopes to contribute to improving the efficiency of modelling HTS cables.

This thesis starts by providing a literature review of the superconductors and their current applications on power transmission cables. Following the literature review, the methodologies applied to build this compact HTS cable model are then presented. The progressive model building process of this HTS cable model and the corresponding simulation results are placed in the succeeding chapters. Consequently, the summary and conclusions are reached at the end chapter of this thesis.

This compact HTS cable model is developed based on the electromagnetic equation system known as the ***T*** formulation. In order to investigate the anisotropic characteristics of the superconducting materials, the finite element method (FEM) is adopted to discretize the equation system in simulated region. Based on solving the current vector potential within the simulated region, a comprehensive profile of the 2G HTS conductor (i.e. current density, perpendicular magnetic field, conductivity, critical current and loss distribution) can be obtained by this model. This project starts by initially building a 2D single HTS wire model. The single wire model is then validated by the experiment data provided by the research collaborators as well as the calculation results derived by analytical equations. Following the validation of the single wire model, a study of HTS wire dynamic loss under various external magnetic field settings is performed using the 2D single wire model and its variants. Since the ultimate target of this project is to build a compact 3D HTS cable model, an anisotropic homogenous-medium approximation is adopted to expand the 2D model into 3D to reduce the workload of calculation while maintaining good accuracy. Upon the completion of a functioning 3D single layer cable model, multi-layered cable structure is then built with the same strategy. In order to fully explore the computation resources on hand, a parallel computing structure is also developed at this stage to employ multi-core operation to unravel the large-scale dense matrix imposed by a 3D problem.

Finally multiple case studies were carried out with the 3D cable models to identify scenarios where 2D models can be used to approximate the 3D cable structure and where accurate 3D models have to be built in order to reflect the realistic properties of HTS cables brought about by different designs. The difference in results and the root causes were analysed. The outcome of this research will be used to help identify more efficient strategies of building superconducting cable models.

List of publications

- Q. Li, M. Yao, Z. Jiang, C.Bumby, N.Amemiya, "Numerical Modelling of Dynamic Loss in HTS Coated Conductors under Perpendicular Magnetic Fields," in *IEEE Transactions on Applied Superconductivity*. Vol. 28, no. 2, March 2018.

- Z. Jiang, W. Zhou, Q. Li, M. Yao, J. Fang, N. Amemiya, C. Bumby, "The dynamic resistance of YBCO coated conductor wire: Effect of DC current magnitude and applied field orientation," in *Superconductor Science and Technology*. Vol. 31, no. 3, January 2018.

- M. Yao, Q. Li, D. Ingram, Y. Xin, S. Wang "Efficient numerical modelling of superconducting power cables – A comparative study between 2D and 3D numerical models." in *IEEE Transactions on Applied Superconductivity*. (Under Review)

Chapter 1. Introduction

1.1. Thesis Background

The power of electricity has long been the dominant driving force for the modern industrial and economic system. With the continuous electrification of various industry sectors, demand for electricity is expected to rise fast between 2018 and 2040 [1]. To meet the rising demand for electricity, many countries have published ambitious power generation expansion plans. However, such a rapid expansion in power generation sector will pose a serious challenge for the concurrent power transmission infrastructure. The overall capacity of the power transmission network has to go through a complete upgrade to withstand the oncoming generation expansion. At the same time, renewable sources have also become the fastest growing energy generation sources with an estimated annual increase of 2.3% during the same period [2]. Although it is an inspiring sight for the traditionally 'dirty' power industry, the challenge accompanied this transition cannot be overlooked. Many of the major renewable sources, such as offshore windfarms and dessert solar plants, are located remotely to demand centres. The increasingly daunting task of transmitting large amount of renewable power over long distances is urging for innovative solutions to cope with this challenge.

The effort of innovation spent to upgrade the power transmission network will also benefit the efficiency of its operation. Research findings have identified that almost 8% of the electrical energy were lost during the transmission as a result of resistance of conductors. Being the backbone and centrepiece of the entire power transmission network, the performance of the conductors and the transmission devices made from them are vitally important to the reliability and efficiency of the power network. Transmission lines / cables made from copper or aluminium have already seen their limits in some circumstances with demanding requirements [3] [4] [5] [6]. Therefore, research that aims to apply innovative solutions to the conductors and the power

transmission devices will have the potential of sparking a revolution to the entire industry.

The phenomenon of superconductivity has been discovered over one hundred years ago. Once a superconducting material was cooled to below the critical temperature, the material gains superconductivity and offers virtually zero resistance so that large amount of power could be carried by this material with minimum losses. Until recent years, the progresses made on the second generation high temperature superconductors (2G HTS) have made the large scale application of this technology closer to realisation than ever. The superior electromagnetic property of the 2G HTS material made it an ideal candidate to address the issue facing the modern power transmission network. Extensive lab and industrial test projects have proven the 2G HTS power applications could carry several times of the power comparing to the conventional ones whilst yielding much lower losses. These merits are invaluable to the development of next generation power transmission systems. The industry as well as the research community have placed a growing and wide spreading interest in the research of the power applications based on 2G HTS materials. Many ambitious projects such as EcoSwing, AmpaCity, ASuMED, Chuo Shinkansen [7] [8] [9] [10] and etc. have witnessed the 2G HTS applications expanded into the area of electric generator, motor, cable and even the public transport sectors.

Despite their great potential and obvious performance advantages, there are still many challenges remain to be addressed in terms of designing the 2G HTS power devices. In order to make the HTS applications competitive comparing to the conventional applications in terms of life cycle cost as well as the operational reliability, extensive research effort must be spent on studying HTS loss characteristics and the corresponding mitigation strategies. It is also widely acknowledged within the power industry that the stability is one of the vital features for the modern power systems if not the most important one. Only with the enough understandings of the HTS loss characteristics can the suitable cooling and auxiliary systems be designed to ensure the long-term stable operation of the HTS applications.

In modern power system, the two common types of power sources (AC and DC) would have different impact over the loss behaviours of the 2G HTS materials.

Although when carrying DC currents in isolated environments, the HTS materials have minimum losses. There has been an increasing number of cases where the DC carrying HTS applications are required to work under complex magnetic environments. HTS materials installed in places such as DC machine armature windings and insufficiently shielded HTS cables will all put HTS materials in contact with various external magnetic fields. The DC carrying HTS materials will experience repetitive magnetization and de-magnetization process if subjected to the influence of a time-varying magnetic field. A considerable amount of energy can be dissipated during this process in the form of heat. It does not take a large time-varying magnetic field to induce a screening current in DC carrying HTS materials. The traversing magnetic flux will create electric field inside the HTS materials and cause losses. In AC carrying cases, superconductors do experience losses due to the presence of alternating self-induced magnetic field. In the designs where multiple AC carrying HTS wires are integrated into a single casing, the AC losses within the HTS wires are even more prominent because of the magnetic coupling. In order for the cryogenic cooling system to efficiently remove the heat generated by HTS losses and avoid any possible heat aggregation points, the electromagnetic characteristics of the HTS materials under different environments must be thoroughly studied.

Throughout the relatively short history of the 2G HTS materials, many effective methodologies have been proposed and tested by the research community [11] [12] [13] [14]. Amongst the popular research methods, building FEA numerical model is one of the most effective method to analyse and predict the electromagnetic behaviour of superconducting power devices. Superconducting cable, being one of the earliest HTS applications, received much attention from the numerical modellers. Many of the effective modelling formulations have been proposed since the discovery of the 2G HTS materials. With the industry bring out more advanced HTS cable designs each year, the modelling of HTS cables also evolved from the initial one dimension to two dimensions until reaching the more complex three dimensional domain. With the increasingly complex structures being proposed, complexity of the HTS cable models and amount of calculations required to solve them grows exponentially these days. Although many research works provided excellent solutions of building

comprehensive electromagnetic models for HTS cables, there is currently a lack of strategy to increase the efficiency of such models while maintaining good accuracy.

1.2. Thesis Statement

Although a number of FEA models have been proposed, there is currently a lack of strategy to increase the 3D modelling efficiency for the HTS cables. The aim of this thesis is to propose a compact 3D FEA model to perform comprehensive electromagnetic analysis to HTS cables comprise of second - generation HTS wires.

1.3. Contributions of the Thesis

This thesis aims to propose a method to build a compact three-dimensional model for 2G HTS cables. Carrying out simulation and detailed case studies with numerical models to study the electromagnetic behaviour of HTS cables remains to be challenging for most of the researchers not only because the difficulty of making 3D numerical models but also due to the sheer amount of calculation and demanding hardware requirements needed to perform such simulation.

The electromagnetic properties of the superconducting materials were highly correlated. The anisotropic characteristic of the 2G HTS materials also adds to the complexity of the problem. For example, the combined surrounding magnetic field will affect the critical current density across the HTS materials and thus affect the transport current density distribution across the material. The transport current distribution in return will affect the surrounding combined magnetic field distribution since the self-induced magnetic field is determined by the transport current distribution of the material. In order to solve this entangled puzzle and obtain a steady result, mathematical iteration method is normally necessary. The amount of calculation needed is still manageable for the common PCs if only a 2D problem is studied. However, when the problem is extended to 3D due to the physical geometry of the actual cable, the size of the equation system and the number of unknown variables can scale up very quickly. The size of the problem along with the correlations between different variables make the convergence of iteration very hard. Calculating a three dimensional HTS cable with twisting pitches can take several days if only operated by a single computation node.

Although for some of HTS cable designs, the problem can be reduced to 2D if geometrical symmetry exists. Most of the concurrent HTS cable designs consist of multiple layers of superconducting tapes with various twisting pitch lengths. Based on the modelling challenges discussed above, it is the focus of this thesis to find out a generalized strategy to build the HTS cable model in 3D whilst reducing the size of the problem. The benefits of building such a compact 3D model are summarised in the following impact statement.

Impact Statement:

"As the 3D FEA models developed for analysing the HTS cables so far have been facing the common problem of low simulation efficiency, a compact solution is, therefore, needed to address this issue. By adopting the simplification method called anisotropic homogenous medium approximation, the compact 3D HTS cable model built in this project successfully improve the simulation speed by several times (performance depends on the specific settings) and allowed this model to operate under normal PC environment. This 3D model maintains the function of simulating different design features neglected by the 2D models while features in higher calculation speed comparing to other conventional 3D FEA models. This model has contributed to the works which lead to the publication of three journal articles with one more under review. This model simulates the current density and magnetic field distributions inside the YBCO wires for the first time under dynamic loss condition. The comparative study carried out using this model also helped to identify scenarios regarding when 2D modelling is acceptable and when 3D modelling is a necessity."

In order to achieve the aim of building this compact 3D FEA model, a 1D HTS tape model is initially built to serve as the foundation of making the complete 3D cable model. Due to the flux pinning effect, the transport current only flow across the surface region of the material and only penetrate a limited depth into the inside of material. To maximise material utilisation rate, many industrial grade 2G HTS wires only contain an extremely thin superconducting layer. Due to the high aspect ratio of the HTS layers (usually thousands to one), it is widely considered that building the 1D cross-sectional model (ignoring the thickness of the HTS layers) is enough to represent the physical properties of a single 2G HTS wire. Out of many widely accepted modelling theories,

T formulation is selected as the formulation because of its relatively high calculation efficiency [15], the rationale behind this choice will be discussed in detail in the later chapters. In order to reflect the anisotropic electromagnetic characteristic of the HTS wires across their width dimension, finite element method (FEM) is introduced to discretize the simulate region. The model is programmed in FORTRAN with open source code to again maximise the simulation efficiency and allow greater flexibility on customizing the functions. After the 1D model is completed, the electromagnetic properties of a single HTS wire are simulated. The simulation results are crosschecked against the results calculated by Norris equation by analytical method as well as the experiment measured results provided by the external academic collaborators to validate the model. After the model is proved functional with good accuracy, the single wire model was extended and used to simulate the dynamic loss behaviour of the DC carrying HTS tapes under different magnetic fields. The research outcome supported by the experiment data is later published.

Since the HTS cables typically contain multiple wires and layers to increase the current carrying capacity, the influence of the combined magnetic environment to each wire must be studied. Based on the validated algorithm for the 1D single tape model, a two dimensional multi-wire model was later built to represent the physical layout of HTS cable cross-section area. The multi-wire model was then extended to multi-layer in order to fully represent the realistic structure of the HTS cables and served as the base ground of developing the full 3D cable model.

Since the most important objective of this PhD project is to address the issue of low simulation efficiency when performing 3D analysis to HTS cables, an effective downsizing strategy has to be adopted whilst not compromising accuracy. During the investigation, it is found that an overwhelming portion of the simulation time was spent on solving the partial derivative equations matrix, which connected unknown electromagnetic variables together. The size of the equation matrix is proportional to the square of element numbers within the mesh. Thus, the size of the equation matrix can scale-up very quickly with the increase in element numbers, which is inevitable when more complex structures are simulated. Since the standardized Successive Under Relaxation method is used to obtain the steady state result, there is not much space left

to speed up the simulation process by reducing the number of iteration. For this reason, it is decided that the effort of downsizing should be concentrated on reducing the mesh density of the 3D HTS cable model. In order to achieve this, a strategy based on anisotropic homogenous medium approximation is adopted to divide the 3D cable structure into a stack consists of several short straight subsections. The different subsections were stacked with a certain phase angle difference to represent the twisting pitch exists in the realistic HTS cable design. By achieving this, the mesh density of this model is reduced drastically while maintaining all the electromagnetic features of HTS cables in 3D.

To further speed up the simulation, the governing equation matrix is split into several sub-matrices with block cyclically distribution method to enable workload sharing between different CPUs. By employing hybrid MPI and OpenMP programming in the FORTRAN model, a multi-thread parallel computing structure is built. This makes the model fully scalable and allow greater performances on better simulation platforms.

After the 3D HTS cable model is completed, the validation of the model is done through cross-checking the 3D simulation results against the 2D cross-sectional simulation results under same settings. As the 2D polygon model can be regarded as the equivalent of the cross-section of an infinitely long HTS cable with straight conductors, the simulation result yielded by the 3D model should be close to which calculated by the 2D model. It is find that the results generated by the 3D model are in close proximity with the simulation results of the 2D model for straight conductor settings. After the validation of the 3D model is completed, case studies are performed to research how the different pitch length and gap width designs will affect the overall loss generations of the HTS conductors. Full electromagnetic simulation of HTS power cables were carried out during the case studies to obtain the details such as current density, magnetic field as well as loss distributions under various conditions.

An outline of the thesis structure is provided in the following section to summarise the content of each chapter.

1.4. Outline of the Thesis

In chapter 2, a comprehensive literature review is presented. At the beginning of the chapter, a brief introduction to the superconducting materials is given with a particular focus on the second generation high temperature superconductors (2G HTS). The current state of the HTS power cable technology and the recent progresses in design topologies are then introduced. Afterwards, a review of the classic analytical models as well as the existing theoretical formulations involved in modelling the electromagnetic aspect of superconducting tapes (especially the YBCO) is performed. The classic analytical models will provide excellent baseline references to the FEM model built in this project and will be referred to in multiple occasions in this thesis. Since the ultimate goal of building this model is to analyze the loss behavior of HTS power cables, a review of both AC and DC loss mechanism for HTS materials are given later in this chapter. The corresponding loss components and their origins are also discussed in this section.

Chapter 3 is used to discuss the rationale behind the choice of the modelling formulation as well as the mathematical techniques implemented to realise the whole algorithm. At the beginning of this chapter, the choice of the modelling theory is discussed, followed by the demonstration of the governing equation deriving process to lay the foundation for building this HTS numerical model. Since the realistic HTS cable designs all have rather complex geometry, the finite element method is adopted to analyse these geometrical features and their impact on the anisotropic electromagnetic characteristics of the HTS tapes. The discretization of the governing equation and the mesh reduction strategy adopted to build this compact HTS cable model are also introduced in this section. The mathematical process used to solve the governing equation is then introduced. After re-arranging the discretized governing equation system into the matrix form, the target matrix is revealed to be a dense linear system matrix. In order to solve the equation matrix efficiently and reliably, a standardized dense matrix solver named LAPACK is selected. As a boundary condition is initially introduced to start the matrix solving process, an iterative calculation process is needed to reach the final steady state result. To maximise the model's efficiency, a Successive Under Relaxation method is adopted as it could reach

a good compromise between the number of iterations before convergence and amount of calculation spent on each iteration. Finally, in order to achieve speed boost in calculation section and make the performance of the code fully scalable, a parallel computing structure is built into the code and enables the equation matrix to be split-up into several sub-matrices and allow workload sharing between multiple CPUs. The adoption of this technique has reduced the simulation time by multiple times.

In chapter 4, the process of building the 3D HTS cable mesh is demonstrated. The model is completed in a progressive style, at the beginning a 2D single tape model is built. After validate the single tape model with both results calculated by analytical equations as well as the experiment data (the validation processes are presented in chapter 5 and 6), a 2D cable cross-section model with multiple tapes is then built. A 3D single tape stacking model is also built at this stage as a test prototype for the stacking strategy later used to build the 3D cable model. The 3D single tape stacking model, when build with enough stacks, is proofed capable of yielding very similar results with small error comparing to the 2D single tape model. Therefore, the stacking method is believed to be a valid strategy for building the 3D cable model. By adopting the homogenous medium approximation, the 3D cable model is eventually built based on modules of short straight 3D sections by stacking method. The 3D cable model is also extended and equipped with the function to study multi-layered HTS cable structure with different twisting directions as more realistic designs often present.

In chapter 5, case studies were performed to analyse the loss characteristics of HTS tapes for DC carrying scenario. When the external magnetic field is absent, the DC carrying HTS tapes were virtually loss free. However, when an AC external magnetic field is presented, dynamic loss will occur within the HTS tapes. The dynamic loss characteristics for an YBCO wire manufactured by SuperPower under AC external magnetic field is simulated with the 2D single wire model developed in this project. The accuracy of the simulation results is satisfying after comparing the model calculated dynamic loss with both the experimentally measured results as well as the analytically calculated results. In order to study the generation mechanism of dynamic loss within the 2G HTS material, more detailed modelling is performed in the later section of this chapter to plot the current density and flux distribution within the

simulated YBCO tape. The relationship between the current / flux distribution under different external field conditions and the resultant dynamic loss is also discussed.

In chapter 6, AC loss characteristics of 2G HTS wires are studied both in isolated condition and within realistic cable structure. At the beginning of this chapter, the AC loss simulation results from both the 2D and 3D single tape model are validated using the analytical method. After that, the validated single tape model is used to performed detailed simulations to study the AC loss characteristics of an YBCO wire under various operating conditions. After finish modelling the single YBCO wire in isolated environments, both the single layered and double layered HTS cables with multiple YBCO wires are simulated with the 3D cable model developed in this project. The impact of different cable design features over the AC losses of YBCO wires are studied with multiple simulation case studies. Based on their loss induction mechanism, the corresponding loss mitigation designs are also studied using the 3D cable model. At the end of this chapter, the difference between the simulation results calculated by 2D and 3D cable models are evaluated. The scenarios when 2D model can be used as an approximation to simulate the realistic HTS cables are also discussed.

In Chapter 7, a summary of the research tasks completed thus far is presented. The contributions of this PhD project is also stated. The discussion of possible improvements and the potential direction of research is also made at the end of this chapter.

Chapter 2. Superconductivity and Superconducting Cables

A brief introduction to superconductivity and its underlying theoretical principle is presented at the beginning of this chapter. Since this project focuses on researching the high temperature superconductors, the next section also introduced the commercially available mainstream high temperature superconductors. In order to identify existing challenges and issues of designing the modern HTS cables, a review of the current HTS cable topologies as well as the design features of their consisting HTS wires is conducted. A summary of the currently ongoing or completed HTS power cable experimental projects is also given. Since a suitable modelling formulation is needed to simulate the electromagnetic properties of HTS cables in a three-dimensional space, the later part of this chapter is dedicated to explore the most widely recognised theoretical models. The AC and dynamic loss mechanism of the HTS materials are introduced at the end of this chapter.

2.1. Superconductivity

Over a hundred years have elapsed since the first discovery of the superconducting phenomenon in 1911 by H. Kamerlingh Onnes. However, until today, despite their distinctively advantageous physical properties, the design and manufacturing of the superconducting applications still remain a challenging task for the industry. The phenomenon of superconductivity is first observed in mercury. When the mercury is cooled down to below a temperature of 4K [16] , electrical resistance of the solid mercury completely disappeared. The same phenomenon was also observed for a range of metals such as lead and tin under various temperature levels. These temperature levels, later become known as the critical temperature T_c, is discovered to be one of the inherent properties that were used to characterise the superconducting property of different materials. The discovery of superconductivity immediately attracted attention

of the research community and later brought Kamerlingh Onnes the Nobel Prize in Physics.

With the relentless research effort of the academia, another major property of the superconducting material, the perfect diamagnetism, was discovered by Meissner and Ochsenfeld later in 1933 [17]. The perfect diamagnetism set the superconductivity apart from the concept of simply being the perfect conductor. It was found that the superconductors will completely expel the magnetic flux from within. The magnetic field, be that self-generated by the current carried by superconductors or applied externally, can only penetrate a small depth λ into the material. This property of the superconductors is known as the Meissner Effect. The penetration depth λ is theorized by the London Model [18] in 1935 and therefore be named as the London penetration depth. The London theory explained that in order for the Meissner Effect to last for the superconductors, a shielding current will be induced at the surfaces of the superconductors. This shielding current only flew at the very shallow surface area within the London penetration depth for the earliest discovered superconductors. Figure 2.1.1 demonstrated the magnetic flux expelling phenomenon of the superconductors.

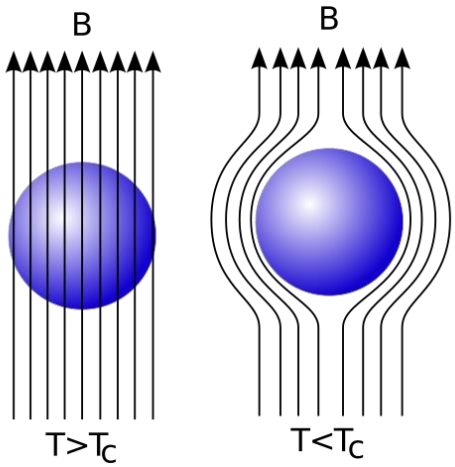

Figure 2.1.1 Magnetic flux expelling phenomenon of the superconductors [19]

However once the applied magnetic field exceeds a certain limit of H_c, the magnetic field will penetrate into the internal of a superconductor and cause the superconductor to lose its superconductivity. The same principle also applied for a given level of the transport current. When the transport current is larger than a value of I_c, it can no

longer be contained within the penetration depth λ and will cause the superconductor to lose its superconductivity. Therefore, the three parameters of T_c, H_c and I_c form the critical boundary which all superconductors must operate within. Figure 2.1.2 illustrated the critical boundaries of the superconducting region for a general superconductor. The theories mentioned above also defined the phenomenon of superconductivity as having zero electrical resistance and meanwhile completely expels the magnetic flux from within.

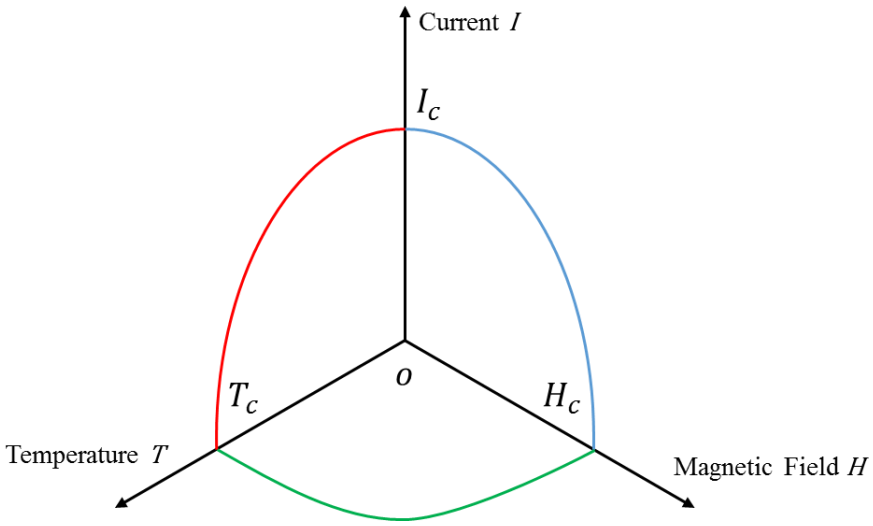

Figure 2.1.2 Critical Boundaries of the Classic Superconductors (Reproduced based on critical boundary theory)

Although the underlying physical mechanism explaining the origin of superconductivity has not been discovered yet at this time, Landau and Ginzburg have managed to propose a mathematical model to simulate the phenomenon of superconductivity [20]. The first successful attempt to explain the microscopic physical origin of the superconductivity is made by Bardeen, Cooper and Schrieffer [21]. The theory they came up later become known as the BCS theory. The BCS theory proposed that the forming of the superconducting current is due to two electrons being pressed into a cooper pair. As the cooper pairs travelled through the lattice structure inherently possessed by the superconducting materials, it is more stable and resistant to the vibrations within the lattice structure comparing to a single electron. Thus, the travelling of the cooper pairs will experience much less resistance. The BCS theory,

Meissner Effect together with the Landau and Ginzburg model and London equation formed the basis of the classic theoretical model for the superconductivity.

2.1.1. *Type I and Type II Superconductors*

As the classic theory system for superconductivity failed to explain the discovery of superconductivity in more and more 'unorthodox' materials. Based on the work carried out by the Landau and Ginzburg, in 1957, Alexei Alexeyevich Abrikosov proposed the concept of Type II superconductors [22]. The classic superconductors, all metals as they are, were therefore classified as the type I superconductors.

As it is mentioned in the previous section, one of the critical boundaries for superconductors is that all superconductor can only demonstrate superconductivity when they are subject to a magnetic field which is weaker than their respective critical magnetic field level H_c. The type I superconductors, due to their strong Meissner effect, will lose their superconductivity almost immediately when field magnitude exceeds H_c. The current carrying region of the type I superconductors were restrained within its shallow magnetic field penetrated depth whilst the bulk of the superconducting material remain idle. Therefore despite their extremely good conductivity, the type I superconductors does not perform too well when it comes to carrying electrical energy in practice when comparing to conventional conductors. The maximum current can be carried by a type I superconductor with a circular cross-section and radius R is identified as expressed in the equation 2.1 below [23]:

$$\boldsymbol{I_c = 2\pi R H_c} \tag{2. 1}$$

When the transport current is above this level, the self-generated magnetic field alone will exceed the critical magnetic field level and cause the superconductor to revert back to normal state. It is also found that the critical magnetic field level H_c is related to the temperature of the ambient environment. This relationship is expressed by the equation 2.2 presented below. The transition process for type I superconductors when the critical current level was exceeded is named as the Silsbee Effect [23].

$$\boldsymbol{H_c(T) = H_0\left(1 - \left(\frac{T}{T_c}\right)^2\right)} \tag{2. 2}$$

Another notable characteristics of the type I superconductors depicted by the Ginzburg Landau theory is their relatively large coherence length ξ. Based on Ginzburg Landau theory, the superconductivity is defined by two parameters: the magnetic penetration depth (London penetration depth) and coherence length. The coherence length limits the variation rate of the superconducting electron density. The density of the superconducting electrons (cooper pairs) can only change for a certain degree within a minimal length. If this change in electron density happens too quickly it will collapse the superconductivity of the material. The coherence length is related to the temperature and can be calculated as presented by equation 2.3 below:

$$\boldsymbol{\xi} = \sqrt{\frac{\hbar^2}{\boldsymbol{4m\alpha(T)}}} \tag{2. 3}$$

Where $\hbar$ is the reduced Plank constant, m is the mass of a cooper pair, α is a temperature dependent function defined by Ginzburg Landau equation.

The type II superconductors possess distinctively different properties comparing to the type I superconductors. The complete Meissner effect does not happen for type II superconductors when the combined magnetic field H is smaller than H_c [24]. Unlike type I superconductors which have overall positive surface energy, the type II superconductors have overall negative surface energy [25]. This results in the type II superconductors having the infamous 'mixed state' where the magnetic flux can penetrate partially into the material in the form of vortexes while allowing the material to maintain its superconductivity [25]. The 'mixed state' is characterised by its property of having two critical magnetic field levels H_{c1} and H_{c2}. When the combined ambient magnetic field is smaller than H_{c1}, the type II superconductors are behaving much like the type I superconductors and demonstrated their perfect diamagnetism with only a small shielding current wrapping around their surface. When the combined magnetic field exceeds H_{c1} but remain smaller than H_{c2}, magnetic flux begin penetrating into larger regions of the superconducting material and thus enabling much greater transport current to be carried by type II superconductors. When the combined magnetic field level exceeds the upper boundary of H_{c2}, the superconducting region is lost and the material revert to its normal state. The type II material will revert to its

normal state under this circumstance. Figure 2.1.3 below demonstrates the phase diagram for the type II superconductors.

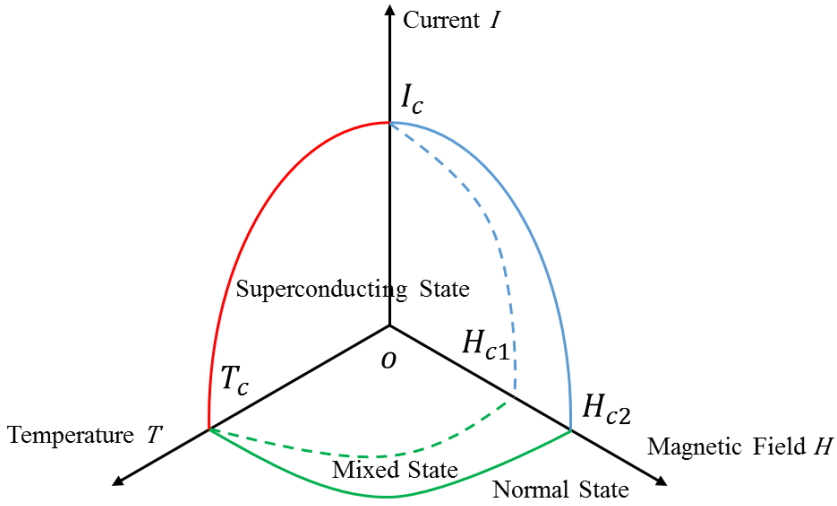

Figure 2.1.3 Critical Boundaries of the Type II Superconductors
(reproduced based on mixed state theory)

Figure 2.1.3 only demonstrates the properties of type II superconductors in an illustrative manner. Overall, type II superconductors are considered to be a superior conductor comparing to type I superconductors. In practice, for type II superconductors, the value of H_{c2} can be hundreds of times larger than the value of H_{c1}. Thus, the mixed state region presented in Figure 2.1.3 can actually be exponentially larger than the perfect superconducting region. Taking one of the most popular type II superconductor YBCO as an example, the H_{c1} of YBCO is 20mT and its H_{c2} value can reach as high as 100T [26]. Although there is another property restrained the practical current carrying capability of type II superconductors. When the combined magnetic field is higher than a certain level, the vortexes which were originally pinned within the superconducting material gradually become de-pinned due to the Lorentz force overpowering the pinning force, the details of this phenomenon will be introduced in later sections of this chapter. The movement of the de-pinned vortexes will cause significantly higher loss due to energy dissipation. This field level is known as the irreversibility field H_{irr}. The value of the irreversibility field H_{irr} can still be tens of times higher than lower critical field irreversibility field H_{c1}. Again taking YBCO as an example, the value of H_{irr} for YBCO can reach 5T at 77K [27]. Figure 2.1.4 below demonstrated a schematic of the vortex pinning effect.

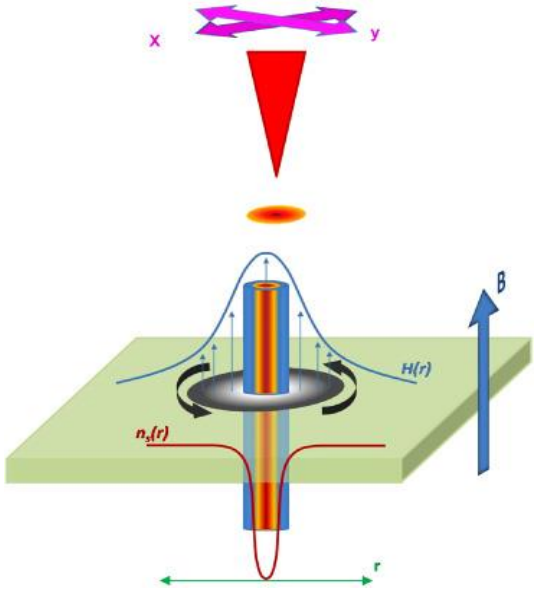

Figure 2.1.4 Vortex Pinning Effect of Type II superconductors [28]

The type I superconductor family was consisted by mainly metal such as mercury (Hg), lead (Pb) and aluminium (Al). Since the type I superconductors generally have lower critical temperature levels comparing to type II superconductors, they are also known as the low temperature superconductors (LTS). Whilst type II superconductors were mainly metal alloys such as YBCO, MgB_2, BiSCCO and Iron based superconductors. It is worth noticed that H_2S being an interesting exception which does not contain any metal elements. It was discover very recently to have superconducting property under extreme pressure and demonstrated a critical temperature as high as 203K. This discovery has triggered wide interests and create the concept of hydrogen based superconductors. It is believed that the hydrogen based superconductors have the potential of leading to the final discovery of the room temperature superconductors. Thus, the family of type II superconductors are mainly comprised of high temperature superconductors (HTS) and a few types of low temperature superconductors (LTS).

The research effort of this thesis will be focused on high temperature superconductors, particularly the YBCO. Since the YBCO is currently the most widely adopted material for making the commercial grade HTS wires due to its advantageous performance.

2.1.2. *High Temperature Superconductors - HTS*

As it is introduced in the previous section, the high temperature superconductors are a sub-group of the type II superconductor family. However the high temperature superconductors form the backbone of the type II superconductor family as most of the type II superconductors are considered the high temperature superconductors. The first high temperature superconductor LSCO ($La_{2-x}Sr_xCuO_2$) was discovered in 1986 by Bednorz and Muller [29]. The discovery resulted in the Nobel Prize being award to them in a record breaking speed. The compound is found still possessing its superconductivity at around 30K, which is significantly higher than any of the low temperature superconductor discovered before. Shortly after, the YBCO ($YBa_2Cu_3O_7$) compound is discovered by Paul C. W. Chu and M-K Wu in later 1986 and 1987 [30]. In 1988, another high temperature superconductor the BSCCO ($Bi_2Sr_2Ca_{n-1}Cu_nO_{2n+4}$, n=1, 2 or 3) is discovered as the first high temperature superconductor which does not contain any rare-earth elements [31]. The superconductivity of these compounds are observed at 93K to 108K and marked a major breakthrough in the superconducting material research area. Later in 2001, the MgB_2 is discovered as yet another type of high temperature superconductor with a typical critical temperature at 39K. The discovery of YBCO is of the greatest significance because it was the first compound found still have superconductivity above the boiling point of the liquid nitrogen (77K). This significantly reduced the cost of maintaining the cryogenic environment needed by the superconducting applications as liquid nitrogen is much cheaper and far easier to come by than the two original coolant of liquid hydrogen (20K) and liquid helium (4.2K). Therefore, the discovery of YBCO greatly increase the economic feasibility of the superconducting applications. Due to the superior performances the YBCO has to offer comparing to the BSCCO and MgB_2, it is classified as the second generation high temperature superconductor (2G HTS). The BSCCO and MgB_2 are commonly known as the first generation high temperature superconductors and are typically manufactured into multi-filamentary structure comparing to the thin film structure offered by the 2G HTS materials.

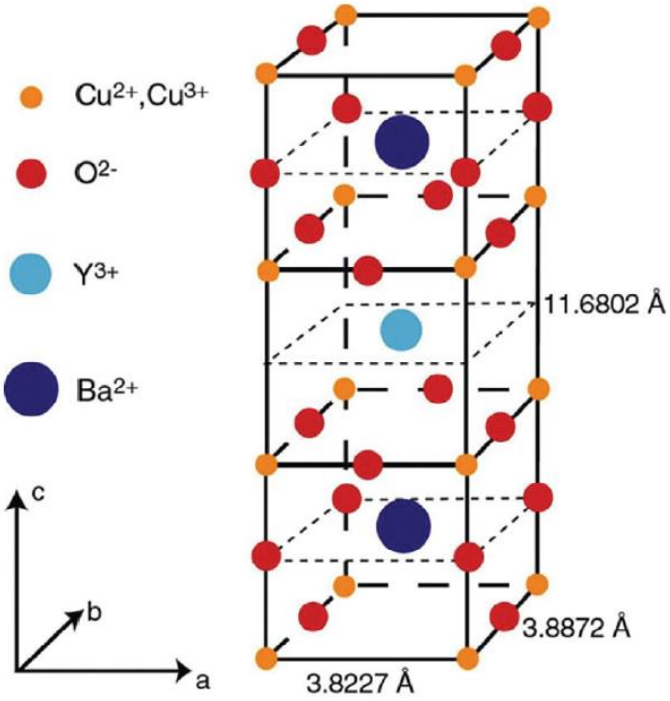

Figure 2.1.5 Crystalline structure of the YBCO compound [31]

The crystalline structure of the YBCO compound is presented in figure 2.1.5 above. It is found by the material scientists that the crystalline structure of the YBCO compound is highly anisotropic as the Yttrium atoms and the Barium atoms are located within different CuO_2 planes. The electric conductivity within the CuO_2 planes are much higher than those of the spaces between the CuO_2 planes [25]. Therefore based on the current divider rule, the supercurrent mostly only flow in the *a-b* planes. The single crystalline structure of the YBCO compound have very high critical current level. This property also makes the YBCO the ideal material to make the commercial grade superconducting wires. Since the majority of the HTS power applications (such as the HTS fault current limiters, HTS energy storage magnets and HTS power cables) are built with superconducting wires, it also make YBCO the most studied material for the high power large scale applications. This also form the reason of choosing YBCO as the primary study target in this thesis when building the HTS power cable models.

2.2. Current HTS Cable Design Topologies with 2G HTS wires

The designs of the HTS power cables can be somewhat different comparing to the conventional copper cables due to the geometry of the commercial HTS wires and the

needs to accommodate additional cooling systems. Based on the cooling strategies employed, the HTS power cables can generally be divided into two types: the warm dielectric HTS cables and the cold dielectric HTS cables. The difference between the two designs are mainly about the position to assemble the dielectric insulations to separate different layers of HTS conductors. However, despite the difference in designing the dielectric layer, most of the HTS cables employ identical designs when it comes to the way of assembling the HTS conductors. In order to reduce the transport loss and increase the number of HTS wires assembled into the cable, both types of HTS cable designs choose to wound the HTS wires helically around the hollow cylindrical cable former. Two kinds of HTS materials are widely used for building the commercial grade HTS wires: YBCO, BSCCO ($Bi_2Sr_2Ca_2Cu_3O_{10}$ or Bi-2223). Whilst the BSCCO is considered the first generation (1G) HTS material, YBCO due to its overall superior in field performance, is considered to be the second generation (2G) HTS material. Since the majority of the HTS wire manufacturers are upgrading towards the second generation HTS wires, this thesis will also focus on the modelling of the HTS cables built with the 2G YBCO wires. An example of the actual YBCO HTS cable design is presented in figure 2.2.1 below.

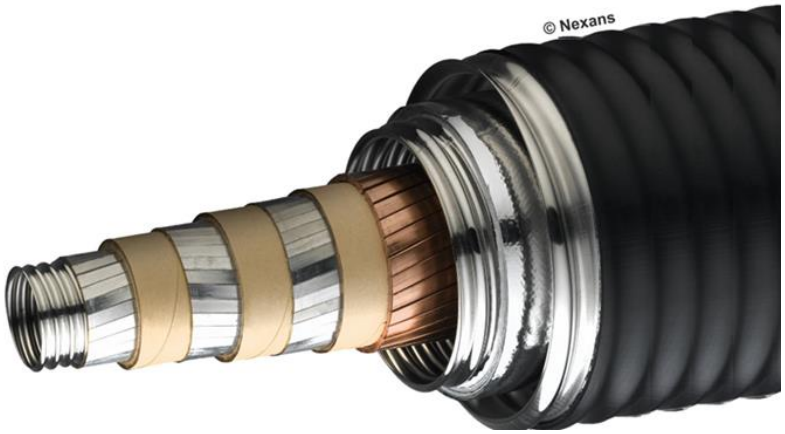

Figure 2.2.1 HTS Concentric Power Cable with YBCO Coated Conductors [32]

2.2.1. *Second Generation YBCO Conductor*

The 2G HTS conductors made with YBCO compound all have pretty similar geometrical features due to the way they are manufactured. Overall, the commercial grade YBCO wires take the form of a thin metallic tape as demonstrated in the

schematic below in figure 2.2.2. The width of the YBCO wires can vary depending on the requirement of the specific application, usually ranging from 4mm to 20mm. However, as it can be observed from figure 2.2.2 below, the total thickness of the tape is pretty thin comparing to its width (below 0.1mm). The transport current carrying layer is marked by (RE)BCO layer in figure 2.2.2. Where the 'RE' represents the rare earth elements used to manufacture the tape. The most popular choice is the Yttrium, hence the name YBCO. It is important to notice that the YBCO layer is solely responsible for conducting the transport current. Due to the current manufacturing process, the YBCO layer actually only takes up a very small portion of the total tape thickness. In most of the designs the YBCO layers are only several micro-meters thick [33] [34] whist the width of the YBCO layers still roughly equals to the width of the wires. Therefore, the main geometrical feature of the YBCO layer is marked by the extremely high aspect ratio (thousands to one). This feature allows the YBCO layer to be assumed as a thin film with very small thickness [35].

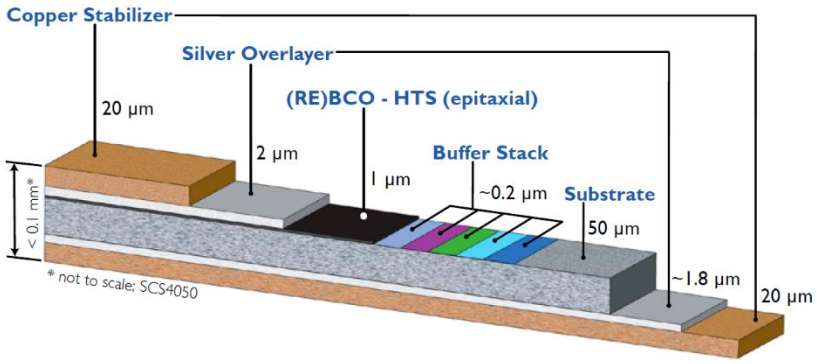

Figure 2.2.2 YBCO Coated Conductor manufactured by Super Power [36]

There are currently several major suppliers of long commercial grade YBCO wires in the market. The most notable companies includes American Superconductor (AMSC) [37], Super Power [38], Fujikura [39] and Shanghai Superconductor [40].

2.2.2. *Design Configurations of the YBCO HTS Power Cables*

As it was discussed in the previous section, the commercial grade YBCO wires used to make the 2G HTS cables are tape shaped and have limited thickness. This geometrical feature led to the design of YBCO wires being attached closely to the hollow former and twisted spirally to minimize the gap between different wires. Apart

from the helically wound YBCO wires and formers, the designs of 2G HTS power cables also contains a lot of other functional components to ensure the stable and robust performance of the whole cable. A typical 2G YBCO cable design schematic is presented below in figure 2.2.3.

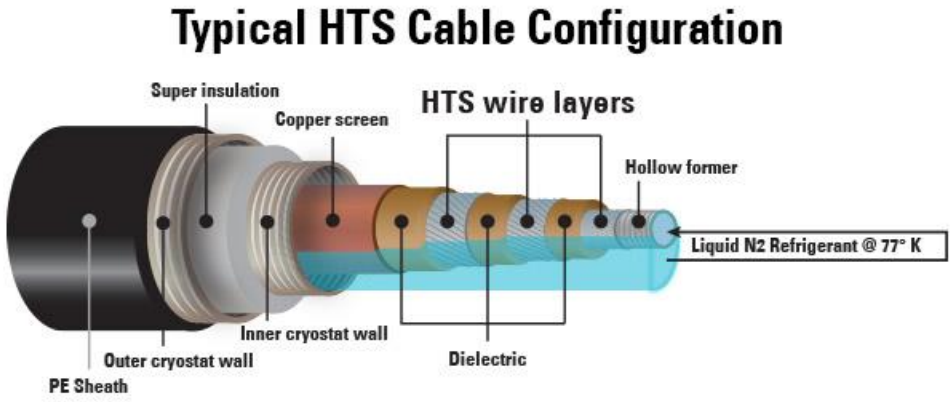

Figure 2.2.3: **Design Schematic of 2G YBCO Cable [41]**

The YBCO HTS cable design demonstrated in figure 2.2.3 is a typical cold dielectric multi-layer concentric design. It contains most of the components necessary for building the HTS cables and is therefore taken as an example. As it can be seen in figure 2.2.3, at the inner most structure of this tri-axial HTS cable locates a hollow former, this hollow former supports the structure of the attached HTS wires while allowing a return path for the liquid nitrogen coolant. Three layers of the HTS wires were attached onto the hollow former. HTS wires of different layers are separated by the dielectric layers to provide electric insulation. A copper screen sheath is attached outside the HTS conductors and dielectric layers to hold the inner structure together. The copper screen sheath also serve the purpose of shielding the magnetic field generated by the transport current and carrying part of the short circuit current when fault occurs [42]. The liquid nitrogen flows within the space between the copper screen and the inner cryostat wall to cool all the HTS layers as well as the dielectrics. A thermal insulation layer is fitted between the inner cryostat wall and the outer cryostat wall. A PE sheath is finally attached at the outer most layer to enclose the whole HTS cable structure.

As most of the HTS cable components demonstrated in figure 2.2.3 are implemented for the cooling and structural supporting purposes, these components do not normally

affect the electromagnetic properties of the HTS wires. Since the aim of this PhD thesis is to study the electromagnetic properties of the HTS cables, only the HTS wires and the magnetic coupling between different wires are considered in this model.

2.2.3. *YBCO HTS Cables Test Projects*

Since the discovery of the high temperature superconducting materials in 1986, a significant amount of research effort has been invested into developing power cables with the HTS material. The first generation of HTS power cables are mainly comprised of BSCCO wires. HTS cables made with YBCO wires were built more recently after the long YBCO conductors become commercially available. The YBCO HTS cables are classified as the second generation HTS cables.

The first YBCO HTS cable which achieved grid integration is developed by Superpower and Sumitomo Electric Industries in 2007 [43] and is installed at Albany, New York in 2008. The YBCO cable manufactured is 30 meters long and consists of over six miles of the YBCO wires [44]. This project is funded by the US department of energy and is aimed to test the feasibility of HTS cable grid integration with the installation of total 350m long of HTS cables (34.5kV, 800A) between two substations. After the Albany project, many YBCO cable experimental projects were carried out worldwide. Shortly after the initiation of Albany project, several small scale YBCO cable testing projects are conducted by Nexans. In 2009, the Furukawa Electric Group developed a 10m long YBCO cable prototype with transmission level voltage (66/77kV) [45]. Later in 2010, LS Cable Ltd designed and installed a 500m long, 22.9kV YBCO cable for distribution network in Seoul and surpassed the length of installation achieved by Albany project [46]. In 2011, American Superconductor (AMSC) installed and tested world's first YBCO transmission level cable in Long Island with a length of 600m and design voltage of up to 138kV [47] during the second phase of the LIPA (Long Island Power Authority) project. More recently, several testing projects for DC YBCO power cables were initiated. In 2014, an 80kV 500MW DC YBCO cable was installed in Jeju Island, Korea by KEPCO (Korea Electric Power Corporation) and LS Cable Ltd [48]. Most recently, a 20kA 1kV DC cable was installed in Ludwigshafen in Germany [49]. A table summarising the projects mentioned in this section is presented below.

Table 1: Major Existing YBCO Cable Test Project

Developer	Installed Location	Length	Power Rating	Time
Superpower / Sumitomo	Albany, New York	30m	34.5kV, 800A	2008
Furukawa	Lab Tested	10m	66 / 77kV	2009
LS Cable	Seoul	500m	22.9kV	2010
AMSC	Long Island, New York	600m	138kV	2011
KEPCO / LS Cable	Jeju Island	500m	80kV 500MW	2014

The experimental projects introduced above provide invaluable experience for the maintenance and design of the new HTS cables. By examining the operation reports compiled by some of the project teams, some of the existing advantages and disadvantages of using YBCO HTS power cables can be summarized.

Advantages of the current YBCO power cables:

- Significantly higher current carrying capacity.
- Minimal power losses over the cable.
- Lower transmission voltage level required.
- Compact structures to reduce installation space requirements.

Disadvantages of the current YBCO power cables:

- Very high capital cost comparing to the conventional copper cables (manufacturing cost can be over 100 times more expensive per unit length).
- Complex auxiliary infrastructure needed (cooling, pressurized container, special joints and terminals, advanced protection systems and etc.).
- Higher maintenance cost due to additional infrastructures and more complex designs.
- Require specially trained maintenance and repair personnel to oversee the system.

The estimated prices of YBCO wires with typical design specifications from some of the major suppliers are recorded in table 2 below, the price of typical copper wires are also provided for reference.

Table 2: Estimated Cost of Typical YBCO Wires and Copper Wires

Manufacturer	Material Type	Price (USD per Meter)
SuperPower	YBCO	30 – 40*
Shanghai Superconductor	ReBCO	25 – 30*
AMSC	YBCO	35 – 50*
RS Component	Copper	0.069 – 3.87*

* The price provided in this table is estimated and for reference only. The actual price of the product can vary due to factors such as amount of purchase and design specifications.

Based on the experiences obtained by the experimental projects, the large-scale implementation of the HTS power cables still faces lots of problem. However, the performance advantages of the existing HTS power cables are also very clear. Overall, with the continuous progress of the HTS cable designing techniques, the outlook of the large-scale implementation of the HTS power cables is still optimistic.

2.3. Modelling Theories for YBCO Superconducting Tapes

Unlike the conventional metallic conductors such as aluminum and copper, the YBCO and other HTS compound possesses highly anisotropic and non-linear electromagnetic properties across their dimension. The performance improvements of the YBCO power cables rely heavily on optimization designs to avoid unnecessary losses. However, such design optimizations can only be achieved with the comprehensive and accurate knowledge of the electromagnetic property distributions across the HTS materials [50]. Therefore, the numeric modelling of the HTS materials' electromagnetic properties become necessary for the design optimization research. Based on the findings of the experimental studies, the modelling theories of the HTS materials have evolved since and can cover more aspects of the material. The development of both the macroscopic and microscopic theories has made the analytical analysis and finite element analysis of the HTS materials viable. The major theories describing the unique electromagnetic properties of the HTS materials will be introduced in this section. Since the YBCO compound is a HTS material, the modelling theories introduced in this section will serve as a foundation for the numerical model built in this project.

2.3.1. *The Bean Model*

The YBCO compound is classified as a type II high temperature superconducting material as introduced in the previous section. Unlike the type I superconductors, the HTS materials are normally operating under a 'mixed state' when carrying currents. Based on the experimental observations, it is found that when carrying a relatively low transport current, the outer part of the HTS material will be firstly penetrated by the magnetic flux. The infiltrated flux will induce superconducting shielding currents around the center of each penetration site and shield the internal part of the HTS material from the magnetic field. The flux penetrated outer region is described as in a 'critical state'. Based on the Faraday's law of induction, superconducting current can flow only in the critical state region whilst the internal shielded region will remain current free. This imbalance of current distribution is initially described by the critical state model (CSM) proposed by Bean and is also known as the Bean model [51].

The Bean model is a simplified theoretical model aims to describe the current and electric field distributions over a HTS material. In Bean's model, assumptions are made that the entire HTS material can be divided in to two different types of regions: the current carrying region and the current free region. In the current carrying region, the HTS material enters the critical state first and the current density in these regions are taken as the critical current density level of $\pm J_c$. For the current free region, the current density is taken as zero. The current free regions only exist at those parts of the HTS materials which have not yet been penetrated by magnetic flux. Based on the Faraday's law of induction, the electric field would not exist without the presence of the magnetic field. Therefore, in current free region defined by the Bean model, the current density will remain zero as no electric field is presented within the region. When the whole HTS material is filled with the magnetic flux, the entire material will carry a current density of $\pm J_c$ and enters critical state. The current density in any part of the material cannot exceeds the critical current density level.

Bean model also described the magnetic field penetration pattern for the HTS materials. In Bean's model, the magnetic field (either externally applied or self-induced) starts to penetrate the material from the edge of the material. The depth of penetration depends on the magnitude of the magnetic field and material's critical current density level. A classic example demonstrating the concept of Bean model by a superconducting slab is presented by the work of [23] in figure 2.3.1 below.

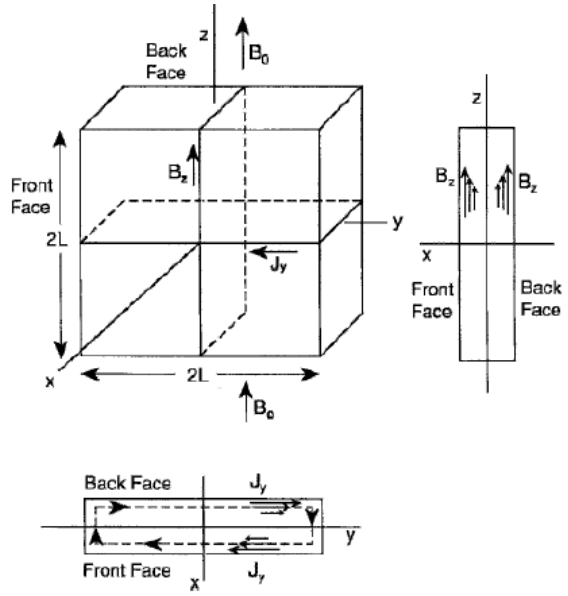

Figure 2.3.1 Superconducting Slab with Externally Applied Magnetic Field [23]

A superconducting slab with the thickness of 2*a* in *x* dimension is presented in figure 2.3.1 above. The slab is applied with an external magnetic field B_z oriented in *z* direction and as a result, a shielding current J_y is induced circulating the cross-section of the slab in *x*-*y* plane. The thickness of the slab is very thin so the shielding current is assumed to be only flowing in *y* direction. The corresponding shielding current distributions with respect to different magnitudes of the external magnetic field are plotted in figure 2.3.2 below.

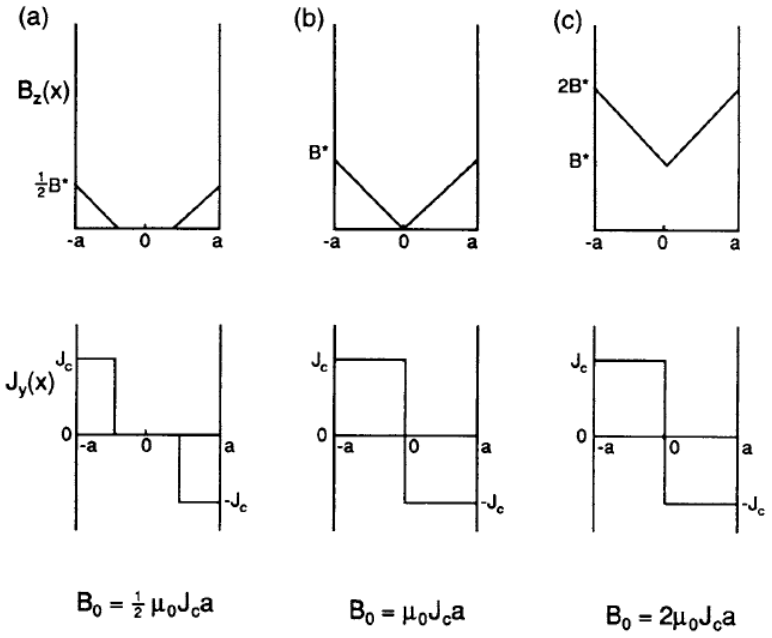

Figure 2.3.2 Relationship between Current Density and Magnetic Field Strength described by Bean's Model [23]

In figure 2.3.2 above, B^* represents the full penetration magnetic field and can be calculated as $B^* = \mu_0 J_c a$ based on the Bean model, B_0 represents the normalized applied magnetic field strength and F_p represents the pining force. As it can be seen in figure 2.3.2 (a), when the applied magnetic field is half of the full penetration field level, the slab is penetrated half way through along its width. The area being penetrated by the external magnetic field carries shielding current with the current density of J_c. In figure 2.3.2 (b), when the magnitude of the applied field is increased to the full penetration level, the entire thickness of the material is filled with the shielding current with current density of J_c. Where in figure 2.3.2 (c), when the magnitude of the applied

field exceeds the full penetration level, the shielding current density do not further increase and remains at J_c.

The Bean model offered a simplified description to the relationship between current density and magnetic field strength across the superconducting material. However, it made the assumption that the local critical current density value remains constant and independent to the magnitude of the magnetic field. Despite its limitations, the theory of Bean model still forms the basis of understandings to the superconductors' electromagnetic property distribution.

2.3.2. *The E-J Power Law*

The Bean model can be well applied to describe the electromagnetic distributions of most of the low temperature superconductors. However, in most of the cases Bean model does not fit very well with the characteristics presented by the high temperature superconductors. One of the key reason of this discrepancy is due to that the Bean model assumes instantaneous transitions at the boundary of the current carrying regions and the current free regions. This assumption caused a discontinuity of the electric field at the boundary between the current carrying regions and the current free regions. Based on the flux creeping theory later proposed by Anderson in [52], the electric field within the HTS material is generated due to the slow propagation of the magnetic flux and it is distributed continuously. Later based on the Anderson's work, Rhyner proposed the $E - J$ power law in [53] to better reflect the non-linear relationship between the electric field and current density within the HTS materials. This relationship is described by equation 2.4 below.

$$\boldsymbol{E} = \boldsymbol{E_0}(\frac{\boldsymbol{J}}{\boldsymbol{J_c}})^{\boldsymbol{n}} \tag{2. 4}$$

Where in equation 2.4, E_0 is the critical electric field and usually taken the value of 10^{-4} V/m. Whereas n is a variable which mostly depends on the material as well as the magnitude of the magnetic field. The relationship between n value and the magnetic field strength is discussed in the next section. Noted that when n is equal to 1, the $E - J$ power law equation is equivalent to the linear relationship presented by Ohm's law. Whilst if n is infinite, the $E - J$ power law reflects the behaviour of the critical state

model proposed by Bean. According to the research work in [54], n=50 is generally the upper limit for most of the HTS and LTS materials. When modelling HTS materials, it is common to set the n value as greater than 20.

2.3.3. *The Kim-Anderson Model*

As it is mentioned in the previous section, in Bean's model, the current density across the superconducting material is assumed to distribute with a step and somewhat discontinuous pattern. The critical current density value J_c of the material is also assumed to be constant and independent to the local magnetic field strength. However, this relationship is later proven to be over-simplified for the type II superconductors. The work of Kim [55] and Anderson [52] provided a more accurate description of the $J_c - T$, $J_c - B$ and $n - B$ relationship for the type II superconductors. This works is later called the Kim – Anderson model and is currently widely adopted to establish the continuous relationship between the local magnetic field strength and critical current density when modelling the HTS materials. The empirical equations proposed by the Kim – Anderson model are presented in equation 2.5 to 2.7 below.

$$\boldsymbol{J_c(B,T)} = \frac{\boldsymbol{J_{c0}(T)}}{\boldsymbol{1+\frac{B}{B_0}}} \tag{2. 5}$$

In equation 2.5, $J_{c0}(T)$ represents the initial critical current density of the material under certain temperature. B represents the magnitude of the magnetic field and B_0 is a material specific field constant. The coupling relationship between the $J_c - B$ and $n - B$ of the HTS material under a specific temperature can be described by the equation 2.6 and 2.7.

$$\boldsymbol{J_c(B)} = \frac{\boldsymbol{J_{c0}}}{\boldsymbol{1+\frac{|B_n|}{B_0}}} \tag{2. 6}$$

$$\boldsymbol{n(B)} = \frac{\boldsymbol{n_0}}{\boldsymbol{1+\frac{|B_n|}{B_0}}} \tag{2. 7}$$

In equation 2.6 and 2.7, $|B_n|$ represents the magnitude of the magnetic field component normal to the surface of the HTS material, n_0 represents the initial value of n in $E - J$ power law under a specific temperature.

Overall, comparing to the Bean model, the Kim – Anderson model better represents the distribution of the local critical current density and n value within the HTS materials by considering the affect imposed by the local magnetic field strength. Therefore, the Kim – Anderson model is adopted by this model to build the HTS cable numerical model.

2.3.4. *Modelling Formulations*

In previous sections, some of the unique electromagnetic properties of the HTS materials have been introduced. However, the theories already introduced only covered individual aspects of HTS materials and described their electromagnetic properties from a macroscopic perspective. In order to perform comprehensive analysis to HTS materials working under complex electromagnetic environments, systematic numerical models must be built. Several numerical modelling formulations for HTS materials have been proposed since the manufacturing of HTS wires become possible. These methods successfully couple the $E - J$ power law, Kim – Anderson model with the Maxwell equations and therefore cover most of the known electromagnetic properties of the HTS materials. The difference between these methods are their methods adopted to solve the resultant equation systems. There are currently three mainstream HTS modelling formulations: the $\boldsymbol{T}$ formulation [56], the $\boldsymbol{A - V}$ formulation [57] and the $\boldsymbol{H}$ formulation [58]. These three formulations are commonly implemented together with the finite element analysis to provide the numerical models with ability of analyzing the anisotropic electromagnetic properties demonstrated by different parts of the HTS materials.

2.3.4.1. *T Formulation*

The $\boldsymbol{T}$ formulation is considered the first comprehensive numerical model to be capable of simulating the current and magnetic field distribution across the HTS materials under different working conditions. It is first proposed by Amemiya in the work of [56]. The $\boldsymbol{T}$ formulation uses current vector potential $\boldsymbol{T}$ to connect the Maxwell equations with superconducting specific electromagnetic theories and solve the resultant governing equation system with FEA. Most of the $\boldsymbol{T}$ formulation HTS models are built with open source codes [59] [60] [61] [62]. Therefore, the $\boldsymbol{T}$ formulation

models generally enjoy higher degrees of flexibility and are open for customization. The $\boldsymbol{T}$ formulation is also considered to have the highest calculation efficiency amongst the three methods and best suited for simulating the thin film HTS materials [15]. The definition of the current vector potential $\boldsymbol{T}$ and the re-arranged Faraday's Law of induction are presented below.

$$\boldsymbol{J} = \nabla \times \boldsymbol{T} \tag{2. 8}$$

$$\nabla \times (\boldsymbol{\rho} \nabla \times \boldsymbol{T}) = -\frac{\partial \boldsymbol{B}}{\partial \boldsymbol{t}} \tag{2. 9}$$

$$\boldsymbol{\rho} = \boldsymbol{\rho}(\boldsymbol{J}) \tag{2. 10}$$

2.3.4.2. *A-V Formulation*

The $\boldsymbol{A} - \boldsymbol{V}$ formulation is proposed by Vinot in [63] shortly after the proposition of the $\boldsymbol{T}$ formulation. The principle of the $\boldsymbol{A} - \boldsymbol{V}$ formulation is similar to the $\boldsymbol{T}$ formulation. However instead of solving the governing equation systems from the current perspective, the $\boldsymbol{A} - \boldsymbol{V}$ formulation choose to solve the coupled equation system from the magnetic field perspective. Similar to the $\boldsymbol{T}$ formulation, the $\boldsymbol{A} - \boldsymbol{V}$ formulation used an intermediate variable $\boldsymbol{A}$, which represents the magnetic vector potential. The $\boldsymbol{A} - \boldsymbol{V}$ formulation has been adopted by a few of the commercial software packages [64] [65] and therefore the HTS model made with $\boldsymbol{A} - \boldsymbol{V}$ formulation can be easily standardized. The definition of the $\boldsymbol{A} - \boldsymbol{V}$ formulation and its version of the Faraday induction equation are presented below.

$$\boldsymbol{B} = \nabla \times \boldsymbol{A} \tag{2. 11}$$

$$\nabla^2 \boldsymbol{A} = \boldsymbol{\mu\sigma}\left(\frac{\partial \boldsymbol{A}}{\partial \boldsymbol{t}} + \nabla \boldsymbol{V}\right) \tag{2. 12}$$

$$\boldsymbol{\sigma} = \boldsymbol{\sigma}(\boldsymbol{E}) \tag{2. 13}$$

2.3.4.3. *H Formulation*

The $\boldsymbol{H}$ formulation adopted a slightly different approach in terms of solving the governing equation system. Unlike the other two methods, the $\boldsymbol{H}$ formulation does not use intermediate variables and instead choose to solve the Maxwell equation by

directly calculated the magnetic component $\boldsymbol{H}$ [66]. The $\boldsymbol{H}$ formulation is widely implemented by the HTS material models built in the commercial software COMSOL and possess the merit of relatively fast convergence speed [67]. However, due to its direct approach of solving the governing equation system, the calculation speed for each iteration step is relatively slow [15]. This feature increases the scaling difficulty for the $\boldsymbol{H}$ formulation models when simulating large and complex HTS applications. The basic equations of the $\boldsymbol{H}$ formulation are presented below.

$$\boldsymbol{B} = \boldsymbol{\mu_0 H} \tag{2 .14}$$

$$\boldsymbol{\nabla} \times (\boldsymbol{\rho \nabla} \times \boldsymbol{H}) = -\frac{\boldsymbol{\partial B}}{\boldsymbol{\partial t}} = -\boldsymbol{\mu_0}\frac{\boldsymbol{\partial H}}{\boldsymbol{\partial t}} \tag{2. 15}$$

$$\boldsymbol{J} = \boldsymbol{\nabla} \times \boldsymbol{H} \tag{2. 16}$$

$$\boldsymbol{\rho} = \boldsymbol{\rho}(\boldsymbol{J}) \tag{2. 17}$$

2.3.5. *Other Modelling Works*

Based on the different modelling formulations introduced in the previous section, several numerical models have been built by various researchers to analyze the electromagnetics performances of the HTS power cables. However, these previous modelling works face a common challenge as stated in the thesis statement: the 2D numerical models cannot fully represent the features of the realistic HTS power cable whilst 3D numerical models place extremely high pressure on the normal computing infrastructures. A selection of the important previous modelling works on HTS power cables will be introduced in this section.

D. Miyagi et al. proposed a macroscopic 3D HTS cable model in the work of [69] in 2004 as one of the earliest 3D FEA models to study HTS cables. In this work, the author simplified the HTS wires surrounding the cable former as a thin-walled cylindrical tube. The separation of different HTS wires were done by setting anisotropic conductivity to the surface region of the tube as presented by figure 2.3.3 below. This approximation dramatically reduced the load for computation as it reduce the geometrical features presented by the realistic HTS power cable designs. However, such equivalent circuit type approximation also makes it hard to study the loss

contributing factors caused by geometrical design features such as gaps between adjacent conductors.

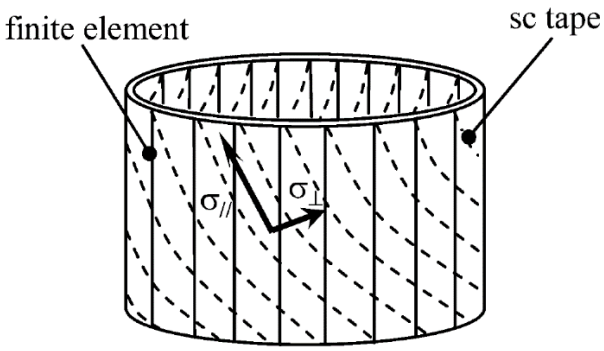

Figure 2.3.3 Separation of Different HTS wires by Anisotropic Conductivity [69]

Z. Hong et al. proposed a 2D electromagnetics model to study the AC loss characteristics of the MgB_2 wires and cables in the work of [70]. This model is developed with ***H*** formulation in COMSOL and focuses on the analysis of multi-filamentary type HTS wires. Although this work presents a comprehensive study on the current density and magnetic field distributions in the 2D MgB_2 wires, it neglects the 3D cable design features such as conductor twisting. In addition, the thin film type HTS wires such as YBCO is not studied in this work.

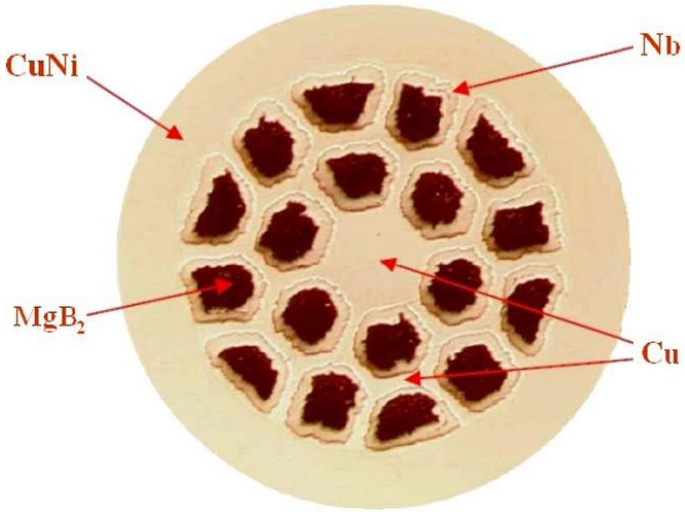

Figure 2.3.4 Multi-filamentary MgB_2 Wire Studied by [70]

K. Takeuchiet et al. presented a first full 3D HTS power cable model for YBCO based HTS wires in the work of in [71] 2011. This FEA model presents a most

comprehensive study over the multi-layered conductor on round core (CORC) HTS cable up to the point of its publication. The effect of the design features such as twisting pitch lengths, gap width between conductors and different layers of conductors have been studied in this work. However, a limitation of this model is it uses the conventional 2D interpolation function to mesh the thin film HTS conductors. Therefore, it puts a demanding requirement for the computing environment in order to operate it.

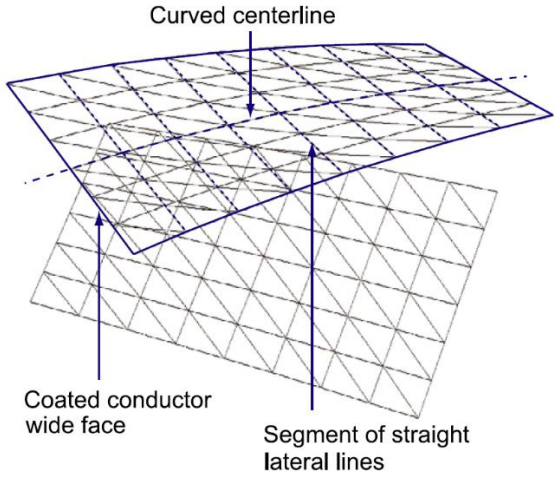

Figure 2.3.5 Conventional 2D Meshing Strategy adopted by the work of [71]

2.4. AC Losses in HTS Cables

Though lossless on its own under DC carrying condition, the HTS materials are not immune to losses when they are carrying AC currents. The majority part of the modern power systems is operating with low frequency AC power sources. The research into the HTS materials' AC loss characteristics is of paramount importance for designing the HTS power applications. Although the AC losses produced by the HTS materials are still significantly lower than those generated by conventional conductors, the loss reduction capability of the HTS materials still need to be exploited as much as possible to justify the additional power consumed by its cooling systems. Usually the energy used to cool the HTS conductors can be of magnitudes higher than their losses. Therefore, keeping the AC losses of the HTS material at minimum level is still the top priority when designing AC HTS power applications.

For superconducting cables, under normal working conditions, most of the losses generated within the cable are produced by the HTS wires as they are solely responsible for carrying transport currents.

2.4.1. *AC loss Types*

AC losses can be generated within the HTS wires due to several different factors. In general, these factors can be divided into two categories: the transport current induced AC losses and external magnetic field induced AC losses. The detail components of the two types of AC losses will be introduced in the sections below.

2.4.1.1. *Transport Current induced AC Losses*

The transport current induced AC losses occur due to the changing magnetic field induced by the alternating transport current. The energy dissipated by this type of AC losses come from the power source supplying the transport current. The content of the transport current induced AC losses can be further split into the hysteresis loss, coupling loss and flux flow loss by the nature of these loss components.

Self-field Hysteresis Loss

The mechanism for the hysteresis loss generation within the superconducting part of the HTS wires can be explained by the changing flux distribution caused by the changing magnitude of the transport current. As it is mentioned previously, when a transport current is passing through the HTS material, the current initially can only flow within part of the material penetrated by magnetic flux. The depth of the penetration and the distribution of the magnetic flux for a certain HTS material are determined by the strength of the magnetic field. Without the presence of the externally applied magnetic field, the distribution of the magnetic flux is solely determined by the transport current induced magnetic field. When the magnitude of the transport current changes so will its induced magnetic field. Therefore, the distribution of the flux lines within the HTS material will change inevitably due to the changing transport current. Based on Faraday's law of induction, the changing flux will generate an electric field within the HTS material and therefore causes losses. The AC transport current induced magnetic field will push the magnetic flux to traverse the HTS material during each cycle and generate the hysteresis loss.

Flux Flow Loss

The flux flow loss can happen when a large transport current is carried by the HTS material. The pinning of the flux at various pinning sites across the HTS material is a result of the balance between the pinning force provided by the HTS material and the Lorentz force exerted by the electromagnetic field within the HTS material. As it is mentioned in the previous paragraph, the pinned flux will become de-pinned by the increasing magnetic field induced by the alternating current until reaching another equilibrium point. If the magnitude of the transport current is large enough, at some point the Lorentz force could overcome the pinning force across part or even all of the HTS material and make some of the flux become completely unpinned [68]. The moving flux being pushed around by the Lorentz force will induce additional electric field within the HTS material and cause flux flow related loss. For an AC transport current with lower magnitude, the hysteresis loss will be more dominant within the HTS material. But when higher AC transport current is applied to the HTS material, contribution of the flux flow loss will become more significant.

2.4.1.2. *Magnetization losses*

The magnetization losses are produced within the HTS materials by the externally applied time - varying magnetic field. Under working environment, the HTS materials could be subjected to the influence of the AC magnetic field generated by other power devices if not shielded completely. In this case, the source of the energy dissipated on HTS material will be the source responsible for producing the magnetic field. The total magnetization losses on HTS materials can generally be split into three components: the external field induced hysteresis loss, the coupling loss and the eddy current loss.

External Field Hysteresis Loss

The external field induced hysteresis loss has the same loss generation mechanism with the self-field hysteresis loss. However, in this case, the source of energy become the source of the external magnetic field. With the time - varying strength of the external magnetic field, the flux distribution within the HTS material will also vary and thus generate an electric field within the HTS material. Even if the HTS material does not carry any transport current initially, the presence of the external field will still

induce a shielding current which circulates the outer region of the HTS material to shield its interior from being penetrated by the magnetic flux. The loss is therefore dissipated by the shielding current and can be calculated as E^*J_s, the external magnetic field is considered the medium to transfer this hysteresis loss energy. An example of the hysteresis loop for one external magnetic field cycle within the HTS material is presented in figure 2.4.1 below. The external field induced hysteresis loss is proportional to the area covered by the hysteresis loop. This magnetisation hysteresis loop is produced with Bean model.

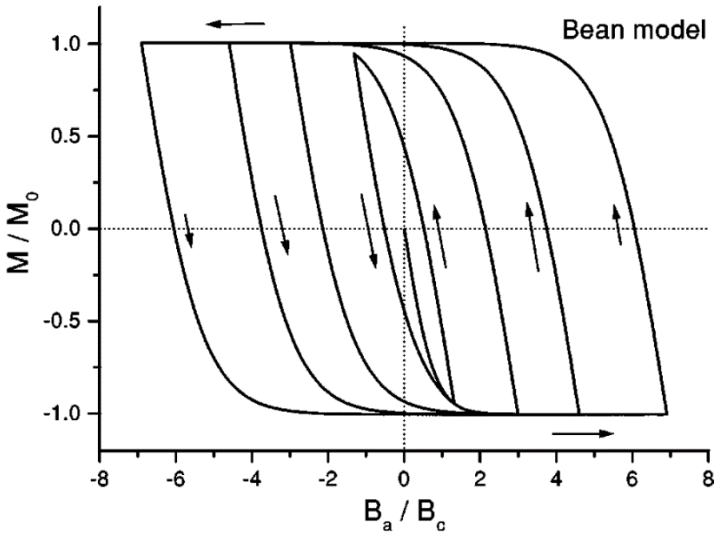

Figure 2.4.1 Magnetisation Hysteresis Loop of HTS Material by Bean Model [73]

An analytical equation is proposed in the work of [73] to calculate the magnetisation of the HTS thin disk material. The magnetisation is defined as the magnetic moment per unit volume. The magnetic moment $\boldsymbol{m}$ can be calculated as equation 2.18 showed below:

$$\boldsymbol{m} = \boldsymbol{\pi} \int_0^R \boldsymbol{r^2 J(r) dr} \tag{2.18}$$

Where R is the radius of the HTS thin disk. In a full penetration state described by the Bean model, assuming the initial critical current of the material to be J_{c0}, the magentisation of this material can be calculated as equation 2.19 below:

$$\frac{\boldsymbol{M}}{\boldsymbol{M_0}} = \frac{\boldsymbol{3}}{\boldsymbol{R^3}} \int_0^R \frac{\boldsymbol{J(r)}}{\boldsymbol{J_{c0}}} \boldsymbol{r^2 dr} \tag{2.19}$$

Where M_0 is equal to $J_{c0}R/3d$, d is defined as the thickness of the HTS disk. Coupling with the knowledge of the current density profile inside the HTS region and Kim's equation, the magnetisation hysteresis loop can be obtained as showed in figure 2.4.1. After obtaining the magnetisation of the HTS material, the energy W_m dissipated during a cycle of applied magnetic field B_a can be calculated as equation 2.20 below:

$$\boldsymbol{W_m = \int_{cycle} B_a(t) \frac{dM(t)}{dt} dt} \quad (2.20)$$

Coupling Loss

The coupling loss mostly exists in HTS conductors manufactured with multi-filamentary structure such as BSCCO and MgB_2. However, YBCO wires with striated design can also suffer from the coupling loss. The coupling loss exists between the superconducting filaments and the normal filling materials. Within the multi-filamentary or striated HTS wires, the alternating external magnetic field will induce an eddy current circulating between different HTS filaments / striates. This eddy current will inevitably pass through the normal material parts and generate losses amongst the normal material region. This type of the loss is less significant for YBCO wires manufactured with one single superconducting layer. Therefore, it is not considered within the scope of this thesis.

Eddy Current Loss in Normal Materials

As it is demonstrated in section 2.2.1, the 2G YBCO wires were manufactured with multiple layers of normal metallic materials sandwiching a thin layer of superconducting material. When an alternating external magnetic field is applied to the YBCO wire, it can affect the entire YBCO wire. Thus eddy current can also be induced within the normal material layers and contribute to a considerable part of the total loss generated. The method of reducing this type of the eddy current loss mainly involves increasing the resistance of the normal material layers to limit the induced eddy current. This type of eddy current loss does not directly relate to the characteristics of the superconducting layer and hence not considered by this model.

2.4.1.3. *Norris analytical equation*

Before the proposal of the first HTS finite element analysis model, Norris proposed an analytical equation in the work of [70] in 1969 to calculate the AC loss for a thin superconducting tape based on the original critical state model. The analytical equation proposed by Norris offered a convenient method to calculate the AC loss of the superconductors without involving computationally heavy finite element analysis and it fits well with the behavior of the low temperature superconductors. However, the critical state model which the Norris equation based on didn't consider the flux creep effect of the HTS materials and assumed discontinuous distribution for both the current density and electric field. The Norris equation also neglects the dependency between the critical current and the combined magnetic field. However, the Norris equation is proven to be successful in calculating the AC losses of the superconductor when no external magnetic field is presented. Although it is less flexible and generally under-estimates the self-field AC losses generated by the HTS material, it can still provide a good reference and check the accuracy of the HTS FEM models qualitatively. The thin film version of the Norris equation is presented in equation 2.21 below.

$$\boldsymbol{Q_{film}} = \frac{\boldsymbol{\mu_0 I_c^2 f}}{\boldsymbol{\pi}} \left[\left(\mathbf{1} - \frac{\boldsymbol{I_t}}{\boldsymbol{I_c}}\right)\mathbf{ln}\left(\mathbf{1} - \frac{\boldsymbol{I_t}}{\boldsymbol{I_c}}\right) + \left(\mathbf{1} + \frac{\boldsymbol{I_t}}{\boldsymbol{I_c}}\right)\mathbf{ln}\left(\mathbf{1} + \frac{\boldsymbol{I_t}}{\boldsymbol{I_c}}\right) - \left(\frac{\boldsymbol{I_t}}{\boldsymbol{I_c}}\right)^{\mathbf{2}}\right] \qquad (2.\ 21)$$

Where I_t represents the magnitude of the transport current, f represents the frequency of the transport current. The calculated power loss have the unit of watt per meter.

2.5. DC Loss in HTS Superconducting Cables

2.5.1. *Dynamic loss*

Under most of the scenarios, high temperature superconducting wires only dissipate extremely low losses when carrying DC currents. However, when such a DC carrying HTS wire is placed in an environment where an AC external magnetic field is presented, the losses on HTS wire will rise significantly. This additional loss incurred on a DC carrying HTS wire is named as the dynamic loss [71] [72] [73]. With HTS wires being applied to more types of power devices, the number of situations where dynamic loss cannot be neglected continue to increase. The impact of dynamic loss is particularly prominent for designs such as HTS machine field windings [74] [75] [76],

HTS fault current limiters [77] [78] [79] and in some cases, HTS power cables [80] [81] [82]. The presence of the dynamic loss can significantly increase the load of the cooling devices. Determining the level of the dynamic loss is thus crucial for the design of these HTS power applications. Since measuring and isolating the dynamic loss component from the total HTS transport loss is relatively difficult without sophisticate experiment setups, building numerical models become an effective method to estimate and study the dynamic loss behavior [83].

2.5.1.1. *Origin of the Dynamic Resistance and Loss*

The dynamic loss is considered as a dissipative loss. The energy dissipated in this process come directly from the transport current carried by the HTS wires. When a DC carrying HTS wire is exposed to an alternating magnetic field, an electrical resistance is observed within the HTS layer. This kind of electrical resistance arises due to the magnetic flux originally pinned in fixed pinning sites start to move around under the influence of the applied AC external field. The motion of the flux will interact with the DC transport current and impede the travel of the electrons. The impedance caused by the moving flux within the DC transport current carrying regions will demonstrate a 'resistive' pattern and therefore be named the dynamic resistance of the HTS material. This resistive behavior will cause an average electric potential drop across the superconducting wire during an AC cycle and thus induce dynamic losses across the HTS wire. The relationship between dynamic loss Q_{dn} and transport current I_t can be expressed by the equation 2.22 presented below where R_{dyn} is the equivalent dynamic resistance:

$$\boldsymbol{Q_{dyn} = R_{dyn} \cdot I_t^2} \quad (2.22)$$

From equation 2.22 above, it can be observed that the dynamic loss is heavily influenced by the transport current. However, it is also important to notice that the dynamic loss originates from the external AC magnetic field. The dynamic resistance is thus dependent to the amplitude of the external magnetic field. The dynamic resistance does not spawn simultaneously with the external magnetic field. Based on the study of [73], the dynamic loss is only significant when the amplitude of the applied external field $\boldsymbol{B_{ex}}$ is larger than a threshold field level B_{th}. This is because when an

external field is applied to the HTS wire, a screening current will be induced at the edge regions of the wire. This screening current will shield the core area of the wire from the external field and allow the magnetic flux to remain pinned during the whole AC cycle. Under this condition, the superconducting current can still flow relatively undisrupted within the shielded region without being subjected to the influence of any time - varying magnetic field. The dynamic resistance in this situation remains zero for the HTS wire. However, when the amplitude of $\boldsymbol{B_{ex}}$ exceeds the value of B_{th}, the induced shielding current can no longer stop the external field from penetrating into the core region throughout the entire AC cycle. The time - varying external field component presents at the wire core region will cause free movement of the flux and dynamic resistance is therefore generated.

Chapter 3. Modelling Method for the HTS Cables

3.1. Introduction

In this chapter will explain the simulation method of the 3D HTS power cable model in detail. Since the main objective of this thesis is to study the high temperature superconducting materials within the HTS cable, the modelling method discussed in this chapter focuses on analyzing the HTS materials. The rest of the non-superconducting structures such as the conductor substrates, the cable formers and the external casings are neglected. In order to establish the theoretical foundations for calculating the electromagnetic quantities of the HTS materials, a governing equation based on $\boldsymbol{T}$ formulation is deduced at the beginning of this chapter. Since the electromagnetic properties of the HTS materials can be highly anisotropic, the finite element method is introduced to discretize the analyzed area. The anisotropic homogenous medium approximation is used to simplify the cable mesh in order to reduce the computational power required to solve the discretized governing equation system. The simplified governing equation system is then solved by an iterative approach until the steady results are yielded. The end of the chapter discusses the process and strategy employed to build the final 3D cable model with details.

3.2. Simulation Governing Equation

Being one of the most promising power industry applications for the high temperature superconducting materials, the HTS power cables have attracted keen interests of the research community. In order to aid the design of the HTS power cables, a significant amount of previous works have been done towards the modelling of the HTS power cables [81] [84] [85] [86] [87]. Although various numerical models have been proposed to study the electromagnetic performances of HTS power cables, an important problem faced commonly by the researchers remain unaddressed: the trade-off between the 2D model and the 3D model. 2D models, though computationally efficient, cannot fully represent the real structure of the analyzed object. Meanwhile,

characteristics of higher accuracy and wider coverage on the details provided by the 3D model comes with heavy computation workload and higher requirements on hardware. The HTS cable model proposed in this thesis aims to find a compromise between the two options and provide a simplified 3D analysis tool to study the electromagnetic characteristics of the HTS power cables.

The model building process starts with establishing an appropriate equation system to represent the major electromagnetic properties of the HTS materials. The principle of this numerical model is based upon solving the Maxwell equation using the $\boldsymbol{T}$ formulation. Although several different formulations have been mentioned in the literature review section, the $\boldsymbol{T}$ formulation is finally selected to build the model for this project due to its better performance in terms of calculation speed, memory efficiency [15] and superior compatibility with the thin film assumption adopted for this model [84] [88] [89]. As the superconducting layer of the commercial HTS coated conductor usually has extremely large aspect ratio and approximate the shape of a thin film, in this model the assumption is made that the thickness of the superconducting layer is negligible. Since in this model, the target of analysis is only the superconducting layer, the region of analysis is divided into two components: the superconducting material and the air. The governing equation building process for the superconducting material starts with defining the iconic variable of the $\boldsymbol{T}$ formulation: the current vector potential $\boldsymbol{T}$. The relationship between the current vector potential $\boldsymbol{T}$ and the current density $\boldsymbol{J}$ in HTS material is presented in equation 3.1 below:

$$\boldsymbol{J} = \boldsymbol{\nabla} \times \boldsymbol{T} \tag{3. 1}$$

The $\boldsymbol{T}$ variable will be used to solve the Maxwell – Faraday equation as presented below:

$$\boldsymbol{\nabla} \times \boldsymbol{E} = -\frac{\boldsymbol{\partial B}}{\boldsymbol{\partial t}} \tag{3. 2}$$

According to Ohm's law, the electric field in the equation above can be rewrite as:

$$\boldsymbol{E} = \boldsymbol{\rho} \cdot \boldsymbol{J} \tag{3. 3}$$

In equation 3.3, ρ represents the resistivity of the superconducting material. The magnetic field in equation 3.2 in this case can be further divided into two parts: the external magnetic field $\boldsymbol{B_e}$ and the self-induced magnetic field $\boldsymbol{B_s}$.

$$\boldsymbol{B} = \boldsymbol{B_e} + \boldsymbol{B_s} \tag{3. 4}$$

If the equation 3.3 and 3.4 are applied back into equation 3.2, then it will yield the following result:

$$\boldsymbol{\nabla} \times (\boldsymbol{\rho} \cdot \boldsymbol{J}) = -\frac{\boldsymbol{\partial}(\boldsymbol{B_e}+\boldsymbol{B_s})}{\boldsymbol{\partial t}} \tag{3. 5}$$

As the self-induced magnetic field (by transport current) can be calculated by Biot – Savart law as represented below:

$$\boldsymbol{B_s} = \frac{\boldsymbol{\mu_0}}{\boldsymbol{4\pi}} \int_{\boldsymbol{V}} \frac{\boldsymbol{J}\times\boldsymbol{r}}{|\boldsymbol{r}|^3}\boldsymbol{dV} \tag{3. 6}$$

Where μ_0 is the permeability of the free space, $\boldsymbol{r}$ is the space displacement vector and V represents the volume of material that the equation integrals over. Combining the equation 3.6 with the equation 3.5 yields:

$$\boldsymbol{\nabla} \times (\boldsymbol{\rho} \cdot \boldsymbol{J}) = -\frac{\boldsymbol{\partial}}{\boldsymbol{\partial t}}\left(\frac{\boldsymbol{\mu_0}}{\boldsymbol{4\pi}} \int_{\boldsymbol{V}} \frac{\boldsymbol{J}\times\boldsymbol{r}}{|\boldsymbol{r}|^3}\boldsymbol{dV} + \boldsymbol{B_s}\right) \tag{3. 7}$$

Now in the form of equation 3.7, it is very hard to isolate the current density variable $\boldsymbol{J}$ with the presence of curl operator. Therefore, it is very hard to directly solve the equation in its current form. In order to tackle this problem, the current vector potential $\boldsymbol{T}$ becomes very useful. Substituting equation 3.1 into equation 3.7 yields the following result:

$$\boldsymbol{\nabla} \times (\boldsymbol{\rho}\boldsymbol{\nabla} \times \boldsymbol{T}) = -\frac{\boldsymbol{\partial}}{\boldsymbol{\partial t}}\left(\frac{\boldsymbol{\mu_0}}{\boldsymbol{4\pi}} \int_{\boldsymbol{V}} \frac{\boldsymbol{\nabla}\times\boldsymbol{T}\times\boldsymbol{r}}{|\boldsymbol{r}|^3}\boldsymbol{dV} + \boldsymbol{B_s}\right) \tag{3. 8}$$

In finite element analysis, the grid points are normally divided into two types: the field points and the source points. Since the $\boldsymbol{T}$ variable at the right side of the equation 3.8 is responsible for the induction of the magnetic field at some point within the analyzed region, it is defined as the $\boldsymbol{T}$ variable at the source element. Meanwhile the $\boldsymbol{T}$ variable at the left side of the equation 3.8 is defined as $\boldsymbol{T}$ variable at the field

element. To avoid confusion, in governing equation, the field element potential is marked as $\boldsymbol{T_1}$ and the source element potential is marked as $\boldsymbol{T_2}$.

$$\boldsymbol{\nabla \times (\rho \nabla \times T_1) = -\frac{\partial}{\partial t}\left(\frac{\mu_0}{4\pi}\int_V \frac{\nabla \times T_2 \times r}{|r|^3} dV + B_s\right)} \quad (3.9)$$

Under the realistic circumstance, the current carried by the HTS material will only flow within the material. Also based on the assumption of negligible material thickness, the direction of the current vector potential can only be normal to the wide surface of the HTS coated conductor. Therefore, this thesis defines unit vector $\boldsymbol{n}$ to be the vector normal to the surface containing the field elements and unit vector $\boldsymbol{n'}$ to be the vector normal to the surface containing the source elements. As a result, equation 3.9 can be re-wrote as presented below:

$$\boldsymbol{\nabla \times (\rho \nabla \times T_1) = -\frac{\partial}{\partial t}\frac{\mu_0}{4\pi}\int_V \frac{\nabla \times (T_2 \cdot n') \times r}{|r|^3} dV - \frac{\partial B_e}{\partial t} \cdot n} \quad (3.10)$$

Based on the thin film assumption made at the beginning of this section, the HTS coated conductor analyzed can be regarded as homogeneous and with isotropic electromagnetic property along its thickness dimension. Assuming the HTS material layer has a thickness of *h*, equation 3.10 can be further simplified and re-arranged as below:

$$\boldsymbol{\rho \nabla^2 T_1 - \frac{\mu_0 h}{4\pi} \cdot \frac{\partial}{\partial t}\int_s \frac{\nabla \times (T_2 \cdot n') \times r}{|r|^3} \cdot n dS - \frac{\partial B_e}{\partial t} \cdot n = 0} \quad (3.11)$$

The continuous integration form of the governing equation system has therefore been derived in equation 3.11. In order to represent the superconducting properties of the HTS material, the resistivity ρ is coupled with the current density $\boldsymbol{J}$ by the $E - J$ power law introduced in section 2.3.2 as:

$$\boldsymbol{E = \rho \cdot J = E_0 \left(\frac{J}{J_c(B)}\right)^n} \quad (3.12)$$

$$\boldsymbol{\rho = E_0 \left(\frac{J}{J_c(B)}\right)^{n-1} \cdot \frac{1}{J_c(B)}} \quad (3.13)$$

As mentioned in the previous section, the other major feature of the HTS materials is the dependency of the critical current level to the magnetic field strength. This dependency is described by the Kim – Anderson model and also built into the equation

system describing this model. These dependency are described in equation 3.14 and below:

$$\boldsymbol{J_c(B) = \frac{J_{c0}}{1+\frac{|B|}{B_0}}} \quad (3.\ 14)$$

Where in equation 3.14, J_{c0} represents the initial critical current density of the HTS material when no magnetic field is presented. $\boldsymbol{B}$ represents the magnetic field strength and B_0 is a constant depend on the property of the specific material.

3.3. Analyzed Region

After deriving the continuous integration form of the governing equation in equation 3.11, measures must be taken to ensure that the equation in 3.11 can be translated into open source code and ultimately solvable for the computer. In order to make equation 3.11 translatable for open source coding and representing the highly anisotropic electromagnetic characteristic of the HTS material, the thin film conductor is divided into a number of elements as illustrated in figure 3.3.1 below, assumptions can be made that the HTS conductor have an infinite length in *x* dimension.

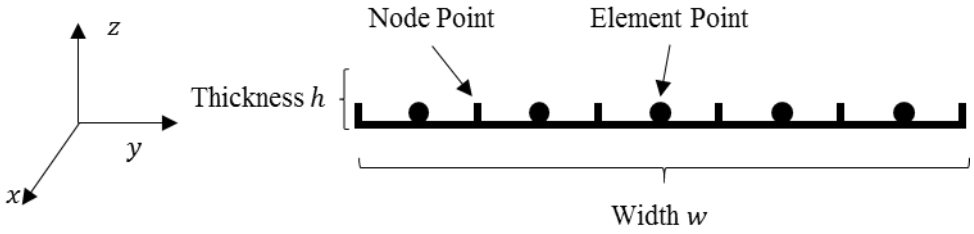

Figure 3.3.1 Node Points and Element Points of a HTS Conductor Mesh

Since in this 2D case, the HTS conductor is assumed to be infinitely long in *x* dimension, combining the Biot-Savart law for infinitely long current lines, the equation 3.11 can be re-wrote as:

$$\boldsymbol{\rho\nabla^2 T_1 - \frac{\mu_0 h}{2\pi}\cdot\frac{\partial}{\partial t}\sum_1^{etot}\frac{l_e\nabla\times(T_2\cdot n')\cdot\hat{x}}{|r|} - \frac{\partial B_e}{\partial t}\cdot n = 0} \quad (3.\ 15)$$

Where $etot$ represents the total number of the source element the conductor is divided into, l_e represents the width of a single element in *y* dimension, $\hat{\boldsymbol{x}}$ represents the unit vector in the direction of *x* dimension.

In the case of building 3D model with this equation system, the evolution of the equation 3.11 has to proceed with the Biot-Savart Law for finitely long current segments. Since the 3D model proposed in this thesis is based on the 2D model, the detailed form of the governing equation used for the 3D model will be explained in later sections.

3.3.1. *Finite Element Analysis (FEA)*

After discretizing the analysed material, the appropriate method must be applied to the discretized governing equation to convert the originally continuous physical variables to their discrete analogue form rigorously. By examining the governing equation in equation 3.15, it can be clearly observed that in general, equation 3.15 contains a big component of partial derivatives. According to the research in [90] [91] [92] [93], the Galerkin method is an effective tool to interpolate the derivative equations. Therefore in order to implement the finite element analysis, equation 3.15 is interpolated by the nodal shape function N_i of the Galerkin method.

$$\int_V \underbrace{N_i\left\{\rho\nabla^2 T_1}_{term\ 1} \underbrace{- \frac{\mu_0 h}{2\pi}\cdot\frac{\partial}{\partial t}\sum_1^{etot}\frac{l_e\nabla\times(T_2\cdot n')\cdot\hat{x}}{|r|}}_{term\ 2} \underbrace{- \frac{\partial B_e}{\partial t}\cdot n\right\}}_{term\ 3} dV = 0 \quad (3.16)$$

The interpolated equation 3.16 can be further breakdown into a linear combination of three integration terms as marked out above. Since the thin film approximation is applied for this governing equation, based on the Green's theorem and applying the dimension reduction, term 1 in equation 3.16 can be transformed as below:

$$\int N_i\rho\nabla^2 T_1 dV = \sum_{boundary}(\rho N_i\frac{\partial T^{boundary}}{\partial z}) - \int \rho\,(\frac{\partial N_i}{\partial y})\cdot(\frac{\partial T_1}{\partial y})dy \quad (3.17)$$

The term 2 of equation 3.16 can also be re-wrote as below:

$$\int N_i\frac{\mu_0 h}{2\pi}\cdot\frac{\partial}{\partial t}\sum_1^{etot}\frac{l_e\nabla\times(T_2\cdot n')\cdot\hat{x}}{|r|}dV = \int N_i\frac{\mu_0 h}{2\pi}\cdot\frac{\partial}{\partial t}\sum_1^{etot}\left(\frac{l_e}{|r|}\cdot\frac{\partial T_2}{\partial y}\right)dy \quad (3.18)$$

After substituting equation 3.17 and 3.18 into equation 3.16, the equation 3.16 can be re-arranged in to the following form:

$$\begin{aligned}&\int\left\{\rho\left(\frac{\partial N_i}{\partial y}\right)\cdot\left(\frac{\partial T_1}{\partial y}\right) + N_i\frac{\mu_0 h}{2\pi}\cdot\frac{\partial}{\partial t}\sum_1^{etot}\left(\frac{l_e}{|r|}\cdot\frac{\partial T_2}{\partial y}\right) + N_i\frac{\partial B_e}{\partial t}\cdot n\right\}dy \\ =\ &\sum_{boundary}(\rho N_i\frac{\partial T^{boundary}}{\partial z})\end{aligned} \quad (3.19)$$

The summation of the boundary current vector potential term on the right side of the equation 3.19 equals to zero. As type one boundary condition is used in this model, and vector $\boldsymbol{T}$ does not change with respect to *z* direction.

Since the thickness of the HTS conductor is neglected, the conductor cross-section can be discretized with line elements with two nodal values. Therefore, based on the property of nodal shape function, the current vector potential $\boldsymbol{T}$ on k^{th} element $\boldsymbol{T_k}$ can be expressed as below:

$$\boldsymbol{T_k = N_{k1} \cdot T_{ka} + N_{k2} \cdot T_{kb}} \quad (3.20)$$

Where $\boldsymbol{T_{ka}}$ and $\boldsymbol{T_{kb}}$ represents the current vector potential $\boldsymbol{T}$ value at two nodes of the element. N_{k1} and N_{k2} are the two components of the nodal shape function. Based on the Galerkin method, the definition for these two components are as presented below:

$$\boldsymbol{N_{k1} = 1 - \frac{y - y_{k1}}{y_{k2} - y_{k1}}} \quad (3.21)$$

$$\boldsymbol{N_{k2} = \frac{y - y_{k1}}{y_{k2} - y_{k1}}} \quad (3.22)$$

In equation 3.21 and 3.22, y_{k1} represents the coordinate of the left node of k^{th} element whilst y_{k2} represents the coordinate of the right node. Since in this model, quadratic type element is used to divide the analysed region as demonstrated in figure 3.3.2. In Galerkin method, a normalized local coordinate system will be assigned to each quadratic element.

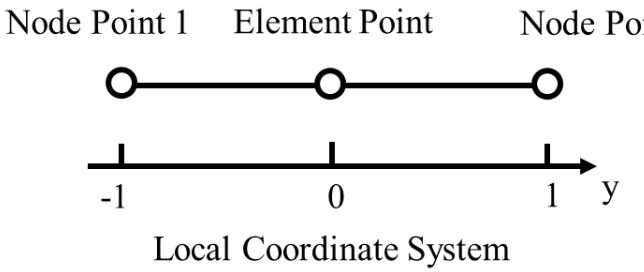

Figure 3.3.2 Normalized Local Coordinate System for Quadratic Elements

As the physically continuous variable being discretised during the finite element analysis, error and mismatches will inevitably occur. The Galerkin method also

provides the way to minimise such errors mathematically by apply an additional layer of integration over each element and equating the governing equation to zero. Therefore, substituting equation 3.20 back into 3.19 and re-writing 3.19 into the ultimate form yields:

$$\sum_{all\ elements}\left\{\int_{-1}^{1}\left[\boldsymbol{\rho}\left(\frac{\partial N_i}{\partial y}\right)\cdot\left(\frac{\partial}{\partial y}\sum_{j=1}^{2}\boldsymbol{N_{ij}}\,\boldsymbol{T_{1j}}\right)+\boldsymbol{N_i}\sum_{j=1}^{2}\boldsymbol{N_{ij}}\frac{\boldsymbol{\mu_0 h}}{\boldsymbol{2\pi}}\cdot\frac{\boldsymbol{\partial}}{\boldsymbol{\partial t}}\sum_{1}^{etot}\left(\frac{\boldsymbol{l_e}}{|r|}\cdot\frac{\boldsymbol{\partial T_2}}{\boldsymbol{\partial y}}\right)+\boldsymbol{N_i}\sum_{j=1}^{2}\boldsymbol{N_{ij}}\frac{\boldsymbol{\partial B_e}}{\boldsymbol{\partial t}}\cdot\boldsymbol{n}\right]\frac{\boldsymbol{dy}}{\boldsymbol{d\psi}}\boldsymbol{d\psi}\right\}=\mathbf{0} \quad (3.\ 23)$$

Where ψ represents the error introduced by applying the finite element analysis. Based on the fully discretized form of the governing equation in 3.23, the equation can then be translated into the open source FORTRAN code. The electric resistivity ρ is coupled with the critical current density J_c according to the E-J power law as discussed in the previous section and J_c is further coupled with the combined magnetic field strength $\boldsymbol{B}$ according to Kim's model. These dependencies are also built into the numerical model. Since the governing equation in 3.23 is solved by assuming an initial boundary condition, an iterative approach is employed in the code to ensure the final solution is stable and consistent. Details of the iteration method used will be discussed in the coming section.

3.3.2. *The Anisotropic Homogenous Medium Approach*

The 2D form of the governing equation has been introduced so far. The primary object of this thesis, which is to build a 3D model capable of demonstrating the realistic design features of the HTS power cables, requires further development of the model. The 3D model can be built with two approaches in general: either to further evolve the governing equation with 3D interpolation functions and adopt full 3D form for all variables or to implement simplify strategies to build the model. It is well known that adopting full 3D analysis for the HTS applications is a daunting task that will need heavy computational power in order to deliver the final results. Many research works have adopted this approach with the help of commercial 3D FEA software to study the HTS power applications [87] [65] [15] [94]. However, the larger amount of calculation often limits this type of model and force many of these 3D models to reduce the mesh density in order to save solving time. This reduces the resolution of the 3D analysis and limits the ability to study into the distributions of the electromagnetic quantities.

To tackle this problem, the model built in this thesis adopts the simplify approach. The strategy implemented in this model is called the anisotropic homogenous medium approach introduced by the works in [95] [96].

The principle of this approach is to apply homogenous approximation to short sections of the material and to represent the electromagnetic characteristics of these short sections with simplified mesh. It is suggested in [95] that the electromagnetic properties of a stack of superconductor tapes can be effectively approached by an equivalent anisotropic bulk model. It is also suggested by [96] that in a large HTS stack, neighbouring wires experience very similar electromagnetic environment. Thus in modelling, a bulk can be breakdown into smaller sub-domains to represent the electromagnetic characteristics of different HTS tapes in a stack. Similar philosophy is also implemented when building this model. The simplified 3D HTS conductor wires are further discretized into several finite length sections as demonstrated in figure 3.3.3 below.

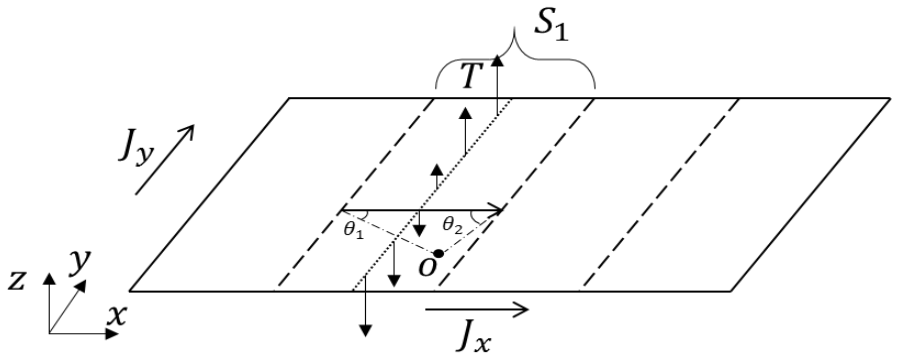

Figure 3.3.3 Anisotropic Homogenous Medium Approximation of the 3D HTS conductor tape.

Angles θ_1 and θ_2 are the angles between the source current vector and the distances from point O to both ends of the source current vector line.

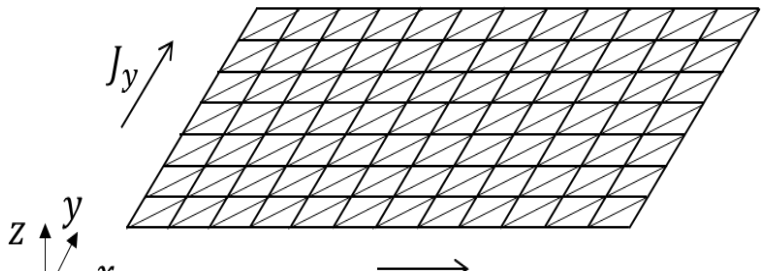

Figure 3.3.4 Conventional finite element analysis meshing method

In figure 3.3.3, each sub-section is assigned a small length in *x* dimension in order to ensure that the combined magnetic field exerted on these sub-sections remains relatively constant along the *x* dimension. Thus, the $\boldsymbol{T}$ vector distribution within each sub-section can be considered homogenous along the *x* dimension and equal to the $\boldsymbol{T}$ vector distribution at the centre cross-section of each sub-sections. The merit of this approach is most significant when a sample with complex geometry (such as a section of HTS cable with twisted conductors) is simulated. The conventional FEA methods mesh the analysed region with either trigonal or rectangular elements as presented in figure 3.3.4. This will treat the analysed region as a continuous surface and provide an accurate estimation. However, such method will inevitably increase the difficulty of solving the governing equation system due to the complexity introduced by using interpolation functions with higher degree of freedom. The method proposed in this study approaches the complex geometry by dividing the object into small homogenous sub-sections. The complexity of the governing equation system is effectively reduced. Thus, reduce the time needed when simulating HTS samples in 3D while maintaining good accuracy.

The net current density for every element was derived from the vector potential $\boldsymbol{T}$ distribution as demonstrated in figure 3.3.3. The net current density is split into two current density components, $\boldsymbol{J_x}$ (perpendicular to the analysed subsection) and $\boldsymbol{J_y}$ (parallel to the subsection). Under the case of the single thin HTS tape simulation, due to the presence of an overall transport current (assuming flowing in *x* direction), the $\boldsymbol{T}$ vectors are generally distributed following a pattern with opposite polarity towards both edges of the tape. Therefore, it is considered that $\boldsymbol{J_x}$ component has overall a predominant role affecting the electromagnetic properties of the tape. For simulation cases with more complex geometry such as when simulating HTS cables with twisted conductors, the effect of $\boldsymbol{J_y}$ will be considered to allow more realistic analysis.

Given the discussion made above, the governing equation can be extended into 3D by applying the 3D Biot-Savart law. Since a particular sub-section within the HTS tape conductor need to be set with a finite length to increase the degree of freedom for the mesh, the finitely long current segment form of the Biot-Savart equation need to be

used. Therefore, the 3D governing equation can be transformed from equation 3.15 to the form as presented below:

$$\boldsymbol{\rho\nabla^2 T_1} - \frac{\boldsymbol{\mu_0 h}}{\boldsymbol{4\pi}} \cdot \frac{\boldsymbol{\partial}}{\boldsymbol{\partial t}} \sum_{\mathbf{1}}^{\boldsymbol{etot}} \frac{\boldsymbol{l_e \nabla \times (T_2 \cdot n') \cdot \hat{x}}}{\boldsymbol{|r|}} (\boldsymbol{cos\,\theta_1 + cos\,\theta_2}) - \frac{\boldsymbol{\partial B_e}}{\boldsymbol{\partial t}} \cdot \boldsymbol{n} = \mathbf{0} \qquad (3.\ 24)$$

After that, the same FEM interpolation process can be applied to equation 3.24 and therefore allows this 3D form of the governing equation to be transformed to its discretized form and allows open source programming to proceed. After solving the governing equation presented in equation 3.24, the distribution of the vector potential $\boldsymbol{T}$ on every field point will be obtained. The 3D current density component $\boldsymbol{J_x}$ and $\boldsymbol{J_y}$ can then be derived according to the definition presented in equation 3.1 as:

$$\begin{bmatrix} \boldsymbol{J_x} \\ \boldsymbol{J_y} \\ \boldsymbol{J_z} \end{bmatrix} = \begin{bmatrix} \frac{\boldsymbol{\partial(T \cdot n_z)}}{\boldsymbol{\partial y}} & - & \frac{\boldsymbol{\partial(T \cdot n_y)}}{\boldsymbol{\partial z}} \\ \frac{\boldsymbol{\partial(T \cdot n_x)}}{\boldsymbol{\partial z}} & - & \frac{\boldsymbol{\partial(T \cdot n_z)}}{\boldsymbol{\partial x}} \\ \frac{\boldsymbol{\partial(T \cdot n_y)}}{\boldsymbol{\partial x}} & - & \frac{\boldsymbol{\partial(T \cdot n_x)}}{\boldsymbol{\partial y}} \end{bmatrix} \qquad (3.\ 25)$$

It is important to note that $\boldsymbol{n_x}$, $\boldsymbol{n_y}$ and $\boldsymbol{n_z}$ are the normal vectors of the HTS wire surface. Since the $\boldsymbol{T}$ vector is always perpendicular to the surface of the HTS wire conductor as its thickness is negligible, the value of $\boldsymbol{J_z}$ will remain zero under all circumstances. This mathematical result is also reasonable for the rules of physics as the direction of $\boldsymbol{T}$ vector effectively confines the current flow within the tape shaped HTS conductor. In case where a short section within a relatively long superconducting tape is studied, two sub-sections with semi-infinite length are added to both ends of the analyzed section to represent the effect of field points beyond the boundary of the analyzed region.

After deriving the current density distribution within the analyzed region, the magnetic field, loss and conductivity distribution can be effectively calculated. Any other electromagnetic quantities of interest can be further derived with the knowledge of the $\boldsymbol{T}$ distributions mentioned above.

Following the discussions made above, the 3D cable mesh can be simplified with the anisotropic homogenization approximation. The complete structure of the HTS cable can also be first discretized into several different short sub-domains. The short sub-

domains can be approximated by the 2D cross-sectional model and further reduce the amount of calculation needed to conduct 3D analysis. The 3D cable building process will be introduced in detail in coming sections.

3.4. Solving the Governing Equation

Since the governing equation system has been established in the previous section, the problem comes next is to develop a process of solving this equation system efficiently and accurately. In this section, the complete process of solving the governing equation system and deriving the final steady state results will be discussed in detail. The mathematical techniques used during this process will also be introduced.

The starting point of solving the governing equation system built with finite element analysis is setting up the boundary conditions. The setting of boundary condition requires proper assumptions to reflect the initial conditions of the equation system. Based on the characteristics of the governing equation, the unknown variable $\boldsymbol{T}$ is immediately separable from the spatial displacement variables (details will be presented in equation 3.27 in the next section), the boundary value of $\boldsymbol{T}$ vector can be directly set by applying the Dirichlet boundary condition. The principle of the Dirichlet condition is presented below:

$$\boldsymbol{\Phi}(\vec{\boldsymbol{r}})|_{\vec{\boldsymbol{r}}\in\boldsymbol{\Gamma}} = \boldsymbol{h}(\vec{\boldsymbol{r}}) \tag{3. 26}$$

Where in equation 3.26, $\boldsymbol{\Phi}$ represents the equation to be solved, $\vec{\boldsymbol{r}}$ represents the spatial displacement vector, Γ represents the boundary of the analysed domain and h represents the initial value of the boundary elements. Implementing the Dirichlet boundary condition simply requires setting all nodal points on the boundary with assumed values of the potential. The interior nodes of the analysed domain are kept as unknowns waiting to be solved. The solution is derived in a progressive manner from the boundary to the centre. In order to set the initial values for the boundary nodal points, assumptions are made that, at the beginning, all the transport current are distributed on the two boundary nodal points for every sub-domain within the analysed region. This assumption is also physically reasonable as the magnetic field penetration of the superconductor indeed starts from the edges of the conductor and gradually infiltrates to the centre region. Therefore, the transport current starts flowing at the

small space around the edges of the conductor and then, following the magnetization of the conductor, finally reaches steady state. The process mentioned above happens very quickly in real world. In order to ensure the continuity of each individual HTS conductor, for sub-domains belonging to the same HTS conductor, identical values are set for all the nodal points.

Since the equation system is solved by assuming the initial boundary condition, the results derived by one direct solution still contain some error. Therefore, iterative solving methods must be introduced to ensure that the final results are steady and can be reproduced. The iterative approach adopted will be introduced in the following section. The general procedure used to derive the final results is presented in the flow chart 3.4.1 below:

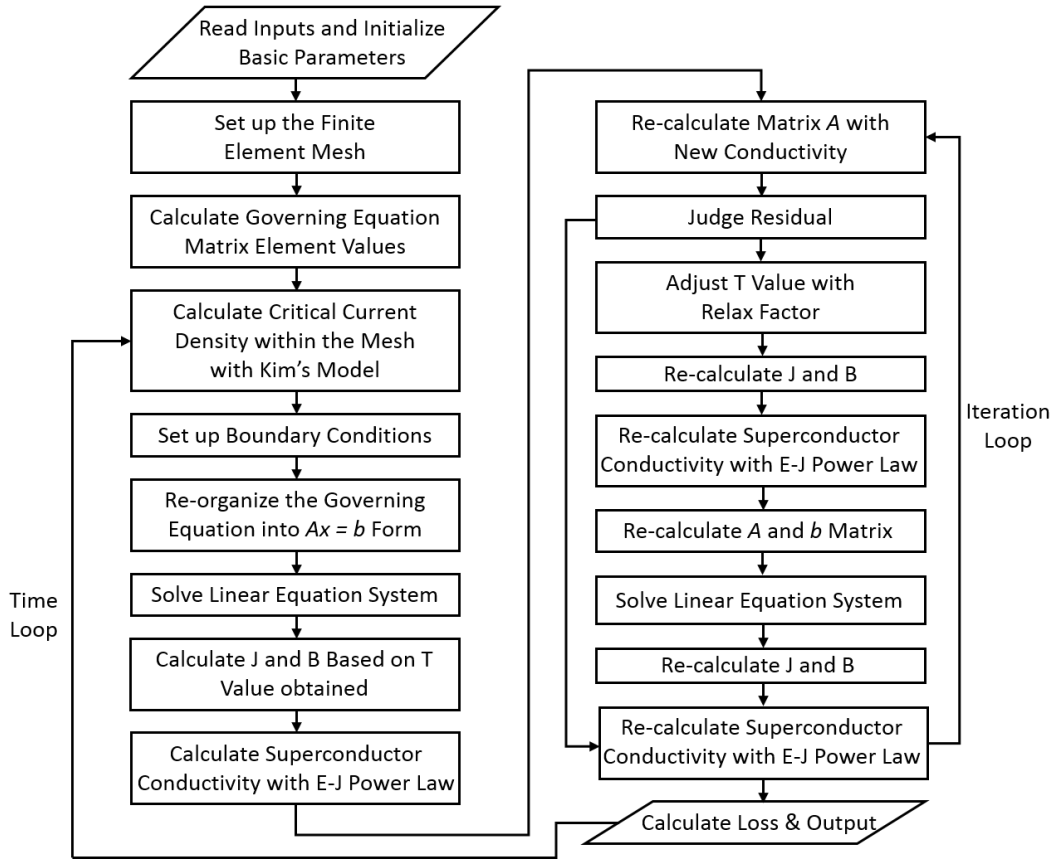

Figure 3.4.1 Flow Chart for Solving the Governing Equation System

As it can be observed from flow chart 3.4.1 above, the final answer for each input is derived through iteration. However, if a time varying transport current is simulated to represent an HTS cable carrying AC current, an additional time loop needs to be

created outside the iteration loop. For this case the full AC cycle will also be broken down into multiple steps, the magnitude of the input current will be adjusted according to the temporal value of the sine shape AC current signal.

3.4.1. *Characteristics of the Target Matrix*

In this section, the resultant matrix form of the governing equation will be presented. The initial boundary condition used to solve the governing equation system have been define in the previous section, the issue presented next will be how to solve such matrix system appropriately. In order to identify the suitable solving tool for the equation matrix, the characteristics of the matrix system must be studied first.

Based on the discussion made in the previous section, if we take a small section of the HTS conductor with 2 elements, 3 nodes as example, the matrix form of the first term of the governing equation is shown as below:

$$2\begin{bmatrix} \boldsymbol{\rho}(-\frac{1}{y_2-y_1})\cdot(-\frac{1}{y_2-y_1}) & \cdots & \boldsymbol{\rho}(-\frac{1}{y_{i+1}-y_i})\cdot(\frac{1}{y_{i+1}-y_i}) & \cdots & \mathbf{0} \\ \vdots & & \vdots & & \vdots \\ \boldsymbol{\rho}(\frac{1}{y_{i+1}-y_i})\cdot(-\frac{1}{y_{i+1}-y_i}) & \boldsymbol{\rho}\left(\frac{1}{y_i-y_{i-1}}\right)\cdot\left(\frac{1}{y_i-y_{i-1}}\right)+\boldsymbol{\rho}(-\frac{1}{y_{i+1}-y_i})\cdot(-\frac{1}{y_{i+1}-y_i}) & & \boldsymbol{\rho}(-\frac{1}{y_{i+1}-y_i})\cdot(\frac{1}{y_{i+1}-y_i}) \\ \vdots & & \vdots & & \vdots \\ \mathbf{0} & \cdots & \boldsymbol{\rho}(\frac{1}{y_{i+1}-y_i})\cdot(-\frac{1}{y_{i+1}-y_i}) & \cdots & \boldsymbol{\rho}(\frac{1}{y_{n+1}-y_n})\cdot(\frac{1}{y_{n+1}-y_n}) \end{bmatrix}\begin{bmatrix} \boldsymbol{T_1} \\ \vdots \\ \boldsymbol{T_i} \\ \vdots \\ \boldsymbol{T_{n+1}} \end{bmatrix} \quad (\mathbf{3}.27)$$

The matrix form of the second term of the governing equation will be:

$$\begin{bmatrix} \frac{\mu_0 h}{2\pi}\cdot\frac{l_1}{r_{11}}\cdot(-\frac{1}{y_2-y_1}) & \cdots & \frac{\mu_0 h}{2\pi}\cdot\frac{l_i}{r_{1i}}\cdot\left(\frac{1}{y_2-y_1}\right)+\frac{\mu_0 h}{2\pi}\cdot\frac{l_{i+1}}{r_{1(i+1)}}\cdot(-\frac{1}{y_2-y_1}) & \cdots & \frac{\mu_0 h}{2\pi}\cdot\frac{l_{(n+1)}}{r_{1(n+1)}}\cdot(\frac{1}{y_2-y_1}) \\ \vdots & & \vdots & & \vdots \\ \frac{\mu_0 h}{2\pi}\cdot\frac{l_i}{r_{1i}}\cdot(-\frac{1}{y_2-y_1}) & & \frac{\mu_0 h}{2\pi}\cdot\frac{l_i}{r_{ii}}\cdot\left(\frac{1}{y_2-y_1}\right)+\frac{\mu_0 h}{2\pi}\cdot\frac{l_{i+1}}{r_{(i+1)(i+1)}}\cdot(-\frac{1}{y_2-y_1}) & & \frac{\mu_0 h}{2\pi}\cdot\frac{l_{(n+1)}}{r_{i(n+1)}}\cdot(\frac{1}{y_2-y_1}) \\ \vdots & & \vdots & & \vdots \\ \frac{\mu_0 h}{2\pi}\cdot\frac{l_n}{r_{1n}}\cdot(-\frac{1}{y_2-y_1}) & \cdots & \frac{\mu_0 h}{2\pi}\cdot\frac{l_i}{r_{ni}}\cdot\left(\frac{1}{y_2-y_1}\right)+\frac{\mu_0 h}{2\pi}\cdot\frac{l_{i+1}}{r_{(n+1)(i+1)}}\cdot(-\frac{1}{y_2-y_1}) & \cdots & \frac{\mu_0 h}{2\pi}\cdot\frac{l_{(n+1)}}{r_{(n+1)(n+1)}}\cdot(\frac{1}{y_2-y_1}) \end{bmatrix}\begin{bmatrix} \frac{T_1-T_{1,old}}{\Delta t} \\ \vdots \\ \frac{T_i-T_{i,old}}{\Delta t} \\ \vdots \\ \frac{T_{n+1}-T_{n+1,old}}{\Delta t} \end{bmatrix} \quad (\mathbf{3}.28)$$

The $\boldsymbol{T_{i,old}}$ in equation 3.28 represents the value of the $\boldsymbol{T}$ vector at previous time step and which is a known value. The matrix form of the third term of the governing equation will be:

$$\begin{bmatrix} \frac{\partial B_e}{\partial t} \\ \vdots \\ \frac{\partial B_e}{\partial t} \\ \vdots \\ \frac{\partial B_e}{\partial t} \end{bmatrix} \quad (3.29)$$

As it can be seen from the matrix form of the governing equation above, the coefficient matrices of the unknown vectors consist mostly of non-zero values. In order to allow the governing matrices be solved by the linear system solver packages of the industrial standard, three terms of the governing matrices are eventually re-arranged into the following form:

$$\boldsymbol{Ax} = \boldsymbol{b} \tag{3. 30}$$

$\boldsymbol{A}$ matrix contains all of the coefficient terms of the unknown vectors. The term $\boldsymbol{x}$ represents the vector containing all the unknown variables, namely $\boldsymbol{T}$ vector on every non-boundary nodal points across the domain. The term $\boldsymbol{b}$ is the vector containing all of the rest constants. After re-arranging the governing equation to its ultimate matrix form, it is found that the coefficient matrix $\boldsymbol{A}$ inherent the characteristic of the coefficient matrices in equation 3.27 and 3.28 and it is also comprised of non-zero values. Although most of the terms within matrix $\boldsymbol{A}$ have very small values due to the superconducting properties of the HTS material, the matrix $\boldsymbol{A}$ has to be identified as a dense matrix.

Given the discussions made above, the governing matrix system cannot be solved by using the sparse matrix solver of generally higher computational efficiency. Therefore the general purpose solver LAPACK is finally chosen to solve the governing matrix system for all the models built in this project. The LAPACK package offers a great computation efficiency as it conducts computation by directly calling Basic Linear Algebra Subprograms (BLAS) libraries to avoid additional layers of command executions. It also offers great compatibility with the programming language used to build this numerical model as the LAPACK package itself is also written under FORTRAN environment. The accuracy and stability of the LAPACK package are widely acknowledged by the industry.

3.4.2. *Workload Sharing and Parallel Computing*

The previous section discussed the method used to solve the governing equation system with details. However, because the coefficient matrix of the unknown $\boldsymbol{T}$ vector is a dense matrix, the computational load for solving such an equation system is still very heavy if a large number of nodal points are presented within the analyzed domain.

It is found during the modelling process that the limited computing power provided by single CPU is not enough to tackle the large equation system brought about by simulating the 3D full HTS cable models. Therefore, it is crucial to find a way to upgrade the code to be scalable and have the ability to utilize the computing power of multiple CPUs. Such task distribution structure is commonly referred to as the parallel computing. The deployment of the parallel computing structure is a common practice for the numerical modelling research community.

The parallel computing structure possesses the advantage of enabling sharing of computing workload between several different CPUs. On the other hand, it comes with drawbacks such as additional synchronizing time, potential risk of racing problem and complexity of workflow management. The over-use of parallel computing structure could result in even worse overall computing performance. Therefore the deployment of the parallel computing structure must be treated with care and only apply to workload that have to be shared. After analyzing the program with the code-profiling tool GRPOF, it is found that the governing equation solving process consumes over 80% of the simulation time. Thus, the workload sharing with parallel structure must be deployed for the governing equation matrix solving section in order for the model to be practical.

Unlike the parallelization of the repetitive execution structure in programming, the workload sharing parallelization needed to solve the governing equation matrix requires careful decomposition and re-distribution of the matrix data and cannot be done just by directly calling functions. In order for multiple CPUs to work concurrently on a same calculation task, one needs to divide the task manually for the CPUs in order for them to work on their individual part of the task. While the direct matrix dividing techniques such as the block distribution and cyclic distribution might work if the dimension of the matrix is fixed, it is very inflexible for the need of the numerical model developed in this project as the number of the grid points will change frequently according to the need of the simulation. The technique of the block distribution is demonstrated in figure 3.4.2 below:

Figure 3.4.2 Block Distribution of Matrix*

* The regions marked by different colour schemes in figure 3.4.2 represent data assigned to different CPU processes. For example, data elements from A_{11} to A_{33} are assigned to CPU 1 while A_{14} to A_{36} are assigned to CPU 2.

In figure 3.4.2 above, the different color in matrix blocks represent different CPU processes. The direct decomposition approach works well as presented above when the matrix dimension is known and the size of the problem matrix can be perfectly divided amongst the CPU processes. However, when the size of the problem matrix is not fixed for direct decomposition, the calculation issue will occur due to the inclusion of the unnecessary data or the missing of the data components as demonstrated below:

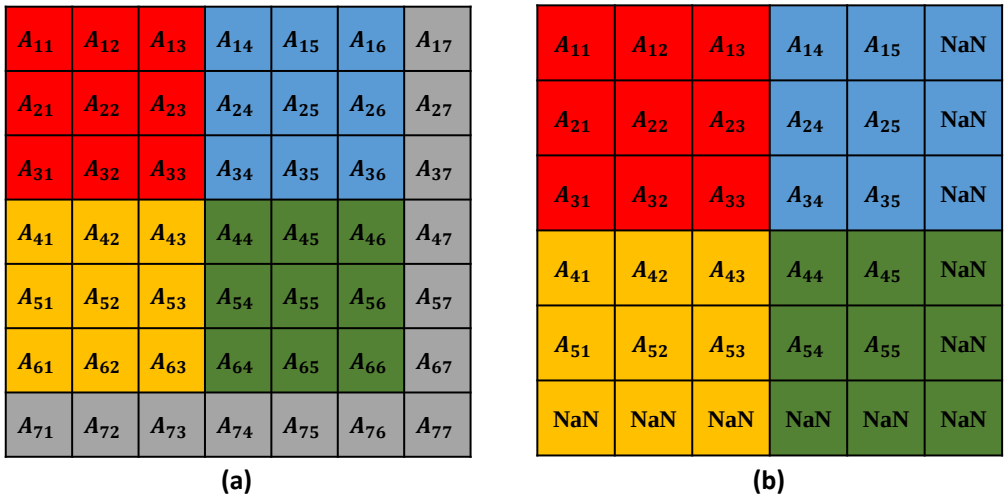

Figure 3.4.3 Issue with Block Matrix Distribution: (a) Inclusion of Unwanted Data (b) Missing of Wanted Data*

* The region marked by grey represents the data missed out by the computation process.

As it can be observed from figure 3.4.3 above, when the change of matrix size happens due to the change of simulation target, different issues can occur for the direct decomposition approach. As it can be seen from figure 3.4.3 (a), if the problem matrix size shrinks, the unwanted data stored in the nearby memory locations could be mistakenly included by the CPU and disrupt the solving process. Similarly, when the matrix size expands, the data could exceed the pre-allocated memory spaces of the different CPU processes and hence be left out. The more complex issue such as local singularity can occur on some of the decomposed sub-matrices and also compromise the solving processes of some of the CPUs.

In response of the problem, the block cyclic matrix decomposition method is used instead to divide the workload of the problem matrix. The CPUs are programmed to extract the data from the governing matrix in a cyclic fashion. Each extraction action will only read a pre-defined unit block of the data from the governing matrix and load it into the corresponding CPU. The residual of the cyclic readings will also be pieced into the corresponding process. The process of this data decomposition method is presented in figure 3.4.4 below.

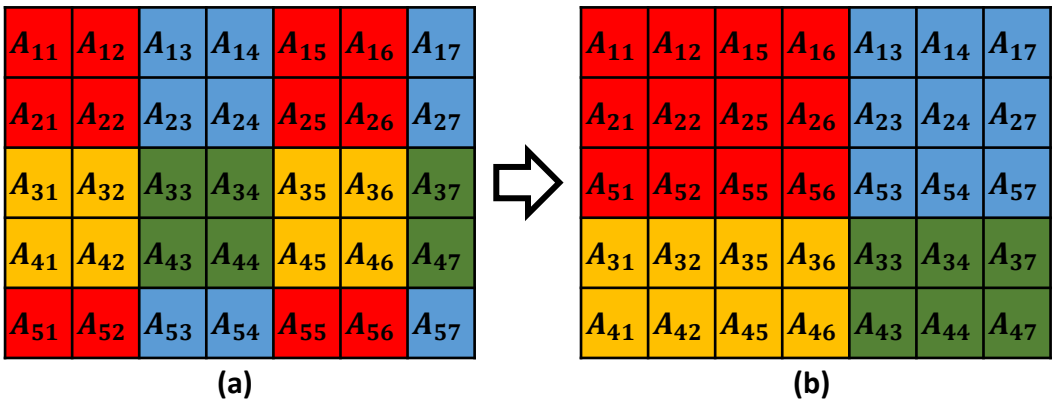

Figure 3.4.4 Block Cyclic Distribution of Matrix

As it can be observed from figure 3.4.4 above, the block cyclic distribution process can effectively avoid either overload or underload problem for different CPUs involved in the equation solving process regardless of the dimension of the matrix and the number of CPUs take part in the workload sharing. The block cyclic distribution strategy possesses great flexibility and only requires a smartly pre-defined unit block

size to function properly and automatically. The additional advantage of adopting this strategy also includes systematically scrambling of data to ensure the original data to be distributed as evenly as possible into the CPU processes to avoid the occurrence of local singularity to the maximum extent. Therefore, the block cyclic work load sharing structure is adopted to enable the parallel computing of the governing equation and provided this model with the scalability it needs.

3.4.3. *Iterative Method*

The approaches and techniques used to solve the governing equation matrix have been discussed in detail. As it was mentioned in previous sections, the steady state result cannot be derived just by a single time solution of the governing matrix system. The final results for any input settings have to be derived through iteration to ensure it is steady and reproducible. Two common iteration method are considered for this model: the Gauss-Seidel method [97] [98] [99] [100] and the Newton Raphson method [101] [102] [103] [104] [105]. The two methods are commonly acknowledged for their performance and are widely applied in various simulation areas to solve finite element models. In order to select the appropriate iteration method for this model, the features of these two different methods need to be discussed.

Overall, the Gauss-Seidel method and the Newton Raphson method are both capable of performing iterations to dense matrices with non-zero terms on the diagonal. The Gauss-Seidel method features in an element-wise residual computing formula. Due to its relatively simple iteration structure, the Gauss-Seidel method is relatively easy to implement in the open source code and has the advantage of relatively short computing time spent per iteration. However, the relatively simple structure and gradual value adjustment method also makes it converges slower; the convergence speed is also affected by the size of the problem. Moreover, the Gauss-Seidel method is mostly used to solve linear equation systems. The Newton Raphson method on the other hand is more powerful and can be generalized to solve non-linear problems. It utilize the principle of calculating the tangent line of the target function and approaching the final answer by finding the intersection point of the function tangent line and known conditions. The Newton Raphson method possesses the merit of faster convergence speed and relative independency of the size of the problem. However, due to its

mathematical principle, it spends a long time during each iteration calculating the derivative of the function and Jacobian matrix, which can be very computationally heavy itself. In addition, to exploit the full performance of the Newton Raphson method initial 'guessed' solution must be selected with care. This reduces the flexibility of the Newton Raphson method when dealing with frequently changing simulation objects.

Based on the discussion made above, both methods have distinct merits and drawbacks of their own. According to the code performance analysis result, a majority of the simulation time is spent on solving the equation systems. Therefore, reducing the time spent on each iteration becomes the top priority. The Newton Raphson method need to calculate Jacobian matrix for each iteration, which is of the same size as the governing equation system, using the Newton Raphson method under this circumstance is less desirable. The time save achieved by reducing the iteration numbers can hardly offset the additional matrix solving time introduced for each iteration. Therefore the Gauss-Seidel method is selected as the iteration method for this numerical model. In order to further save the simulation time, an adapted variant of the Gauss-Seidel method called the Successive Under Relaxation method (SUR) is used. The SUR method benefit from the introduction of relaxation factor F within the iteration function to cut the iteration numbers needed before convergence.

The principle of the Successive Under Relaxation method can be used to solve the $\boldsymbol{Ax} = \boldsymbol{b}$ type equation system. Which fits well with the need of this model. Again suppose that the unknown vector $\boldsymbol{x}$ contains n unknown variables. The coefficient matrix $\boldsymbol{A}$ can be first breakdown by the DLU decomposition into three components as presented below:

$$\boldsymbol{A} = \boldsymbol{D} + \boldsymbol{L} + \boldsymbol{U} \tag{3. 31}$$

Where in equation 3.31, $\boldsymbol{D}$ matrix contains the diagonal elements of the coefficient matrix $\boldsymbol{A}$, $\boldsymbol{L}$ matrix contains the lower triangular components and $\boldsymbol{U}$ matrix contains the upper triangular components. The contents of the $\boldsymbol{D}$, $\boldsymbol{L}$ and $\boldsymbol{U}$ matrix can be demonstrated as below:

$$\boldsymbol{D} = \begin{bmatrix} \boldsymbol{A_{11}} & \boldsymbol{0} & \cdots & \boldsymbol{0} \\ \boldsymbol{0} & \boldsymbol{A_{12}} & \cdots & \boldsymbol{0} \\ \vdots & \vdots & \ddots & \vdots \\ \boldsymbol{0} & \boldsymbol{0} & \cdots & \boldsymbol{A_{nn}} \end{bmatrix} \tag{3. 32}$$

$$\boldsymbol{L} = \begin{bmatrix} \boldsymbol{0} & \boldsymbol{0} & \cdots & \boldsymbol{0} \\ \boldsymbol{A_{21}} & \boldsymbol{0} & \cdots & \boldsymbol{0} \\ \vdots & \vdots & \ddots & \vdots \\ \boldsymbol{A_{n1}} & \boldsymbol{A_{n2}} & \cdots & \boldsymbol{0} \end{bmatrix} \tag{3. 33}$$

$$\boldsymbol{U} = \begin{bmatrix} \boldsymbol{0} & \boldsymbol{A_{12}} & \cdots & \boldsymbol{A_{1n}} \\ \boldsymbol{0} & \boldsymbol{0} & \cdots & \boldsymbol{A_{2n}} \\ \vdots & \vdots & \ddots & \vdots \\ \boldsymbol{0} & \boldsymbol{0} & \cdots & \boldsymbol{0} \end{bmatrix} \tag{3. 34}$$

Based on the DLU decomposition, the original $\boldsymbol{Ax} = \boldsymbol{b}$ equation system can be re-written as presented below:

$$(\boldsymbol{D} + \boldsymbol{FL})\boldsymbol{x} = \boldsymbol{Fb} - [\boldsymbol{FU} + (\boldsymbol{F} - \boldsymbol{1})\boldsymbol{D}]\boldsymbol{x} \tag{3. 35}$$

Where the constant *F* is called the relaxation factor, based on the theory of the SUR, the value of the relaxation factor *F* is between zero and one. The iteration of SUR is achieved through calculating the $\boldsymbol{x}$ value at the left side of equation 3.35 by applying the previous $\boldsymbol{x}$ value at the right side of equation 3.35. Therefore if the value of $\boldsymbol{x}$ is known for the k^{th} iteration, than the value of $\boldsymbol{x}$ at $(k+1)^{\text{th}}$ iteration can be calculated as below:

$$\boldsymbol{x}^{(\boldsymbol{k+1})} = (\boldsymbol{D} + \boldsymbol{FL})^{-\boldsymbol{1}}\left(\boldsymbol{Fb} - [\boldsymbol{FU} + (\boldsymbol{F} - \boldsymbol{1})\boldsymbol{D}]\boldsymbol{x}^{(\boldsymbol{k})}\right) \tag{3. 36}$$

Although by the appearance of equation 3.36, it might seem daunting to calculate the inverse matrix of the term ($\boldsymbol{D}$+$F\boldsymbol{L}$). It can be noticed that both matrix $\boldsymbol{D}$ and $\boldsymbol{L}$ are the triangular matrix. Therefore by applying the forward substitution method, the elements of the $(k+1)^{\text{th}}$ iteration can be calculated element-wise without directly solving the inverse of the term ($\boldsymbol{D}$+$F\boldsymbol{L}$). The i^{th} element in the $\boldsymbol{x}^{(k+1)}$ vector can be calculated as below:

$$\boldsymbol{x_i^{(k+1)}} = (\boldsymbol{1} - \boldsymbol{F})\boldsymbol{x_i^{(k)}} + \frac{\boldsymbol{F}}{\boldsymbol{A_{ii}}}\left(\boldsymbol{b_i} - \sum_{\boldsymbol{j<i}} \boldsymbol{A_{ij}}\boldsymbol{x_j^{(k+1)}} - \sum_{\boldsymbol{j>i}} \boldsymbol{A_{ij}}\boldsymbol{x_j^{(k)}}\right) \tag{3. 37}$$

Given the discussions made in this section, the Successive Under Relaxation method is identified as the best fit to build this numerical model. By applying the SUR, the governing equation matrix calculation results can be iterated methodically until the steady value is yielded.

3.5. Conclusion

In this chapter, the theories and methods applied to build the 3D HTS cable model are discussed in detail. The numerical model proposed in this thesis is built with the ***T*** formulation using the open source code under FORTRAN environment. The process of deriving the governing equation is presented at the beginning of this chapter. The finite element analysis is then applied to discretize the continuous physical equations into multiple elements. After deriving the matrix form of the discretized governing equation, the characteristics of the governing equation coefficient matrix are analyzed. The corresponding matrix solving package is selected after identifying the properties of the coefficient matrix. The workload sharing structure is also implemented in the code to offer scalability to the model and provide necessary computing power for the modelling of more complex cases. Since the solving of the governing equation system requires setting up the initial boundary condition by assumption, an iteration process is needed in order to derive the stable results. Two major iteration methods the Newton Raphson method and the Gauss-Seidel method were compared and finally based on the specific need of this model, an variant of Gauss-Seidel method, the Successive Under Relaxation method is finally selected as the optimum choice to meet the needs of this model.

Chapter 4. Mesh Construction of HTS Power Cables

4.1. Introduction

In the previous chapter, the physical and mathematical background of this HTS numerical model have been introduced in detail. Since the governing equation system of the HTS material domain has been derived, the corresponding mesh for the HTS wires and eventually the HTS cables must be constructed in order for this numerical model to function successfully. In this chapter, the mesh building process of the eventual 3D HTS power cable model will be introduced, along the path of building the 3D power cable mesh, a few other useful models have also been developed and can be used to assist the future research into other HTS applications. Since the primary objective of this model is to achieve the simulation efficiency improvement when modelling the HTS cables in 3D, a new mesh structure must be made based on the anisotropic homogenous medium approximation mentioned in section 3.3.2 to achieve the maximum efficiency improvement with the proposed governing equation system. Therefore, in this chapter, a new 3D mesh representing the realistic geometry of HTS conductors within the power cable structure is built with a modular stacking strategy by connecting short straight 3D cable sections to finally form the desired shape. As the 3D cable mesh is designed with modules, it allowed the 3D cable mesh to be built in a progressive manner, the building process of the final 3D cable mesh will be introduced in this chapter.

4.2. Foundation: Single HTS Conductor Model

The methods and techniques involved in building the HTS thin film model have been introduced in detail in the previous chapter. Based on the previous discussions, the 2D single wire model is built at the beginning to serve as the foundation for the later more complex models. In this section, the definitions and the basic functions of this single conductor base model will be introduced. The combination of anisotropic homogenous

approximation and stacking strategy is also tested later to expand the thin film mesh of the original model into rectangular mesh to allow simulation of anisotropic electromagnetic distributions on thickness dimension of the HTS conductor. After the successful test, the same strategy is applied to build more complex 3D models.

Based on the governing equation of 3.23, the HTS single conductor model can be defined as below in figure 4.2.1. In figure 4.2.1, if a 2D HTS conductor with a width of *w* is divided into *n* elements, the total current carried by this conductor can also be divided into *n* strands of sub-currents accordingly. The sub-current represents the current flow on each element and is defined to locate on the element point at the center of each element. Since the 2D HTS conductor model represents the cross-section of a HTS thin film, the direction of its transport current is defined to be flowing along the positive direction of the *x* axis. The current vector potential ***T*** is defined on nodal points of each element. Based on discussions made before, the direction of vector ***T*** will always be normal to the wide surface of the conductor. Since the curl of vector ***T*** is the current density, the vector ***T*** on each node across the HTS wire will be arranged in a pattern represented in figure 4.2.1 based on the right hand rule.

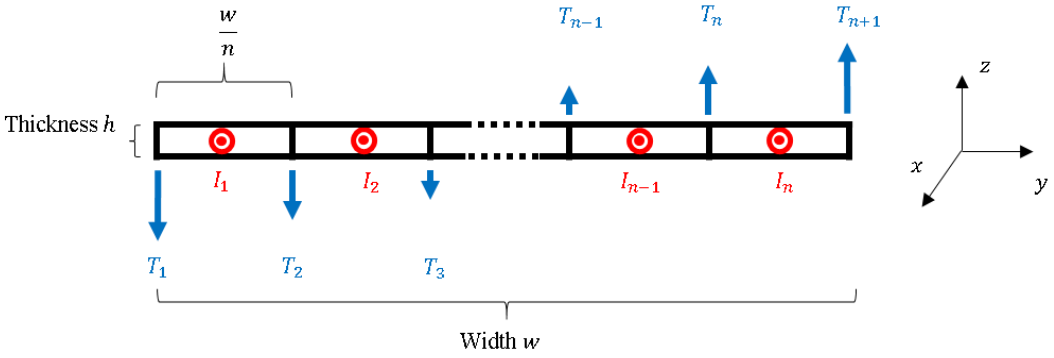

Figure 4.2.1 Transport Current and T Vector Distribution

In order to study the AC loss distribution within the HTS thin film material, the distribution of the basic electromagnetic quantities (such as current density, magnetic field, electric conductivity, and critical current density) must be derived at the beginning. A single HTS conductor carrying DC transport current is initially simulated using this numeric model to qualitatively demonstrate the electromagnetic quantity

distributions across its width. The distributions of the electromagnetic quantities were demonstrated in figure 4.2.2 below.

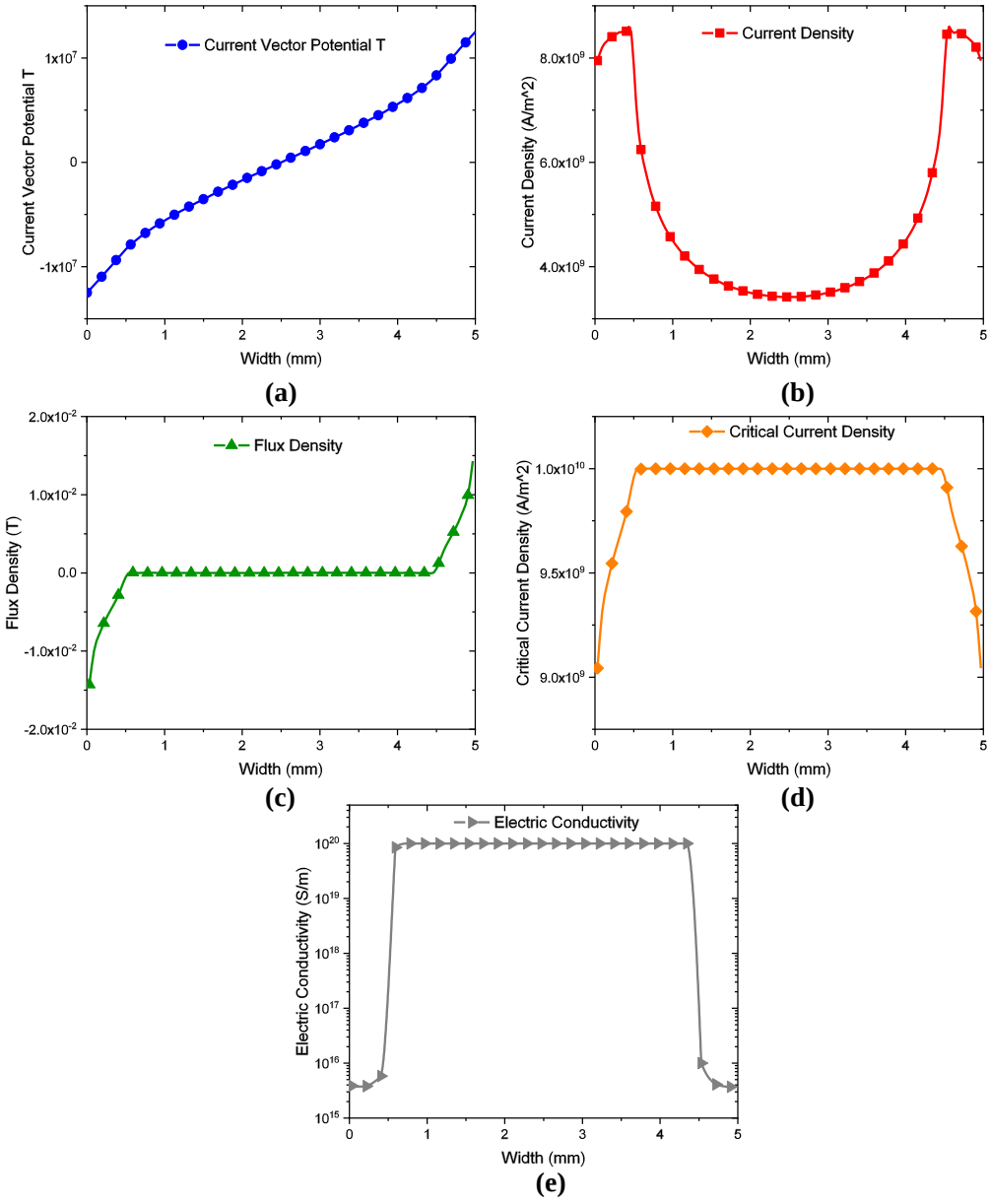

Figure 4.2.2 Example of Electromagnetic Quantities Distributions for DC Carrying HTS Wire*

* The electromagnetic quantity distributions presented here is for illustrative purpose only. The results are not necessarily from the same simulation object.

As can be observed from figure 4.2.2 (a) above, the magnitude of the current vector potential on each element is symmetrical about the center of the conductor. The current vector potential calculated on left half of the HTS conductor have opposite directions to the current vector potential calculated on the right half of the conductor. Therefore,

after calculating the curl of this current vector potential distribution, a 'U' shape current density distribution is derived for the cross-section area of the HTS conductor as in figure 4.2.2 (b). Since the direction of the transport current is defined as flowing along the *x* direction (perpendicularly out of the paper), the magnetic field induced by the transport current will also have opposite direction at both edges of the conductor. This distribution is represented in figure 4.2.2 (c). The magnetic field in this demonstration case has not penetrated the entire conductor, therefore the center region of the conductor remains magnetic field free. Since in this model, the dependency of the HTS critical current to the magnetic field strength in the surrounding regions is described by the Kim's model, the critical current density distribution across the conductor cross-section can be further derived as presented in figure 4.2.2 (d). The critical current density at the edge regions of the conductor is suppressed by the presence of the self-induced magnetic field. Where in the center region of the conductor, the critical current density remains constant at initial level as it is unaffected by the magnetic flux. The HTS conductivity also has a similar distribution pattern as presented in figure 4.2.2 (e). As the electric conductivity of the HTS material is coupled with the critical current density by the $E - J$ power law as presented in equation 3.13. After obtaining the distributions of the electromagnetic quantities across the HTS conductor, the loss on each element can be easily derived. The total loss across the HTS conductor can be calculated by adding the element-wise loss together.

4.2.1. *Mesh Expansion and 2D Electromagnetic Results*

In practice, the thickness of the HTS conductor is negligible. Therefore, for the purpose of simplification, assumption has been made that the HTS conductor is homogenous along its thickness dimension. In case the need of inspecting the 2D current density distributions arises, a mesh expanding technique is developed to derive the current density distribution in 2D.

In the previous section, if we assume the HTS conductor is homogeneous along its thickness dimension, the overall current distribution across the width of the HTS conductor can be derived. Since the HTS thin film conductors have very large aspect ratios (2500 to 1 or higher), the current distribution across the width dimension can be

taken as the overall current distribution across the entire conductor cross-section. Therefore, the current distributed on each element calculated this way can be regarded as the total current carried by a unit area covered by this element as presented in figure 4.2.3 below.

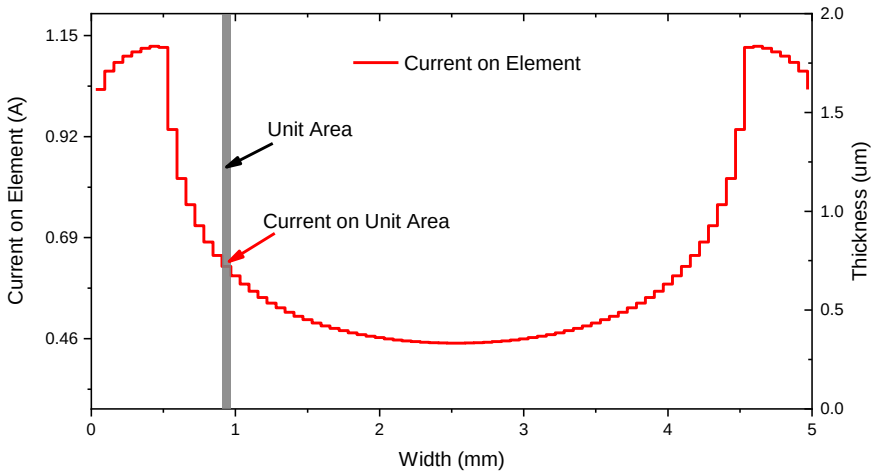

Figure 4.2.3 Transport Current Carried by a Unit Area on HTS Wire

If we apply the same thin film analysis to each unit area and restrict the total current passed through this unit area to the value calculated by the initial FEM analysis, the anisotropic current density distribution can be derived across the thickness dimension of the HTS conductor. The resultant 2D current density distribution across the HTS conductor's cross-section area is presented below in figure 4.2.4. Note that in figure 4.2.4, the physical dimension of the conductor cross-section area is re-scaled for the demonstration purpose.

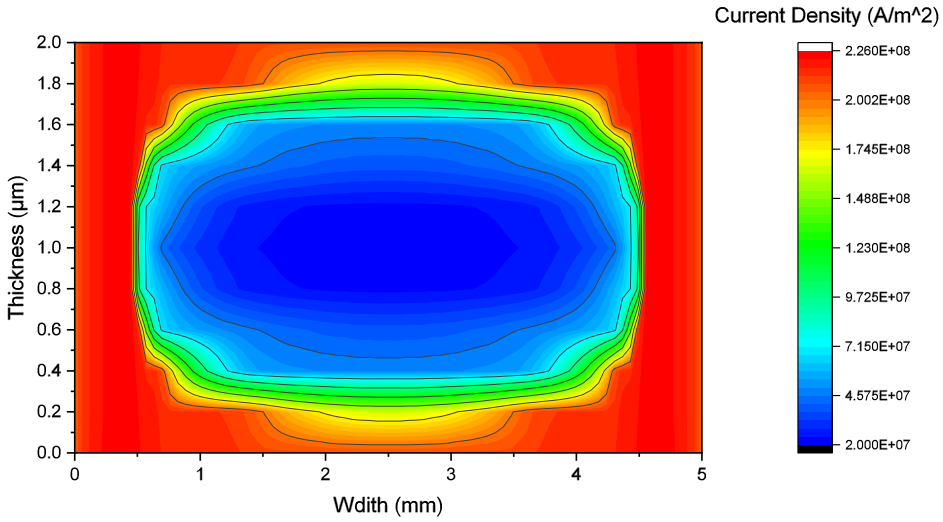

Figure 4.2.4 2D Current Density Distribution on a HTS Wire*

* The fuzzy current density boundary in figure 4.2.4 is generated due to the resolution limit of the simulation results.

This mesh expansion technique can be utilized as a qualitative tool to observe the overall 2D current density distribution across the HTS coated conductor. This method saves the time comparing to performing full numeric analysis with 2D FEM interpolation functions. It can be a useful tool if the needs for inspecting such 2D distribution on HTS conductor arises at some point. However, under most of the cases, the high aspect ratio of the HTS coated conductor determines that obtaining an overall current distribution across its width dimension is more important. Therefore, this thesis will only focus on the electromagnetic distribution across the width dimension of the HTS coated conductors.

4.3. Progress: 2D Multi-Conductor Model

In previous section, discussions have been made regarding building cross-section model for the single HTS coated conductor. Since HTS power cables normally consists of more than one coated conductor, the analyzed domain of this numeric model must be extended into 2D to allow for the simulation of multiple coated conductors. Since the thin film assumption stands true for each individual HTS conductors, the same governing equation system can be easily extended to a group of conductor without much change. However, when a 2D analysis domain is needed, the spatial displacement distance r in equation 3.23 must be calculated in 2D. Apart from this,

the building of the 2D multi-tape model simply requires building the mesh in a 2D space. Two different 2D multi-conductor models are developed in this section: the HTS conductor stack model and the multi-conductor HTS cable model.

4.3.1. *HTS Wire Stack Model*

The multi-conductor stack model is developed to analyse the cross-section of a HTS wire stack. The HTS wire stacks are widely used by many HTS power applications, such as HTS coils for strong electromagnets or HTS power cables. Stacking multiple HTS conductors together into a single rectangular wire is a common strategy employed in order to carry higher amount of transport current. This 2D multi-conductor stack model can also be used to analyse the cross-section of a large HTS coil with multiple turns. As it is suggested by research works in [96] [106] [107], when the radius of the coil is much larger than the width of the HTS conductor, the electromagnetic environments experienced by the conductors are very similar to those experienced by the HTS conductors in infinitely long wire stacks. Therefore by applying the Clem's assumption proposed in [107], this 2D multi-conductor stack model can also be used to analyse the electromagnetic quantity distributions of a HTS coil's cross-section area. This model can be used to study the magnetic field and current distributions for HTS coils installed in power applications such as electric machines, magnets and fault current limiters. The mesh built for a 4-conductor stack is demonstrated below in figure 4.3.1.

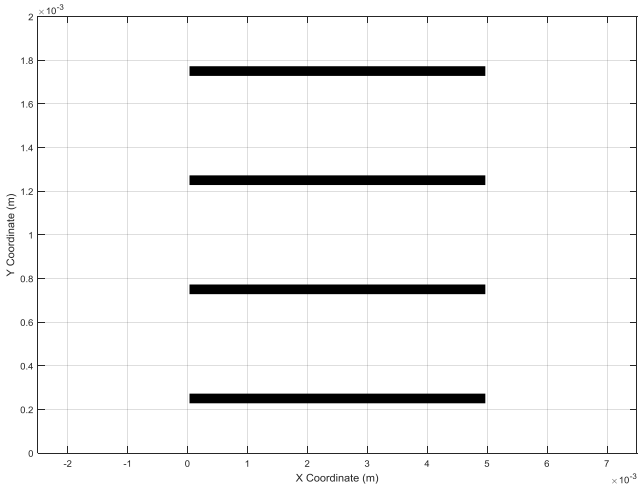

Figure 4.3.1 Mesh of the 2D Multi-Conductor Stack Model

This multi-conductor stack model has been deployed to study the dynamic loss of HTS pancake coils within the HTS claw-pole machines. A 27-turn coil cross-section current density distribution is presented in figure 4.3.2 below to demonstration the function. The model represents half of the pancake coil which was placed under an AC external magnetic field. The left side of figure 4.3.2 represents the external side of the coil whereas right side represents the internal side. Comparing to the internal side, the external side of the coil is in direct contact with the external AC field. A screening current is induced in the edge area to try to shield the coil internal area from the external magnetic field. Therefore, comparing to the internal side of the coil, the elements on external side have significantly higher levels of current density.

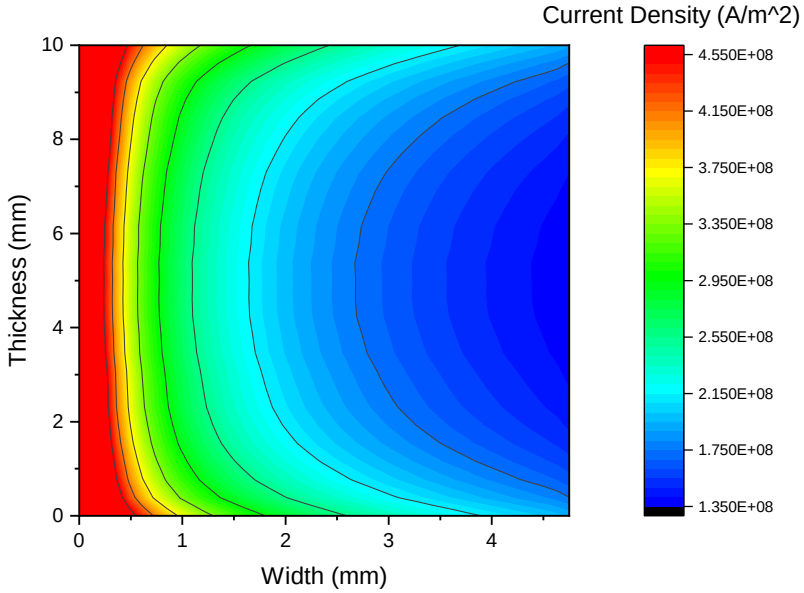

Figure 4.3.2 Current Density Distribution on Half of the 27-turn HTS Coil

4.3.2. *2D HTS Cable Model*

The mesh of the 2D multi-conductor model is also extended into the geometry similar to the HTS cable cross-section area. As it is presented in figure 2.2.1 of chapter 2, the HTS conductors within the cable structure are designed to be attached to the cylindrical cable former. In order for the HTS coated conductors can be attached as closely as possible to the cable former to reduce the gap left between adjacent coated conductors, the HTS conductors are usually twisted spirally. However, due to the mechanical

strength of the HTS conductor's substrate layer, the cross-section of the HTS conductor will not be bent to become fully attached to the surface of the cable former. Also, in practice, the over strong twisting stress could damage the micro-structure of the superconducting layer of the coated conductor as it is usually very thin and fragile. The actual HTS cable design will limit the twisting force exerted on the coated conductors and therefore further limit the bending effect of conductor cross-section. Since in practice the bending effect is relatively limited, this model assumes that the cross-section of the coated conductors remains flat. Therefore, given the discussion above, the cross-section area of the HTS cable can be approximated with multiple coated conductor being arranged into a polygon shape with air gaps left between the adjacent conductors. The HTS cables normally consist of multiple layers of the conductors in order to increase the space utilization rate and to carry larger amount of total transport current. The extra layers of conductors will normally be arranged into a coaxial structure. Therefore, based on the description made above, the 2D cross-section mesh of a double layer coaxial cable consists of 4 conductors at the internal layer and 6 conductors at the external layer can be made as demonstrated below in figure 4.3.3.

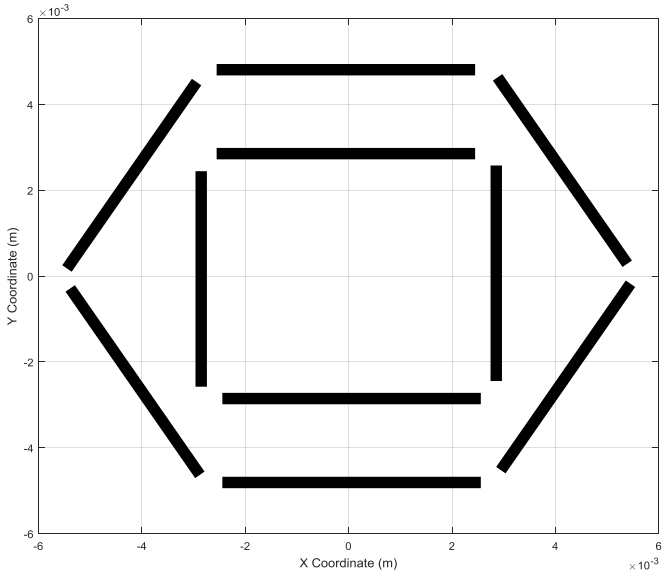

Figure 4.3.3 Mesh of a 2D HTS Cable Cross-section Model

As the mesh in figure 4.3.3 represents the cross-section of a double layer coaxial HTS cable, the transport current flowing direction is defined as perpendicular to this cross-section surface and coming out of the paper (flowing in the z direction). The magnetic coupling between transport currents carried by different HTS conductors must be considered in this case. This effect is readily taken into consideration by the governing equation in 3.23 as long as all current carrying elements within this domain is assembled into the same global governing equation matrix. The only thing needs extra attention when building this 2D cable cross-section model is that the spatial displacement vector $|r|$ needs to be calculated with the 2D distance between the source points any corresponding field points.

It is also worth noticing that in this 2D case, the magnetic field induced by the current carried by each source point is calculated by the Biot-Savart law for infinitely long line current. This 2D model is not able to represent the continuously changing current flow direction in a spirally twisted HTS cable. Therefore, this 2D cross-section model can only be used to analyse HTS cables without the conductor twisting design. The accurate simulation of the HTS cables built with conductor twisting design requires 3D models being built. The building process of the 3D HTS cable model will be presented in the next section.

4.4. 3D HTS Cable Model

In this section, the mesh building process of the 3D HTS cable model will be presented. Since the mesh of the 2D HTS cable cross-section model has been built in the previous section, the remaining task to build the 3D cable model is to combine the 2D cross-section model with the homogeneous approximation and the stacking strategy. Since the major difficulty of building the 3D HTS cable model lies in the constantly changing current direction within the twisted HTS coated conductors, the transport current within the source points can no longer be defined as the infinitely long straight line current. Therefore, the originally continuous transport current must be broken down into different finitely long current segments in order to represent this physical feature in the 3D model. The 3D variation of the governing equation in equation 3.24 is used to represent this feature. The direction of the transport current on each source points can be manipulated so that they joint each other in a piece wise

way. The magnetic coupling on each field point is calculated with the 3D Biot-Savart equation for finitely long current segments and then adding up the effect generated by all the source points within the analyzed domain.

4.4.1. *3D Single HTS Conductor Model*

In order to build the 3D HTS cable model in a progressive manner, the 3D single HTS conductor model is initially built as a prototype to test the algorithm. A straight 3D single HTS conductor model is initially built. After verifying the function of the straight single conductor model, the mesh building algorithm is extended to consider the additional features brought about by the twisting design.

The mesh of the straight single HTS conductor model is built as presented below in figure 4.4.1. The governing equation system adopts the form presented in equation 3.24.

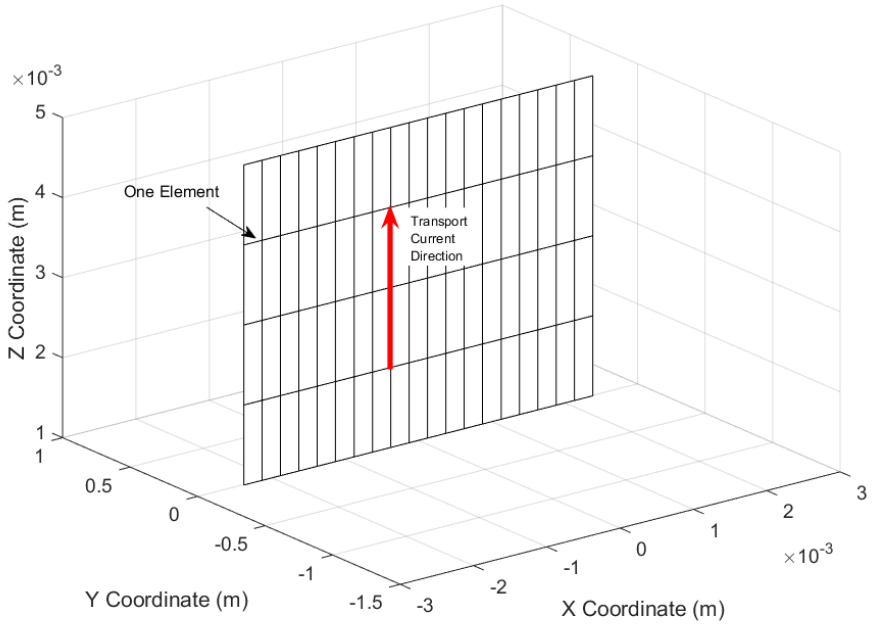

Figure 4.4.1 Mesh of the 3D Single Conductor Model (Straight)

In figure 4.4.1 above, the direction of the transport current carried by each element is marked by red arrow. One single element is defined as a line segement demonstrated in figure 4.4.1. Applying the homogenious approximation, the one single line element will actually cover the small rectangular area both above and below the line element.

The electromagnetic property across the width dimension of the HTS conductor remains anisotropic. In this case, if an inifnitely long straight 3D single conductor is simulated, two sections of semi-inifnitely long (infinitely long at one end and terminates at the other end) sections are attached to both ends of the analysed section to serve as the additional source points to immitate the magnetic environment of an infinitely long HTS conductor. After building the mesh of the 3D straight single conductor, the simulation results are cross-checked against the results simulated by the 2D models to verify the functionality of the 3D model. When using the 3D single conductor model to simulate an infinitely long straight HTS tape, the 3D model should yield very similar results comparing to the 2D model. By checking the error between 2D and 3D models under inifinitely long straight simulation cases, the functionality of the 3D model can be determined. The verification of the 3D algorithm will be presented in chapter 6.

After completing the 3D straight single conductor model, the conductor twisting design is then considered. The method used to introduce the twisting structure to the mesh is as demonstrated below in figure 4.4.2.

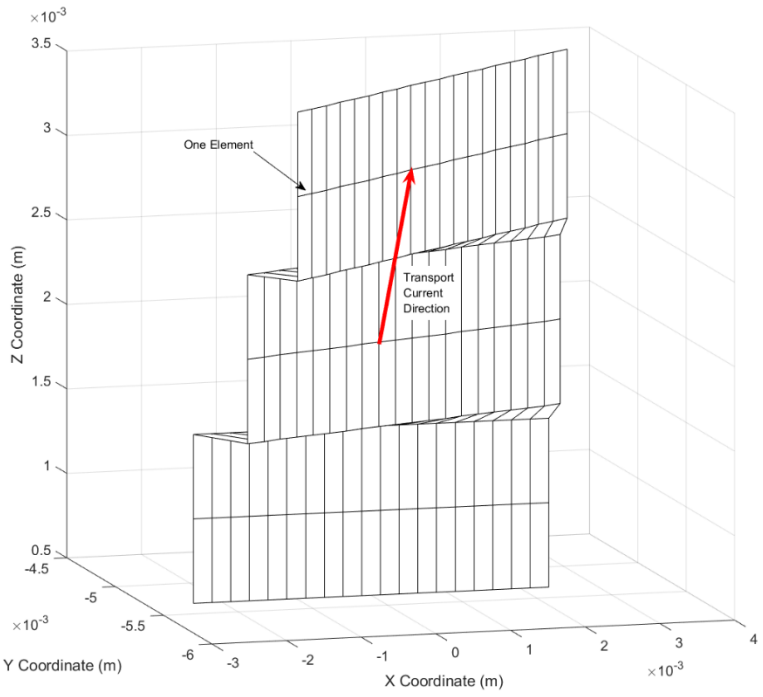

Figure 4.4.2 Mesh of the 3D Single Conductor Model (Twisted)

The strategy used in this model to represent the 3D HTS conductor twisting structure is breaking down the continuous 3D structure into different sub-domains as described previously. Each sub-domain covers a short length on *z* dimension and remains straight on its own, the twisting is introduced by applying a phase difference to different sub-domains and makes the center line of the consecutive sub-domains twist following the trajectory of a helix line. The transport current direction is again marked out by the red arrow in figure 4.4.2. Therefore, by stacking up a number of block type sub-domains together, the structure of the twisted single conductor mesh will approach the shape of a twisted tape.

4.4.2. *3D HTS Cable Model*

After building the mesh for the single HTS conductor with both straight and twisted design, same principle can be extended to build the mesh for the complete HTS cable model. Similar to the 3D single conductor model, the 3D HTS cable model is also built with the stacking strategy demonstrated in the previous section. Only in the 3D cable model the mesh is stacked up using the 2D multi-conductor HTS cable model described in section 4.3.2. The 3D cable model without the twisting structure is firstly built as presented in figure 4.4.3 below.

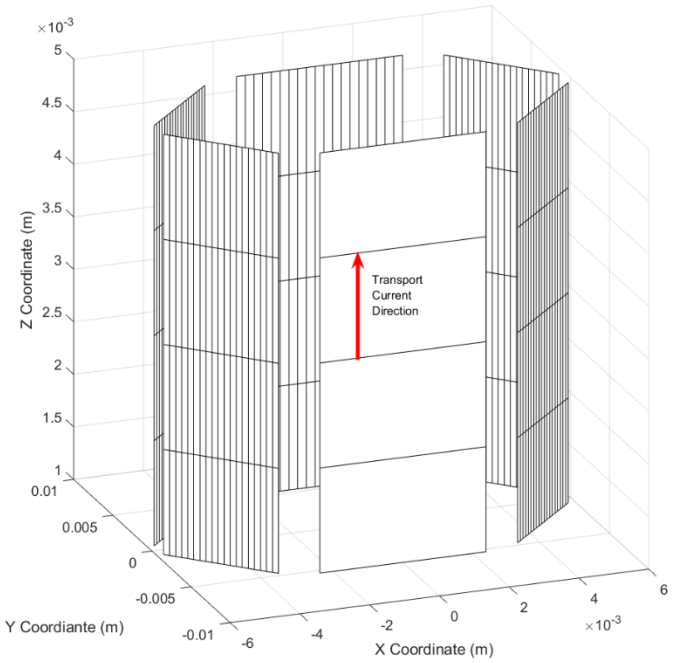

Figure 4.4.3 Mesh of the 3D HTS Cable Model (Straight)

In figure 4.4.3 above, the 3D mesh for a short section of HTS cable consisting of six straight HTS conductors is built. The compressing and bending effect of the conductor's cross-section is neglected as discussed previously. The thin film assumption is also applied to each one of the coated conductors so that the coated conductors are represented by a rectangular surface in 3D space. The direction of the transport current defined in this model follows the red arrow. Again, the functionality of this 3D model with straight conductors can be verified by cross-checking its simulation results with the 2D cross-section model.

After the 3D straight conductor mesh is being built, phase angle differences are again introduced to different blocks of sub-domains to introduce the conductor twisting feature. The twisted structure of the 3D cable mesh in presented in figure 4.4.4 below.

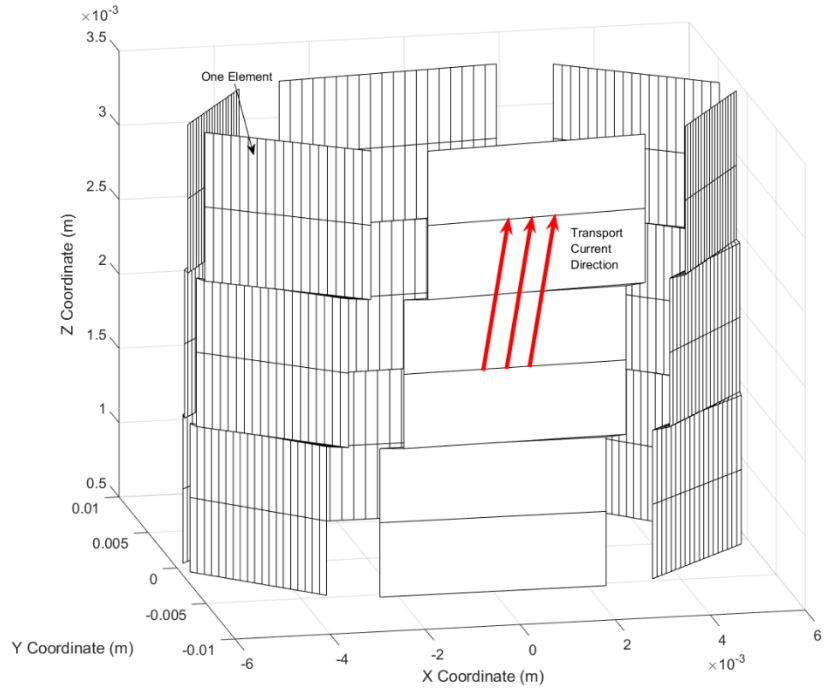

Figure 4.4.4 Mesh of the 3D HTS Cable Model (Twisted)

The schematic of the 3D mesh for an HTS cable with twisted conductors are presented in figure 4.4.4 above. As it can be seen from the figure above, different sub-domain cross-sections are stacked up with a phase angle difference. The transport current are defined to flow from one sub-domain to the other as marked out by the red arrow. The transport current is defined to be piece-wise linear between different sub-

domain blocks. In the modelling process, after solving the 3D governing equation, the distribution of the current vector potential $\boldsymbol{T}$ will be acquired. With the knowledge of the $\boldsymbol{T}$ distribution, the two components of the total transport current $\boldsymbol{J_x}$ and $\boldsymbol{J_y}$ can be calculated using equation 3.25 as demonstrated in figure 4.4.5 below.

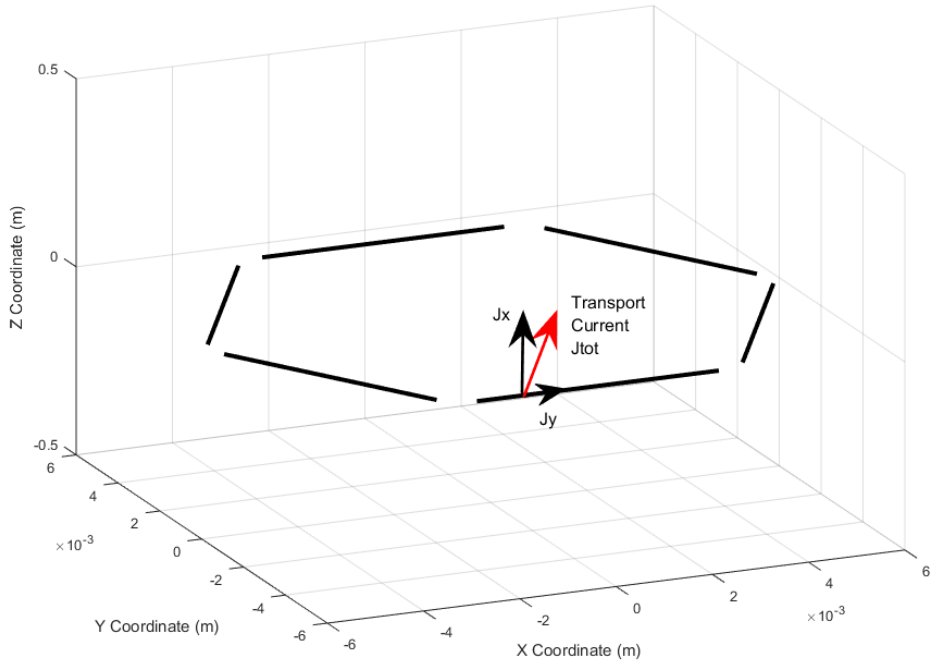

Figure 4.4.5 Break Down of Total Transport Current in 3D Cable Model

As it can be seen from figure 4.4.5, the current distribution the cross-section of each sub-domain block can be calculated with the distribution of $\boldsymbol{T}$ vector. $\boldsymbol{J_x}$ represents the current component normal to the cross-section of the conductor surface and in parallel with the *z* direction. $\boldsymbol{J_y}$ represents the current component flowing across the width of the conductor cross-section. Although in 3D space, the direction of the total transport current on each element could contain a $\boldsymbol{J_z}$ component which is normal to the wide surface of the HTS conductor and pointing out towards at the radial direction. Due to the negligible thickness of the HTS conductor, this $\boldsymbol{J_z}$ component is also neglected during the dimension reduction process. As it is discussed in the previous section, in order to preserve the structural integrity of the extremely thin superconducting layer, it is not possible to twist the HTS coated conductors too heavily. A relatively mild conductor twist also would not cause a big displacement in

radial direction on HTS conductor across a short length. Therefore, neglecting the J_z component would not have big impact on the overall simulation results. After deriving the current distributions across the entire analysed region, other electromagnetic quantities can be derived accordingly as discussed in the previous sections.

4.5. Conclusion

The mesh construction process of this numerical model is introduced in this chapter. The assumptions and the simplifications made during the mesh building process is also discussed in detail. The mesh building process in this chapter followed a progressive manner to suit the modular design of this numerical model. This enables the simulation results from different stages of model to be checked independently and allow potential issues to be addressed more easily. The modular mesh design also offers great flexibility for the model, allowing the model to be easily adapted for various geometries. The mesh building process starts with building the 2D model for a single HTS conductor. Then it is extended with the ability of modeling a system of multiple HTS conductors in 2D. Afterwards the stacking strategy is first applied to build the single HTS conductor in 3D. After verifying the single conductor model, the same strategy is applied to the 2D cable cross-section model to build the final cable model with conductor twisting design in 3D. A completed 3D HTS cable mesh is presented at the end of this chapter.

Chapter 5. HTS DC Loss Characteristics Modelling and Analysis

5.1. Introduction

After completing the HTS numerical model with the methods introduced in the previous chapters, the model is first put to use studying the electromagnetic properties of the 2G HTS wires under DC carrying conditions. As the HTS wires are virtually lossless on their own when carrying DC power flows, a number of experimental projects have been carried out around the world to test the performance of DC carrying HTS cables as introduced in chapter 2. In this chapter, the basic properties of the HTS materials under DC carrying condition such as the $E-J$ curve and I_c-B curve are first simulated to test the functionality of this model. After that, this model is implemented to model the dynamic loss characteristics of a commercial HTS wire when carrying different DC currents. As the dynamic loss is the only major source of loss for HTS wires carrying DC currents, the simulation study of this type of loss is very important for the design of DC HTS power applications. This model provides the first comprehensive simulation study for the dynamic loss within the 2G HTS wire. The simulated loss results agree well with the experiment measurements provided by the external collaborators and further validate the accuracy of this numerical model. The detailed current density and magnetic field distributions of the HTS wire when generating dynamic losses are also simulated at the end of this chapter to aid the study regarding the dependence and mechanism of dynamic losses.

5.2. HTS DC Loss Modelling

5.2.1. DC Loss in Single HTS Tape

It is well known that the HTS wires carrying steady state current produce extremely low loss when subject to no external magnetic fields due to their superconducting property. Since the self-induced magnetic field generated by the transport current do

not vary with time, the loss incurred in DC carrying HTS tapes were purely Ohmic loss.

Although the Ohmic resistances of the HTS materials are physically infinitesimal, it does not translate well mathematically into the numerical model. The current decay experiments suggest that the resistivity of the HTS materials can be lower than 10^{-20} Ω. Thus, a maximum resistivity of 10^{-20} Ω is set for this numerical model to perform simulations under the worst-case scenario. As it is stated in the section 3.4.3, the calculation of Ohmic resistivity in this model adhere to the rule of the extended Ohm's law and is calculated iteratively until the convergence criteria is met, the selection of this maximum resistance value will not affect the final results.

Unlike the AC loss mechanism to be discussed in the following sections, factors that can affect the HTS DC loss simulation results are relatively simple and few. In fact, the most dominant factor that can affect the overall DC loss simulation result is the selection of the '*n*' value incorporated in the $E - J$ power law. The value of '*n*' is dependent to the property and microstructure of the simulated HTS material. Figure 5.2.1 and 5.2.2 below presented the simulated $E - J$ and $Q - J$ curve of the DC carrying single HTS tape model simulated with the standard parameter setting table (table 4 in section 6.2) with a selection of *n* values.

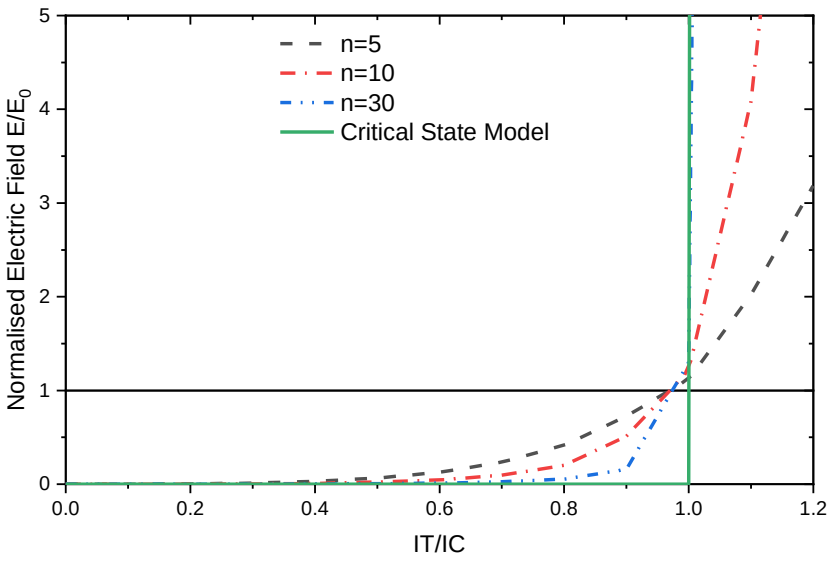

Figure 5.2.1 Simulated E-J Curve for a HTS wire

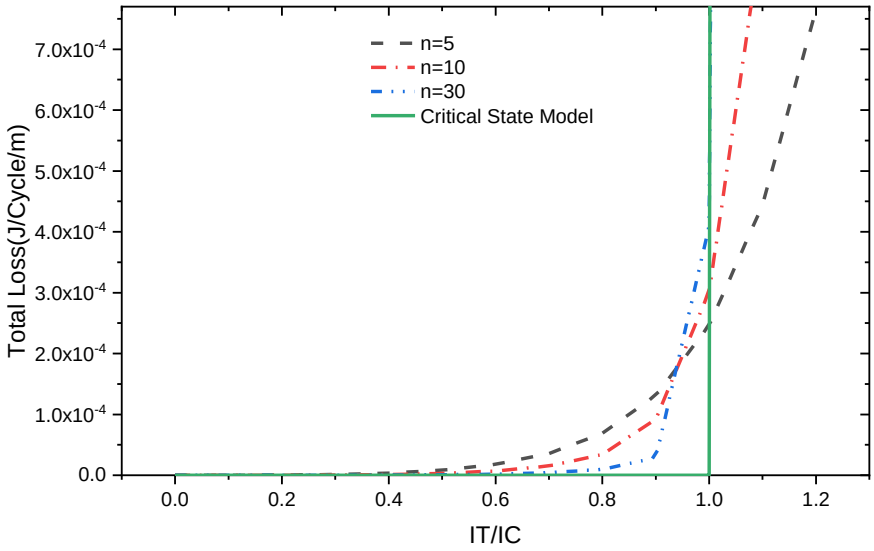

Figure 5.2.2 Simulated Q-J Curve for a HTS Wire

It can be observed from figure 5.2.1 that for the larger *n* value settings, the $E - J$ curve simulated with the increasing current carrying rate become better approximation of the Critical State Model proposed by Bean. For a larger '*n*' value, the simulated electric field rises more slowly before the critical current level and increases drastically sharper when the transport current ratio exceeds 1.0. Upon reaching the critical current level where the transport current ratio is 1.0, the simulated electric field for all three cases fall closely to the value of the characteristic field E_0 and demonstrates a good fit to the theory of the $E - J$ power law. The deviation from the E_0 value is because that the electric field value is calculated from the FEM method and slight accumulated numerical errors are magnified by the power of *n*. This feature naturally translates to a lower simulated total loss for high '*n*' settings when the transport current ratio is below 1.0 and higher simulated total loss when over-critical level of currents are applied. Since the impact of '*n*' value to the simulation results stand for all simulation conditions, the selection of an appropriate '*n*' value is very important for numerical simulation of the HTS devices.

Another factor that can increase the overall loss on a DC carrying HTS conductor is the external magnetic field. When a DC carrying HTS conductor is operating under the influence of the external magnetic field, the amount of flux penetration will

increase significantly. According to the theory proposed by the Kim's model introduced in section 2.3.3, the critical current of the HTS material depends on the strength of the external magnetic field applied to it. This dependency is also simulated by this numerical model. The simulated $J_c - B$ curve for a HTS coated conductor under an increasing DC external magnetic field is presented in figure 5.2.3 below. The $J_c - B$ curve simulated in figure 5.2.3 is based on the Kim – Anderson equation introduced in section 2.3.3 and equation 2.4.

$$J_c(B,T) = \frac{J_{c0}(T)}{1+\frac{B}{B_0}} \tag{2.4}$$

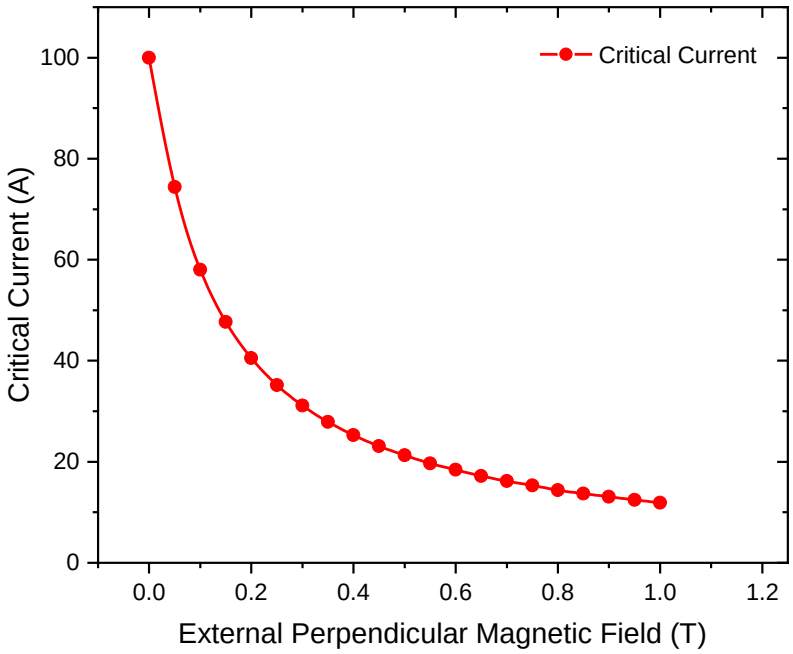

Figure 5.2.3 Simulated I_c – B Curve for an HTS Wire

As it can be observed from figure 5.2.3, the critical current of the standard HTS conductor is inversely proportional to the magnitude of the DC external field. This agrees well with the $J_c - B$ relationship described by the Kim's model. Since the critical current of the conductor deteriorate with the increasing external field strength, if a constant transport current is carried by the conductor, the load current ratio (I_t / I_c) will become larger. Based on the results showed in figure 5.2.3, the total loss on the conductor will rise with the increasing load current ratio. Therefore, it should be

noticed that as an external factor, the presence of a DC external magnetic field will induce additional losses on a DC carrying HTS conductor. The influence of an AC external magnetic field to the DC carrying HTS conductors will be discussed in detail in the following section 5.2.2.

5.2.2. *Dynamic Loss in 2G HTS Wire*

As it has been introduced in the literature review chapter, although the HTS material does not generate much loss on its own when carrying DC current, it is not immune to the losses induced by an externally applied changing magnetic field. If an AC external magnetic field is applied to a 2G HTS wire, a shielding current will be induced around the edge region of the wire and thus change the simple 'U' shape distribution of the current within an HTS wire. In this section, the dynamic loss characteristics of the HTS wire will be studied through simulating the detailed current and magnetic field distribution of a HTS wire when an AC external field is presented. Since the dynamic loss only occurs at the DC carrying region of the HTS tape, this finite element analysis model can be a very helpful tool in terms of simulating the HTS dynamic loss characteristics. An example of the shielding current induction process within the HTS tape is given in figure 5.2.4 below. Where the direction of the external magnetic field is defined as negative if applied downward into the HTS tape wide surface, the width of the HTS tape is w, I_s represents the shielding current induced.

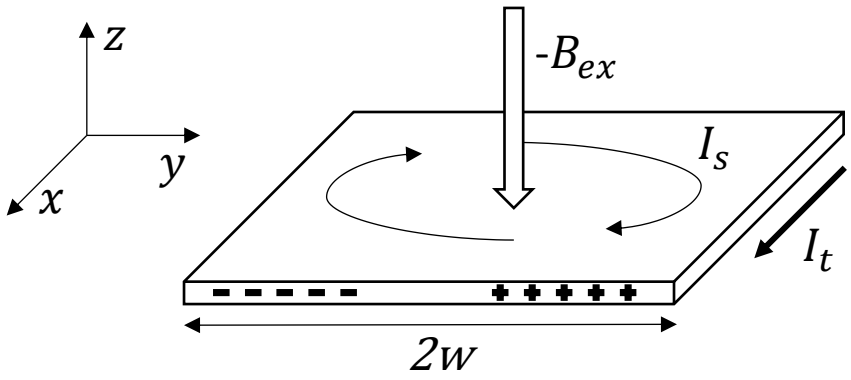

Figure 5.2.4 Shielding Current Induction in a HTS Wire

Based on Faraday's law of induction, the induced current will strengthen the current flow on one side of the HTS tape (marked by plus symbols) and cancel some of the current flow on the other side of the tape (marked by minus symbols). Since the applied

field $\boldsymbol{B_{ex}}$ is an AC magnetic field, the effect to the current distribution changes following the magnetic flux traverse through the tape cross-section during a full cycle. An example of the simulated current distribution for a cycle is given below in figure 5.2.5.

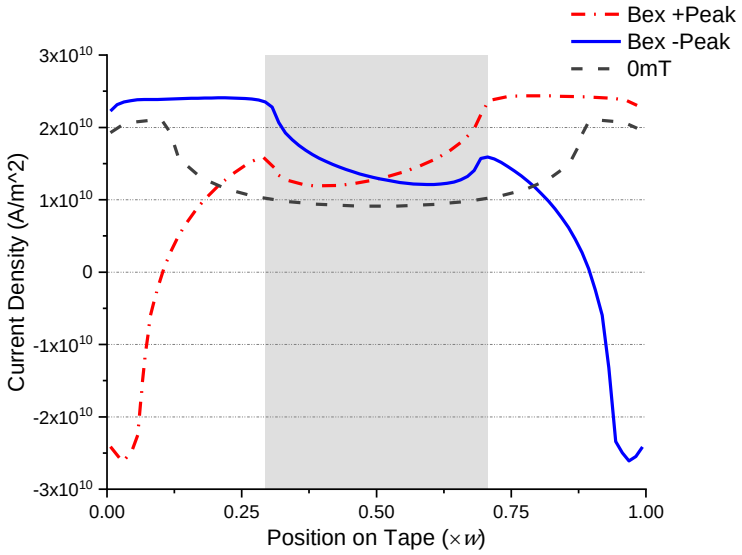

Figure 5.2.5 Current Density Distribution for a DC Carrying HTS Wire under Weak AC Field

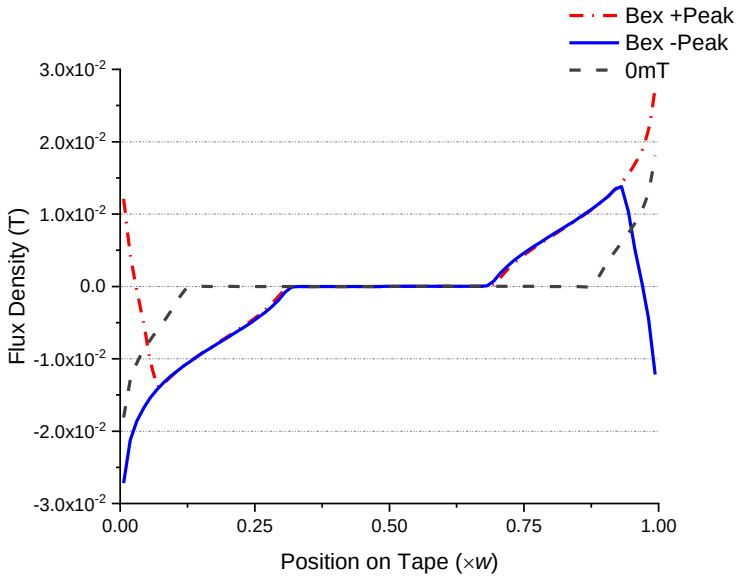

Figure 5.2.6 Magnetic Field Distribution for a DC Carrying HTS wire under Weak AC Field

Figure 5.2.5 above presents an example of the current and magnetic field distribution across the tape when a relatively weak (5mT peak amplitude) AC external field is applied to the tape. It can be observed from figure 5.2.5 that, the middle area marked by the grey zone has not been filled by the induced shielding current whilst the edge area outside the grey zone at both sides of the wire demonstrates opposite current flow directions. This indicates that the shielding current are still capable of screening the core area of the tape to allow it remains relatively free from the influence of the external AC field. Therefore, it can be seen from figure 5.2.5 that, the current density distribution in the grey area still somewhat adhere to the pattern of current distribution of HTS tapes free from external field.

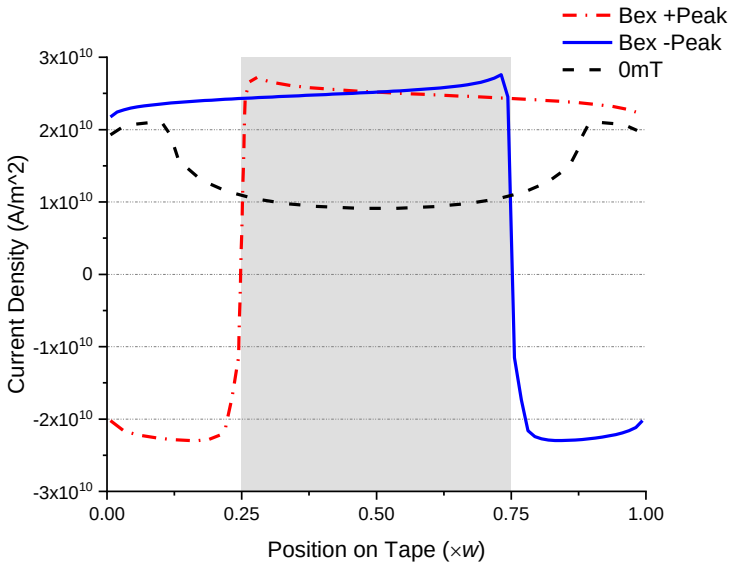

Figure 5.2.7 Current Density Distribution for a DC Carrying HTS Wire under Strong AC Field [83]

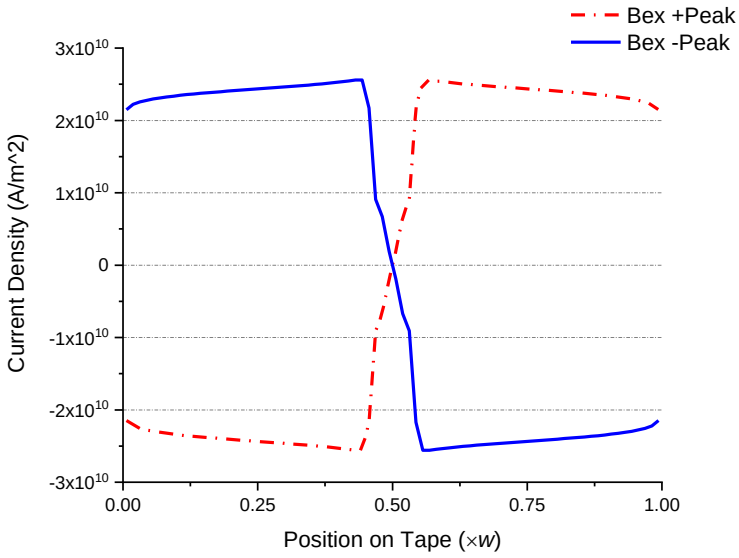

Figure 5.2.8 Induced Current Density Distribution for a HTS Wire under Strong AC Field (No Transport Current)

When the magnitude of the external AC field exceeds the level of the threshold field B_{th}, the shielding current can no longer prevent the external magnetic field from entering the core region of the HTS tape. Figure 5.2.7 demonstrate the current density distribution of an HTS wire when such situation occurs. The current density distribution for the same tape carrying no transport current under same external field is plotted in figure 5.2.8 for the purpose of comparison. In figure 5.2.7, the induced current now fills the entire cross-section of the HTS wire and the area marked by grey now represents the area where the DC transport current flow. It can be seen from figure 5.2.8 that when no transport current is presented in the tape, the induced current distributes in a symmetrical way with opposite directions at both sides of the tape. When the HTS tape is transporting 50% of the critical current as it is represented in figure 5.2.7, the grey area in the center region is created by the offset of the DC transport current. As it can be observed from the figure 5.2.7, since 50% of the critical current is flowing through the tape, roughly half of the tape wide face is occupied by the flow of the transport current. This result agrees well with the research of [108].

Since the dynamic loss only occurs at the region where DC transport current is impeded by the motion of flux induced by the external magnetic field, simulating the current distribution across the HTS tape becomes vital for accurate determination of

the scale of the total dynamic loss. Based on the discussion made in Chapter 3, the $\boldsymbol{T}$ formulation governing equation system composed for this numerical model is capable of simulating the current distribution across the HTS tapes. To simulate the influence of the AC magnetic field, a sine function was introduced to shape the external magnetic field term $\boldsymbol{B_e}$ as presented in equation 5.1 below:

$$\boldsymbol{B_e = B_{peak} \cdot \sin\left(2\pi f \Delta t \cdot N(t)\right) \cdot \sin(\theta)} \quad (5.1)$$

A complete AC period for this external field is broken into N steps, Δt is the time elapsed in each step. $N(t)$ represents the number of time steps. Where B_{peak} is the peak magnitude of the external AC field, θ is the insertion angle between the external field and the wide surface of the tape.

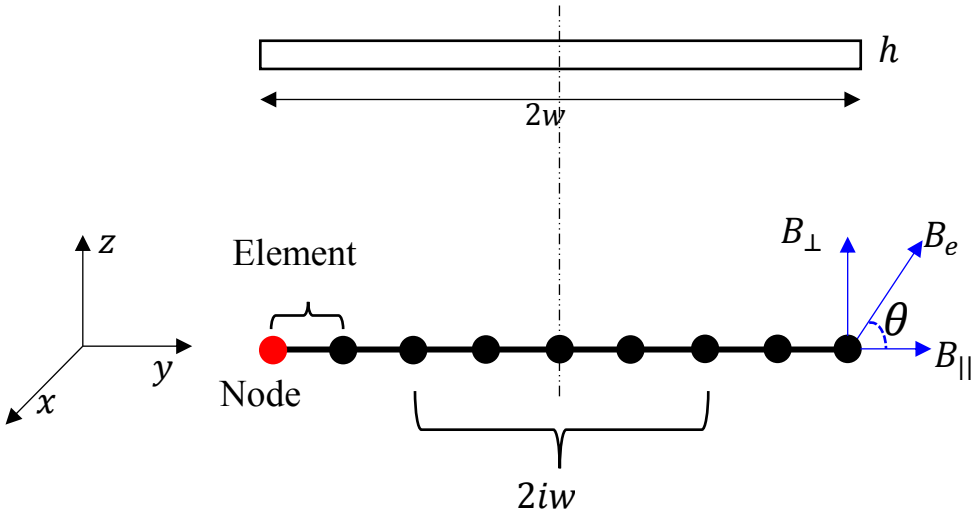

Figure 5.2.9 Applying AC External Field in Single HTS Wire Model

Based on the research of [109], if the HTS wire is carrying a DC transport current with a current ratio of i, for a HTS wire of $2w$ wide, the DC transport current will only flow in the middle region of the wire with $2iw$ in width as presented in figure 5.2.9 above. After simulating the current distribution with the 2D single tape model developed in this project, the dynamic loss Q can be calculated as equation 5.2 below:

$$\boldsymbol{Q = \int_{(1-i)w}^{(1+i)w} JE \cdot h\, dy = \int_{(1-i)w}^{(1+i)w} \frac{J^2}{\sigma_{sc}} \cdot h\, dy} \quad (5.2)$$

The σ_{sc} is the anisotropic conductivity for each superconducting element on HTS tape and it can be determined by the $E - J$ power law characteristics discussed in Chapter 3. The thickness of the tape simulated is marked by h.

After deriving the current density distribution, the resultant total magnetic field distribution $\boldsymbol{B_{tot}(y,t)}$ across the tape cross-section area can be calculated by combining perpendicular component of the transport current induced magnetic field $\boldsymbol{B_s}$ with the external magnetic field $\boldsymbol{B_e}$ as presented in equation 5.3 and 5.4 below:

$$\boldsymbol{B_s(y,t) = \frac{\mu_0}{2\pi}\int_0^{2w}\frac{J(u,t)}{y-u}\,du} \tag{5. 3}$$

$$\boldsymbol{B_{tot}(y,t) = \frac{\mu_0}{2\pi}\int_0^{2w}\frac{J(u,t)}{y-u}\,du + B_{peak}\cdot\sin(2\pi f\Delta t\cdot N(t))\cdot\sin(\theta)} \tag{5. 4}$$

Where in equation 5.3 and 5.4, u represents the position of the source points and y represents the position of the field points in the meshed area of the finite element analysis.

5.2.3. *Dynamic Loss Simulation with FEM Model*

In order to verify the effectiveness of this FEM model, simulation case studies are performed with the specification of a commercial YBCO coated conductor tape manufactured by SuperPower Inc. The parameters used for simulation is documented in table 3 below. The frequency of the external magnetic field is set as 26.62Hz. In order to validate the effectiveness of the HTS model proposed in this thesis, the numerical model simulated dynamic loss results and the analytically calculated results are compared with the experiment results measured by the researchers of the Robinson Research Institute, Victoria University of Wellington. The experiment setup is presented in figure 5.2.10 below.

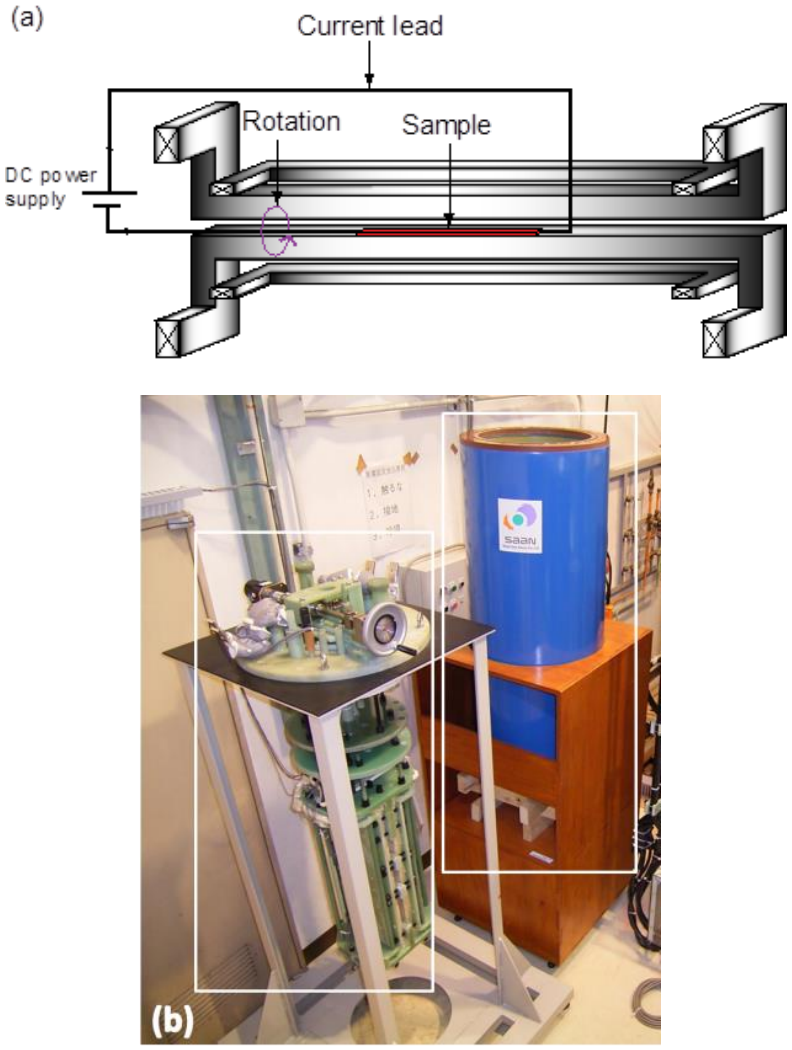

Figure 5.2.10 Dynamic Loss Measuring System Setup [115]

The experiment setup is presented in figure 5.2.10 above. The HTS coated conductor sample was placed in a custom-built AC magnet as demonstrated in the schematic of figure 5.2.10 (a) which can generate a uniform dipole AC magnetic field of up to 100 mT peak within the sample region. The wire sample was powered by a DC current supply that provides 0-300 A to simulate transport current at different load rates. The voltage drops along the HTS wire sample were measured by voltage taps. The voltage drops were measured in a segmented way leaving a space of 50 mm in between. The signal wires of the voltage taps were twisted in a spiral way to cancel the induction. At the right side of the AC magnet in figure 5.2.10 (b) is the cryogenic container used to maintain the operational temperature at 77 K. Time-averaged DC voltages were measured using a Keithley 2182 nano-voltage meter at different transport current

settings. The measured voltage drops along with the corresponding transport currents were used to calculate the total dynamic losses across the HTS sample. The experimentally derived total dynamic losses were also recorded in figure 5.2.11 below and marked by red hollow circles.

The simulation is performed for tapes carrying various level of transport current ranging from 10% of the critical current to 90% of the critical current. External magnetic fields with peak amplitudes ranging from 0mT to 100mT with an increment step of 5mT are applied for each transport current setting. The simulation results of the total dynamic losses for each case are normalised by the length of the coated conductor and are recorded in figure 5.2.11 below.

Table 3: SuperPower YBCO Tape Simulated

Self-field critical current I_c (A)	105.3
Critical current density J_c ($\times 10^{10}$ A/m^2)	2.63
***n*-value**	22.5
Coated conductor width (mm)	4.0
HTS layer thickness (μm)	1.0
Substrate thickness (μm)	50.0

In order to verify the simulation results, the analytical equation calculating the time averaged dynamic loss across a HTS wire in a full cycle (proposed in the work of [110] [111] [112]) is employed. The dynamic loss dissipated on HTS wire can be calculated from the equation 5.5 below. The calculated analytical results are also recorded in figure 5.2.11 and are plotted with the solid black line.

$$\boldsymbol{Q = I_t \Delta \varphi = \frac{4wfLI_t^2}{I_c}(B_\perp - B_{th})} \quad (5.5)$$

In equation 5.5 above, f is the frequency of the external magnetic field, L is the unit length of the simulated HTS wire, $\boldsymbol{B}_\perp$ is the perpendicular component of the external magnetic field and B_{th} is the threshold field level at which the perpendicularly applied external magnetic field can fully penetrate the HTS wire. This threshold field of B_{th}

will have different values when the HTS wire is carrying different transport currents. The value of the B_{th} can be calculated by equation 5.6 below as proposed by [110]:

$$\boldsymbol{B_{th} = B_p(1 - \frac{I_t}{I_c})} \quad (5.6)$$

In equation 5.6 above, B_p is the full penetration field of the simulated HTS coated conductor when no transport current is carried by the HTS conductor. Based on the work of [113], in this simulation case the $B_p$value can be calculated with equation 5.7 below:

$$\boldsymbol{B_p = 2.4642 \frac{\mu_0 J_c h}{\pi}} \quad (5.7)$$

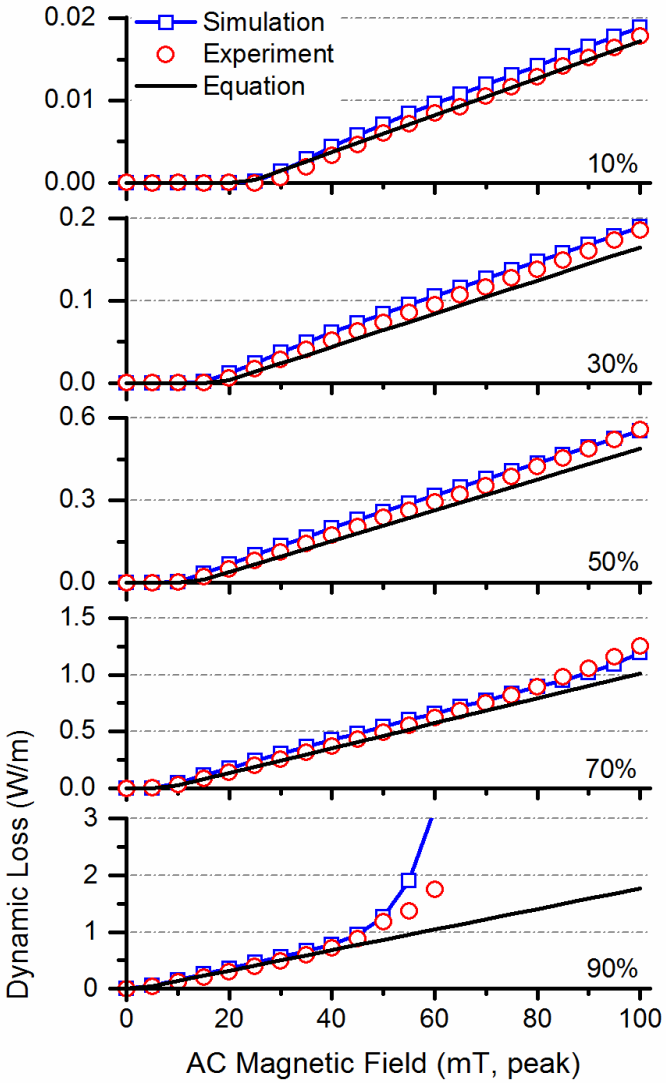

Figure 5.2.11 Dynamic Losses Obtained by Experimental Measurements, Numerical Modelling, and Analytical Equation

It can be observed from figure 5.2.11 above that when the simulated wire is carrying a smaller transport current ranging from 10% of I_c to 50% of I_c, the simulation results demonstrated good accuracy and agree closely with both the measured results and the results calculated from the analytical equation. Below the threshold field level, the simulation results show almost no dynamic loss for each transport current setting. When the external field amplitude exceeds B_{th}, the dynamic loss experience linear increase. This phenomenon also agrees well with the results presented in the research of [114] [115] [116]. The threshold field B_{th} of the simulated HTS wire decreases with the increasing magnitude of the transport current. This is anticipated and verified by equation 5.6 above. This phenomenon is caused by higher amount of magnetic flux generated by the transport current become normal to the HTS wire. Therefore, the flux density required from the external magnetic field to reach the threshold field level is reduced as reported in the works of [74] [110].

It is also interesting to notice that for high transport current and high external field settings, the dynamic losses both simulated by the numerical model and measured by the experiment deviate significantly from the results calculated by the analytical equation. The numerical modelling results still agree well with the experimentally measured results.

When the HTS wire is carrying 70% of I_c and the applied field is greater than 80mT, the dynamic loss calculated by the numerical model and measured by the experiment start to increase in an exponential pattern. The same exponential rise is also observed when the tape is carrying 90% of I_c while the external AC field magnitude is greater than 40mT. This exponential rise was not reflected on the analytically calculated results which only follows a linear increase pattern after the external field grows beyond the threshold level. This difference exists because the loss of HTS material is also heavily influenced by the critical current which has a significant dependence to the magnetic field strength present in the environment. This dependency is approximated by the Kim's model and is built in the algorithm of the numerical model. For the cases where strong AC magnetic field is presented, the critical current level of the HTS tape will decrease in a period of time during the complete AC cycle. When the critical current level is temporarily reduced to be smaller than the transport current,

the conductivity of the HTS tape decrease dramatically. This in turn will result in rapid total loss increase across the tape. Since the dynamic loss is defined as the loss caused by the AC external magnetic field in the superconducting region that carries the DC transport current, the loss in this region will also rise quickly and thus the exponential rise in dynamic loss is observed. For the analytical equation mentioned in previous section, this relationship between the critical current and the magnetic field strength is neglected and the equation only assumes a constant critical current value. Therefore, the rapid loss increase was not represented in the analytically calculated results.

For cases where transport current is 90% of I_c and the external field is greater than 40mT, the simulation results start to become larger than the measured results with increasing error. This is due to the *n* values of the superconducting material start to drop due to the influence of the combined magnetic field [117]. Based on the discussions made in the section 5.2.1, a smaller *n* value will lead to a smaller loss across the HTS wire. However, under nominal operating conditions, the effect the magnetic field have on the *n* value is limited. Therefore, for the sake of calculation efficiency, the numerical model did not take into account of this dependency and assumed a constant *n* value. The measured results for AC applied field larger than 60mT cannot be obtained from the experiment when the wire is carrying 90% of I_c. As in this circumstance the transport current alone is very close to the critical current level, combined with the induced current produced by the AC field the total current flowing on the HTS tape can easily exceed critical level and damage the HTS wire.

5.2.4. *Magnetic Field and Current Density Profiles*

One of the most important advantage of building the finite element numerical model is its capability of modelling the detailed current and magnetic field distributions inside the HTS wire. The ability to examine these detail distributions will greatly help the research in understanding the loss generation mechanisms of the HTS materials. The experiments could not measure these microscopic distributions with enough resolution and accuracy, whilst analytical methods can only provide a rough estimation and lack the flexibility of considering the influences of multiple correlated variables. Therefore, building the finite element model becomes an invaluable tool to study these detailed phenomena.

In order to study the change of dynamic loss during a complete AC magnetic field cycle, current density and magnetic field distribution on the HTS wire is simulated with this numerical model. An HTS wire carrying a transport current of 50% of I_c is first simulated. An AC external field with 20mT peak magnitude is applied perpendicularly to the wire. The current density and magnetic field distribution across the wire in one AC field cycle are demonstrated in figure 5.2.12 and 5.2.13 below.

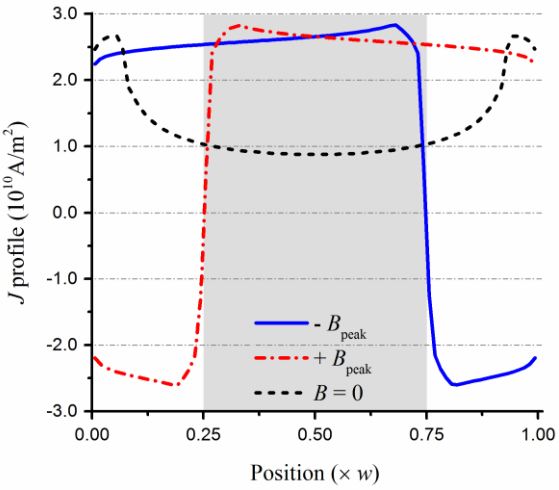

Figure 5.2.12 Current Density Distribution of the HTS wire under 20mT AC Field*

*The grey area marked in figure 5.2.12 above represents the area that carries the superconducting DC transport current within the cross-section of the HTS wire. This applies to the grey area in the following figures within this chapter.

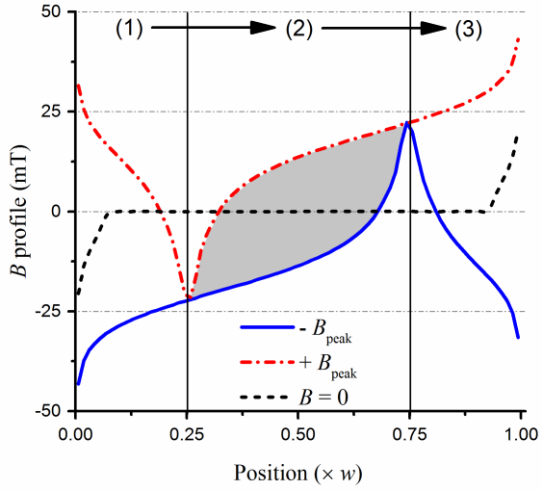

Figure 5.2.13 Magnetic Field Distribution of the HTS wire under 20mT AC Field

In figure 5.2.12 above, the current density distributions under both positive peak and negative peak of the 20mT AC field are plotted and labeled as $+B_{peak}$ and $-B_{peak}$

respectively. The corresponding magnetic field distributions are plotted in figure 5.2.13. In figure 5.2.12, the grey area marked out the region where the current distribution remain relatively constant during a complete AC cycle. The current density outside of the grey area changes from positive to negative during the AC cycle. The current density in the grey area remain largely constant as the DC transport current flows in this region. The slight drop on current density distribution at the edges of the wire is due to the relatively strong magnetic field reduced the local critical current density level. The current density distribution when zero AC field is applied is also plotted as a reference.

From figure 5.2.13, the magnetic field distribution across the width of the HTS wire experienced a cyclic change during its AC period. It can be clearly observed from figure 5.2.13 that the magnetic flux swept through the wide face of the HTS tape during the cycle. The grey area enveloped by the positive and negative peak magnetic field distribution demonstrate the hysteretic change pattern of the magnetic flux and the width of the grey area is in accordance with which in the current density plot of figure 5.2.12. If in this case, a complete AC cycle is defined as starting at $-B_{peak}$ and increase until $+B_{peak}$ then end up dropping back to $-B_{peak}$, than the magnetic flux will enter the tape from area (1) and end up in area (2) during first half of the AC cycle with magnetic field changing from $-B_{peak}$ to $+B_{peak}$. The same flux will than exit the tape from area (2) to area (3) during the second half of the cycle when magnetic field drop from $+B_{peak}$ to $-B_{peak}$. The traverse of the flux will induce a DC voltage across the HTS wire as described in [114] and thus cause the dynamic loss across the HTS wire.

Based on the discussion made above, it can now be seen that the HTS dynamic loss is heavily dependent on both the transport current and the external magnetic field. In order to study how these two factors influence the overall HTS dynamic loss, more detailed magnetic field and current distribution profiles are plotted in figure 5.2.14 and figure 5.2.15 below. It is found that the dependency of the dynamic loss can be clearly explained by studying the detail of the current and field distribution plot. In order to study the two factors individually, the transport current on simulated HTS wire is first

fixed at 10% of I_c. The current density and magnetic field profile are plotted for different external AC magnetic field settings.

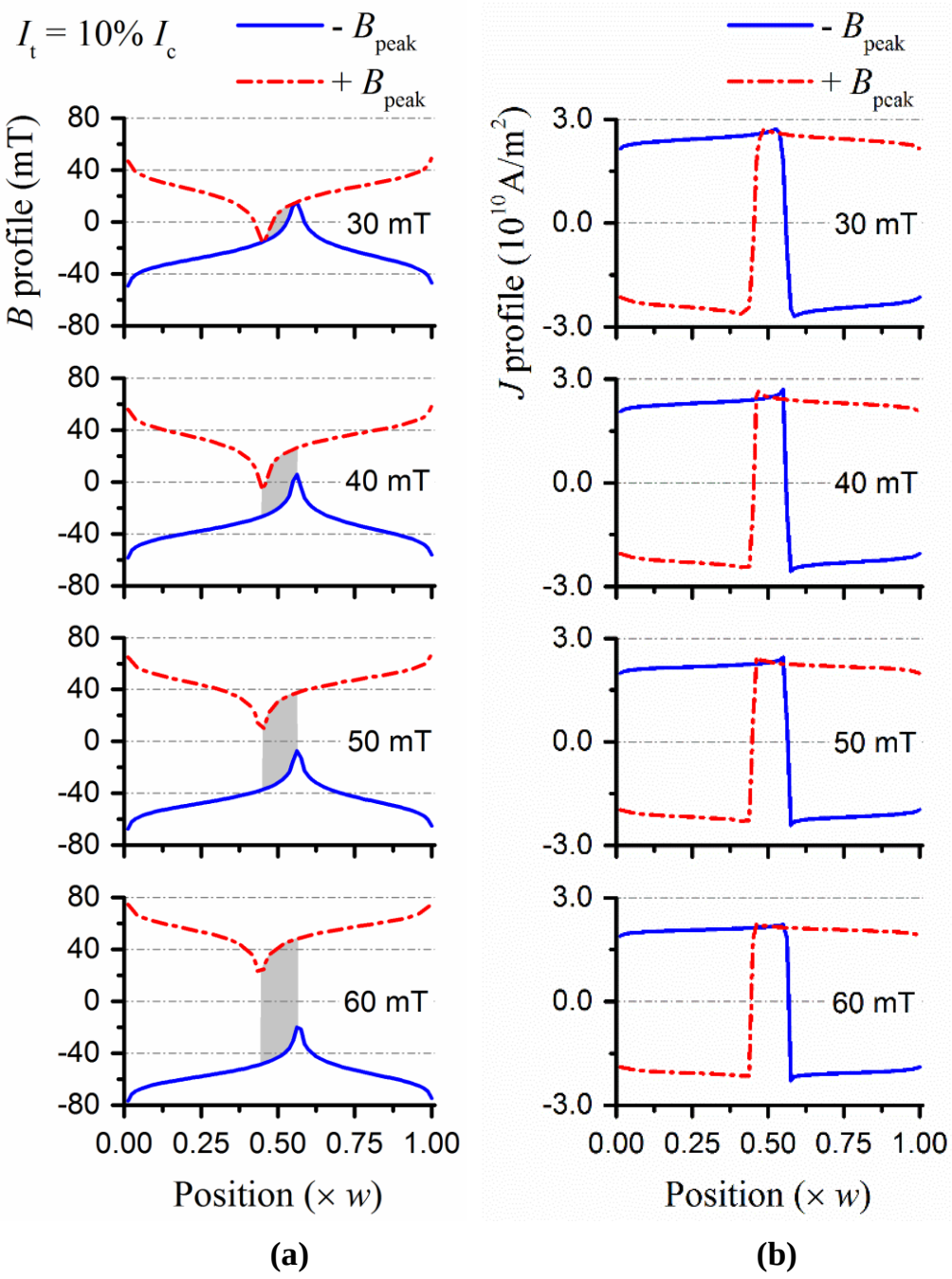

Figure 5.2.14 Magnetic Field and Current Density Profile for HTS wire carrying a DC current of 10% I_c, whilst exposed to a magnetic field of amplitudes ranging from 30~60 mT

The current density and field distribution for the wire carrying 10% of I_c is first plotted in figure 5.2.14 above. From figure 5.2.14(b), it can be observed that the area

carrying the DC transport current is again around 10% of the wire width located at the center of the wire. The current density distribution profile remain largely unchanged with the increasing magnitude of the external magnetic field after the wire is fully penetrated by magnetic flux. Slight drops of the current density are observed in the center region of the wire for higher external field settings and the overall current distribution on wire become more even. This is due to the increase of the external field suppressed the critical current density across the wire and the current was forced to spread more evenly and fill the regions where the critical current density level has not been reached. The grey zone enveloped by the $\boldsymbol{B}$ profile curve in figure 5.2.14(a) maintained its overall hysteretic shape. But the increase in external magnetic field strength increases the area of the grey zone. This indicates that more magnetic flux is driven to traverse the surface of the HTS wire during one cycle by the stronger external AC field. Therefore, for an HTS wire carrying certain DC transport current, a stronger external AC field will still cause larger flux changes across the DC current flowing region during one cycle. Thus, it is understandable that higher external field will induce larger dynamic loss after the threshold field is exceeded and the wire is fully penetrated by the magnetic field. For weaker external AC field that is below threshold field level, the current and field distribution on HTS tape can be referred to as presented in figure 5.2.6 in section 5.2.2. In this case the grey zone has not yet exist as the magnetic flux could not reach the DC carrying region of the tape. The traverse path is not formed and thus no significant dynamic loss would occur.

To study how different transport current levels would affect the overall dynamic loss, the AC external field is set as 20mT for its peak amplitude. Current and magnetic field profile is plotted for transport current settings of 50%, 70% and 90% of I_c in figure 5.2.15 below.

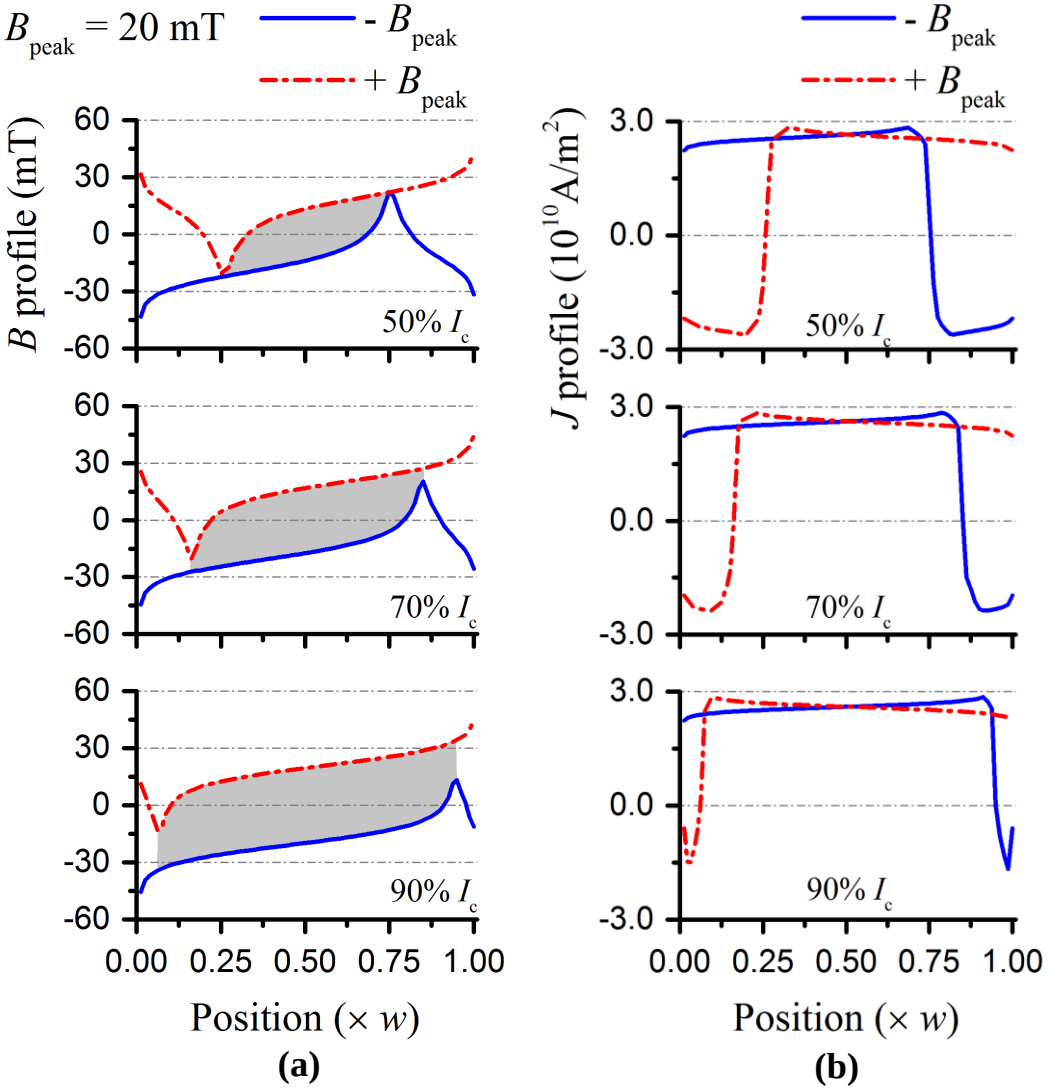

Figure 5.2.15 Magnetic Field and Current Density Profile of an HTS wire carrying DC currents ranging from I_t = 50%~90% I_c, whilst exposed to a constant 20mT AC magnetic field

From figure 5.2.15 above, it can be observed that for a fixed AC field, the grey zone enveloped by the magnetic field distribution curve expanded from the center region towards both edges of the tape to occupy larger area with the increase of the transport current. This is as expected as larger DC transport current will take up more flowing space in the HTS wire. Since the width of the grey zone is directly correspond to the part of the wire that carrying DC transport current, a fixed amount of magnetic flux in this case will traverse through a much larger space where dynamic loss can be induced if larger DC current is carried by the same HTS wire. The increased grey zone in this

case will also contain more magnetic flux traversing the wire and further increase the dynamic loss incurred on the tape.

By comparing the effect of both the transport current and AC external field strength, conclusion can be drawn that the transport current magnitude will play a more significant role in determining the HTS dynamic loss level. The increase of the transport current will cause the HTS dynamic loss to rise more quickly comparing to increasing the external field strength. This is also backed up by the simulation and experiment results recorded in figure 5.2.11.

5.3. Conclusion

In this chapter, the DC loss characteristics of the HTS wires have been studied extensively. Efforts have been focused on simulating the dynamic loss characteristics of the HTS wire particularly and a comprehensive study covering the HTS wire total dynamic losses as well as the current density and magnetic field distributions is delivered. By analyzing the simulation results, it is found that the HTS dynamic loss is influenced by the magnitude of the transport current as well as the external AC magnetic field. In order for dynamic loss to take effect, the magnitude of the applied AC magnetic field must exceed the threshold field level. The increase in transport current will reduce the value of the threshold field and make the dynamic loss to rise more easily for larger external AC fields. The simulation of the microscopic current density and magnetic field distribution helped the understanding of the HTS dynamic loss mechanism by establishing direct correlation between the total dynamic loss and the electromagnetic distributions. For a HTS wire carrying a certain amount of DC current, the increase in external field magnitude increases the dynamic loss by injecting more magnetic flux into the HTS material and increase the amount of flux traversing the material. For a HTS wire under a fixed AC field, the increase in DC transport current will increases the area where the dynamic loss can be induced and thus increase the total dynamic loss generated on the wire. The flux traverse phenomenon inside the HTS material during the dynamic loss is also successfully demonstrated by simulating the detailed magnetic field distribution inside the material.

Chapter 6. HTS AC Loss Characteristics Modelling and Analysis

6.1. Introduction

In the previous chapter, the DC loss characteristics of the HTS wires under AC external magnetic field, namely the dynamic loss, has been studied with the numerical model developed in this project. The simulation results were verified by the experimental measurements. In this chapter, the AC loss characteristics of the 2G HTS wires will be studied with this numerical model. Unlike the DC carrying scenarios, the HTS materials are not lossless when carrying AC current even when operating in perfectly isolated environments. Since the modern power systems commonly operate with AC power supplies, the modelling of HTS AC loss characteristics is of great scientific interest for both the HTS industry and research community. At the beginning of this chapter, the AC loss modelling results simulated by this numerical model will be validated by theoretical tools such as the 2D equivalent models and established analytical equations. After validating the HTS AC model, case studies are performed to study the AC loss characteristics of the HTS wires under various conditions to establish a full profile for the simulated 2G HTS wire. After finish studying the single HTS wires, different HTS cable structures are simulated with the full 3D cable model. Design factors affecting the overall AC losses of the HTS cables are analyzed and discussed with multiple case studies. Detailed current density and magnetic field modellings are also performed to study the generation mechanism of loss hot spots within HTS cables. The corresponding loss mitigation strategies are also proposed.

6.2. AC Model Validation

The primary objective of this thesis is to build the numerical model in 3D to analyze the electromagnetic characteristics of HTS cables. Since most of the realistic HTS cable designs consist of a single type of HTS coated conductor to reduce the manufacturing complexity, assumption was made for this project that the cable models

simulated in this project all use the same type of HTS coated conductor to allow comparable results from different case studies. As we aim to build the HTS cable models with multiple identical single coated conductor modules, it is vital to validate the 3D single wire model at the beginning.

The standard HTS coated conductor used for all the simulation case studies in this chapter is defined by the standard parameter table (table 4) below. In chapter 5, the 2D single wire model has been validated with the experiment results when studying the HTS DC dynamic losses in section 5.2.3. For long straight HTS wires, the 2D model is equivalent to the 3D model in principle. Therefore, the 2D model can be used as a reference to check the functionality of the 3D model when long straight HTS conductors are simulated. The aim of this section is to verify the 3D model using theoretical tools such as the widely recognized Norris analytical equation as well as comparing the 3D simulation results with those generated by 2D equivalent models.

Table 4: Standard HTS Coated Conductor Parameter Table

Parameter Name	Value Setting
Conductor Width	5 mm
Conductor Thickness	2 μm
***n* value**	30
Characteristic Electric Field E_0	1×10^{-4} V/m
Critical Current	100 A
Maximum Conductivity	1×10^{20} S/m
Characteristic Magnetic Field B_0	0.135 T

The 3D single HTS wire model is built with the stacking strategy introduced in section 4.4.2 in chapter 4. In order to first verify the AC simulation function of this model, the HTS wire is simulated without external magnetic field in this section. In this section, the total AC loss was used as the flag parameter to check the accuracy of the model under different load conditions. The AC losses of a single HTS coated conductor wire under different load conditions calculated by the Norris analytical equation (introduced in section 2.4.1.3) are provided as a reference. The total AC losses calculated by 3D single conductor model are compared to those calculated by the 2D model. Since the 2D model is equivalent to the 3D model for an infinitely long straight HTS wire, the results produced by the 2D and 3D models should not deviate from each other for too much. The total AC losses calculated with these different methods for a single HTS coated conductor carrying transport current ratio ranging from 0.1 to 0.9 (10% to 90% of critical current) are presented in figure 6.2.1 below.

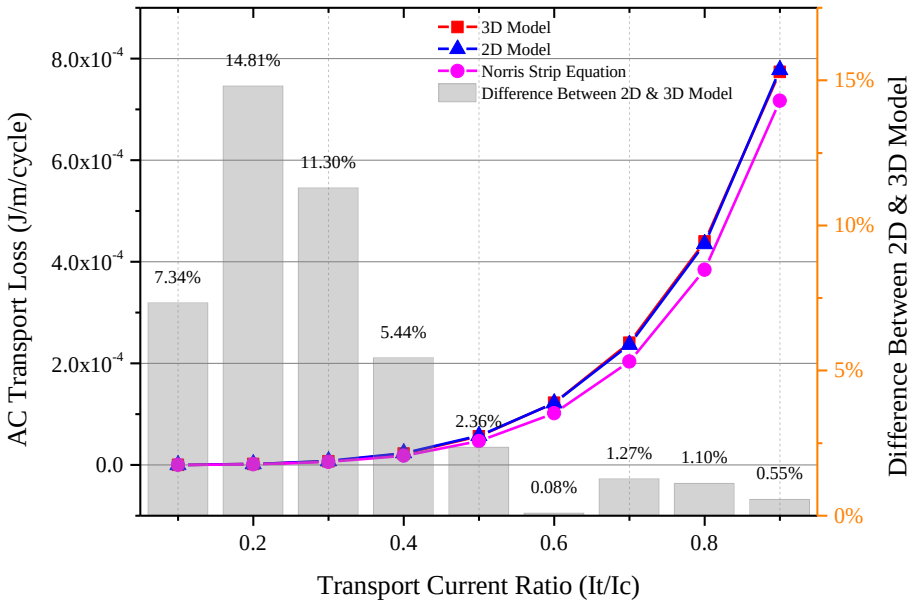

Figure 6.2.1 The AC transport losses obtained from 3D model, 2D cross-section model and Norris Strip equation.

The *x*-axis represents the ratio of transport current over the critical current where I_t stands for transport current and I_c represents the HTS conductor's critical current.

It can be seen from figure 6.2.1, the total AC loss (per meter) calculated by the 3D model is overall very close to the result calculated by the 2D mode. The AC loss calculated by both the 3D and 2D model also agrees well with the analytical results calculated with Norris thin strip equation. The FEM model calculated AC losses tend

to be around 20% higher than the Norris equation calculated results under the same current loading condition. This is reasonable and within expectation as explained previously in section 2.4.1.3. The Norris equation employs London model which only considered idealised current distribution within the HTS material. As a result, the Norris equation overlooked part of the AC losses generated within the centre region of the material. The FEM model proposed in this thesis employs the latest and more accurate $E - J$ power law and Kim – Anderson model to describe the non-linear relationship between the current density and electric field within the superconductor. Therefore, it is within expectation that the FEM model generated results are bigger than the ones calculated by the Norris equation.

The grey bar in figure 6.2.1 represents the difference in percentage between the 2D and the 3D FEM model. When the HTS conductor is loaded with higher transport currents, the difference between the results of 2D and 3D model are below 6%. Since in most realistic cases coated conductors within the HTS cables will be carrying transport current with magnitudes well above 50% of their critical current level, it can be said that the 3D model functions well under the common operating condition. The difference between the 2D and 3D model become larger when smaller transport current was set to be carried by the conductor. The difference is around 10%. The reason for this increase in difference is due to that the value of the AC losses calculated under low transport current cases are very small. Therefore even though the absolute difference between results calculated by two models are very small, the difference in percentage can still be relatively high. Another reason for causing this increase in difference is that the FEM models used an iterative approach as described in section 3.4.3 to produce converged final results. However, the iterative algorithm used employs a static convergence criteria. Therefore when the final result of a simulation case has a value close to the convergence criteria, the convergence criteria will become less sensitive to errors. The potential mitigation method to this issue is to employ dynamic convergence criteria in the future.

In this section, the simulation results of the 3D single conductor model are examined against the reference results provided by the 2D model and the Norris analytical equation. In general, the calculation results produced by the 3D model agrees well with

the 2D model and also fit the overall trend calculated by the Norris equation. The causes of error are also discussed and analysed. Overall, it can be concluded that the 3D single wire model functions well and showed good accuracy.

6.3. AC Loss in HTS Coated Conductors

In this section, electromagnetic analysis of the HTS coated conductors under different working environments are performed with the FEM model in order to study the factors affecting the AC loss generation of the HTS materials. As the application of the HTS power cables is normally a decision based on financial feasibility, the operation cost of the HTS cables must be kept as low as possible to justify the need for additional cooling systems and higher life cycle maintenance costs. By modelling and studying the AC loss characteristics of the HTS material, corresponding loss mitigation strategies can be proposed to improve the performance of the HTS power devices. In general, factors affecting the HTS AC loss characteristics can be divided into two categories: the external factors and internal factors. The internal factors are related to the microscopic properties of the HTS conductors, for example the material's crystalline structure. The external factors refer to those exists in the working environment, such as the external magnetic field, the transport current and the design features of the HTS power devices. Since this project aims to study the HTS power cables from an application prospective, the modelling work in this section will focus on the external factors affecting the HTS AC losses.

6.3.1. Magnetic Field and Current Density Profiles

When an AC transport current is carried by the HTS coated conductor, the current and magnetic field distributions across the conductor's wide surface will not stay constant comparing to the DC carrying scenarios. The alternating transport current will produce periodically changing current and magnetic field distributions. As discussed in section 2.4.1, the transport current induced magnetic field (self-field) will traverse through the wide surface of the conductor periodically. This according to the Faraday's law of induction will induce an electric field within the coated conductor and cause hysteresis loss. The energy dissipated by this hysteresis loss will have to come from the transport current. Therefore, an AC carrying HTS conductor will produce a much

larger amount of total loss compared to when it is carrying a DC current with the same magnitude. In order to observe the periodically changing electromagnetic distributions on HTS wire, detailed electromagnetic analysis is performed with the FEM model.

In this section, the current density and magnetic field distributions of an AC carrying HTS coated conductor are simulated. The load current ratio is varied from 0.1 to 0.9 (10% to 90% of the critical current magnitude). The frequency of the AC transport current is set as 50Hz. The HTS coated conductor in this case is defined using the standard parameter table (table 4). Two cases were selected to demonstrate the difference in current density and magnetic field distributions under low load current condition and high load current condition. The low load current condition is represented by the case where 20% of the critical current is carried by the conductor whilst high load current condition is represented by the case simulated with 80% of the critical current. The distribution results obtained from the two cases are presented in figure 6.3.1 to 6.3.2 below.

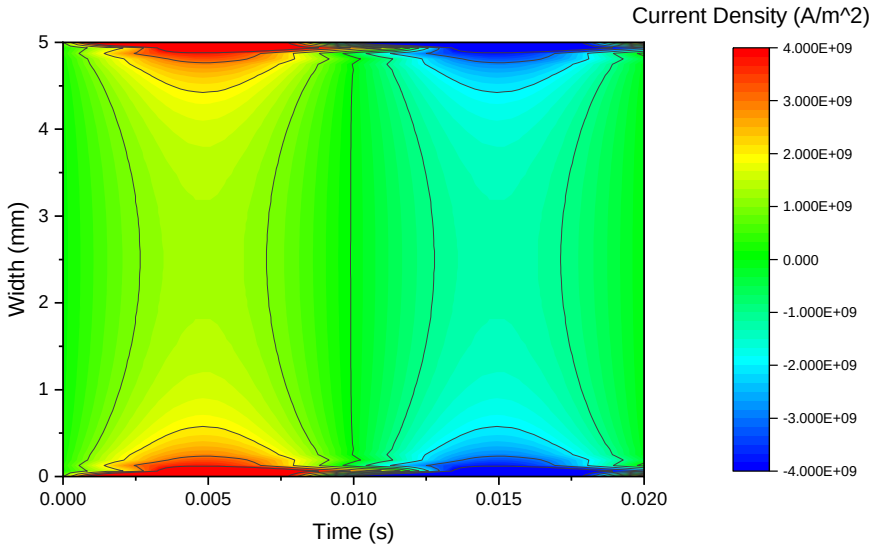

Figure 6.3.1 Current Density Distribution for an HTS Wire carrying an AC Current of 20% I_c

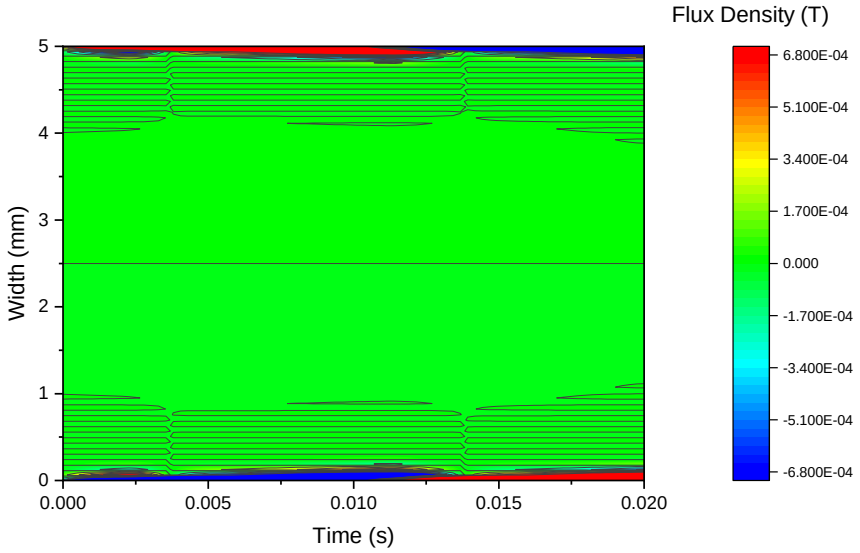

Figure 6.3.2 Magnetic Field Distribution for an HTS Wire carrying an AC Current of 20% I_c

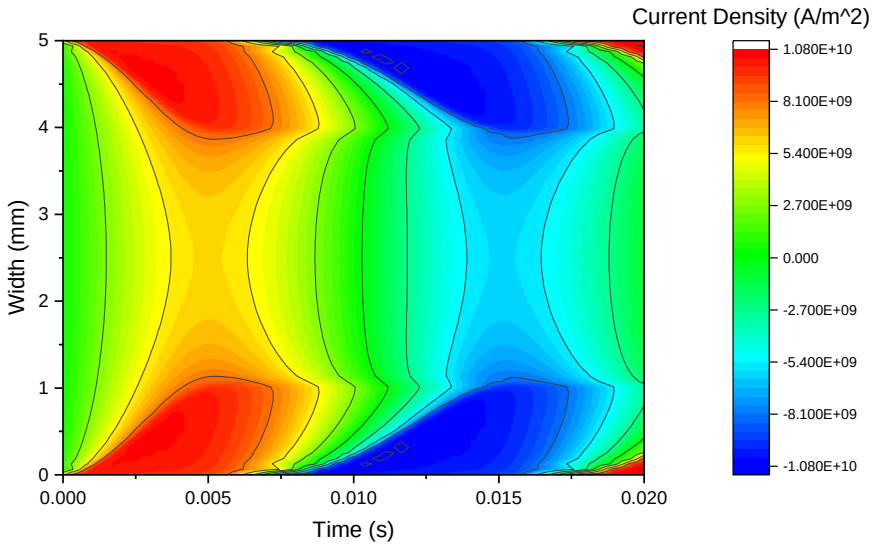

Figure 6.3.3 Current Density Distribution for an HTS Wire carrying an AC Current of 80% I_c

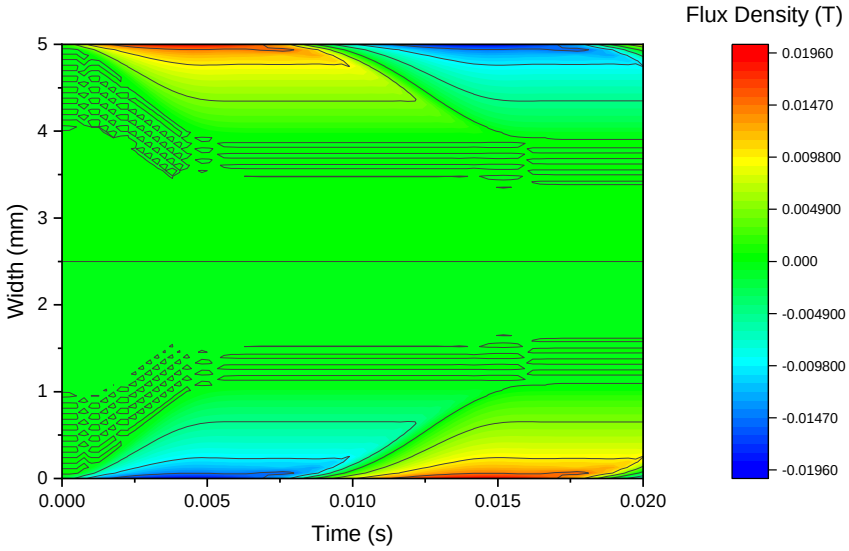

Figure 6.3.4 Magnetic Field Distribution for an HTS Wire carrying an AC Current of 80% I_c

As it can be observed from figure 6.3.1, for the low load current condition, the transport current mainly concentrated at the edge area of the conductor. For the first half cycle of an AC period. The magnitude of the transport current first rises from zero to the peak magnitude and then falls back to zero. With the rising current magnitude, the transport current induced magnetic field also becomes larger and creeps towards the center of the conductor. In the second half of the AC cycle, the current again increased to the peak value and then falls back to zero, only with an opposite flowing direction. Following the creeping magnetic flux, the current also distributes further into the center of the conductor. Since in this section, the magnetic field is purely induced by the transport current, the magnetic field at two edges of the conductor have opposite directions according to the right hand rule.

For the high load current case in figure 6.3.3, both the magnitude of the current density and the area of distribution grows significantly comparing to the low load current case. The distribution of the magnetic field also follows the same pattern described for the low load current case.

The total AC losses calculated for all the different AC load current ratios are summarized in figure 6.3.5 below. The total DC losses for those load current ratios are also provided as references.

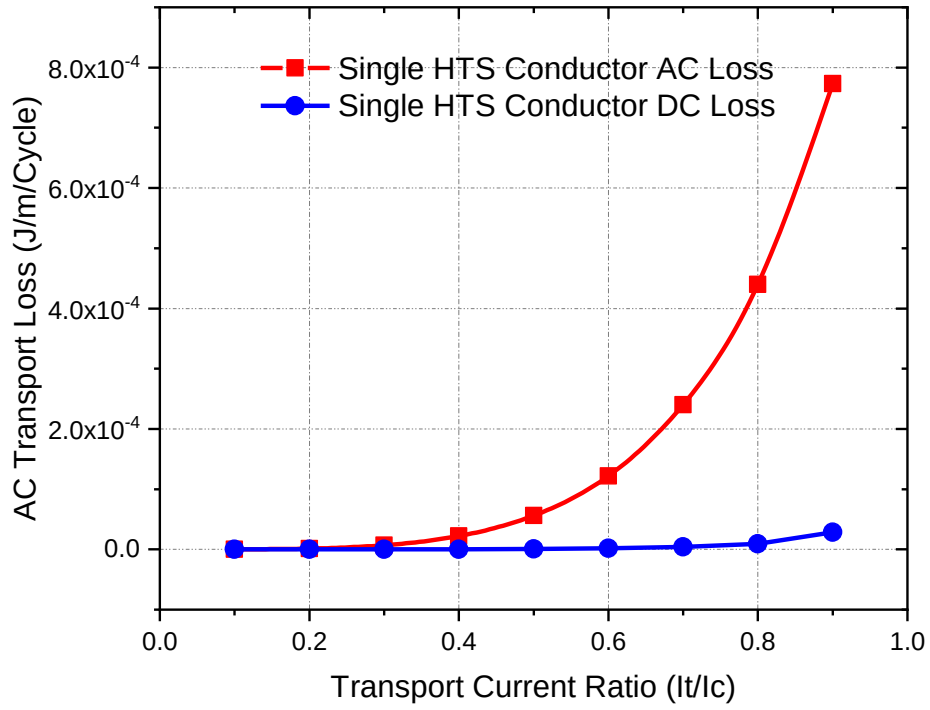

Figure 6.3.5 Total Loss of a HTS Wire when either carrying AC or DC Current

As it is presented in figure 6.3.5, both the total AC losses and the DC losses on HTS conductor rise with the increasing load current ratio. Only that the AC losses of the conductor rise much faster comparing to the DC losses. Overall the AC losses of the HTS conductor have much larger magnitudes comparing to the DC losses under the same load current ratio as discussed at the beginning of this section. The total DC losses on the HTS conductor remains extremely small over most of the load current settings. Only when the load current ratio is increased to 0.9 did the total DC loss increases visibly.

6.3.2. *Dependencies of AC Loss in HTS Coated Conductor*

In the previous section, the AC loss characteristics of the HTS conductor is discussed in an isolated environment. As the number of the HTS AC electric power applications grows steadily in recent years, it is natural to see that in the future the HTS coated conductors will be deployed in increasingly complex working environments where AC

external magnetic fields can exist. Therefore the study of HTS AC loss characteristics under AC external magnetic fields has become an important topic.

The AC loss characteristic of HTS coated conductor under different applied AC field will be studied in this section. In order to observe the effect of the AC external field, it is helpful to start the discussion in a relatively simple environment where the HTS wire carries no transport current. Figure 6.3.6 and 6.3.7 below presented the current density as well as the magnetic flux density distribution of the YBCO wire for a full cycle with standard parameter setting under a 50Hz AC external field with 15mT peak magnitude. The external AC field is applied perpendicularly to the wide face of the wire and pointing downwards toward the wire.

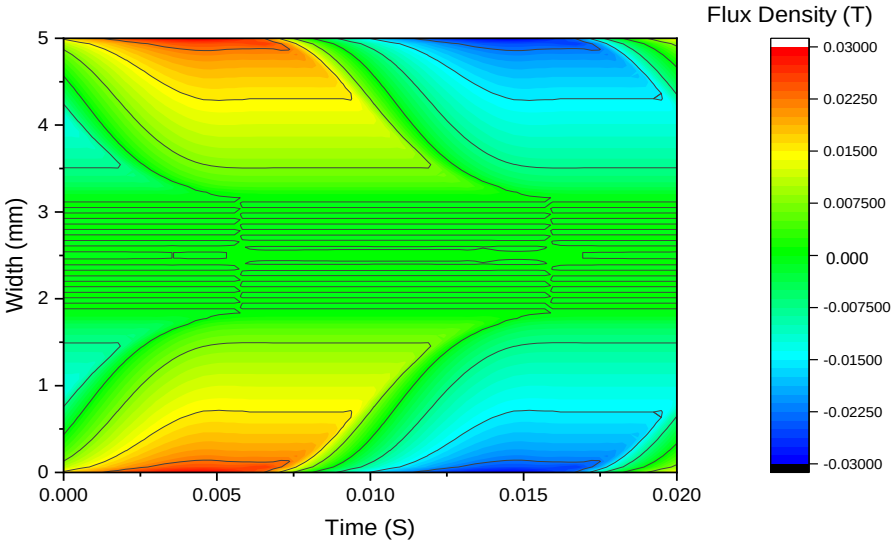

Figure 6.3.6 Induced Magnetic Field Distribution for an HTS Wire carrying no Current under 15mT AC External Field

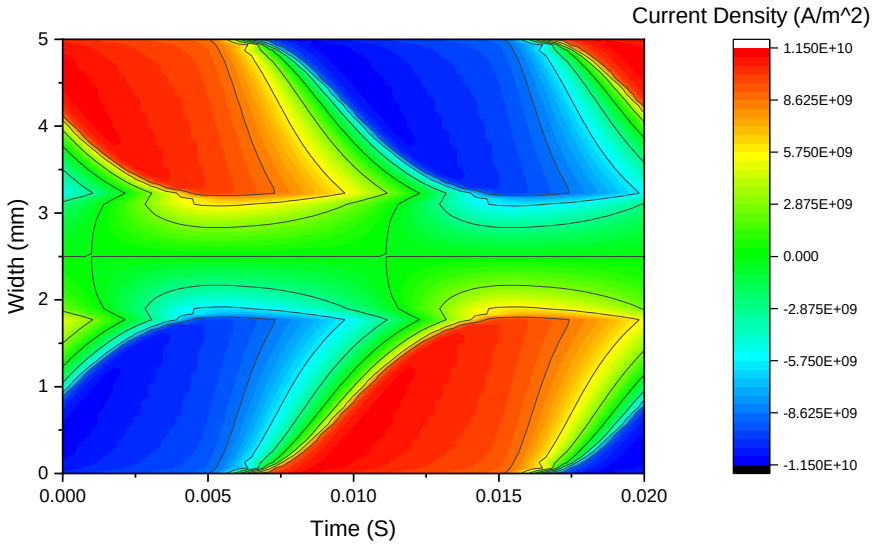

Figure 6.3.7 Induced Current Density Distribution for an HTS Wire carrying no Current under 15mT AC External Field

As it can be observed from figure 6.3.6, the 15mT AC external field has not penetrated fully into the center of the simulated HTS wire. The flux penetration starts at the edge of the wire. It can be observed that in the magnetic flux penetrated region, the induced current density roughly reached the critical current density. Whilst in the flux-free region, the induced current density is a lot smaller and decreases rapidly towards the center of the wire (as can be referenced more clearly by figure 6.3.12 and 6.3.13). The induced screening current effectively shield the center region of the wire from the applied AC field and thus the combined flux distribution profile in figure 6.3.6 exhibited highest flux density at the edge of the simulated tape.

The center region carries nearly zero induced current since no flux has been pinned within this region of the tape as showed in figure 6.3.7. The induced current at edges of the wire follows the Faraday's law of induction and show opposite flowing direction which changed after half of the AC period elapsed. The current distribution returns to its original state at the end of the cycle.

When the peak magnitude of the applied AC field increases to 30mT, the magnetic flux just about fully penetrates and magnetized the whole wire. The corresponding current density and magnetic flux distribution is presented in figure 6.3.8 and 6.3.9 below. As it can be observed from figure 6.3.8, the induced current has now flow in

the entire cross-section area of the HTS wire with the very center region of the wire carries a trace amount of induced current. The magnetic flux has now fully penetrated the entire wire with the center region carries a flux density of nearly zero.

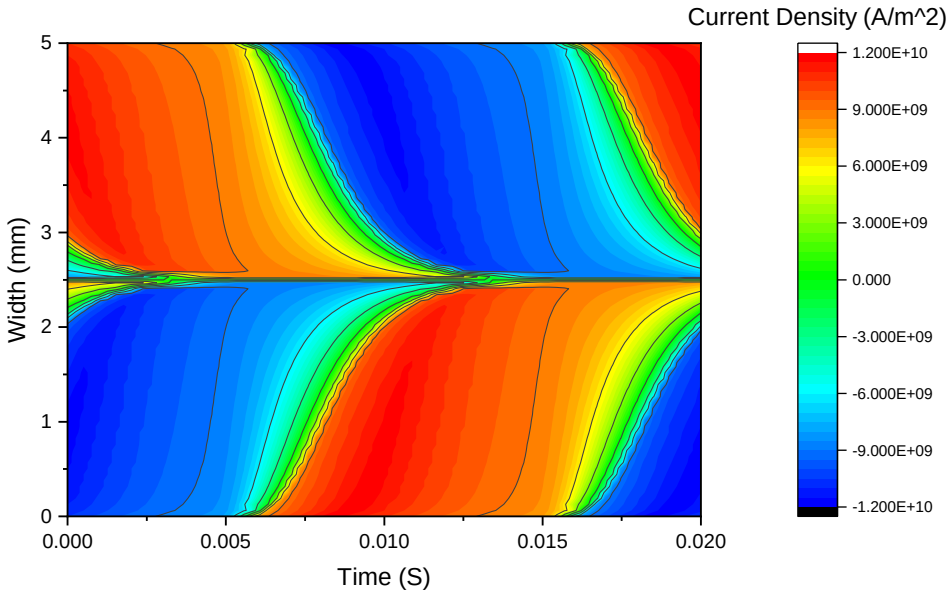

Figure 6.3.8 Induced Current Density Distribution for an HTS Wire carrying no Current under 30mT AC External Field

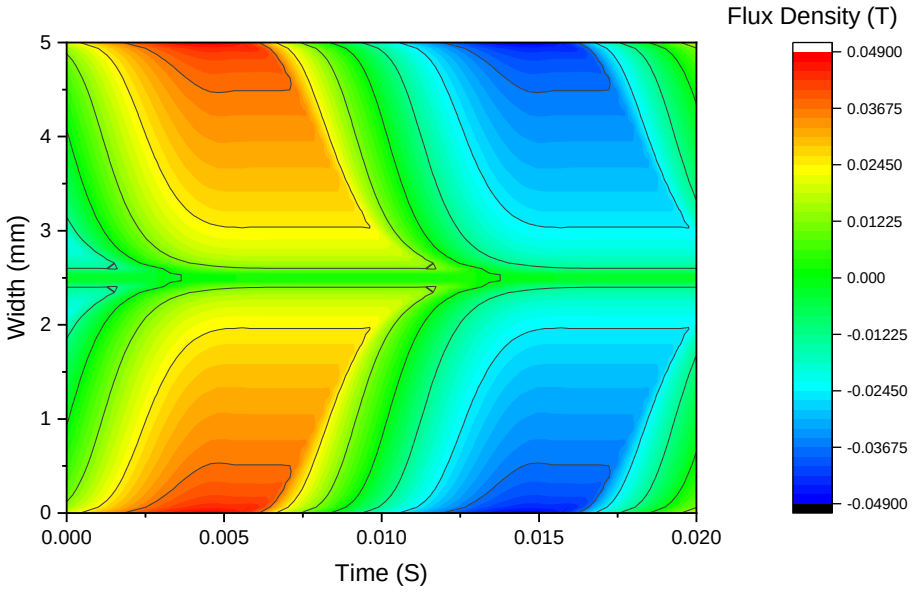

Figure 6.3.9 Induced Magnetic Field Distribution for an HTS Wire carrying no Current under 30mT AC External Field

When the applied field magnitude exceeds the full penetration level and increased to 45mT, the current density and flux distribution of the wire are plotted in figure 6.3.10 and 6.3.11 below. The pattern of the current density distribution does not have much change as the induced current has been flowing within the entire wire. However, the magnitude of the induced current is increased as a result of stronger magnetic induction effect. As demonstrated in figure 6.3.11, the flux density at the very center of the wire is no longer zero, this represents the flux penetration process has been completed. Further increase in the applied magnetic field amplitude will only increase the flux density within the HTS wire and it will not change the spatial distribution pattern significantly.

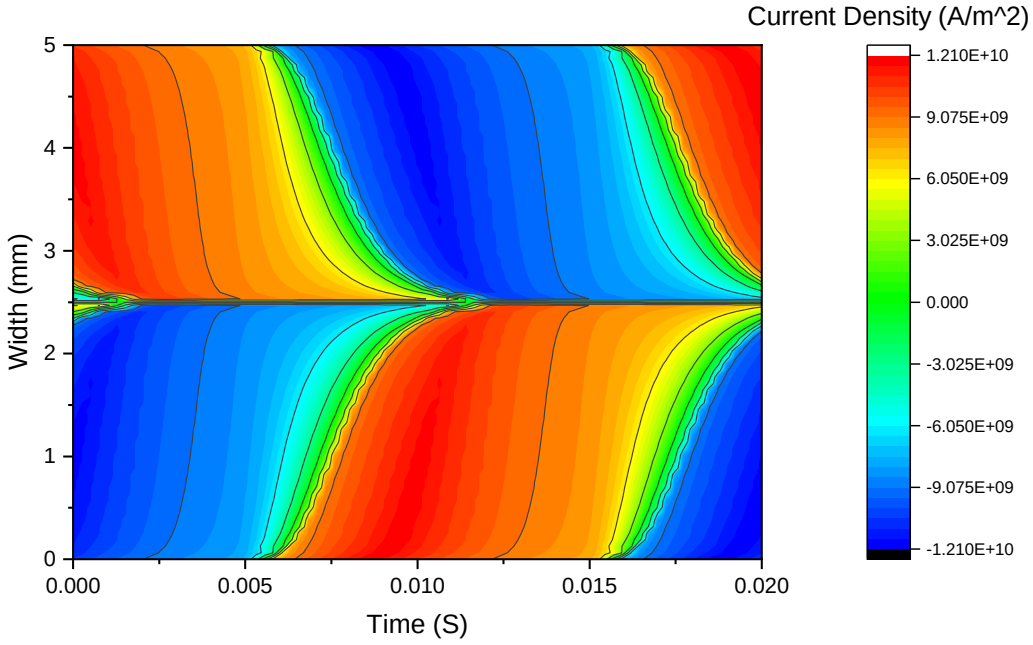

Figure 6.3.10 Induced Current Density Distribution for an HTS Wire carrying no Current under 45mT AC External Field

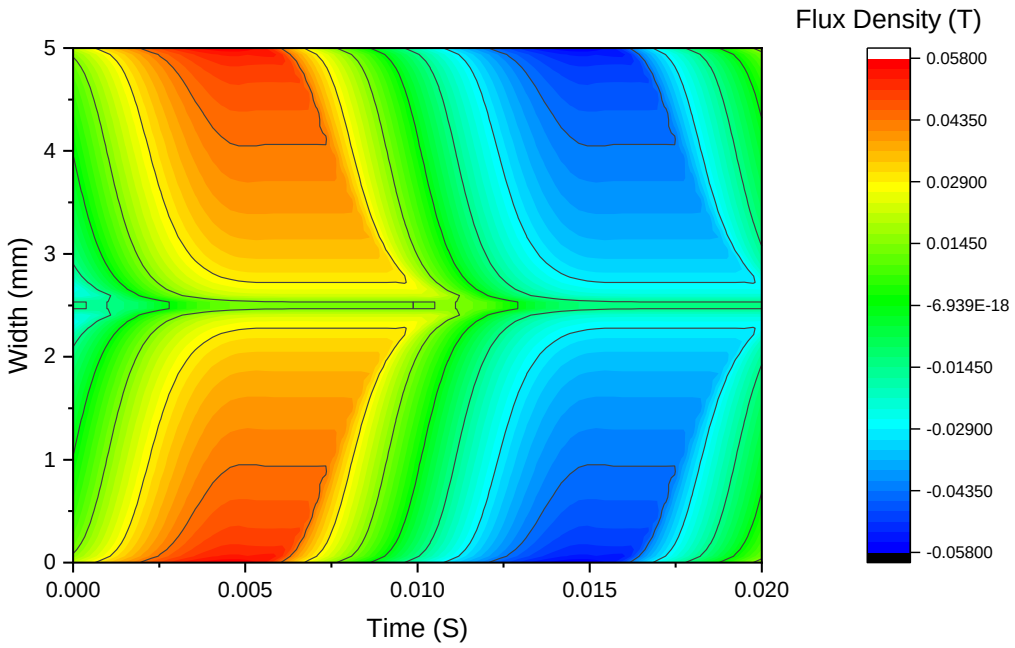

Figure 6.3.11 Induced Magnetic Field Distribution for an HTS Wire carrying no Current under 45mT AC External Field

The flux and induced current density distributions for different applied field magnitude at their peak value are summarised in figure 6.3.12 below. The flux density distribution results agree well with the current density distribution plots in figure 6.3.13 and clearly shows that the applied field realizes full penetration of the wire at 30mT and allows the induced current to cover the entire cross-sectional region of the simulated wire.

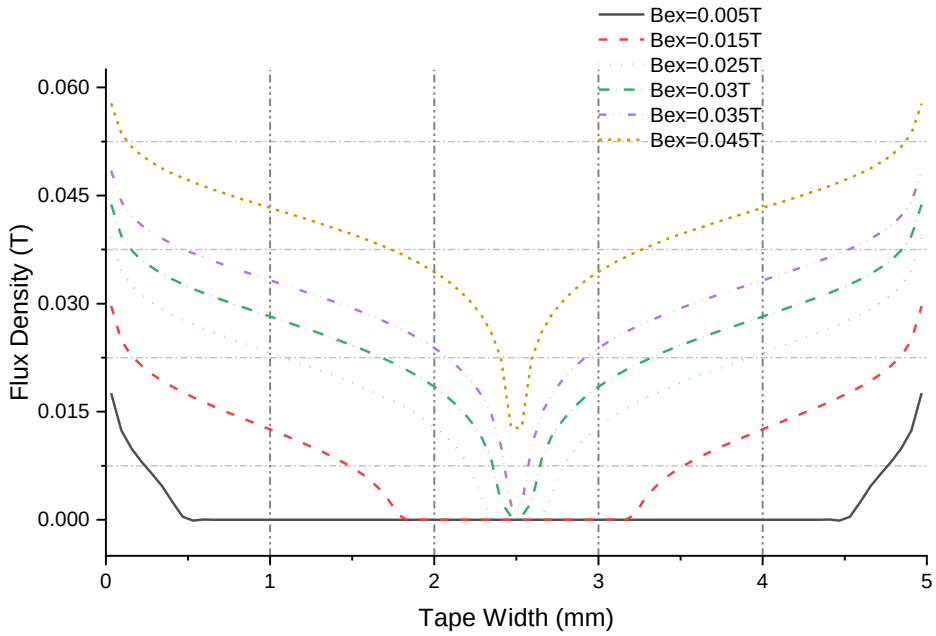

Figure 6.3.12 Peak Field Flux Distributions in an HTS Wire under various External Field Amplitudes

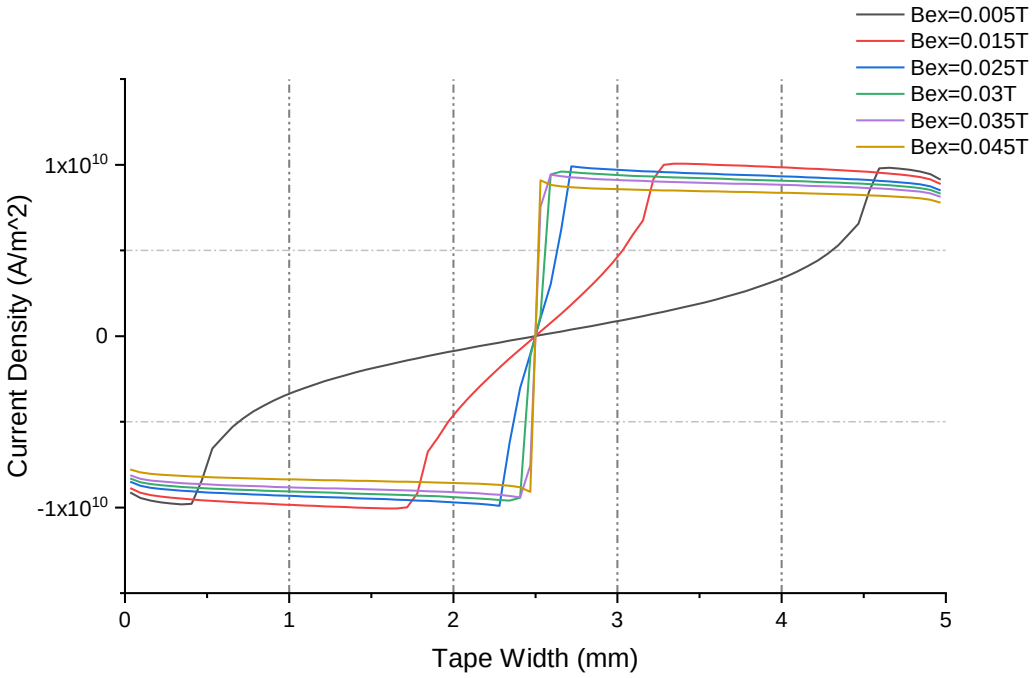

Figure 6.3.13 Peak Field Current Density Distributions in an HTS Wire under various External Field Amplitudes

Angular Dependence of AC loss

Apart from the magnitude of the external applied magnetic field, the insertion angle in which the external field is applied to the wire wide surface can also affect the AC loss characteristic of the HTS wire. Figure 6.3.14 below demonstrates the AC loss characteristic of the simulated HTS wire under different external magnetic field with various insertion angles, the frequencies of the AC fields are fixed at 50Hz. The external fields are again applied with the HTS wire carrying zero transport current. It can be observed from figure 6.3.14 that the overall AC loss incurred by the external fields increases with the magnitude of the applied field. It is also interesting to notice that roughly before the full penetration field magnitude of 30mT, the AC losses rise much more quickly. After the HTS wire is fully penetrated, the AC losses increase in a gentler way along with the increasing applied field amplitude. This is due to that before the full penetration field level, the majority of the AC loss is contributed by the magnetization of the HTS material. The transport loss contributed by the induced current is not yet dominant since the current induced remains relatively small. After the HTS wire is fully magnetized, with the increasing applied field, the amplitude of the induced current continues to rise and contributes more significantly to the increase of the overall AC loss whilst the magnetization loss stops to grow. Such phenomenon is also reported in the research of [118] [119] [120].

It can also be observed from figure 6.3.14, for a given external magnetic field, the AC loss incurred within the HTS wire increases with the increase of the insertion angle θ. As the superconducting layer within the simulated tape is extremely thin (2μm), the applied field component parallel to the wide face of the wire does not contribute much in terms of the induced AC losses. The perpendicular external field component contributes predominantly to the induced AC losses of the HTS wire. Therefore, for an applied field with θ closer to 90 degree, the perpendicular component will be larger and induce a higher level of AC loss.

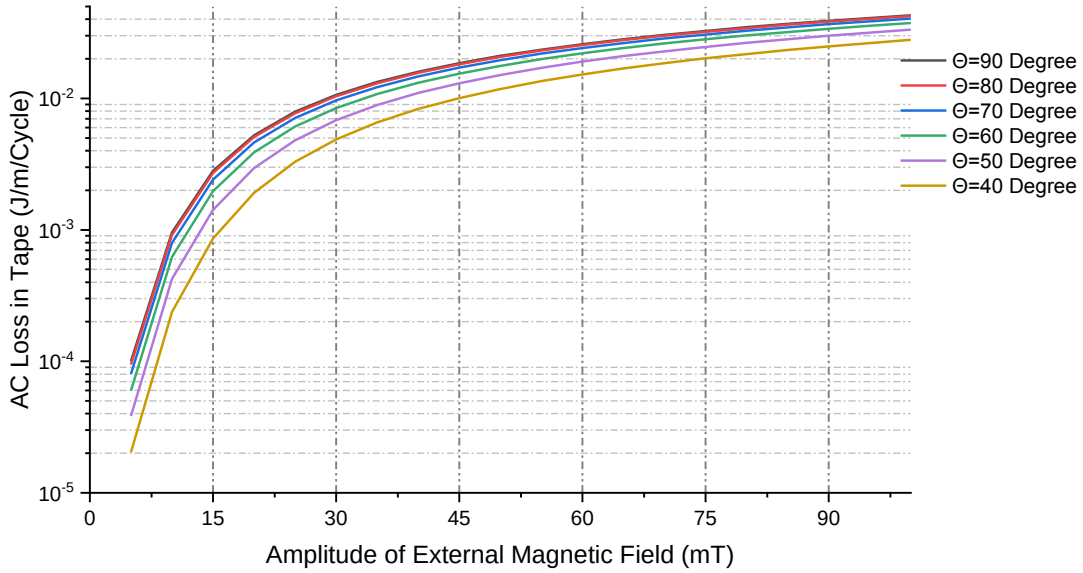

Figure 6.3.14 HTS wire AC losses with no initial current subject to various magnetic field under different angles*

*The simulation parameter used to produce the results in this graph is presented in table 4 of section 6.2.

Transport Current Dependence

The purpose of making the discussion about the external field induced AC losses on HTS wire under zero current condition is to better demonstrate the effect of the external magnetic field in an isolated condition. Since the HTS wires are designed to carry large amount of current, it is only nature to explore their AC loss characteristics with the impact of transport current considered. Although to avoid the additional losses the HTS wires in power cables normally work in magnetically shielded environments. Recently with the increasingly complex application designs, it is a lot more common to see HTS wires work in un-shielded conditions.

Figure 6.3.15 below summarized the AC loss results for an HTS wire carrying transport currents ranging from 0% to 70% of its critical current. The frequency of the transport current is set as 50Hz. It can be observed from the figure 6.3.15 that for each transport current setting, the total loss incurred on wire per cycle increases along with the magnitude of the external field applied. Similar to the AC loss increase pattern introduced in the previous section, the total AC loss per cycle increases rapidly before

the full penetration field is reached. Afterwards, the AC loss per cycle increases more gently with the increasing applied field magnitude. For a certain applied field magnitude, the AC loss per cycle increases along with the amplitude of the transport current. This is as expected as larger transport current will contribute to a more significant part of the transport loss.

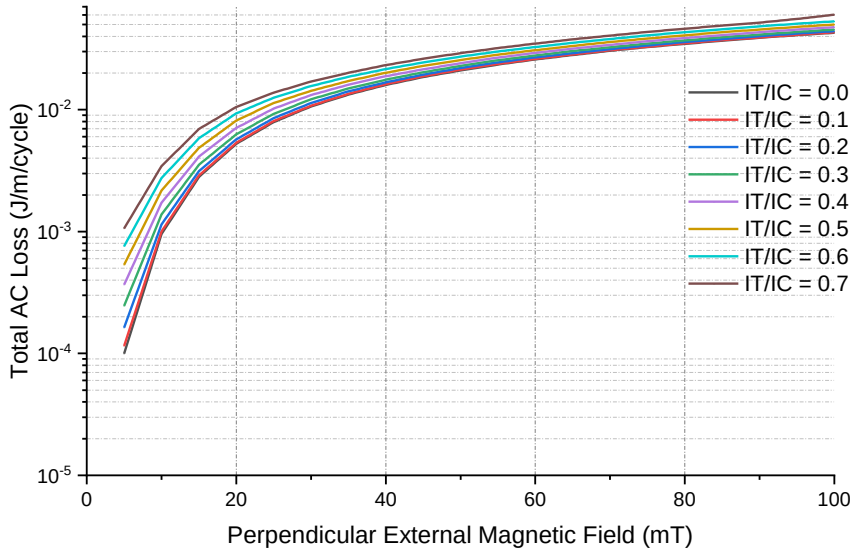

Figure 6.3.15 HTS wire AC losses under different perpendicular AC field when carrying various transport currents*

*The simulation parameter used to produce the results in this graph is presented in table 4 of section 6.2.

Frequency Dependence of AC Loss

It is well known that there are two important factors which define the property of an AC power supply: magnitude and frequency. In the previous sections, the impact of the magnitude of the AC transport current to the loss characteristic of HTS conductor wires has been addressed. This section will be used to discuss the impact of the frequencies of transport current and external field towards the overall AC loss on an HTS wire.

The impact of the of AC transport current frequency to the HTS wire AC loss per cycle is initially studied. Figure 6.3.16 below presents the AC loss per cycle results for HTS wire with transport current ratios ranging from 0.1 to 0.9. The simulated cases

cover the frequency from 50Hz to 5000Hz. Since for power applications, the frequency of the power source rarely go beyond kilo-Hertz level, this frequency range of study is believed to be sufficient. The simulation results below are calculated in an external magnetic field free environment.

From figure 6.3.16, it can be seen that for each frequency setting, the AC loss per cycle for HTS wire increases with the magnitude of the transport current. However, it is interesting to notice that when no external field is applied, the AC loss per cycle for each transport current setting decreases with increasing transport current frequency. Similar loss patterns are also observed when small external magnetic fields such as 2mT and 4mT are applied to the HTS wire. The loss results under 2mT and 4mT external magnetic field are presented in figure 6.3.17 and 6.3.18 below.

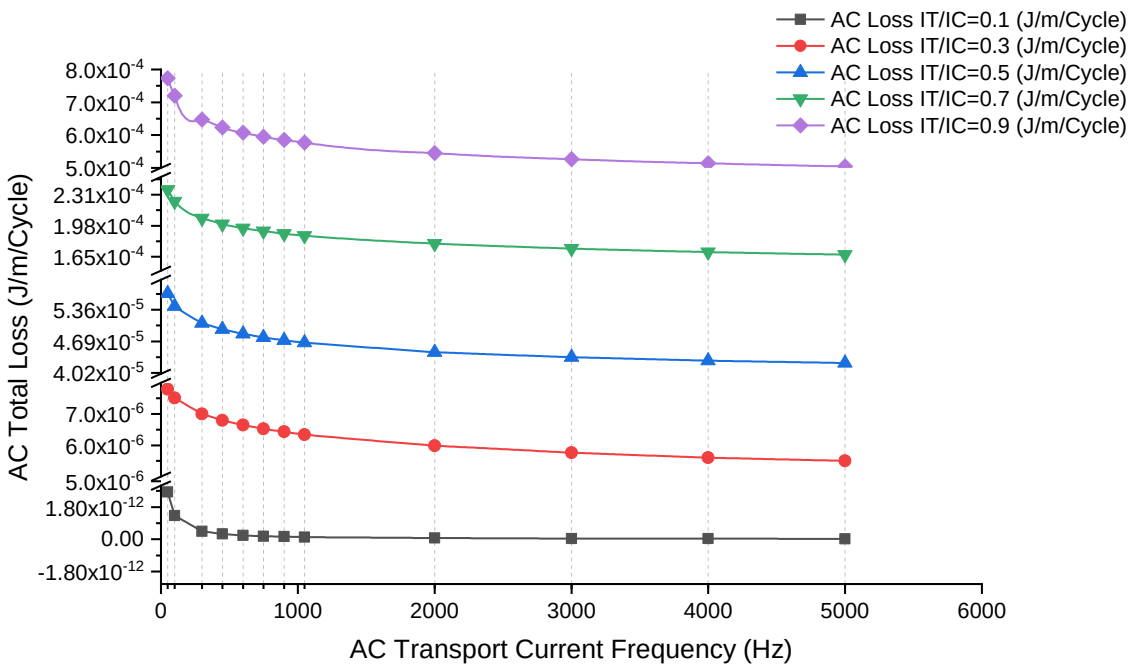

Figure 6.3.16 HTS wire AC losses when carrying transport currents with different frequencies*

*The simulation parameter used to produce the results in this graph is presented in table 4 of section 6.2. Breaks are applied to the *y*-axis for better result demonstration.

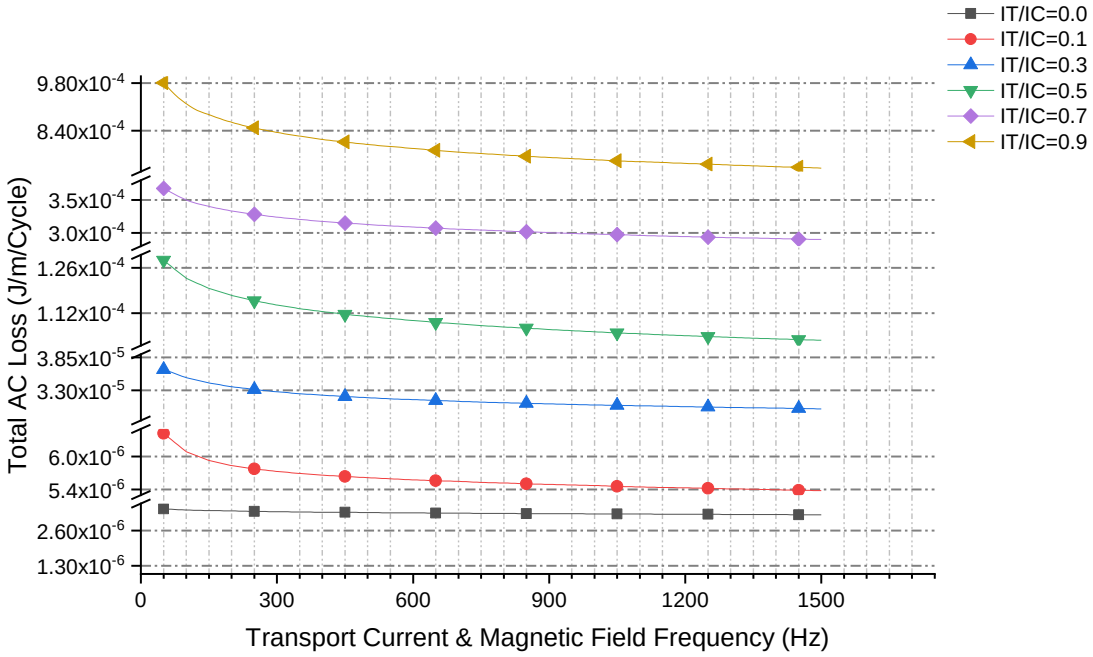

Figure 6.3.17 HTS wire AC losses when carrying transport currents with different frequencies under 2mT external AC field*

*The simulation parameter used to produce the results in this graph is presented in table 4 of section 6.2. Breaks are applied to the *y*-axis for better result demonstration.

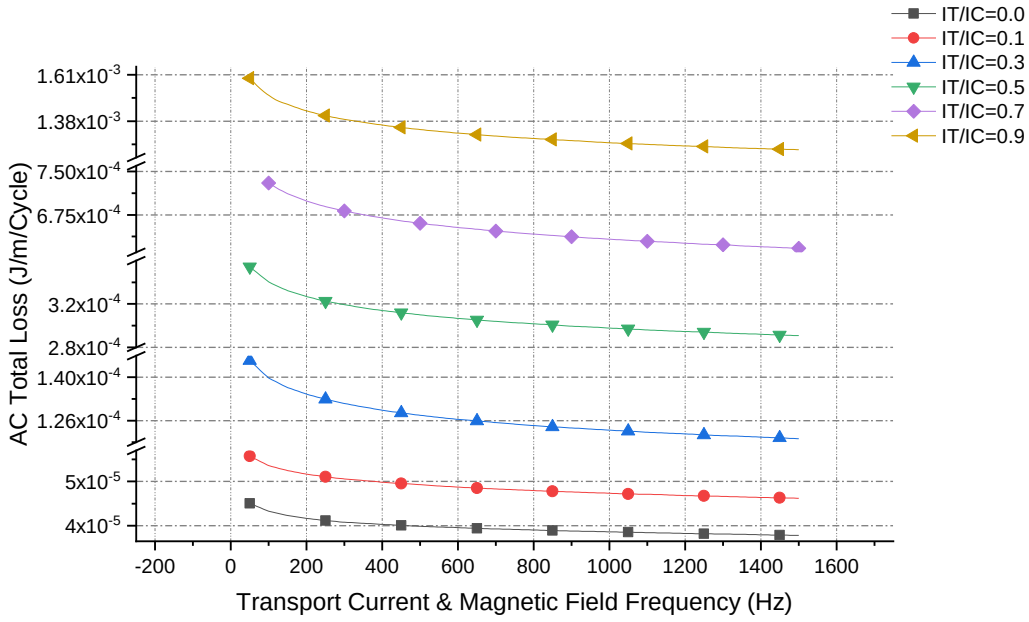

Figure 6.3.18 HTS wire AC losses when carrying transport currents with different frequencies under 4mT external AC field*

*The simulation parameter used to produce the results in this graph is presented in table 4 of section 6.2. Breaks are applied to the *y*-axis for better result demonstration.

However, when the magnitude of the external magnetic field is increased to a larger value such as 25mT or 35mT as present below in figure 6.3.19 and figure 6.3.20, the behavior of the AC losses per cycle for the simulated HTS wire changes dramatically. The AC losses per cycle instead of decreasing with the increment of the frequency, now rising with the increase of the frequency regardless of the transport current ratio settings. It is also revealed that for HTS wire carrying a certain AC transport current with a certain frequency, a larger external magnetic field always causes increased AC losses per cycle overall.

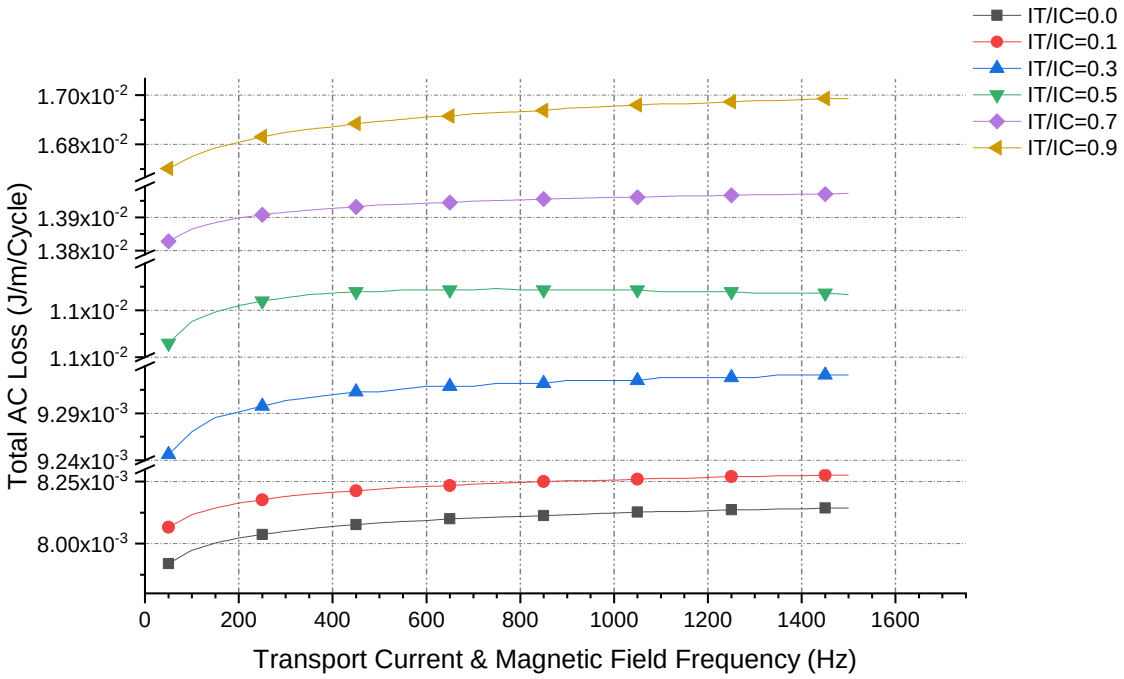

Figure 6.3.19 HTS wire AC losses when carrying transport currents with different frequencies under 25mT external AC field*

*The simulation parameter used to produce the results in this graph is presented in table 4 of section 6.2. Breaks are applied to the *y*-axis for better result demonstration.

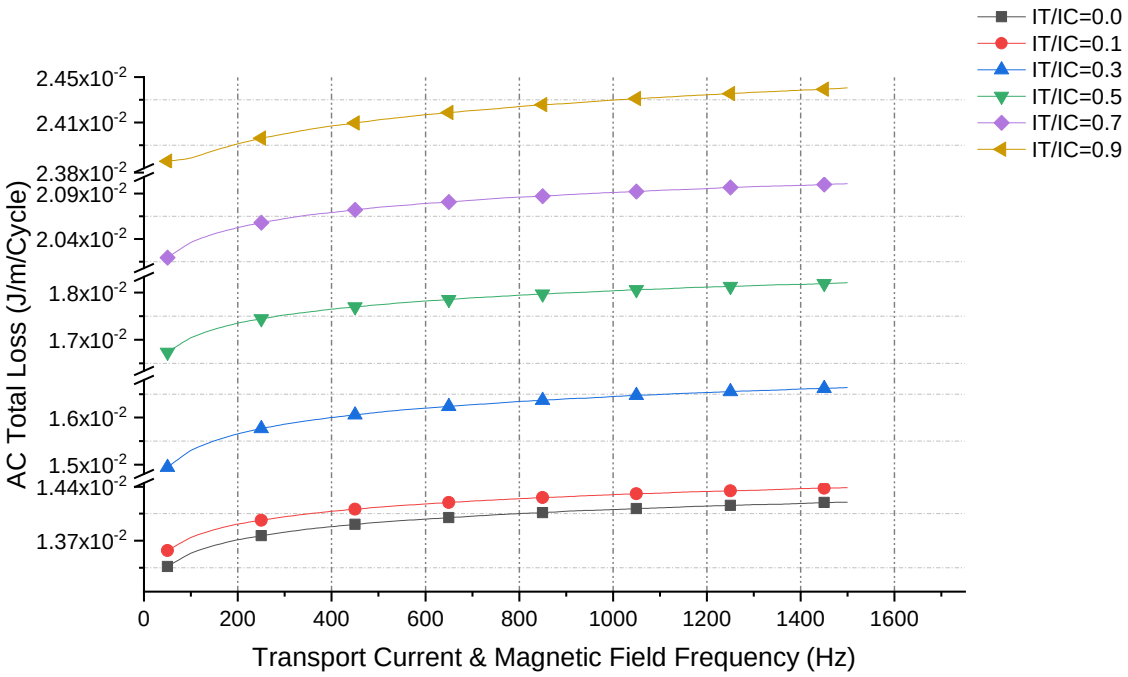

Figure 6.3.20 HTS wire AC losses when carrying transport currents with different frequencies under 35mT external AC field*

*The simulation parameter used to produce the results in this graph is presented in table 4 of section 6.2. Breaks are applied to the *y*-axis for better result demonstration.

Similar phenomenon was also observed in the study of [121]. The root cause of this significant change in the AC loss characteristic per cycle is that when the external magnetic field is relatively small, the penetration of the combined magnetic field (self-induced magnetic field and the external field) is limited to the small area around the edge part of the superconducting tape. In this situation, the flux pinning site is also concentrated around the edge part of the superconducting tape. During one AC cycle of the transport current, the flux can be subjected to changing Lorentz force and become de-pinned from its site. When the combined magnetic field is still weak, some of the de-pinned flux can be pushed out of the surface of the HTS wire and do not contribute to the loss dissipation during the cycle. Therefore, with the increase in frequency, the AC total loss of each cycle decreases. However, when a larger external magnetic field (around or above the full penetration field level) is applied, the HTS wire becomes fully penetrated by the magnetic flux. Since the flux is now spread across the entire width of the wire, based on the Faraday's law of induction, the increased frequency will increase the rate of change in flux and thus induce stronger

electromotive force across the surface of the wire. Higher induced EMF will fuel the AC loss across the entire wire and hence the total AC loss per cycle will rise along with the increasing frequency.

6.4. AC Loss in Single Layer HTS Cables

The AC loss characteristics of an HTS coated conductor wire have been studied in detail in the previous section. As it is introduced in chapter 2, the commercial HTS cables usually contain multiple HTS wires to increase their current carrying capacity. For HTS coated conductor wires assembled within the HTS cable, the AC losses generated by each wire will be different from the standalone cases because of the magnetic coupling between different wires. Therefore, accurate HTS cable models are needed to study the AC loss characteristics of the HTS wires integrated into the cable structure. In this section, the AC loss characteristics of HTS wires installed within single layer cables are simulated with the numerical model proposed in this thesis.

6.4.1. Zero External Magnetic Field Condition

Under most of the cases, due to the existence of the shielding layer, the HTS cables are working under an external magnetic field free environment. Therefore in this section, the AC losses of the single layer HTS cable are firstly calculated without considering the external magnetic field. Based on the model building method introduced in chapter 4, both the 2D cross-section model and the full 3D model are built for the single layer HTS cable. The 3D cable is built based on the stacking strategy introduced in chapter 4. A polygon section with short length along *z* dimension is initially built based on the governing equation. Several similar sub-sections are then stacked on top of one another with a constant phase angle difference to reflect the conductor twisting design commonly introduced in HTS cables in order to minimize gaps between adjacent conductors.

An HTS cable comprised of six conductors were simulated in this section. The HTS coated conductors in this single layer cable model are defined with the standard parameter table in section 6.2. The length of each sub-section on z dimension is defined as 1mm in order to ensure the electromagnetic environment covered by each sub-section stays relatively similar. The gap width between the conductors are defined as

the horizontal distances between edges of two adjacent conductors. Due to the large aspect ratio of the HTS layer within each conductor, the thin HTS layer is also assumed to be homogenous over its thickness dimension. The bending of the HTS conductors due to twisting is neglected in this model as discussed previously in chapter 4.

Similar to the previous section, in order to first make sure the 3D model is functioning as intended, a 3D single layer cable comprised of straight conductors are initially simulated. Since the 2D cable cross-section model can approximate the electromagnetic properties of the infinitely long HTS cable with straight conductors, the simulation results of the 2D cross-section model can be used as a reference for those calculated by the 3D model as they are equivalent in principle. Therefore, AC losses on each HTS conductor calculated by the 3D model are compared to those generated by the 2D cross-section model in figure 6.4.1 below. The AC losses in both the 2D and 3D model are calculated with transport current settings ranging from 10% of the critical current to 90% of the critical current. The simulated AC loss results on a single conductor within the cable are presented in figure 6.4.1.

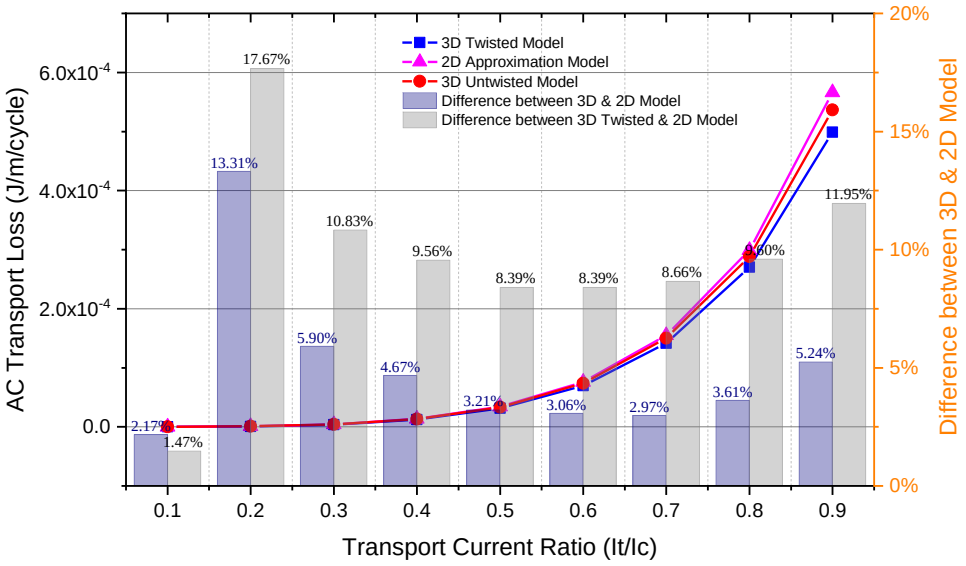

Figure 6.4.1 AC loss results and difference between 3D model & 2D model with various transport current ratios in a single layer HTS cable*

*The simulation parameter used to produce the results in this graph is presented in table 4 of section 6.2.

As it is presented above in figure 6.4.1, the difference between the AC losses calculated by the 2D and 3D model of HTS cable with straight conductors are generally very small. For cases where higher transport currents are carried by the HTS conductors (above 30% of the critical current level), the difference between the two models are below 6%. Greater differences occur when the transport current is relatively low, for example when the transport current is 20% of the critical current level. Similar to the case of 3D single conductor model, it is due to the fact that an iteration method is used to calculate the steady state final results as discussed in section 6.2. The convergence criteria of this iteration method is set as a static value. For case where a smaller transport current is carried, the value of the result is very small and close to the magnitude of the convergence criteria. Therefore, the static convergence criteria will lose part of its ability to constrain the accuracy of the result. However, the difference between the 2D and 3D model under the small current settings is very small in absolute value. Therefore, it can be confidently said that the 3D single layer HTS cable model is functioning as intended.

A set of AC loss results from the same cable but with conductor twisting design are also provided in figure 6.4.1. The conductor twisting design is a widely applied technique aiming to reduce the AC losses generated on HTS cables, the detail of this design will be introduced in the following section. When the HTS wires were twisted, the loss difference between the 3D cable model and the 2D approximate model becomes more significant. The transport losses calculated by the 3D twisted cable model under this pitch length is overall around 10% smaller than the results calculated by the 2D model. This is due to the conductor twisting effectively reduced the transport loss of the cable. It is worth noticing that shorter twisting pitches can further reduce the loss of HTS cables. However, being equivalent to the cross-section of an infinitely long straight cable, the 2D model cannot directly simulate the effect of the different conductor twisting designs. Thus, for cables where the HTS wires are heavily twisted, the building of an accurate 3D model is more beneficial and would justify a larger amount of simulation time for the sake of accuracy.

6.4.2. *Magnetic Field Distortion*

Since most of the contemporary power system is operating with AC power supplies, the design of HTS power cable must consider the measures to reduce the overall HTS AC losses. As it is discussed in section 2.2.1, the second-generation YBCO coated conductors within the HTS power cable are consisted of very thin superconducting layers. For a certain construct of HTS cable operating under a particular AC power system, the AC loss of the coated conductors depended on two major factors: the transport current they carry and the magnetic environment they work under. The magnitude and frequency of the AC transport current are solely depend on the configuration of the local AC power system. Therefore, the AC loss reduction techniques discussed in the following sections are mainly focused on optimizing the magnetic performance of the HTS power cables.

In order to better understand the principles behind the AC loss mitigation designs for HTS power cables, it is helpful to start by exploring the factors that could influence the AC losses magnetically within HTS power cables. The magnetic field induced by the transport current within the HTS cable can be divided to a circumferential component and an axial component. Since coated conductors within the HTS power cable only have extremely thin superconducting layer, the axial component will not induce much loss within the HTS wires due to minimal contact area. The majority part of the AC loss induced on the HTS coated conductors is due to the magnetic field component applied normally to the conductor wide surface. According to studies of [80] [84], this magnetic field component normal to the wide surfaces of HTS conductors is generated mainly from two sources: the distortion of circumferential field component caused by gaps between adjacent conductors assembled at the same layer and the circumferential magnetic field generated by HTS conductors in other layers. The effect of the magnetic field generated by HTS conductors from other layers will be discussed in the following section introducing the 3D double layer cable model. In this section, discussion will be focused on the gap distortion effect as it has the biggest impact on the AC loss generated by the HTS cables with only one layer of HTS conductors.

Gap Distortion Effect

Due to its geometry and mechanical constraints, current HTS coated conductors, when attached to the round cable former, will leave gap between adjacent conductors. An illustrative figure depicting the magnetic field distortion within the HTS cable caused by the gaps is presented in figure 6.4.2 below.

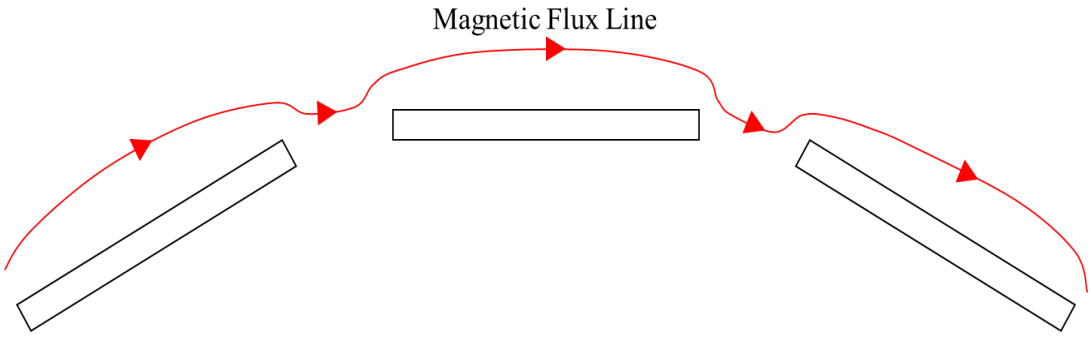

Figure 6.4.2 Magnetic Field Distortion Effect by Conductor Gaps

As it is presented in figure 6.4.2 above, when the transport current induced circumferential magnetic field component is distorted due to different magnetic permeability of the air when passing through such gaps. This field distortion will cause some flux line to inevitably touch the wide surface of adjacent wires and cause additional AC losses. The distorted field component perpendicular to the HTS conductors' wide surfaces will also suppress the critical current level of the wire and thus reduce their performance. In order to optimize the flux path to make the circumferential field circulate the cable cross-section plane as much as possible, the HTS coated conductors are usually wound around the former tightly in a spiral fashion. The twisting will reduce the gaps between different HTS wires and therefore reduce the circumferential field distortion. In the designs where coated conductors are not twisted, the tapes will be attached closely to each other where possible to minimize the gap effect. The gap effect is considered to mainly affect the AC losses of the HTS wires locate in the same layer of a HTS cable and is considered the most dominant additional AC loss-causing factor in the single layer HTS power cables [122].

6.4.3. *AC Loss Mitigation with Conductors Twisting*

As it is introduced in the previous section, the gaps between adjacent conductors in the HTS cable will distort the circumferential magnetic field to cause additional losses in the HTS wires. The strategy widely employed to mitigate this type of additional losses is to twist the HTS coated conductor wires spirally to minimize the gap left between adjacent wires as suggested by various previous works in this area [88] [126] [71] [127]. The AC loss reduction mechanism of the conductor twisting design is that by twisting the HTS conductors spirally, the transport current induced magnetic field component perpendicular to the wide surface of the HTS wires is reduced because of a more compact cable structure could minimize the gap width between adjacent conductors according to the research presented by [71]. By reducing the flux density exerted on the HTS wire's wide surface, the resistivity of the HTS wire induced by the changing AC field is also reduced based on the derived equation of 3.13 in section 3.2. Therefore, the AC transport loss can be effectively reduced by applying the conductor twisting design. Another benefit brought about by the conductor twisting design is the increase of the critical current for HTS wires installed in the cable with the same diameter. This can be explained by the $E - J$ power law introduced in section 2.3.2.

Since multiple previous research works acknowledge the conductor twisting design is helpful for reducing the AC losses of the HTS cables, it naturally brings about the question as to how to identify the optimal twisting pitch length design when designing HTS cables. In the research work of [126], an analytical equation is proposed to establish direct relationship between the current carrying capacity of the HTS wires within a multi-layered HTS cable and the twisting pitch length applied to them. The relationship between the maximum current carried by the HTS wires located in the j^{th} layer and the twisting pitch length is presented below:

$$\boldsymbol{I_j = \alpha_j I_1 = \frac{r_1 l_1}{r_j l_j} \sqrt{\frac{4\pi^2 r_j^2 + l_j^2}{4\pi^2 r_1^2 + l_1^2}}\, I_1} \tag{6.1}$$

Where I_j is the current carried by HTS wire located in the j^{th} layer, r_j is the radius of the j^{th} conductor layer and l_j is the twisting pitch length of the j^{th} layer. Moreover, for

a helix line, the relationship between radius r and the twisting pitch length l_{pitch} can be expressed by equation 6.2 below.

$$\boldsymbol{l_{pitch} = \frac{2\pi r}{tan(\beta)}} \tag{6.2}$$

Therefore combining equation 6.1 and 6.2, we can find that if allowed to expand freely, the radius of the HTS cable will increase with the increasing pitch length. Since the cable radius and the twisting pitch length of the HTS wires are located in the denominator position on the left side of the equation 6.1, a longer twisting pitch length will reduce the maximum current carried by the HTS wires in outer layers (assuming a fixed amount of current is carried by the HTS wires in the first layer). A reduced critical current level on HTS wires will mean the higher equivalent resistivity is induced within the HTS wires locate in the outer conductor layers and hence higher overall AC losses. This design property is also reported and verified by multiple other research works such as [71][84][88][128]. Thus, we can reach the conclusion that in order to minimize the AC losses of the HTS cable, shorter pitch lengths are generally more desirable.

However, the analytical equation of 6.1 can only consider the case when the number of HTS wires is increasing along with the increasing twisting pitch. In addition, the equation cannot predict the anisotropic distribution of the electromagnetic properties such as current density and flux density distributions. Therefore, in order to study the AC loss reduction effect of the conductor twisting design with more details, a simulation case study with our FEA numerical model is performed in this section.

A single layer cable consists of six 2G HTS wires is simulated in this section. The coated conductors simulated in this section are also defined by the parameters given in the standard wire parameter table presented in section 6.2. In order to control the number of variables involved in this case study, the AC transport current carried by each wire within the HTS cable is fixed at 50% of the critical current level.

The conductor twisting design of HTS cables is defined by two major features: the twisting direction and the degree of twisting. The influence of the conductor twisting direction will be discussed in the next section since the cable studied in this section

consists of only one layer of conductors. In this section, the effort will be focused on studying the influence of the degree of twisting. As the pitch length is commonly used to describe the degree of twisting, four different pitch lengths are simulated to study this effect.

The overall geometry of a HTS cable consists of twisted conductors can be defined by three key parameters: the diameter of the former, the width of the coated conductor and the twisting pitch length. After a certain type of coated conductor is selected to make the HTS cable, the width of the conductor becomes a fixed value. Since the diameter of the cable former has direct geometric correlation with the twisting pitch length, it is impossible to vary these two parameters freely at the same time. For example, if the coated conductors with a certain width are twisted too heavily around a fixed cylindrical former with small diameter, the coated conductors can end up overlapping each other and reduce the gap width to a negative value. Such action is although theoretically achievable but will exert strong mechanical stress on coated conductors and potentially degrade the electrical performance of the HTS wires heavily [123] [124] [125]. Therefore, in this case study, we keep the diameter of the cable former fixed meanwhile limiting the range of the twisting pitch length to keep the gap width between adjacent conductors positive.

In this model, the HTS conductors are defined as being spirally twisted around the former of the cable. This is achieved by defining the center lines of the HTS conductors using helix lines wounded around the surface of the cylindrical former as demonstrated in figure 6.4.3 below. As the conductor bending effect is neglected in this model, the cross-section of the conductor is defined as being a straight line tangent to the surface of the cylindrical former

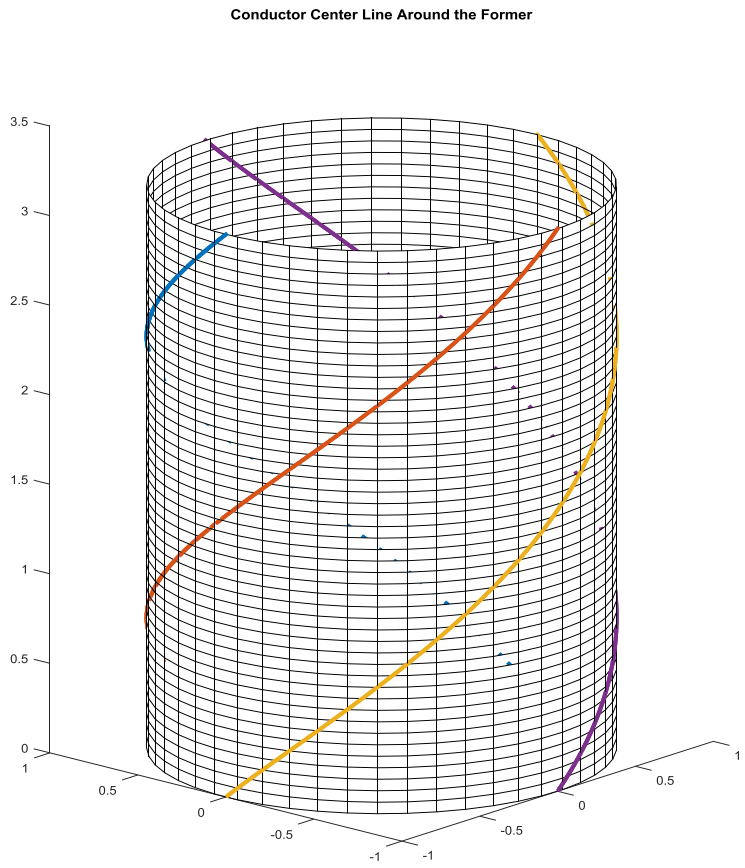

Figure 6.4.3 Twisted HTS Conductor Centre Lines on the Surface of Cable Former

The equations used to define the helical center lines of the twisted HTS conductors are presented below:

$$\boldsymbol{x(h) = r\cos(h)} \tag{6. 3}$$

$$\boldsymbol{y(h) = r\sin(h)} \tag{6. 4}$$

$$\boldsymbol{z(h) = kh} \tag{6. 5}$$

Where r is the radius of the cylindrical former, k is the constant used to define the pitch length of the conductor, a complete pitch length is equal to $2\pi k$. The slope of the helical conductor center line is defined as k/r. Since the width of the gaps have direct relationship with the radius of the cable former, in order to keep the former diameter fixed for different pitch length design, the gap width between adjacent coated conductors cannot be maintained as constants. As with harder twisting of the coated conductors, the cross-sections of the wires will become wider and thus infringe the actual width of the gaps. The AC loss simulation results for single layer HTS cables with different twisting pitch lengths are recorded in Table 5 below.

Table 5: AC Loss in Single Layer HTS Cables with Different Twisting Pitches

Pitch Length	Transport Loss (10^{-5} J/m/cycle)	External Magnetic Field (mT)	Initial Gap Width (mm)	Gap Width After Twisting (mm)
72mm	2.33	0	0.8	0.386
180mm	2.95	0	0.8	0.731
360mm	3.04	0	0.8	0.783
3D (Infinite)	3.07	0	0.8	0.8
2D (Infinite)	3.09	0	0.8	0.8
72mm	2.69	0	1.0	0.554
180mm	3.22	0	1.0	0.926
360mm	3.29	0	1.0	0.981
3D (Infinite)	3.30	0	1.0	1.0
2D (Infinite)	3.43	0	1.0	1.0

In Table 5, cases marked by 3D (Infinite) represents the 3D cable composed of straight conductors (with infinitely long pitch length). 2D (Infinite) represents the cases where 2D approximate model was used.

In table 5 above, the 2D approximate model and 3D cable with straight conductors can be considered to have infinite pitch lengths. A reduced amount of AC losses are generated by HTS cables with shorter pitch length settings. It can be observed from table 5 that the AC losses for 3D non-twisted models are very close to the loss results obtained with 2D cross-section models. When finite twisting pitch lengths are applied,

the AC losses generated by the HTS cables are found to be effectively reduced by introducing shorter twisting pitch lengths according to the 3D cable model. This is due to the conductor twisting increased the width of the HTS conductors' cross-section. Since the diameter of the cable former is fixed in this case, the gap width will also be infringed due to the conductor twisting design. The shrinking gap widths will reduce the magnetic field distortion effect at the edges of the HTS conductors and therefore reduce the losses induced by the distorted magnetic field around the gap area [126] [127]. The AC loss reduction effect is found more prominent if shorter pitch lengths are applied to the simulation cases. The magnetic field distribution around the edges of the conductor are plotted in figure 6.4.4 to figure 6.4.5 below.

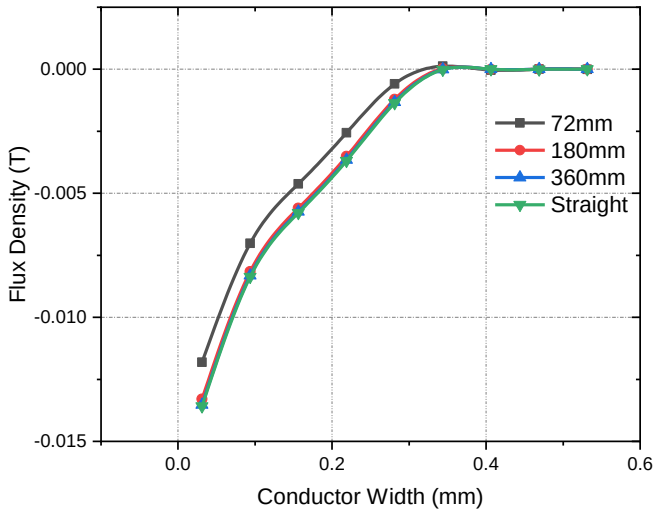

Figure 6.4.4 Magnetic Flux Distribution on Left Edge of a HTS Wire with 1.0mm Gap

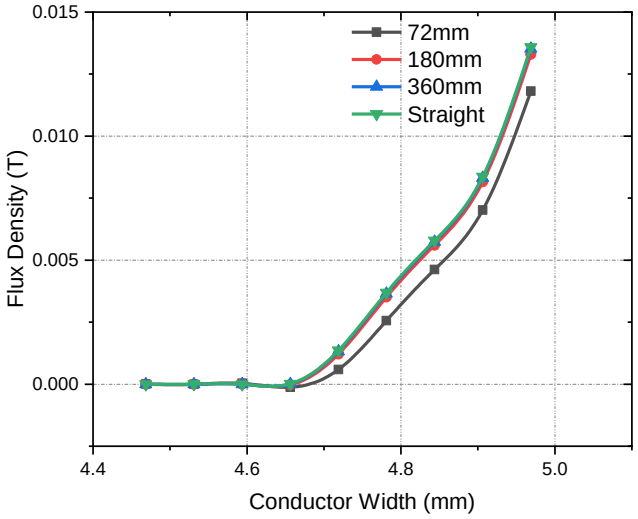

Figure 6.4.5 Magnetic Flux Distribution on Right Edge of a HTS Wire with 1.0mm Gap

As it can be seen from figure 6.4.4 and 6.4.5, the straight HTS conductors have the highest flux density distribution around their edge regions. The flux density around the edges of the HTS conductors become smaller in magnitude with shorter pitch length designs. Since the diameter of the cable former is fixed in this case study, this means that by introducing shorter twisting pitch lengths, the gap widths between HTS conductors are effective reduced. Therefore the magnetic field distortion effect caused by the gaps are also reduced. This is reflected by the reduction in magnetic flux density distributed around the edges of the HTS conductors as showed in figure 6.4.4 and figure 6.4.5 above. The same effect is also observed for HTS cables with a smaller initial gap design (smaller former diameter). The flux density distribution for HTS conductors assembled in cable with 0.8mm initial gap width are demonstrated in figure 6.4.6 to figure 6.4.7 below.

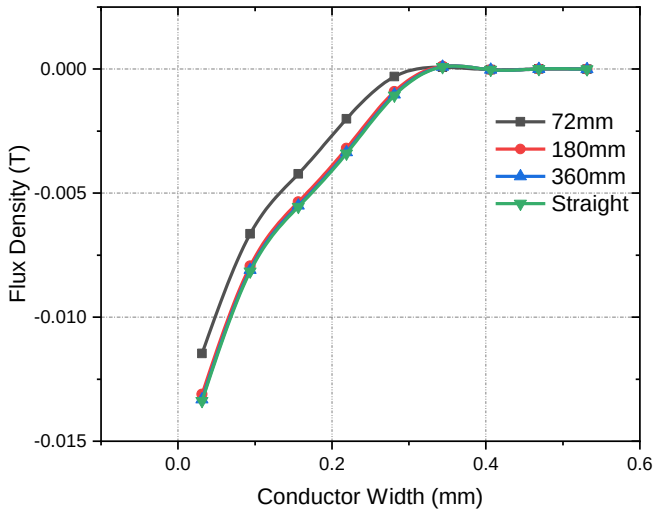

Figure 6.4.6 Magnetic Flux Distribution on Left Edge of a HTS Wire with 0.8mm Gap

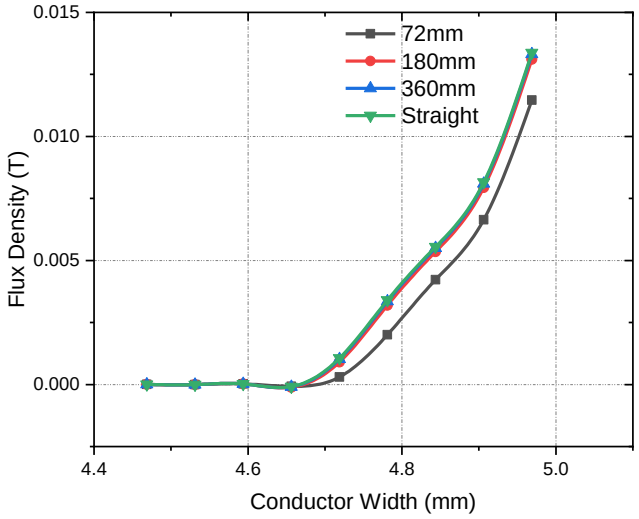

Figure 6.4.7 Magnetic Flux Distribution on Right Edge of a HTS Wire with 0.8mm Gap

As it mentioned above, the same conclusion can also be extended to HTS cables with a different gap width setting. For HTS cables with certain twisting pitch design, if the gap width of the cable is directly reduced by compressing the diameter of the former, the AC losses generated by the HTS cables can be further reduced. As it can be observed from table 5, for all three groups of twisting pitch designs, the overall AC losses calculated by the 3D cable models are further reduced with a narrower initial

gap setting. This phenomenon is also reported by the work in [128]. This AC loss reduction technique also applies to the HTS cables with straight conductor design. As it is demonstrated in table 5, the AC losses calculated by the 3D straight cable model and 2D cross-section model are both reduced for a narrower initial gap design. As without the conductor twisting design, reducing conductor gap widths through reducing the former diameter becomes the only option available for single layer straight HTS cables.

Another interesting finding from the case study presented in this section is that for cables with longer twisting pitches, the 2D cross-section model can generate results with relatively good accuracy to predict the total AC loss on HTS conductors within the cable. However, for more heavily twisted cables, the differences between the 2D and 3D simulation results rise rapidly following the decrease of the twisting pitches. More accurate 3D model is thus needed in order to reflect the true electromagnetic properties of heavily twisted HTS cables.

Transport Current Distribution in Single Layer HTS Power Cable

The 3D peak current distributions for the single layer HTS power cable studied in this section is plotted in figure 6.4.8 and 6.4.9 below as a demonstration of function. The transport current carried by the cable model is set as 30% of the critical current in figure 6.4.8 and 90% of the critical current in figure 6.4.9. It can be observed in figure 6.4.8 and 6.4.9 that the current density around two edges of the wire is significantly higher than the current density in the center region. This indicates that the current mainly flows at the two side regions in an HTS wire. Since in a single layer HTS power cable, the HTS wires were arranged in a symmetrical way, the current distribution across the cross-section area of each HTS wires will be identical at the same section of the cable.

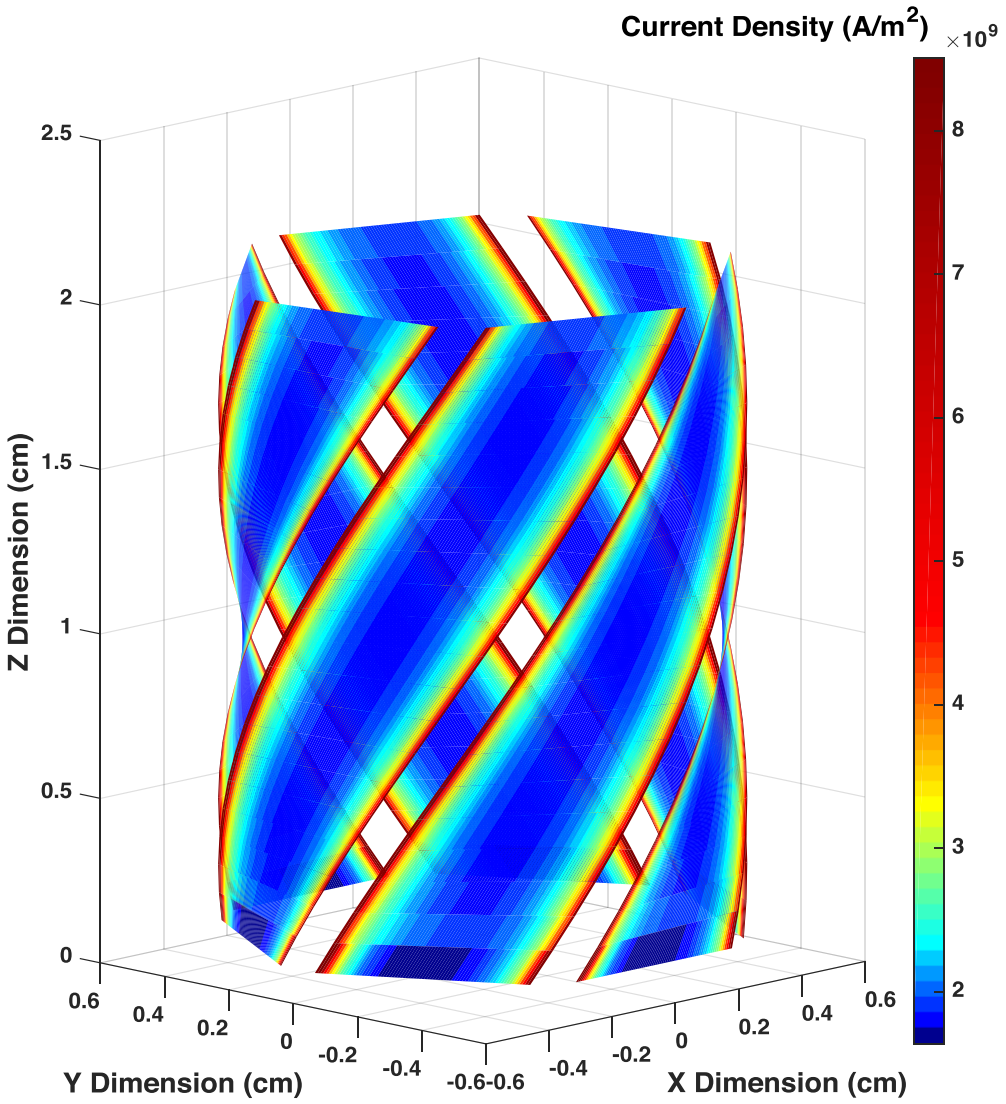

Figure 6.4.8 Current density distribution in a single layer HTS cable carrying AC current with peak amplitude of 30% of I_c

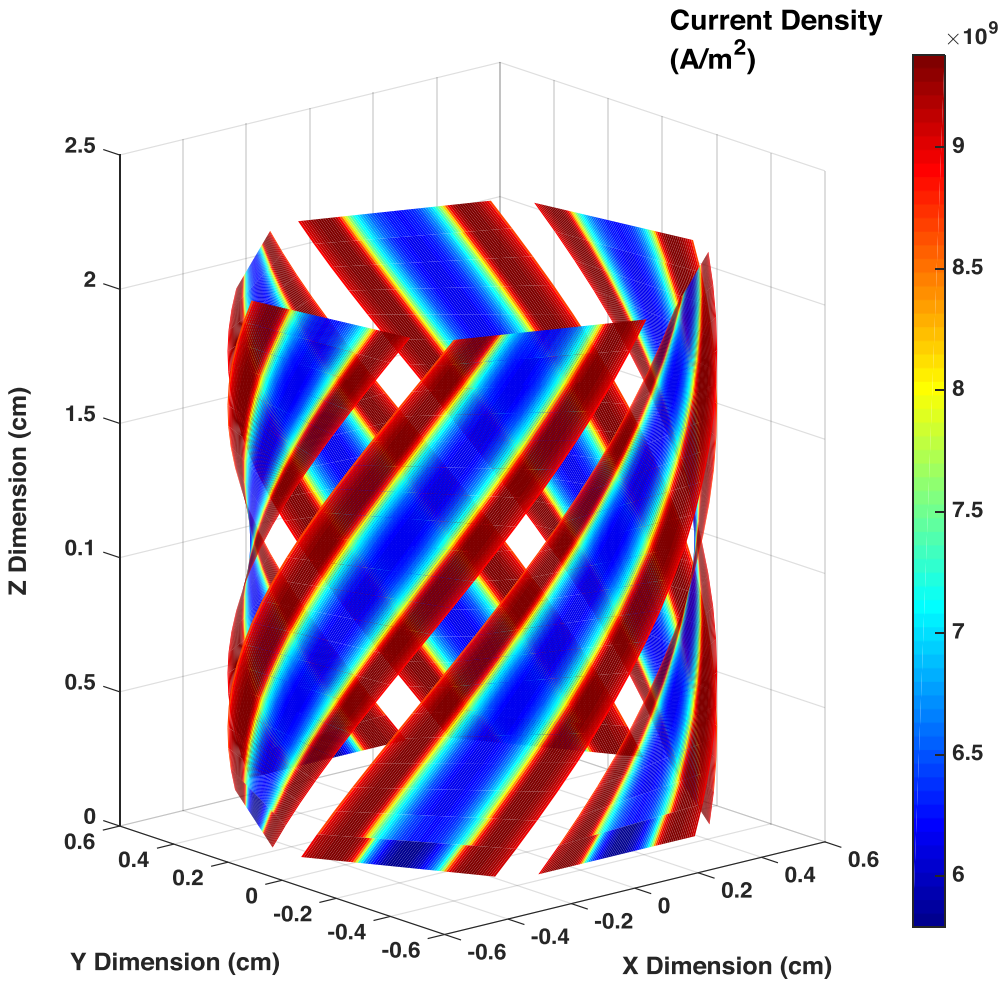

Figure 6.4.9 Current density distribution in a single layer HTS cable carrying AC current with peak amplitude of 90% of I_c

6.4.4. *AC Loss with AC External Magnetic Field*

The AC loss characteristics of single layer HTS cables under external magnetic field free environment is studied by simulation cases in the previous section. As it is common in many practical HTS cable designs, shielding layers are usually added outside of the HTS conductors to screen out the effect of the external magnetic fields. However, since the HTS power cables can sometimes work in close proximity with other high magnetic field power applications such as high rating power machines, it is likely in certain situations that the external magnetic field could breach the shielding layer and affect the HTS materials inside the cable. Therefore, case studies are performed in this section to explore the AC loss characteristics of single layer HTS cables under the influence of an AC external magnetic field. The cable designs used for simulation is the same as in the previous section. The simulated total AC losses are recorded in table 6 below.

Table 6: AC Loss in Single Layer HTS Cables with Different Twisting Pitches under 10mT AC External Magnetic Field

Pitch Length	Transport Loss (10^{-5} J/m/cycle)	External Magnetic Field (mT)	Initial Gap Width (mm)	Gap Width After Twisting (mm)
72mm	442.1	10	0.8	0.386
180mm	366.8	10	0.8	0.731
360mm	356.5	10	0.8	0.783
3D (Infinite)	353.1	10	0.8	0.8
2D (Infinite)	335.6	10	0.8	0.8
72mm	438.7	10	1.0	0.554
180mm	359.6	10	1.0	0.926
360mm	348.7	10	1.0	0.981
3D (Infinite)	345.1	10	1.0	1.0
2D (Infinite)	326.6	10	1.0	1.0

In Table 6, cases marked by 3D (Infinite) represents the 3D cable composed of straight conductors (with infinitely long pitch length). 2D (Infinite) represents the cases where 2D approximate model was used.

When a 10mT AC magnetic field is applied to the model, the loss pattern for HTS cables with twisted conductors changed significantly. Overall, the total loss generated by HTS conductors within the single layer cable increased by more than two orders of magnitude for all pitch length designs. Similar to the section of 6.3.2, this is due to the fact that the externally applied AC field induced a larger electric field and a shielding current inside the HTS conductor. When compared to the external field free cases, the larger electric field and the shielding current will cause additional loss dissipation on the conductor. The additional magnetic field will also suppress the critical current level across the HTS conductors and in turn, increase the resistivity according to equation 3.13 and 3.14 in chapter 3. Therefore, the total losses generated by the HTS conductors are eventually increased drastically. Another major difference is, in this circumstance, simulation cases with shorter pitch lengths now have significantly larger AC transport losses comparing to the cases with longer pitch lengths. This loss pattern is completely different from the cases where the external magnetic field is absent. This is potentially due to the reason that the externally applied magnetic field together with the induced shielding current, disrupted the symmetry of the original current and magnetic field distributions across the HTS conductor. In this situation, the final magnetic field and current distribution on both sides of the HTS conductor will no longer be balanced. Instead, one side of the HTS conductor (either left or right, depend on the phase angle of the external field) will see significantly larger current / magnetic field concentration at any point of the AC cycle as demonstrated in figure 6.4.10 and 6.4.11. As it is mentioned in the previous section, a more compact cable design offered by either applying shorter twisting pitches or reducing former diameter will reduce field distortion caused by the gaps and allow a more even current distribution across HTS conductors. In this case, as the symmetry of magnetic field distribution on HTS wires are disrupted by the external AC field, the circumferential magnetic field components generated by each wire no longer circulates the cable cross-section as showed in figure 6.4.2. A more compact cable design will now allow the magnetic flux generated by adjacent HTS wires to penetrate deeper into the center of an HTS wire and creates a larger high loss area within the conductor as presented in figure 6.4.12 below.

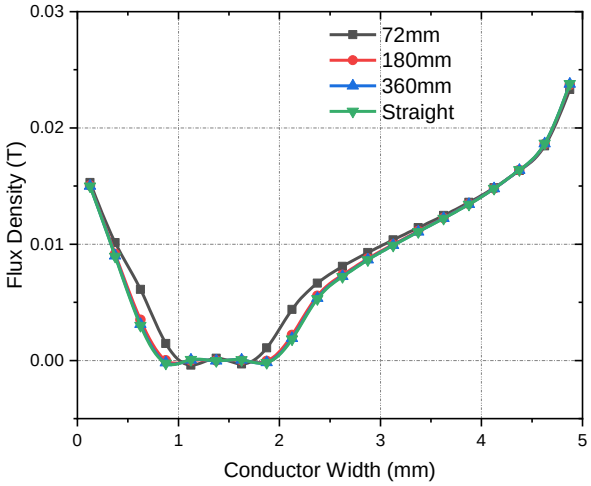

Figure 6.4.10 Magnetic Flux Distribution of a HTS Wire with 0.8mm Gap under 10mT AC Field

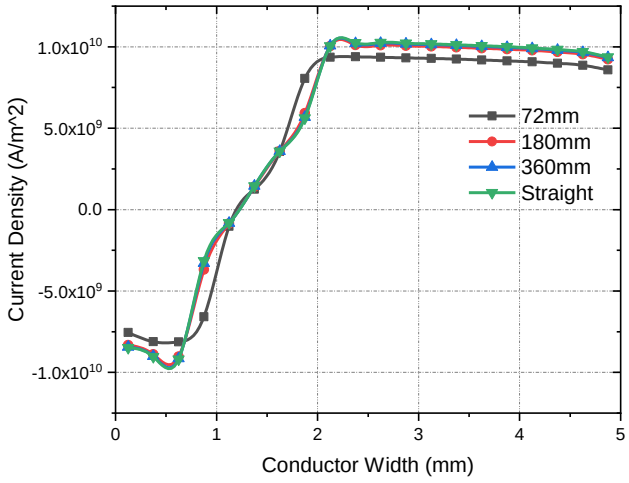

Figure 6.4.11 Current Density Distribution of a HTS Wire with 0.8mm Gap under 10mT AC Field

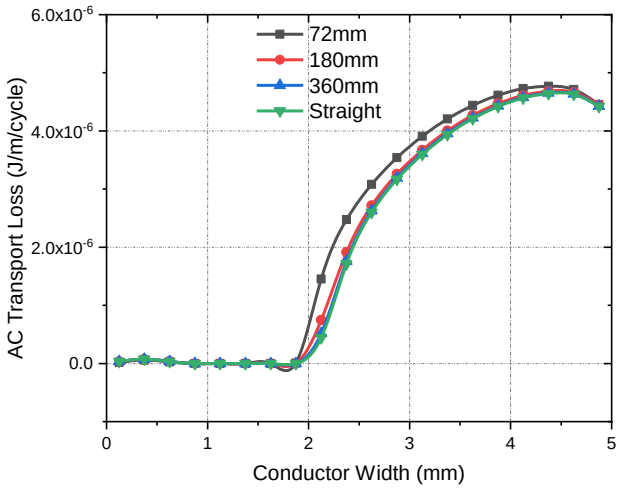

Figure 6.4.12 AC Loss Distribution of a HTS Wire with 0.8mm Gap under 10mT AC Field

Based on the discussions made above, it can be noticed that a more compact cable design, though more desirable under normal circumstances, is also more vulnerable to the effect of external AC magnetic field and will generate higher losses under the presence of the external AC field. Therefore, for single layer HTS cables with short twisting pitch designs, the magnetic shielding protection is very important. In addition, it can be observed that simulation cases with longer pitch length settings (such as 180 mm and 360 mm) still have relatively closer total loss results when comparing to the 3D infinite model and 2D approximation model. However for a shorter pitch length setting of 72 mm, the loss results show great difference from both 2D approximation model and the 3D infinite model. Thus, when simulating heavily twisted HTS cables working under the influence of an external AC magnetic field, the building of a realistic 3D model becomes very necessary. Using a 2D approximation to calculate AC losses under this circumstance is not viable.

6.5. AC Loss in Double Layer Cables

As it is introduced in chapter 2, the commercial YBCO HTS cables are normally consisted of more than one layer of HTS wires. In order to study the AC loss characteristics of the multi-layer coaxial cables, the model for multi-layer coaxial HTS cables is built. It is believed that the two layers of conductors can already represents

the characteristics of the multi-layer coaxial cables as a higher number of conductor layers will not introduce any new structural variable. Therefore the simulation case studies performed in this section will take double layer coaxial HTS cables as the study subjects. Similar to the previous section, the model for double layer coaxial cable with straight conductors is built first. The simulation results of the 3D straight double layer coaxial cable are cross-checked against those results obtained from the 2D model to validate the results. The simulated AC losses for a single HTS wire from both the inner layer and the outer layer obtained from the 2D and 3D models are presented below in figure 6.5.1. The total AC losses on the wires are calculated under different transport current ratios.

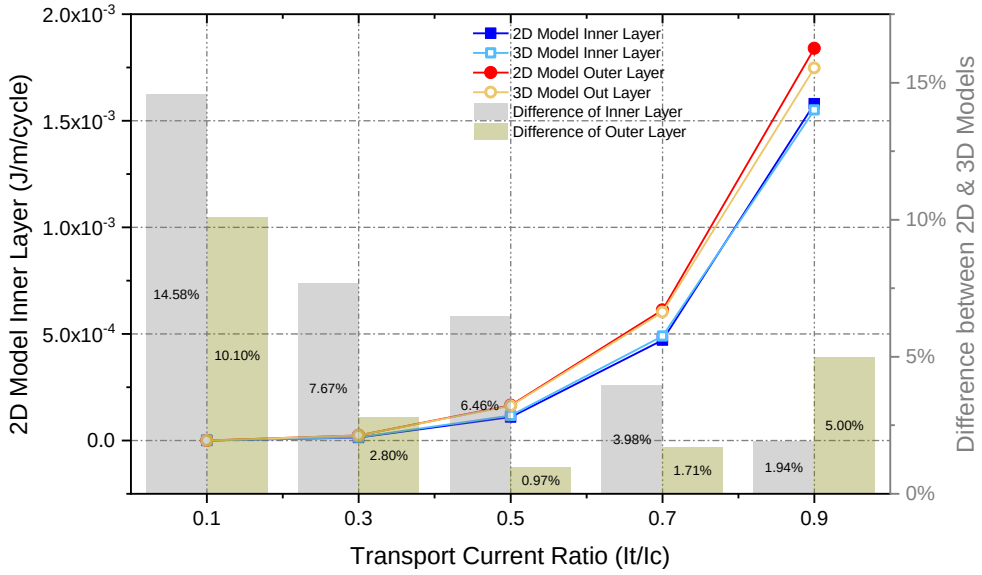

Figure 6.5.1 AC Losses Calculated by the 3D and 2D Double Layer Cable Model with Straight HTS Conductors

As it can be observed from figure 6.5.1, the AC losses calculated by the 2D model and 3D model are very close. The differences in percentage are below 8% for higher transport current settings (above 30% of the critical current). The difference for low transport current setting (10% of the critical current) is higher. Again this is due to the AC losses calculated are very small in value and approach the magnitude of the convergence criteria. The difference in percentage for this case will be relatively higher.

6.5.1. *AC Loss Mitigation Design*

Although the additional HTS conductor layer will significantly increase the power carrying capacity for double layer HTS power cables, the presence of the additional conductor layer will also induce additional AC losses on HTS conductors comparing to the single layer cable designs. The design features that cause additional AC losses in double layer HTS cables and their corresponding loss mitigation techniques will be studied in this section.

Gap Distortion Effect

Similar to the single layer cable introduced in the previous section, for double layer HTS cables, the magnetic field distortion effect caused by the gaps between conductors are still very much a problem. As it is introduced in section 6.4.2, the field distortion effect is considered only affect the HTS conductors assembled within the same layer. Although it is worth noticing that due to the different geometry of the two layers (inner layer and outer layer), the additional AC losses contributed by the gap distortion effect are likely to be very different in two layers.

Inter-Layer Magnetic Field Coupling Effect

Since the modern HTS cable designs normally contain multiple different layers of coated conductors to maximize the current carrying capacity, in addition to the gap distortion effect occurs at the local layer, the coated conductors installed at the outer layer of the double layer HTS cables will be subjected to the effect of the magnetic field induced by the transport current carried by the internal layer. An illustrative figure depicting the circumferential magnetic field component of a HTS cable conductor layer is presented in figure 6.5.2 below.

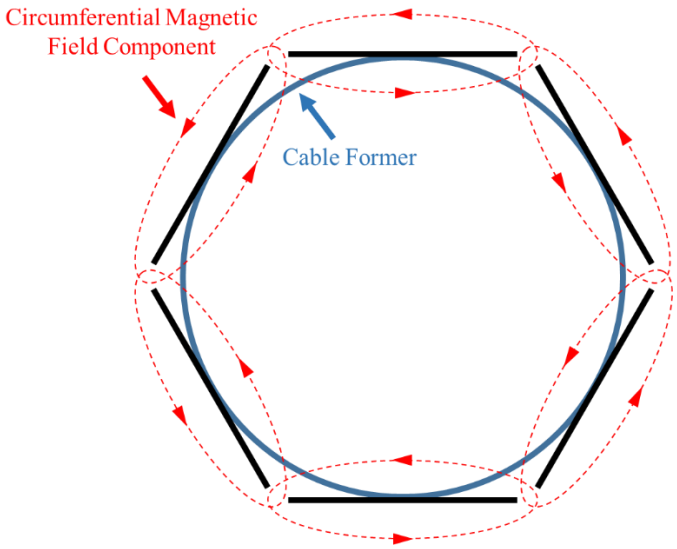

Figure 6.5.2 Circumferential Magnetic Field Component Induced by Transport Currents

It can be observed from figure 6.5.2 above that the magnetic field induced by transport current on different coated conductors travels around the conductor layer and getting distorted around the gaps. The magnetic field induced outside the former circle will inevitably affect the coated conductors located in the outer layer if there are any [82]. The reason that the inner layer induced magnetic field could affect the coated conductors of the outer layer is that the HTS cable cross-section is arranged in a polygonal geometry. Since the circumferential magnetic field generated by the internal layer transport current is flowing in a circular path around the cable cross-section as roughly depicted in figure 6.5.2, part of the internal layer circumferential field will inevitably come into contact with the wide surfaces of the coated conductors assembled in the outer layers. This part of the circumferential field will induce additional losses on the outer layer coated conductors. This is the reason why outer layer coated conductors will produce higher AC losses when comparing to same type of conductors located in the inner layer of HTS cable. Although in practice, if the coated conductors are heavily twisted and pressed against the former surface, the HTS wire will bend and make the cable cross-section somewhat more circular. The wide surface of a bent coated conductor will reduce the amount of circumferential field it come into contact with and therefore reduce the additional AC losses. However, the bending of the wire is limited by its mechanical properties and it is impossible to form a perfect circle with the coated conductor wires. The bending of each wire will be

further limited if a large number of wires are assembled in a conductor layer of the HTS cable. Therefore, despite the conductor bending effect, the additional AC loss generated by the inner layer circumferential field cannot be eliminated. The overall cross-sectional geometry of the HTS cable will remain largely polygonal in practice. Thus, from the perspective of simulating the worst-case scenario to prevent over heating from happening, the model proposed in this thesis neglected the bending effect of the HTS coated conductor and assume a polygonal geometry for the cross-sections of HTS cables.

Based on the discussions made above, it can be summarized that coated conductors located in the inner layer of the double layer HTS cable will be affected only by the local gap designs. Whilst coated conductors located in the outer layer will be affected by both the gap width of outer layer and the magnetic field induced by coated conductors assembled in inner layer [82].

Given the knowledge about the additional AC loss generation mechanism within the HTS double layer cables, different loss mitigation strategies have been proposed by many researchers to address the issues accordingly [129] [130] [131]. Since the causes of the additional AC losses can be mainly attribute to the gaps between adjacent conductors and the polygonal geometry of the cable cross-section, the current loss mitigation designs put much emphasis on minimizing the gap widths as well as reducing polygon effect of the cable cross-section. These design features are also integrated in the 3D model proposed in this thesis to aid the design of the modern HTS multi-layer cables. Case studies have been carried out in the following sections in order to obtain a more detailed understanding of the effect of these loss mitigation strategies.

6.5.2. *AC Loss Mitigation with Conductors Twisting*

The AC loss mitigation effect of the conductor twisting designs in double layer HTS cables are studied in this section. A double layer cable consists of four wires in the inner layer and six wires in the outer layer is simulated. In order to eliminate the potential influence of different gap widths on AC losses at both layers, the gap widths between adjacent conductors are set as 0.5mm for both internal and external layer when the conductors are untwisted. Since the gap widths are set as the same for both

layers, two more coated conductors are installed in the external layer to increase its diameter so that it can contain the internal layer. The coated conductors simulated in this section are also defined by the parameter given in the standard parameter table presented in section 6.2. In order to control the number of variables involved in this case study, the AC transport current carried by each wire within the HTS cable is fixed at 50% of the critical current level.

Different to the conductor twisting designs of the single layer HTS cables, the conductor twisting designs of the double layer HTS cable are now defined by two major features: the twisting direction and the degree of twisting. Since the cable studied in this section consists of two layers of conductors, the twisting direction for two layers can either be in the same direction or in the opposite direction. Four different pitch lengths are simulated for each twisting direction setting to study its effect.

Again, the overall geometry of a HTS cable with twisted conductors can be defined by the diameter of the former, the width of the coated conductors and the twisting pitch length. Similar to the case studies performed in section 6.4.3, in the first section of this case study, we keep the diameter of the cable former fixed for each layer and meanwhile provide a limited range of the twisting pitch lengths to test the AC loss mitigation effect of the conductor twisting designs.

The AC loss simulation results for cable with inversed twisting direction is recorded in table 7 below whereas the loss results for cable with the same twisting direction is recorded in table 8.

Table 7: AC Loss of Double Layer HTS Cable with Different Twisting Pitch Designs (Different Twisting Direction)

Pitch Length (+/-)	Transport Loss (Inner Layer) (10^{-5} J/m/cycle)	Transport Loss (Outer Layer) (10^{-5} J/m/cycle)	Diameter Inner/Outer (mm)	Gap Width Inner/Outer (mm)	Conductor Width Inner/Outer (mm)
100mm	4.866	9.449	5.71/9.66	0.444/0.305	5/5
120mm	4.918	10.16	5.71/9.66	0.461/0.364	5/5
240mm	5.040	10.44	5.71/9.66	0.490/0.466	5/5
300mm	5.542	11.37	5.71/9.66	0.494/0.478	5/5

Table 8: AC Loss of Double Layer HTS Cable with Different Twisting Pitch Designs (Same Twisting Direction)

Pitch Length (+/+)	Transport Loss (Inner Layer) (10^{-5} J/m/cycle)	Transport Loss (Outer Layer) (10^{-5} J/m/cycle)	Diameter Inner/Outer (mm)	Gap Width Inner/Outer (mm)	Conductor Inner/Outer (mm)
100mm	4.762	9.118	5.71/9.66	0.444/0.305	5/5
120mm	4.790	9.781	5.71/9.66	0.461/0.364	5/5
240mm	5.006	9.923	5.71/9.66	0.490/0.466	5/5
300mm	5.497	11.09	5.71/9.66	0.494/0.478	5/5

It can be observed in table 7 and table 8 after fixing the former diameter, the gap width for each layer decreases with the reducing twisting pitch length. As a result of the gap width shrinking, the magnetic field distortion caused by the gap also become

less significant. The mitigation of the field distortion effect reduces the normal circumferential field components come into contact with the HTS wires located within the same layer. Therefore, for coated conductors located in both the internal and external layer, the transport losses are reduced if smaller pitch lengths are applied.

It can also be observed from table 7 and table 8, for the coated conductors installed within the same cable design, the conductors located in the outer layer generate much higher total AC loss (almost doubled the amount) when comparing to the HTS wire located in the inner layer. The higher total loss generated in the outer layer is due to the inter-layer magnetic field coupling effect discussed in the previous section. The AC loss reduction provided by the twisting design is more significant in outer layer comparing with inner layer. This is due to the fact that more HTS coated conductors are arranged in the outer layer. Since in external layer, more conductors are twisted with the same pitch length as the internal layer, the actual gap widths are reduced more severely. Therefore the gap distortion effect on outer layer is mitigated more significantly comparing to the inner layer.

Another factor that can impact the overall AC loss generation on HTS cables is the twisting direction of the HTS coated conductors. From table 7 and table 8, it can be observed that if the same twisting direction is adopted for both layers, the AC losses generated on both layers are reduced when comparing to the case where two layers are twisted in different directions. This phenomenon is also reported by the previous research work in [130] [131]. Although different approaches are used to explain this phenomenon, they can all be attributed to the inter-layer magnetic field coupling effect. As it is discussed previously, the magnetic field generated by the inner layer transport current will induce additional losses in the external layer. The twisting direction of the two layers will affect the spatial distribution of the internal layer induced magnetic field on coated conductors at external layer. As a result, the generation of the AC loss hot spots on external layer will be affected. Generally speaking, an identical twisting direction will mitigate some of the additional AC loss generated in outer layer conductors by reducing the strength and the amount of loss hot spots induced in external layer. Therefore, it is more desirable to design the multi-layer co-axial HTS

cable with the same twisting directions for different layers. The details about the AC loss hot spot generation will be discussed in the next section.

6.5.3. *AC Loss Mitigation with Gap Design & Hot Spot Study*

In the previous section, cables with fixed former diameter and various twisting pitch lengths are simulated to explore the AC loss mitigation effect of the conductor twisting designs. However, if conductors from the internal layer and external layer are twisted in different directions, hot spots may be induced on certain sections of the cable to increase the total AC losses. These hot spots are induced by the circumferential magnetic field components generated at the internal layer. The heat generated at these AC loss hot spots can build up if left un-noticed. Therefore, the simulation study of the hot spots generated by conductor twisting is crucial for the design of the HTS cable cooling system. A more detailed case study is performed in this section to research the factors that can influence the generation of hot spots on HTS double layer cables.

Again in order to limit the number of variables involved in the case study, the twisting pitch length in this case is fixed as 144mm, the transport current is set as 50% of the critical current level. The coated conductors simulated in this case study are defined with the parameters recorded in the standard parameter table. In order to simplify the geometry and eliminate the variable of different number of conductors on two layers, four coated conductors are assembled in both layers. As the same number of conductors are used for both layers, the gaps between conductors in the external layer must be larger than those of the internal layer. Therefore, in this study, the gap widths of external layer are fixed as 2 mm. According to Biot-Savart Law, for a certain HTS cable carrying a fixed amount of transport current, the magnitude of internal field induced AC loss on the outer layer is determined by the distance between the two layers. In order to examine how changes in distance between the two layers will affect the AC loss on outer layer coated conductors, the diameter of the internal layer is changed by varying the inner layer gap widths (increased from 0.5mm to 0.7mm). The three HTS cables with different inner layer gap settings are marked as cable A, B and C respectively and their physical dimension parameters are summarized in table 9 below.

Table 9: Dimension Parameters of Cable A, B and C

	Gap Width (Inner / Outer Layer)	Cable Former Diameter (Inner / Outer Layer)
Cable A	0.5mm / 2.0mm	5.71mm / 7.83mm
Cable B	0.6mm / 2.0mm	5.85mm / 7.83mm
Cable C	0.7mm / 2.0mm	5.99mm / 7.83mm

Since the spiral twisting structure is largely repetitive for a long section of HTS cable, the electromagnetic properties of the coated conductors will change periodically along cable axis. For the purpose of simplicity, we call this periodic change of the electromagnetic properties the 'electromagnetic cycle'. This period of change depends on the relative position of the internal layer conductors and the external layer conductors as the relative position of the conductors located in the same layer remain static throughout the twist. The double layer co-axial cable simulated in this section is designed with four tapes by four tapes structure as demonstrated in figure 6.5.3 and figure 6.5.4 below. Assuming the external layer is rotated along the cable axis while the internal layer remains static, the minimum twisting angle needed for conductors of both layers to reach the same relative position again is 90 degree. In this case, the conductors of both layers are designed to be twisted toward opposite directions. Therefore, the minimum twisting angle needed for a full electromagnetic cycle along the cable axis is actually 45 degree (12.5% of a full twisting cycle) for each layer. The corresponding twisting length for a full electromagnetic cycle is thus 18mm. Given the discussion made above, we only need to examine an 18mm section of the cable for the study of its electromagnetic property distributions.

In order to study the relationship between the relative conductor positions and AC loss hot spots distributions in detail, we borrow the definition made in the research work of [84] and refer to the conductor layout presented in figure 6.5.3 below as the 'tape on tape' section and the layout in figure 6.5.4 as the 'tape on gap design'. The 18mm long analysed region is defined as starting from a tape on tape section,

progressing to contain a tape on gap section in the middle and ending with another tape on tape section.

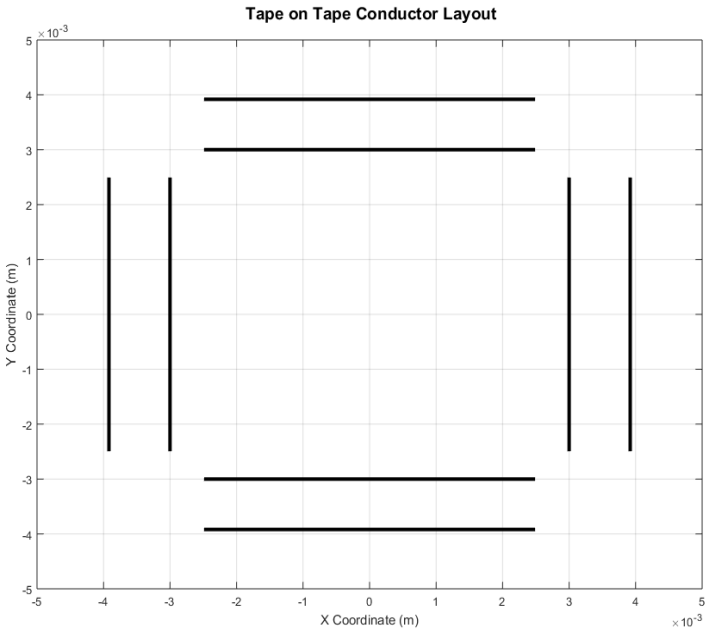

Figure 6.5.3 'Tape on Tape' Conductor Arrangement in Double Layer HTS Cable

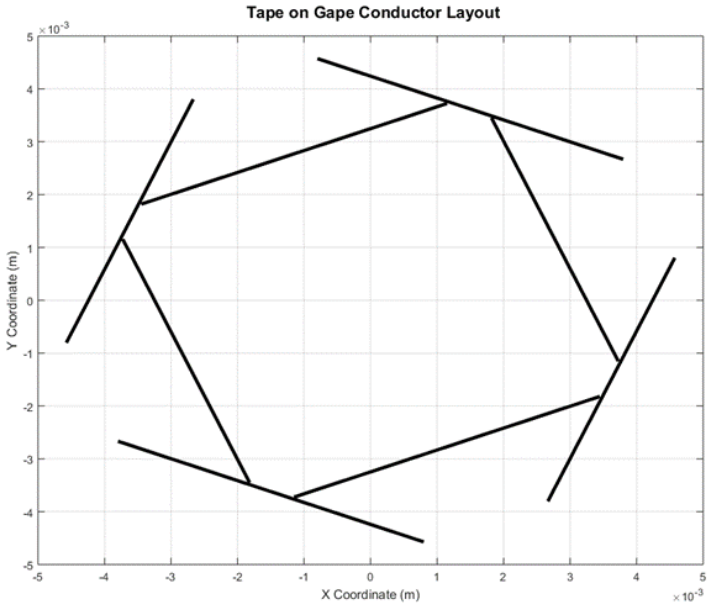

Figure 6.5.4 'Tape on Gap' Conductor Arrangement in Double Layer HTS Cable

AC Transport Loss Distribution along the Cable Axis

As discussed in the previous section, a section of 18mm long double layer coaxial cable is simulated. The overall AC loss distribution results along the cable axis for three different inner layer diameter settings are simulated by the 3D cable model and presented in figure 6.5.5 to 6.5.7 below. The AC loss results listed in figure 6.5.5 to 6.5.7 are the loss result of one single wire within the corresponding layer. In this case, the number of conductors for the two layers are the same. Coated conductors assembled in the same layer are experiencing a symmetric magnetic environment and thus generate the same amount of AC losses. AC loss results simulated by the 2D approximation model are also plotted in figures below to provide verification and references.

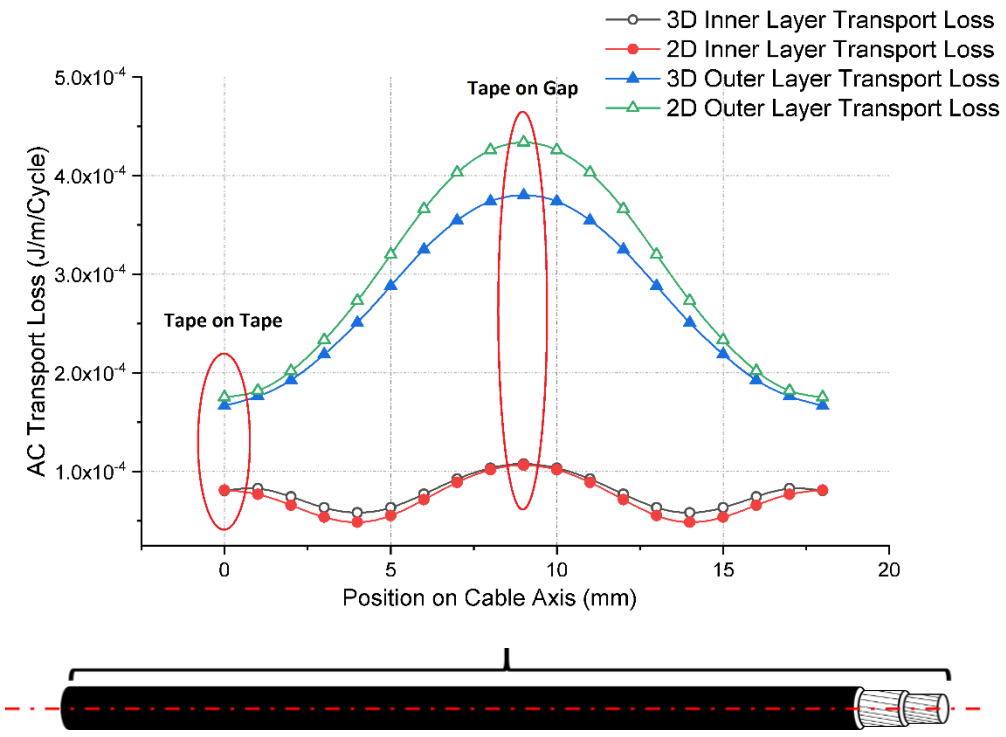

Figure 6.5.5 AC Loss Distribution on HTS wires along the Cable axis for Cable Design A

The *x*-axis title 'Position on Cable Axis' refers to the location of point along the length of the cable where HTS wires from different conductor layers can have different AC loss magnitude due to their relative position to each other as demonstrated by figure 6.5.3 and figure 6.5.4 as examples.

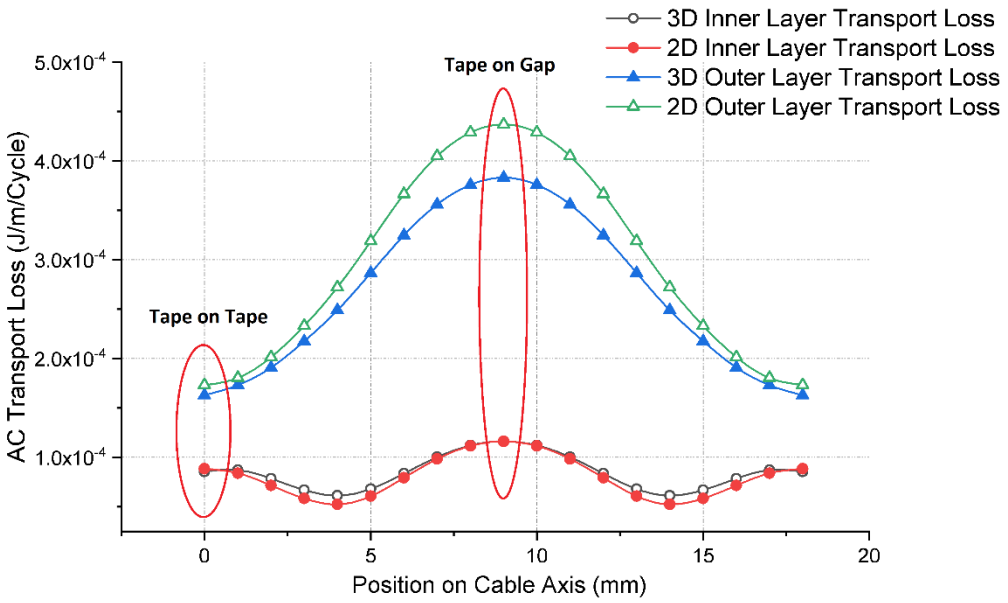

Figure 6.5.6 AC Loss Distribution on HTS wires along the Cable axis for Cable Design B

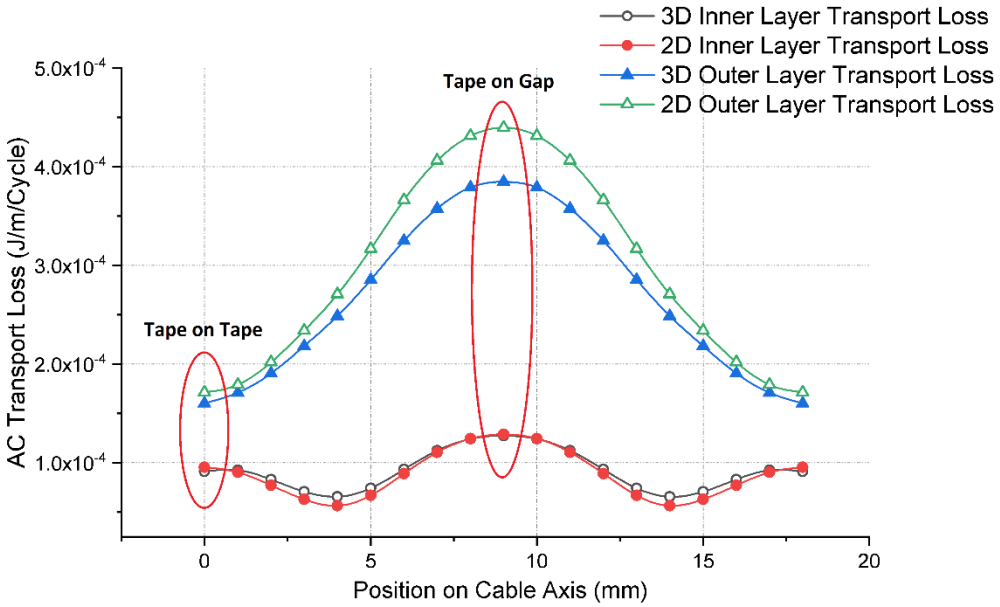

Figure 6.5.7 AC Loss Distribution on HTS wires along the Cable axis for Cable Design C

It can be observed from figure 6.5.5 to 6.5.7 that the 3D model simulation results generally agree well with the results simulated by the 2D approximation model. The AC losses simulated by the 2D model are larger than the results calculated by the 3D model for both the internal and external layer. As the 2D model physically represents the cross-section of an infinitely long untwisted HTS cable. In this case the 2D results are derived by adjusting the twisting angle differences between the internal layer and

the external layer. The AC losses generated by the tape on tape section and tape on gap section are marked out by red circles in figures above.

Table 10 AC Transport Loss at Tape on Gap Section for Cable A, B and C

	AC Loss Simulated by 2D Model (10^{-4} J/m/Cycle)		AC Loss Simulated by 3D Model (10^{-4} J/m/Cycle)	
	Wire on Outer Layer	Wire on Inner Layer	Wire on Outer Layer	Wire on Inner Layer
Cable A	4.336	1.065	3.801	1.078
Cable B	4.369	1.116	3.829	1.116
Cable C	4.396	1.288	3.846	1.274

It can be observed from figures 6.5.5 to 6.5.7 above that for the coated conductors installed in the external layers, the AC losses are at their minimum during the tape on tape section. This is due to the fact within the tape on tape section, the external layer coated conductors are in perfect parallel with the internal layer conductors. In this case, the circumferential magentic field induced by the internal layer transport current is also relatively in parallel with the external layer conductors. Therefore a least amount of inner layer induced magnetic field compoenent will become normal to the wide surfaces of the external conductors. For the sections where the twisting angle differences between two layers start to increase, the AC losses of the external layer conductors also increase with the twisting angle difference. This is due to the increasing misalignment between conductors of intenal and external layer. The increasing misalignment will cause more internal layer induced magnetic flux to become normal to the wide surfaces of the external layer conductors and thus induce higher losses on the external layer conductors. This effect peaks at the tape on gap section where the largest amount of internal magnetic field component touches the wide surfaces of the external conductors and induces the highest additional AC losses. After the tape on gap section, the absolute value of the twisting angle difference starts to drop and eventually the cable reaches another tape on tape section to finish a

complete cycle. Therefore the total AC losses produced by the external layer drop back to the original level.

For coated conductors installed in the internal layer, the overall AC loss distribution along the cable axis also follows a similar pattern. The AC loss for the internal layer conductors peaks at the tape on gap section due to the largest twisting angle difference. As it is well known that the magnetic field influence is mutual for both layers. During the tape on gap section, the edge regions of an internal layer conductor will come into contact with the highest amount of external layer induced magnetic flux. Therefore a higher amount of additional AC losses will be induced on the edge regions. However, unlike the conductors of the external layer, the lowest loss section for the internal layer conductors did not occur at the tape on tape section. Instead the AC losses for the internal layer conductors initially decrease with the rise of the twisting angle difference. The lowest AC loss for internal layer conductors occur at where the absolute twisting angle difference is around 20 degree. After that, the AC loss start to increase with the increasing twisting angle difference. This phenonmenon can be explained by the inner layer gap effect being partially offsetted by the induced magentic field of the outer layer conductors.

Another pattern can be found when examining figure 6.5.5 to 6.5.7 is that for a wider internal layer gap design such as when the internal gap width is 0.7mm, the overall AC losses of the coated conductors are higher than the coated conductos assembled in cables with smaller internal gap width designs. Two factors are found to be responsible for this phenonmenon. A wider gap width at the internal layer will distort the magnetic field generated by the internal layer conductors more serverly as discussed in the previous section. This will increase the AC losses generated within the internal layer. The other reason is that the increase of the gap width at the internal layer will inevitably increase the diameter of the internal layer. Since the diameter of the outer layer remains constant (gap width for outer layer is set as 2.0mm fixed), the distance between the inner layer conductors and the outer layer conductors will be smaller. This results in stronger internal layer magentic field component reaching surfaces of the external layer conductors and causes higher losses in the external layer. The current density

distributions and the details of the hot spots simulations will be demonstrated and studied in the following section.

Induced Hot Spot on External Layer Coated Conductors

Following the discussions made in the previous section, to facilitate the study of the hot spots on external layer coated conductors, more detailed simulations are performed to acquire the current density distributions on an outer layer conductor along the cable axis under different designs. The simulated distributions are presented in this section. As the AC losses on coated conductor surfaces is directly proportional to the current density distribution. By inspecting the current density distribution results, better understandings towards the generation mechanism as well as the locations of the hot spots can be acquired.

Current density distribution results of the tape on tape sections for cable A and C are demonstrated in figure 6.5.8 to figure 6.5.13 below. The design parameters for the three cables (cable A, B and C) are recorded in table 9 in the previous section. The current density distribution figures in this section contain the current variations within one AC cycle for wires from both the internal and external layer.

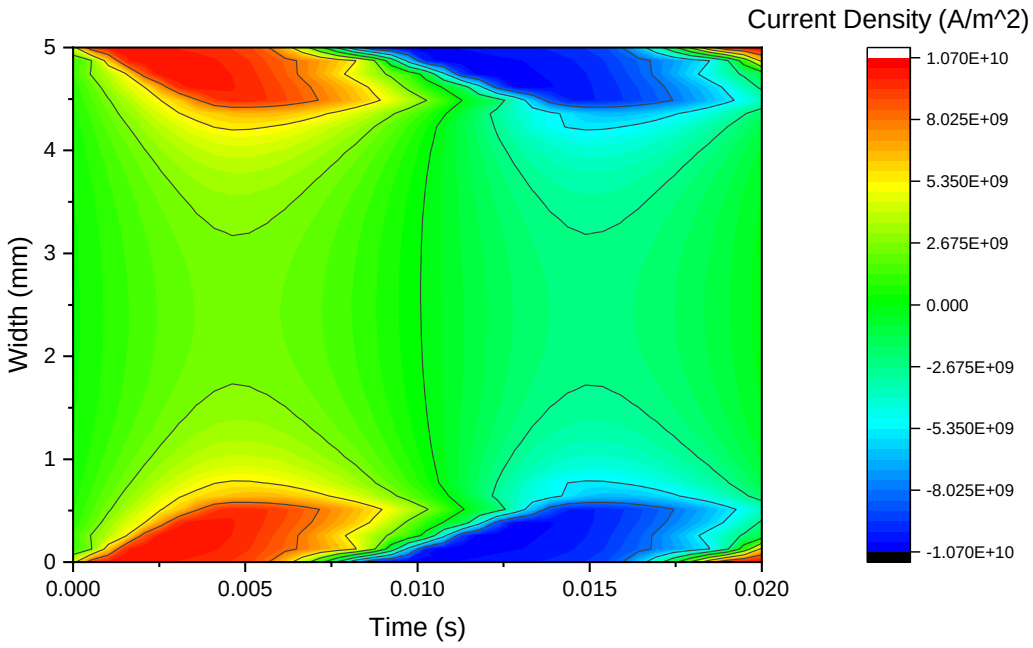

Figure 6.5.8 Current Density Distribution for 'Tape on Tape' Section of HTS wires installed in Outer Layer of Cable A

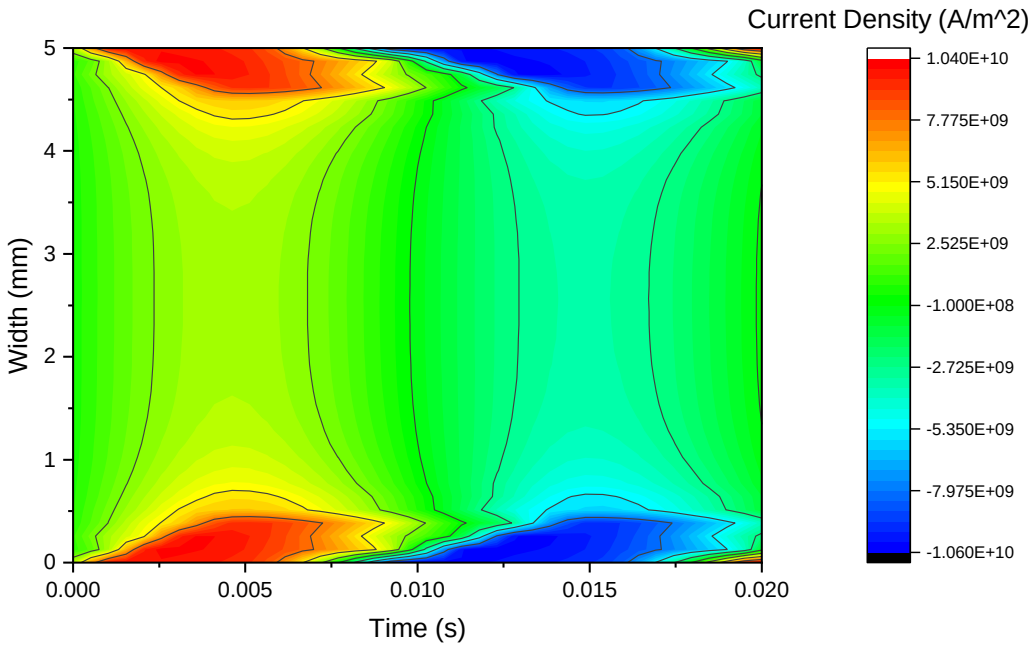

Figure 6.5.9 Current Density Distribution for 'Tape on Tape' Section of HTS wires installed in Inner Layer of Cable A

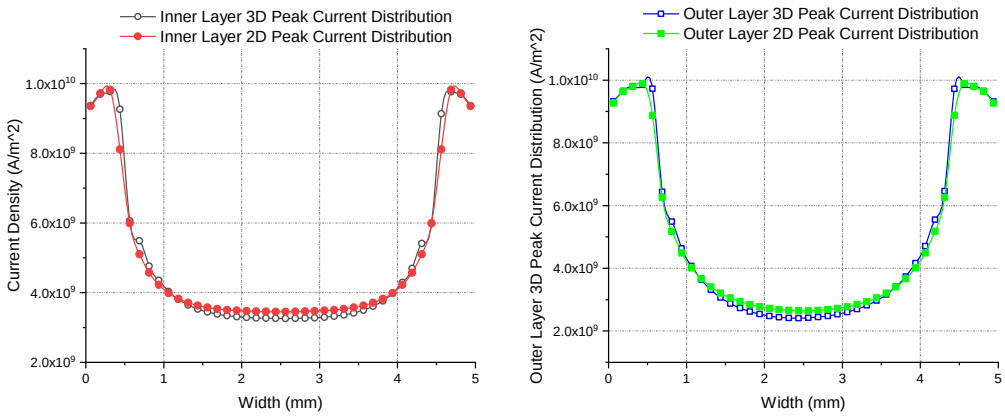

Figure 6.5.10 Peak Current Distribution for 'Tape on Tape' Section of HTS wires installed in Inner and Outer Layer of Cable A

It can be observed from figure 6.5.8 to 6.5.9 above that comparing to a coated conductor assembled within the inner layer, coated conductors of the outer layer have a higher level of current density concentration around the edge area. For both edges of an outer layer coated conductor, the high current density regions expanded further into the center region with higher magnitude. This is due to the fact that a larger gap width

is applied to the outer layer. As a result, a more severe magnetic field distortion is created on the outer layer coated conductors. A higher level of the flux creep leads to a larger amount of current density being distributed at the edge regions. As the transport current carried by the coated conductors remain constant, higher current distribution at the edge areas directly leads to a lower level of current density at the central region of the outer layer conductors. This difference in current density distribution can also be observed from the peak current density distribution graph plotted in figure 6.5.10 above. More importantly, as the conductor studied here is at the tape on tape section, the inner layer conductors are relatively in parallel with the outer layer conductors. The majority of the circumferential magnetic field induced by inner layer conductors will, in this case, also be in parallel with wide surfaces of the outer layer conductors. Therefore, no hot spot is observed across the wide surfaces of the outer layer coated conductors during this section of the cable.

The argument made above holds true for the tape on tape sections within cables of different internal layer diameter designs. The current density distributions of the internal and external layer conductors from Cable C are presented in figure 6.5.11 to 6.5.13 below. It can be found that the current density distribution pattern for conductors of Cable C is the same for those of Cable A. No particular hot spot is observed for Cable C. The same pattern also applies to Cable B. Therefore, conclusion can be made that no additional hot spot will be induced within the tape on tape sections of a cable regardless of the distance between internal and external layer.

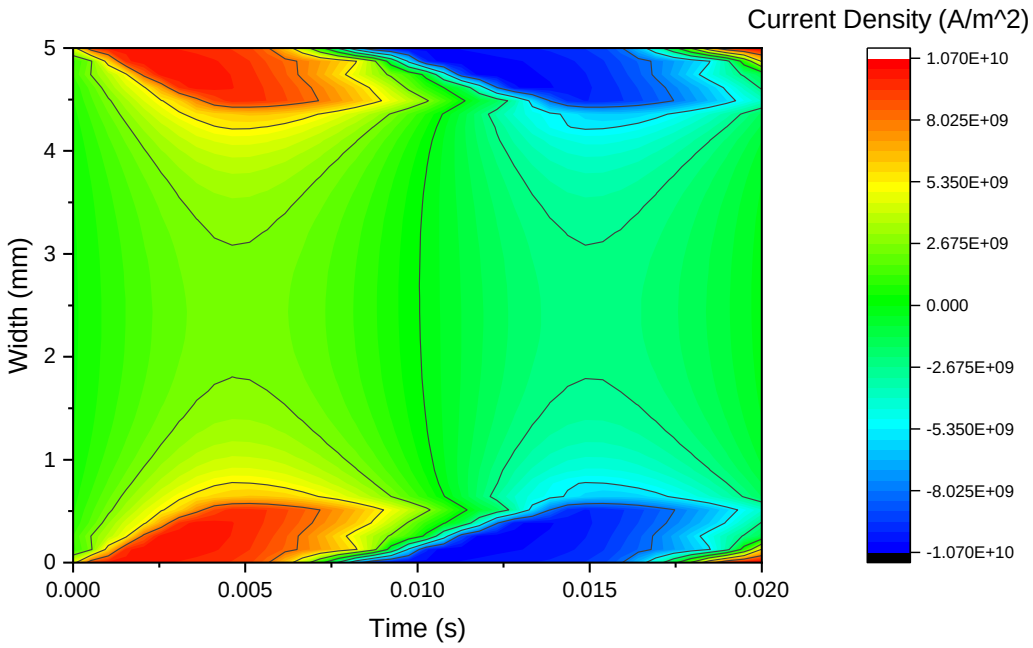

Figure 6.5.11 Current Density Distribution for 'Tape on Tape' Section of HTS wires installed in Outer Layer of Cable C

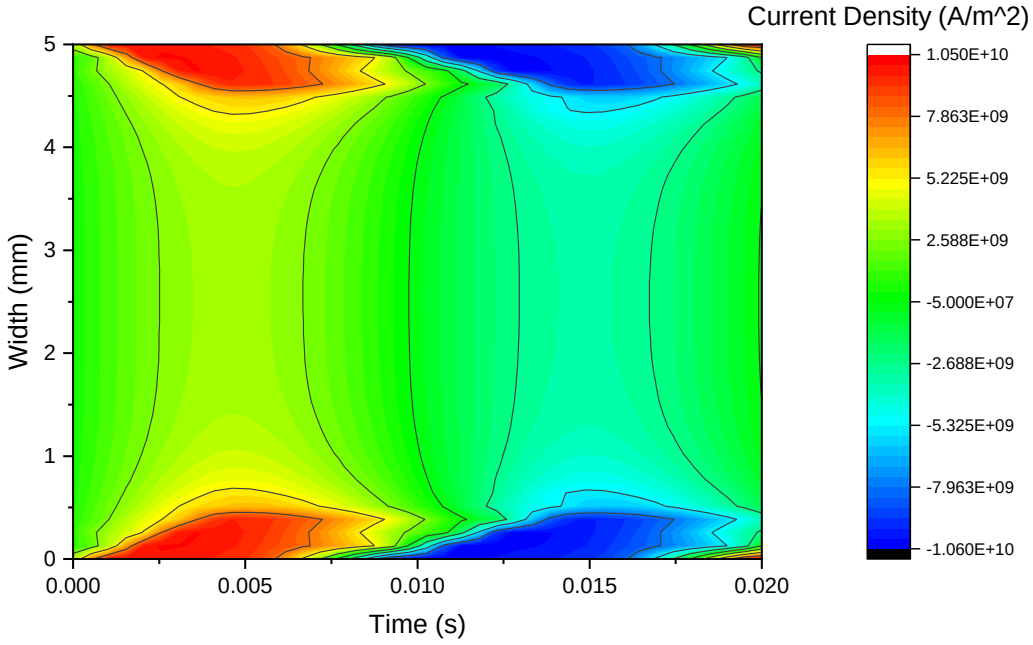

Figure 6.5.12 Current Density Distribution for 'Tape on Tape' Section of HTS wires installed in Inner Layer of Cable C

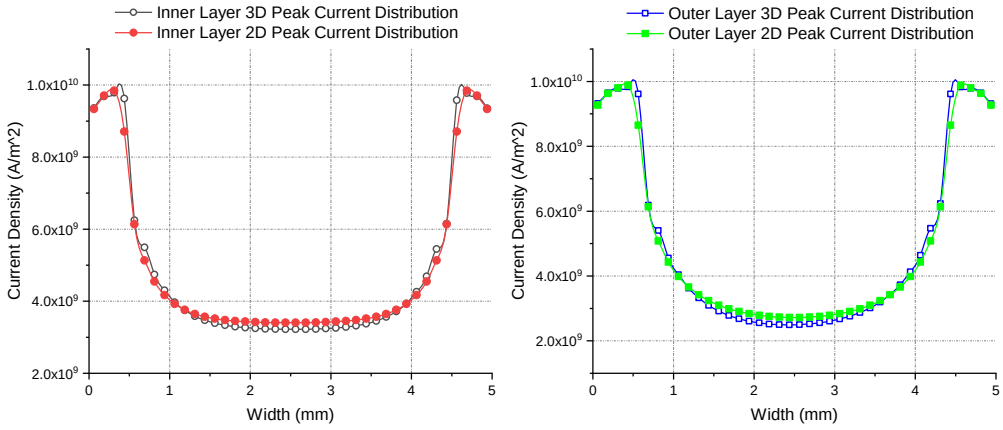

Figure 6.5.13 Peak Current Distribution for 'Tape on Tape' Section of HTS wires installed in Inner and Outer Layer of Cable C

However, for the tape on gap section, the situation can be very different. As it is discussed previously, the tape on gap section generated highest AC losses within an electromagnetic cycle of the double layer HTS cable. The reason to this higher loss level is believed due to the presence of the hot spots on the external layer conductors. Since the hot spots are induced by the circumferential magnetic field component generated by the inner layer conductors, the distribution and the strength of hot spots will be heavily dependent on the relative positions of the internal and external coated conductors. The current density distributions across the internal and external layer conductors for cable A and cable C are again simulated and presented in figure 6.5.14 to 6.5.19 below. The peak current distributions within an AC cycle for the internal and external layer conductors are provided in figure 6.5.16 and 6.5.19. The corresponding 2D model simulation results are also provided to verify the current density distributions simulated by the 3D model.

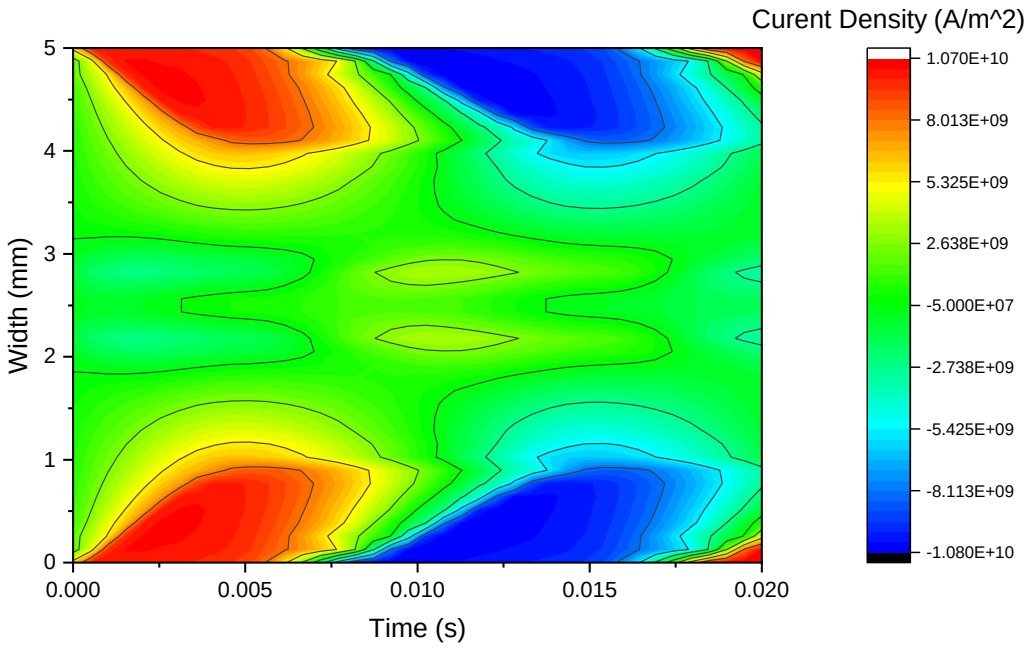

Figure 6.5.14 Current Density Distribution for 'Tape on Gap' Section of HTS wires installed in Outer Layer of Cable A

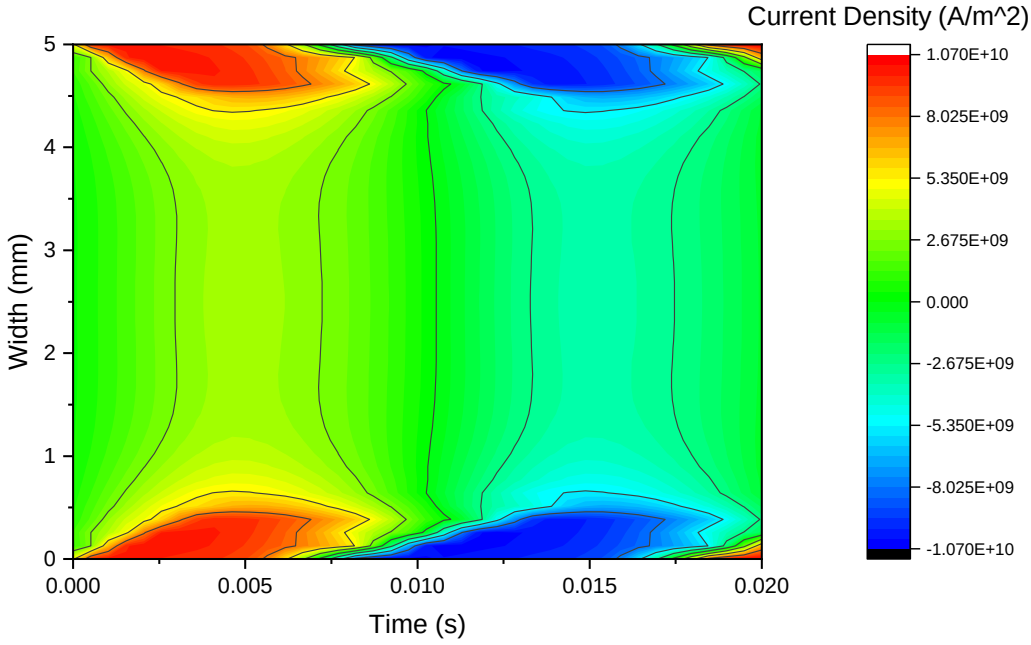

Figure 6.5.15 Current Density Distribution for 'Tape on Gap' Section of HTS wires installed in Inner Layer of Cable A

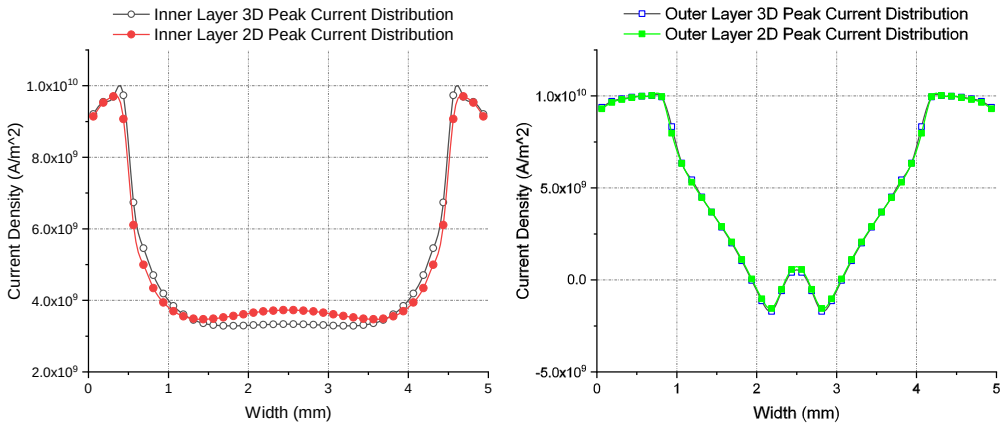

Figure 6.5.16 Peak Current Distribution for 'Tape on Gap' Section of HTS wires installed in Inner and Outer Layer of Cable A

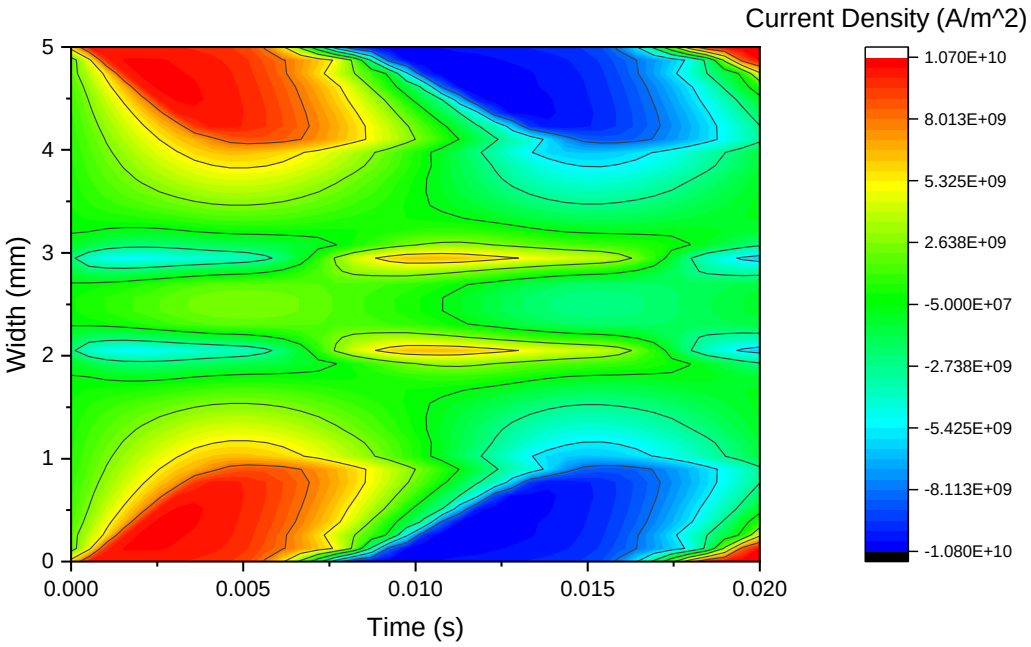

Figure 6.5.17 Current Density Distribution for 'Tape on Gap' Section of HTS wires installed in Outer Layer of Cable C

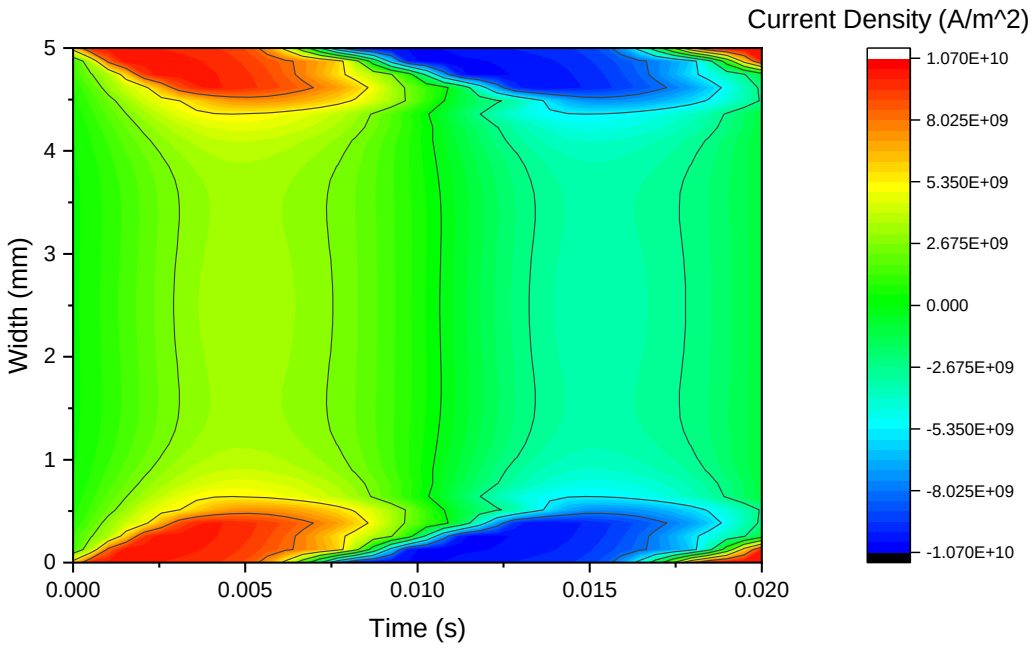

Figure 6.5.18 Current Density Distribution for 'Tape on Gap' Section of HTS wires installed in Inner Layer of Cable C

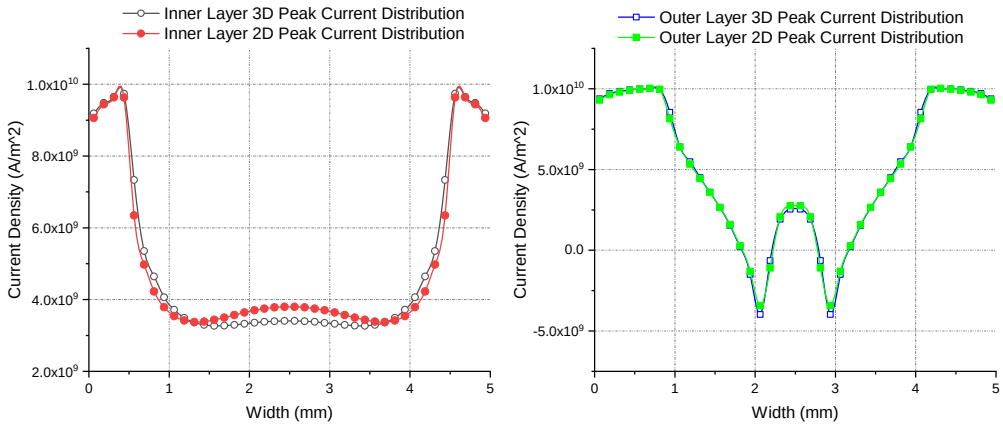

Figure 6.5.19 Peak Current Distribution for 'Tape on Gap' Section of HTS wires installed in Inner and Outer Layer of Cable C

As it is showed in figure 6.5.14 and 6.5.16 above, two symmetrical current inversion zones are observed on wide surface of the external layer conductor within the 1mm wide region at Cable A's center. Within these current inversion zones, the current density distribution indicates the current flows in a reversed direction with visibly higher amplitude comparing to the current flowing in normal regions surrounding

them. The combined factor of both reversed current flowing direction and the higher amplitude leads to the AC losses within these two zones to be considerably higher comparing to the surrounding normal regions. Thus, the two current inversion zones on the external conductors are identified as the AC loss hot spots. The positions of these hot spots are closely aligned with the edges of the internal layer conductors. As most of the transport current carried by the internal layer conductors also flow at their edge regions, the strong magnetic field produced at the edges of the internal conductors induced these AC loss hot spots on external conductors at the points where the distance between two conductors are at minimal. The magnetic field, which induce the hot spots, is a circumferential field. Since the shielding current produced at the hot spots will be counter-acting the effect of this inner layer induced magnetic field, the direction of the shielding current has to be in the opposite direction of the transport current carried by the inner layer. As the transport current carried by all the conductors are set as identical, the shielding current will thus be in the opposite direction of the outer layer transport current. Since the influence of the inner layer circumferential field is at its peak at the hot spot locations, the amplitude of the corresponding shielding current can also be very high as to demonstrate an overall negative current density at those locations on external layer conductors. This is also verified by the current density distribution results showed in figure 6.5.17 where, due to a bigger inner layer diameter of the Cable C, the distance between the outer layer conductors and the edges of the inner layer conductors become smaller. The magnitude of the shielding current is larger in this case due to the presence of stronger inner layer circumferential magnetic field. Therefore, both the covering area and the strength of the hot spots are increased comparing to the simulation results of Cable A.

Additional simulation cases were also produced to further ascertain the relationship between the distance of two adjacent conductor layers and the strength of the outer layer AC loss hotspots. The strength of the AC loss hotspots simulated in different cable diameter designs are represented by the total AC losses of outer layer HTS wires as they are in direct proportion. Combined with those obtained from the cable design A, B and C from the previous part, the AC losses of HTS wires in tape on gap section for a range of different inner layer diameter settings are recorded in table 11 below.

Table 11 AC Losses of HTS Wires at Tape on Gap Sections with Different Inner Conductor Layer Gap Width Designs

Inner Layer Gap Width (mm)	Outer Layer Gap Width (mm)	Distance Between Inner Layer and Outer Layer HTS Wires (mm)	AC Loss of Inner Layer HTS wire (10^{-4} J/m/Cycle)	AC Loss of Outer Layer HTS wire (10^{-4} J/m/Cycle)
0.40	2.0	1.131	0. 978	3.753
0.45	2.0	1.096	1.027	3.774
0.50	2.0	1.061	1.078	3.801
0.55	2.0	1.025	1.116	3.826
0.60	2.0	0.990	1.124	3.829
0.65	2.0	0.955	1.216	3.846
0.70	2.0	0.919	1.274	3.857

As it can be observed from table 11 above, with larger inner layer gap width designs, the distances between inner and outer layer HTS wires become smaller (the distance here refers to the difference between the radiuses of two conductor layers). With inner layer and outer layer conductors become more closely located at 'tape on gap' sections of the cable, higher AC losses are clearly observed from the outer layer HTS wires. This indicates stronger AC loss hotspots are induced on the outer layer HTS wires. Therefore, to mitigate the negative effects caused by the AC loss hotspots, the distance between the inner and outer conductor layers should be ideally larger. This translates into narrower inner layer conductor gap widths and can further help mitigates the magnetic field distortion effect caused by the inner layer conductor gaps.

For the internal layer conductors, no significant hot zones are observed. As the current density distribution of the internal layer conductors are mostly affected by the local gap designs. Since in this case, the internal layer coated conductors are arranged in a symmetrical way. Each wire will be affected equally by the gap distortion effect.

Therefore, the internal layer current density distributions for cable A, B and C generally follow the common 'U' shape distributions. Although it is interesting to notice that in figure 6.5.16 and 6.5.19, a slight 'bump' is observed at the center bottom of the peak current density distribution curve. This is due to the effect of the magnetic field induced by the outer layer transport current. However, as the center regions of the inner layer coated conductors are relatively far from the edges of the external conductors, this effect is very mild and almost negligible. The current density curves simulated by the 2D model showed a slightly stronger effect from the external layer currents by having a higher 'bump'. This is due to the transport currents in 2D models are set as infinitely long. Whereas in the 3D models, segmented current vectors are used. Therefore by applying different variance of the Biot-Savart Law, the magnetic field calculated using the 2D model will be higher than those calculated by the 3D model under same input condition.

In this section, the impact of different gap designs over the total AC losses on the double layer HTS cables are studied. The generation mechanism and the distribution of the hot spots over the HTS conductor tape are also discussed. Based on the discussions made above, it is more desirable to keep the gap width between adjacent conductors as small as possible. A larger gap width design will not only increase the AC loss on local layer conductors by worsening the magnetic field distortion at tape edges but also increase the diameter of the local layer unnecessary. Although the generation of the hot spots is related to the relative position between the internal and external conductors, the increased diameter will still increase the strength of the hot spots induced in the outer layers if there are any.

6.5.4. *AC Loss Mitigation with Increased Conductor Numbers in the Outer Layer*

So far, two AC loss mitigation design techniques for the double layer HTS cables have been discussed. Both designs, either by applying various twisting pitch lengths or by directly altering gap widths are mainly based on the principle of reducing the effect of magnetic field distortion produced around the gap area. According to the discussions made in section 6.5.1, apart from the magnetic field distortion effect caused by the gaps, another major source of the additional AC losses are caused by the polygonal geometry of the cable cross-section. In this section, the AC loss mitigation

design based on the principle of reducing the polygonal effect will be explored. The reduction of the polygonal effect of the cable cross-section is mainly achieved by using an increased number of coated conductors in the outer layer.

As it is stated in the previous section, increase the number of coated conductors assembled in a cable layer will make the cross-section of this cable layer more circular and thus reduce the chance of inner layer induced circumferential field component being normal to the wide surfaces of the conductors. A case study is performed in this section with three different cable designs. The dimensional parameters used to design the three cable models are presented in table 12 below. Again, to limit the number of variables affecting the overall cable AC losses, all three cables are designed with the same coated conductors defined by the standard parameter table in section 6.2 and the cables are twisted by the same pitch length of 300mm. Since in this case study we mainly want to research the AC loss reduction effect on the external layer, the number of coated conductors assembled in the external layers is increased from 10 to 12 and then to 15. Meanwhile to ensure the inner layer induced circumferential field remains constant, identical inner layers are designed for all three cables. Since in this case, we are maintaining the width of the coated conductors and the diameters of the external layer, the gap width of the external layer cannot be maintained. With more conductors being installed into the external layer, the width of gaps will be taken up by the additional conductors. Therefore, part of the AC loss reduction effect will be contributed by the decrease in gap width.

Table 12: Dimension Parameters of Cable D, E and F

	Gap Width (Inner / Outer Layer)	Cable Former Diameter (Inner / Outer Layer)	Number of Conductors (Inner / Outer)
Cable D	0.41mm / 1.5mm	17.01mm / 25.93mm	10 / 10
Cable E	0.41mm / 0.84mm	17.01mm / 25.93mm	10 / 12
Cable F	0.41mm / 0.16mm	17.01mm / 25.93mm	10 / 15

The cross-section schematics of the Cable D, E and F are demonstrated in figure 6.5.20 to 6.5.22 below. As it can be observed from figure 6.5.20 to 6.5.22, with the increase in the number of conductors, the overall shape of the external layers become more circular with smaller gap widths between adjacent conductors.

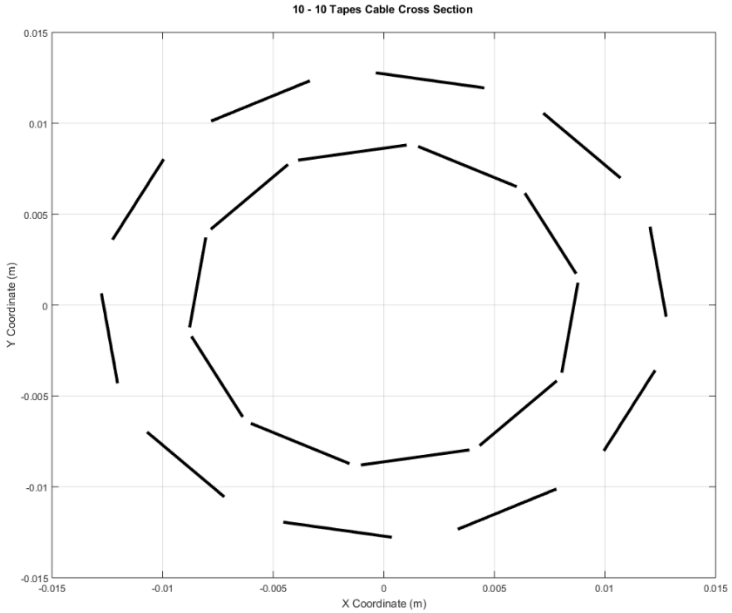

Figure 6.5.20 Cross Section Mesh of Cable D

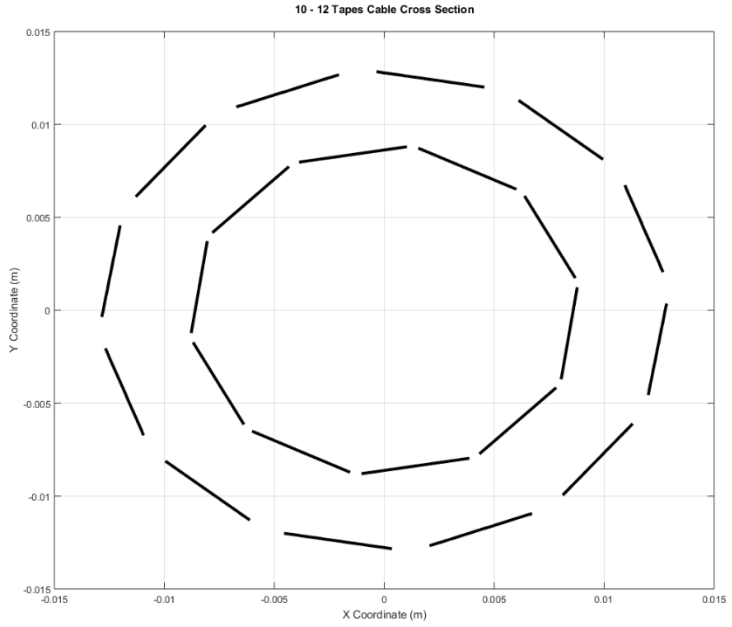

Figure 6.5.21 Cross Section Mesh of Cable E

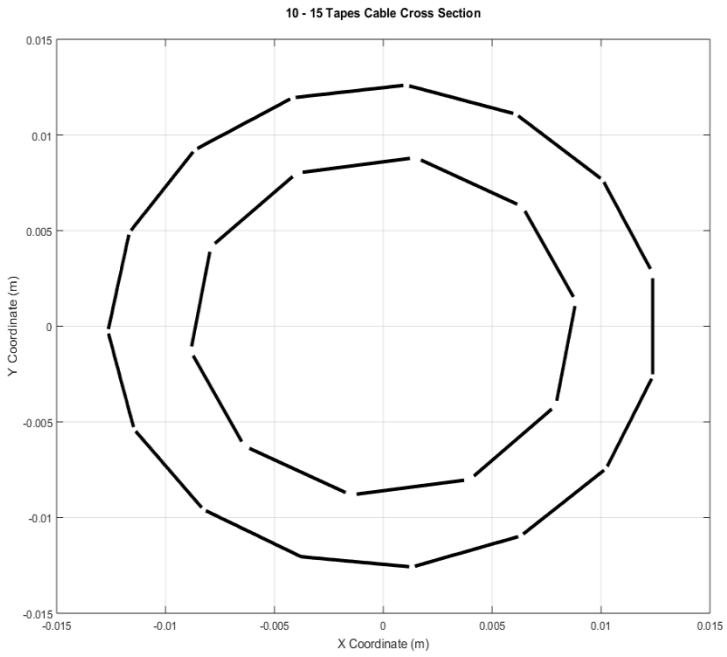

Figure 6.5.22 Cross Section Mesh of Cable F

Since this AC loss mitigation design of increasing the external layer conductor numbers is based on the principle of minimizing the impact of the inner layer induced circumferential field, detailed current density and magnetic field distributions are needed in order to study the mechanism of this loss reduction design. Therefore, 3D analysis were performed for all three cable models. The 3D current density distribution of Cable F during one time step of a complete AC cycle is presented below in figure 6.5.23 as a demonstration of the function. The detail of both the inner layer and outer layer peak current density distributions can be observed in figure 6.5.24 to 6.5.26 below.

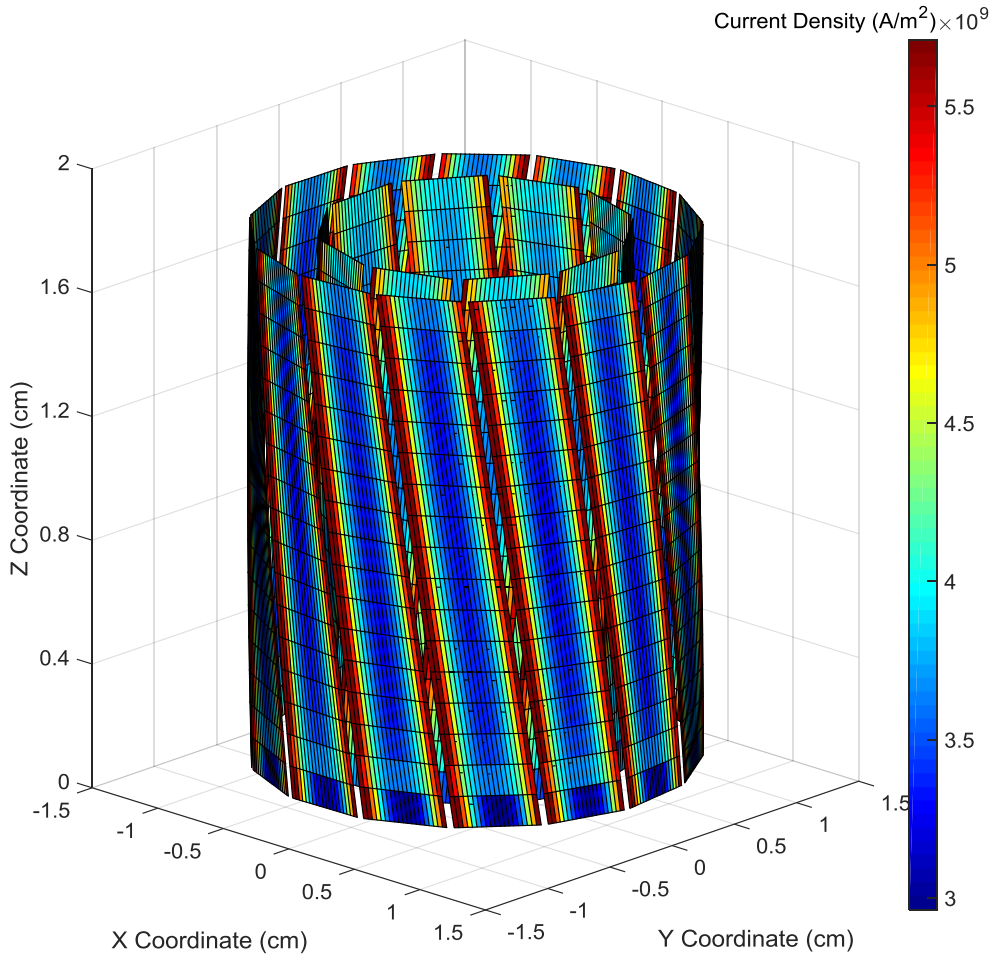

Figure 6.5.23 3D Current Distribution of Cable F at one Time Step

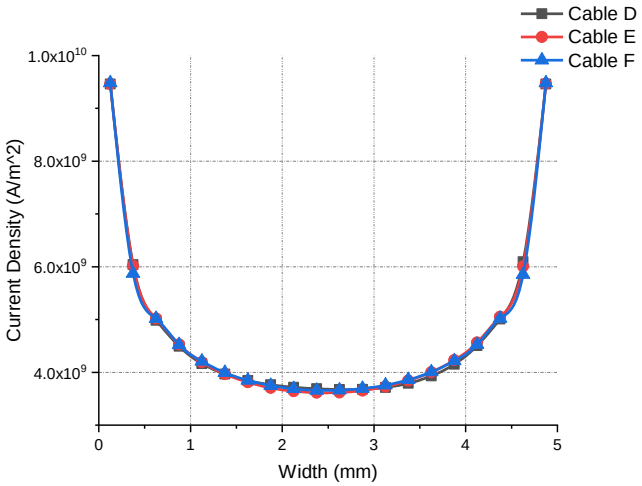

Figure 6.5.24 Peak Current Density Distribution for Inner Layer HTS Wires of Three Cable Designs

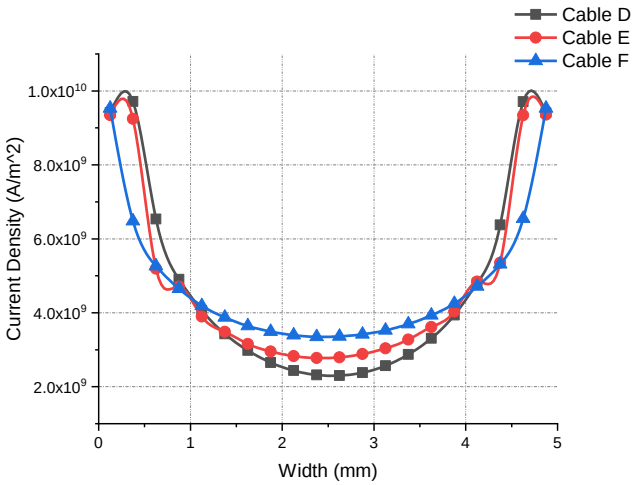

Figure 6.5.25 Peak Current Density Distribution for Outer Layer HTS Wires of Three Cable Designs

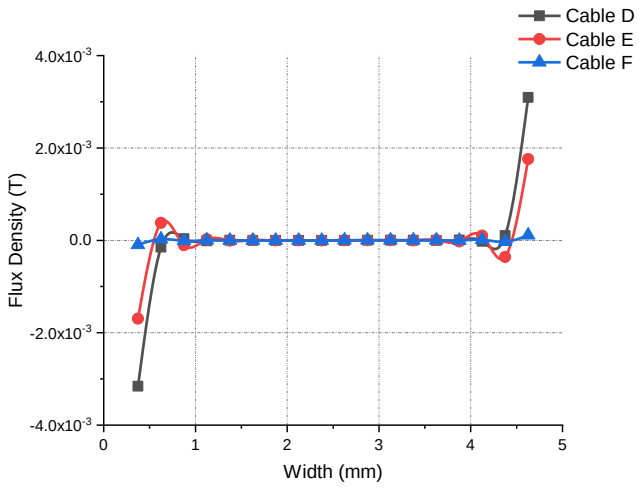

Figure 6.5.26 Peak Magnetic Field Distribution for Outer Layer HTS Wires of Three Cable Designs

As the transport current carried by the inner layer coated conductors is responsible for inducing the circumferential magnetic field that affected the outer layer, the discussion can be started by examining current distributions for three cable designs of the internal layer. Since the inner layers of all three cables are designed with the same parameters, the peak current density distribution for inner layer conductors of all three cables are almost identical as it is presented in figure 6.5.24. The identical inner layer current distributions ensure that the same circumferential magnetic field is generated for all three cases.

As it can be observed from the current density distribution plots of figure 6.5.25, with more tapes being assembled into the external layer, the current density distribution in the outer layer conductors become more even. For Cable D, conductors installed in the outer layer have the largest current density value at the edge area and lowest value at the center region comparing to the current distribution of the other two designs at the same location. Whereas for the outer layer conductors of Cable F, more transport current is carried by the center region of the HTS conductor and the overall current density distribution becomes more even. As the majority of the AC loss generated on the HTS conductors is produced at the edge areas (of magnitude of order higher than the center area), the reduced current density at the edge greatly reduces the total AC loss generated by the external conductor. This difference in outer layer conductors' current density distribution is caused by the significant change in the

combined magnetic field surrounding these outer layer conductors. The detail of this change in the combined magnetic field is simulated in this section.

The peak combined magnetic field distributions on one external layer conductor from each cable designs are plotted in figure 6.5.26 above. As it can be seen from figure 6.5.26, both external layer conductors from Cable D and Cable E have significantly higher flux density distribution around their edge regions comparing to their flux density distribution in the middle of the conductor (the flux density at the edge elements can be up to 100 times higher than those of the center elements). For Cable D and Cable E, the flux density fluctuates around some edge points. This is due to the field distortion effect caused by the wider gap width. For Cable F, however, the flux density distribution is much more even. Although the flux density is still higher around the edges of the conductor, the magnitude of the edge flux density becomes comparable to those in the middle of the conductor. This massive reduction in edge flux density is mainly due to that the overall shape of the Cable F's external layer has become much more circular than that of the other two cases. This has effectively reduced the chance that the inner layer induced circumferential field become normal to external layer conductors. The reduced gap width also contributed in an extent to this reduction in flux density. This influence factor cannot be removed as stated at the beginning of this section. The fluctuation of the flux density also disappears due to that in this case, the gap width has become extremely small for the external layer conductors. The overall AC losses on HTS conductors from the three different cable designs are also simulated and recorded in table 13 below.

Table 13: AC Losses for HTS Wires in Different Layers for Cable D, E and F

	Inner Layer Conductor AC Loss (J/m/cycle)	Outer Layer Conductor AC Loss (J/m/cycle)
Cable D	1.70E-05	8.90E-05
Cable E	1.55E-05	5.08E-05
Cable F	1.51E-05	1.51E-05

As it is presented in table 13, the AC loss of external layer conductor is reduced significantly following the increase in the number of conductors for Cable E and F. This indicates that the reduced flux density around the conductor edge and a more even current density distribution helps mitigate the additional AC losses incurred on the cable external layer. For conductors of Cable F, the total AC losses for the inner layer conductors and the outer layer conductors are almost identical. This indicates that the combined effect of adding more coated conductors and reducing the gap width in outer layer has, in this case, almost mitigate the additional AC losses incurred in the external layer of Cable F. For the inner layer conductors of Cable D, E and F, the AC losses also drop a little with the increase of the outer layer conductor number. This is due to that a more circularly distributed outer layer induced magnetic field will have less impact on the internal layer conductors. However, this loss reduction effect is not very significant. Another bonus brought about by increasing the outer layer conductor number is that higher total transport current can now be carried by the HTS cable with similar diameter and can thus increase the space utilization rate of considerably.

6.6. Conclusion

This chapter carries out simulations studying the AC loss characteristics of the 2G HTS wires and cables. At the beginning of this chapter, the AC calculation result of the 2D single tape conductor is validated by the Norris analytical equation, then the 3D straight HTS conductor model is further validated by the 2D model and the Norris equation. After validating the AC simulation results of the model by theoretical means, the AC loss characteristics of the 2G HTS conductors as well as the HTS cables are analyzed with the models built in this project. The AC loss dependency of a single HTS conductor is first studied in both the external AC magnetic field and isolated environment. It is found that overall, the presence of the external field greatly increases the total AC loss induced on HTS wire comparing to the shielded scenario. It is found that the AC loss of the 2G HTS wire also depends on the frequency of the AC current it carries. After studying the AC loss characteristics of the single HTS wire, the AC loss characteristics of HTS conductors assembled within various HTS cable structures

are studied with the 3D cable models. The AC loss mitigation effect of various loss reduction designs are also investigated in this section. It is found that overall, a compact design (either by twisting the HTS conductors or reducing former diameter) is beneficial in terms of reducing the AC losses within the HTS cables. For double (or multi) layer HTS cables, AC loss hot spots could be induced on certain parts of the cable due to difference in twisting angles between different layers of conductors. It is desirable to add more HTS wires into the outer layers of the HTS cables to make the cross-section of outer layers more circular to mitigate the additional AC losses caused by both circumferential magnetic field component induced by inner layer transport current and the conductor gaps of the local layer. For HTS cables with longer twisting pitch designs, the 2D models can provide reasonable estimation to the AC losses generated on them. However, for the cases where short twisting pitches are applied, accurate 3D modelling is necessary.

Chapter. 7 Conclusion and Future Works

7.1. Conclusions

This thesis proposes an efficient finite element numerical model to study the electromagnetic characteristics of the HTS wires and cables. This model is based on the theoretical foundation laid by the ***T*** formulation. To address the issue identified in the thesis statement, the work completed in this thesis can be concluded as below:

"This work proposed an efficient 3D FEA model with anisotropic homogeneous approximation for the analysis of the electromagnetic performance of HTS cables. The modelling strategy applied in this model effectively reduced the computing load while maintaining most of the realistic design features."

Key Contributions of this Thesis

During the development of this FEA numerical model, a number of key targets of this project is achieved and the contributions of scientific significance can be summarised as follows:

1) The anisotropic homogenous medium approximation is used to build this HTS cable numerical model. By adopting this approximation strategy, the 3D modelling efficiency of this model is significantly improved. The same strategy can be easily extended to model other HTS applications.

2) This FEA model simulates the current density and magnetic field distributions within the YBCO wires for the first time when the wires are generating dynamic losses.

3) A comprehensive study is performed with this FEA model to examine how different design features will affect the overall performance of the HTS cable.

4) A comparative study is performed to identify the scenarios when 2D analysis can be used to simulate the HTS cables and when 3D simulation must be performed.

The findings of this comparative study can help identify strategies to allocate simulation resources more efficiently.

5) A distributed parallel computing structure is built for this model to enable simulation workload sharing and make the model compatible with the university supercomputing infrastructure.

The model is built to simulate the electromagnetic distributions on 2G YBCO wires assembled in HTS power cables with a particular focus on simulating the AC loss and DC dynamic loss of the YBCO wires. The detailed current and magnetic field distribution within the YBCO wire when it is generating the dynamic loss is simulated for the first time using this model. In order to address the issues of long calculation time and harsh hardware requirement commonly posed by performing 3D analysis to HTS power cables, this model employs an anisotropic homogenous medium approximation to greatly reduce the computational load of modelling HTS power cables in 3D. The primary contribution of this thesis is successfully building the 3D HTS power cable model by stacking up multiple short straight cable subsections approximated by the 2D cross-section area of the cable and thus achieving a compromise between the calculation efficiency and simulation accuracy. This modelling method successfully reduces the computational load of performing the 3D analysis while retaining the ability to model the 3D design features (such as conductor twisting) of HTS power cables. The same method can easily be applied to model other HTS applications in 3D. By comparing the simulation results of the 3D and 2D models, this thesis also highlights the situation when the 2D modelling can be applied and when 3D modelling is necessary. Such knowledge is helpful for identifying the optimal modelling strategy to study the HTS power applications. The objectives accomplished during this project can be summarized as followed:

- In order to lay the foundation for this project and to build the 3D HTS cable model in a progressive way, a 2D single HTS wire model is initially built based on the equation system of the ***T*** formulation. Since the thin film assumption can be applied to the YBCO coated conductors, within the model the YBCO wires are assumed homogenous along their thickness dimension. The anisotropy of the electromagnetic properties is only considered along the width of the HTS wire to

further increase the calculation efficiency. Since the governing equation system of the model is solved based on assumed boundary conditions, an iteration method is later built into the model to make sure the final results are steady state results. The model is verified by the Norris analytical equation and later by the experimentally measured data provided by the external collaborators. In order to address the occasional need of inspecting the full electromagnetic distributions across a HTS wire, a mesh expansion technique is developed to simulate the current and magnetic field distribution of an HTS wire over its thickness dimension based on the simulation results across its width dimension. The 2D single HTS wire model is later expanded with the function to simulate the wire dynamic loss of YBCO wires. By simulating the detailed current and magnetic field profile within the YBCO wire, the generation mechanism and dependencies of the HTS dynamic loss are clearly explained. The dynamic loss results simulated by this model are verified by both the analytical equation and the experiment data.

- After validating the modelling algorithm with the 2D single wire model, the algorithm is expanded to build 2D multi-wire models by taking the magnetic coupling between different wires into consideration. The 2D multi-wire models are then arranged into geometries of the HTS cable cross-sections to build the 2D HTS cable model. The 2D HTS cable models assume the transport current carried by each source points to be infinitely long line currents. Therefore, the 2D HTS cable model built this way can only model the electromagnetic characteristics of a long HTS cable without the conductor twisting designs. In order to consider the conductor twisting designs possessed by most of the commercial HTS power cables, the modelling algorithm is further expanded into 3D.
- The effort of building the 3D HTS cable model starts with expanding the 2D single wire model into 3D. Since the target of this thesis is to build an efficient 3D HTS cable model, measures are taken to simplify the model and reduce the calculation workload. The anisotropic homogenous approximation strategy is applied to discretize the 3D analyzed domain of a single HTS wire into several short sub-sections. Each sub-section is assumed homogenous and straight over a short length while their anisotropic electromagnetic properties are retained across width

dimension. By applying this approximation, the anisotropic electromagnetic properties of the HTS wire are considered by this model. In the meantime, the mesh density is effectively reduced. By stacking several of these sub-sections together, the 2D mesh of the HTS wire is extended into 3D. The conductor twisting design is approximated by introducing phase angles and spatial displacements between different sub-sections. The governing equation systems of the 3D model is also modified to change the originally infinitely long source current vectors into 3D current vectors with limited length to approximate the physical reality. The verification of the 3D single wire model is achieved by cross-checking its simulation results with the already verified 2D model. Then the same stacking strategy is extended to build the complete 3D multi-layer HTS cable model. In order to make this model scalable and take full advantage of the multi-core hardware, a block cyclic workload sharing structure is introduced to the model to allow multiple CPUs to work on the governing equation system simultaneously. This workload sharing structure also provides the model with practical ability of simulating large and complex problems.

- After completing the 3D HTS cable model, simulation case studies are performed for both the single layer HTS cables and double layer HTS cables. It is found that for single layer HTS cables, without the influence of the external magnetic field, the total loss generated is proportionate to the gap width between adjacent wires. Either by applying shorter twisting pitches or by directly reducing the gap between straight HTS wires, the gap reducing designs can all help reduce the total AC losses generated on the single layer HTS cables. The presence of the external magnetic field increases the total AC losses on the single layer HTS cables significantly. The AC losses generated by the double layer HTS cables are affected by more structural variables. The impact of these variables to AC losses of the double layer HTS cables is also studied in case studies. It is found that similar to the single layer cables, reducing the gap width will also reduce the overall AC losses generated by conductors of both layers. However, the twisting pitch design for outer layer conductors are, in this case, limited by the diameter of the inner layer. As the outer layer conductors cannot be overly twisted so that they come into contact with the inner layer conductor. This constraint also leads to angular misalignments being

created for inner layer and outer layer conductors at the same of length of the cable. This leads to the hot spots being induced at the outer layer conductors at certain sections of the cable. Another major structural variable introduced by the double layer design is the number of conductors assembled at outer layer. Apart from the local magnetic field distortion effect caused by the local gaps, the outer layer conductors are also subjected to the influence of the circumferential field component induced by the inner layer transport currents. It is found by the case study that increasing the number of conductors assembled in the outer layer helps mitigate the additional AC loss induced by this circumferential field component. Since further increase of the layer numbers will not introduce any new structural variables, the results derived from the double layer cable case studies can be generalised to multi-layer HTS cables. In addition, it is found during the simulation case studies that the electromagnetic properties of the HTS cables with straight conductor designs can be effectively modelled with the 2D cross-section model. Therefore, full 3D analysis is not necessary when simulating HTS cables with straight conductors. With appropriate phase angle difference settings, the 2D cable cross-section model performs qualitatively analysis to the outer layer hot spot induction pattern for double layer HTS cables. However, the total loss of the cable will be over-estimated with only the 2D analysis.

7.2. Future Works

A calculation efficient 3D HTS cable model is developed during this PhD project. Although this model applied a number of different techniques to increase the 3D modelling efficiency for 2G HTS cables, some improvements can be made in the future to further boost both the functionality and the speed of this model. The potential points of improvements are outlined as below:

- In section 4.3.2, it is stated that in this model, the cross section bending of the HTS wires caused by the twisting design is neglected due to its relatively limited influence. A further study could consider adding the function to simulate the conductor bending effect into this model to quantitatively analyse the influence of the conductor bending effect. Adding this function will improve the model's

accuracy particularly when analyzing extreme cases where HTS wires are heavily twisted or where cable's diameters are extremely small.

- Currently this model only analyzes the electromagnetic characteristics of HTS wires under steady state operating condition. With the rapid development of the HTS power cables and ever-increasing demand of the modern power system, in the future, the HTS cables would be expected to be integrated into the power system and operate under complex and practical environments. This could expose HTS cables to the impacts of various level of faults occur either locally or at other parts of the power grid. Therefore, modelling of HTS cable's transient state characteristics is becoming increasingly important and can make an interesting research project for the future.

- Although multiple different methods have been applied in this model to increase the speed of solving 3D governing equations of HTS power cables, further improvements are still possible by applying advanced linear algebraic techniques. One of the most notable techniques is the hierarchical matrices (***h***-matrices) method. As it is discussed in section 3.4, the governing equation matrix for this numerical model is a dense matrix. The calculation of dense matrix will need more computational resources comparing to the sparse matrix due to higher number of non-zero unknowns. By finding an effective sparse approximation to the original dense matrix, the ***h***-matrices method can drastically reduce the computational resources needed as well as improve the problem solving speed. Integration of the ***h***-matrices method into this model can be a potential topic worth further exploration.

- Currently this model only focuses on studying the superconducting layers of the second generation HTS wires and didn't consider components such as the substrate layer and the shielding layer. For HTS wires working under steady state in conventional power transmission applications this simplification is sufficient as materials in other layers does not interfere with the superconducting layer. However, under fault condition, the fault current will be shared between different layers. Therefore, in the future, the function analyzing materials of different

substrate layers can be added into this model to enable full transient state simulation function.

- This model uses the most popular HTS wires consist of YBCO as the study subject. However, HTS wires manufactured with other HTS materials such as MgB_2 also becomes increasingly popular due to their advantageous cost. Therefore, in the future the function of this model can be expanded to analyze HTS wires with multi-filamentary structure.

References

[1] International Energy Agency, "World Energy Outlook 2018," International Energy Agency, Paris, 2018.

[2] The US Energy Information Administration, "International Energy Outlook 2016," The US Energy Information Administration, Washington, D.C. , 2016.

[3] S. S. Fetisov, V. V. Zubko, S. Y. Zanegin, A. A. Nosov, S. M. Ryabov and V. S. Vysotsky, "Study of the First Russian Triaxial HTS Cable Prototypes," *IEEE Transactions on Applied Superconductivity,* vol. 27, no. 4, pp. 1-5, 2017.

[4] H. J. Kim and K. Hur, "Expanded Adoption of HTS Cables in a Metropolitan Area and its Potential Impact on the Neighboring Electric Power Grid," *IEEE Transactions on Applied Superconductivity,* vol. 22, no. 3, p. 5800704, 2011.

[5] L. Ren, Y. Tang, J. Shi, L. Li, J. Li and S. Cheng, "Techno-Economic Feasibility Study on HTS Power Cables," *IEEE Transactions on Applied Superconductivity,* vol. 19, no. 3, pp. 1774-1777, 2009.

[6] L. R. Lawrence, C. Cox and D. Broman, "High Temperature Superconductivity: The Products and Their Benefits," U.S. Department of Energy , 1 July 1998. [Online]. Available: https://www.osti.gov/. [Accessed 5 12 2018].

[7] EcoSwing, "EcoSwing," EcoSwing, 23 11 2017. [Online]. Available: https://ecoswing.eu/project. [Accessed 22 04 2019].

[8] M. Stemmle, F. Merschel, M. Noe and A. Hobl, "Ampacity project — Worldwide first superconducting cable and fault current limiter installation in a German city center," in *22nd International Conference and Exhibition on Electricity Distribution (CIRED 2013)*, Stockholm, 2013.

[9] E. Pardo, "Advanced Superconductor Motor Demonstrator (ASuMED)," 28 February 2018. [Online]. Available: http://h2020.cvtisr.sk/buxus/docs//HORIZONT_2020/Doprava/2018/ASuMED_Zilina_20180305_upload.pdf. [Accessed 23 4 2019].

[10] M. Uno, "Chuo Shinkansen Project Using Superconducting Maglev System," *Japan Railway and Transport Review,* vol. 1, no. 68, pp. 14-25, 2016.

[11] J. Mateu, C. Collado and J. M. O'Callaghan, "Nonlinear model of coupled Superconducting lines," *IEEE Transactions on Applied Superconductivity* , vol. 15, no. 2, pp. 976-979, 2005.

[12] M. D. Ainslie, D. Hu, V. M. Zermeno and F. Grilli, "Numerical Simulation of the Performance of High-Temperature Superconducting Coils," *Journal of Superconductivity and Novel Magnetism,* vol. 30, no. 7, pp. 1987-1992, 2017.

[13] V. Stanev, C. Oses, A. Kunsne, E. Rodriguez, J. Paglione, S. Curtarolo and I. Takeuchi, "Machine learning modeling of superconducting critical temperature," *npj Computational Materials,* vol. 4, no. 29, pp. 1-14, 2018.

[14] G. Mikitik, Y. Mawatari, A. Wan and F. Sirois, "Analytical Methods and Formulas for Modeling High Temperature Superconductors," *IEEE Transactions on Applied Superconductivity,* vol. 23, no. 2, pp. 8001920-8001920, 2013.

[15] H. Zhang, M. Zhang and W. Yuan, "An efficient 3D finite element method model based on the T–A formulation for superconducting coated conductors," *Superconductor Science and Technology,* vol. 30, no. 2, p. 024005, 2016.

[16] H. Onnes, "The Superconductivity of Mercury," *Comm. Phys. Lab. Univ., Leiden,* pp. 122-124, 1911.

[17] W. Meissner and R. Ochsenfeld, "A new effect when superconductivity occurs," *Naturwissenschaften*, vol. 21, no. 44, pp. 787-788, 1933.

[18] F. London and H. London, "The electromagnetic equations of the supraconductor," *Proc. Roy. Soc.*, vol. 149, no. 886, pp. 71-88, 1935.

[19] W. Yuan, Second-Generation High-Temperature Superconducting Coils and Their Applications for Energy Storage, London: Springer, 2011.

[20] V. L. Ginzburgh and L. D. Landau, *Zh. Eksp. Teor. Fiz.*, vol. 20, p. 1064, 1950.

[21] J. Bardeen, L. N. Cooper and J. R. Schrieffer, "Microscopic theory of superconductivity," *Phys. Rev.*, vol. 106, pp. 162-164, 1957.

[22] A. A. Abrikosov, "On the magnetic properties of superconductors of the," *Sov. Phys. JETP-USSR*, vol. 5, no. 6, pp. 1174-1183, 1957.

[23] C. P. Poole, Superconductivity 2nd Edition, Elsevier Ltd., 2007.

[24] A. A. Golubov, Handbook of Applied Superconductivity., IOP Publishing, 1998.

[25] G. Fuchs and L. Schultz, Concise Encyclopedia of Magnetic and Superconducting Materials 2nd Edition, Elsevier Ltd., 2005.

[26] Oak Ridge National Laboratory, "Fundamentals of Superconductors," [Online]. Available: http://www.ornl.gov/info/reports/m/ornlm3063r1/pt3.html. [Accessed 13 9 2018].

[27] D. U. Gubser, "Superconductivity: An emerging power-dense energy-," *IEEE Transactions on Applied Superconductivity*, vol. 14, no. 4, pp. 2037-2046, 2004.

[28] H. Suderow, I. Guillamon, J. G. Rodrigo and S. Vieira, "Imaging superconducting vortex cores and lattices with a scanning tunneling microscope," *Superconductor Science and Technology*, vol. 27, no. 6, p. 063001, 2014.

[29] J. G. Bednorz and K. A. Muller, "Possible high Tc superconductivity in the Ba-La-Cu-O system," *Zeitschrift fur Physik B Condensed Matter*, vol. 64, no. 2, pp. 189-193, 1986.

[30] M. Wu, J. R. Ashburn, C. J. Torng, P. Hor, R. Meng, L. Gao, Z. Huang, Y. Wang and C. Chu, "Superconductivity at 93 k in a new mixed-phase y-ba-cu-o compound system at ambient pressure," *Physics Review Letter*, vol. 58, no. 9, pp. 908-910, 1987.

[31] H. Maeda, Y. Tanaka, M. Fukutomi and T. Asano, "A New High-Tc Oxide Superconductor without a Rare Earth Element," *Japanese Journal of Applied Physics*, vol. 27, no. 2, pp. L209 - L210, 1988.

[32] Laboratory of Advanced Energy Systems, Helsinki University of Technology, "High-Temperature Superconductivity," [Online]. Available: http://tfy.tkk.fi/aes/AES/projects/prlaser/supercond.htm. [Accessed 23 7 2016].

[33] Nexans, "Nexans Superconducting Cable Systems," [Online]. Available: https://www.nexans.de/eservice/Germany-de_DE/fileLibrary/Download_540144810/Germany/files/Nexans_Superconducting_cable_systems.pdf. [Accessed 5 1 2016].

[34] J. C. Hernandez-Liambes and D. Hazelton, "Advantages of Second-Generation High Temperature Superconductors for Pulsed Power Applications," in *2009 IEEE Pulsed Power Conference*, Washington, D.C., 2009.

[35] D. T. Verebelyi, U. Schoop and C. Thieme, "Uniform performance of continuously processed MOD-YBCO-coated conductors using a textured Ni-W substrate," *Superconductor Science & Technology,* vol. 16, no. 5, pp. L19-L22, 2003.

[36] M. Polak, L. Krempasky, S. Chromik, D. Wehler and B. Moenter, "Magnetic field in the vicinity of YBCO thin film strip and strip with filamentary structure," *Physica C: Superconductivity,* Vols. 372-376, no. 3, pp. 1830-1834, 2002.

[37] SuperPower, "SuperPower 2G HTS Wire Specifications," [Online]. Available: http://www.superpower-inc.com/system/files/SP_2G+Wire+Spec+Sheet_for+web_2012FEC_v2_1.pdf. [Accessed 6 5 2017].

[38] American Superconductor Corporation, "American Superconductor Corporation," American Superconductor Corporation, [Online]. Available: https://www.amsc.com/.

[39] SuperPower, "SuperPower 2G HTS Wire," SuperPower Inc., [Online]. Available: http://www.superpower-inc.com/content/2g-hts-wire.

[40] Fujikura, "Superconducting Wire - Fujikura," [Online]. Available: http://www.fujikura.com/solutions/superconductingwire/.

[41] Shanghai Superconductor , "Shanghai Superconductor," [Online]. Available: http://www.shsctec.com/en/introduce/89.

[42] Superconductor Technologies Inc., "High Power Superconducting Transmission and Distribution Cables," [Online]. Available: https://www.suptech.com/transmission_cables_n.php.

[43] X. Wang, A. Ishiyama, M. Ohya and N. Fujiwara, "Over-Current Characteristics of 66-kV RE123 HTS Power Cable," *IEEE Transactions on Applied Superconductivity*, vol. 21, no. 3, pp. 1013-1016, 2011.

[44] M. Watanabe, H. Yumura, H. Takigawa, H. Ito, Y. Ashibe, T. Kato, C. Suzawa, T. Masuda, K. Sato and S. Isojima, "Development of HTS Cable System for ALBANY Project," in *Journal of Physics: Conference Series*, 2006.

[45] H. Yumura, M. Watanabe, M. Ohya, Y. Ashibe, H. Ito, T. Masuda and K. Sato, "30 m YBCO cable for the Albany HTS cable project," in *Journal of Physics: Conference Series*, Brussels, 2008.

[46] S. Mukoyama, M. Yagi, H. Hirata and M. Suzuki, "Development of YBCO High-Tc Superconducting Power Cables," *Furukawa Review*, no. 35, pp. 18-22, 2009.

[47] S.H.Sohna, J.H.Lima, B.M.Yanga, S.K.Leeb and e. al, "Design and development of 500 m long HTS cable system in the KEPCO power grid, Korea," *Physica C: Superconductivity and its Applications*, vol. 470, no. 20, pp. 1567-1571, 2010.

[48] J. F. Maguire, J. Yuan, W. Romanosky, F. Schmidt and e. al, "Progress and Status of a 2G HTS Power Cable to Be Installed in the Long Island Power Authority (LIPA) Grid," *IEEE Transactions on Applied Superconductivity*, vol. 21, no. 3, pp. 961-966, 2011.

[49] B. Yang, J. Kang, S. Lee, C. Choi and Y. Moon, "Qualification Test of a 80 kV 500 MW HTS DC Cable for Applying Into Real Grid," *IEEE Transactions on Applied Superconductivity*, vol. 25, no. 3, pp. 1-5, 2015.

[50] M. Noe, "National High Magnetic Field Laboratory," [Online]. Available: https://nationalmaglab.org/images/magnet_development/asc/searchable_docs/asc_resources/coated_conductors/2016/io_11_noe.pdf.

[51] Z. Hong, A. M. Campbell and T. A. Coombs, "Numerical solution of critical state in superconductivity by finite element software," *Superconductor Science and Technology*, vol. 19, pp. 1246-1252, 2006.

[52] C.P.Bean, "Magnetization of hard superconductors," *Physics Review letters*, vol. 8, p. 250, 1962.

[53] P. Anderson, "Theory of flux creep in hard superconductors," *Physics Review Letters*, vol. 9, no. 7, pp. 309-311, 1963.

[54] J. Rhyner, "Magnetic properties and AC-losses of superconductors with power law current-voltage characteristics," *Physica C*, vol. 212, pp. 292-300, 1993.

[55] S. S. e. al., "Comparison of numerical methods for modeling of superconductors," *IEEE Transactions on Magnetics*, vol. 38, no. 2, pp. 849-852, 2002.

[56] Y. B. Kim, C. F. Hempstead and A. R. Strnad, "Critical persistent currents in hard superconductors," *Physics Review Letters*, vol. 9, no. 7, pp. 306-309, 1963.

[57] A. Naoyuki, M. Shun-ichi, B. Nobuya and M. Kengo, "Numerical modelings of superconducting wires for AC loss calculations," *Physica C: Superconductivity*, vol. 310, no. 1-4, pp. 16-29, 1998.

[58] S. Stavrev, F. Grilli, B. Dutoit, N. Nibbio, E. Vinot and e. al, "Comparison of numerical methods for modeling of superconductors," *IEEE Transactions on Magnetics*, vol. 38, no. 2, pp. 849 - 852, 2002.

[59] K. Kajikawa, T. Hayashi, R. Yoshida, M. Iwakuma and K. Funaki, "Numerical evaluation of AC losses in HTS wires with 2D FEM formulated by self magnetic field," *IEEE Transactions on Applied Superconductivity,* vol. 13, no. 2, pp. 3630 - 3633, 2003.

[60] A. Naoyuki, M. Kengo, M. Shun-ichi, M. Hideki and O. Kazuya, "Finite element analysis of AC loss in non-twisted Bi-2223 tape carrying AC transport current and/or exposed to DC or AC external magnetic field," *Physica C: Superconductivity,* vol. 310, no. 1-4, pp. 30-35, 1998.

[61] N. Masahiro, A. Naoyuki and N. Taketsune, "Three-dimensional model for numerical electromagnetic field analyses of coated superconductors and its application to Roebel cables," *Superconductor Science and Technology,* vol. 25, no. 9, p. 095011, 2012.

[62] Y. Sogabe, M. Yasunaga, Y. Fuwa, Y. Kuriyama and e. al, "AC Losses in HTS Coils of Superferric Dipole and Combined-Function Magnets," *IEEE Transactions on Applied Superconductivity,* vol. 29, no. 5, 2019.

[63] H. Ueda, Y. Imaichi, T. Wang, A. Ishiyama and e. al, "Numerical Simulation on Magnetic Field Generated by Screening Current in 10-T-Class REBCO Coil," *IEEE Transactions on Applied Superconductivity,* vol. 26, no. 4, p. 4701205, 2016.

[64] E. Vinot, G. Meunier and P. Tixador, "Different formulations to model superconductors," *IEEE Transactions on Magnetics,* vol. 36, no. 4, pp. 1226 - 1229, 2000.

[65] Altair | Hyperworks, "Flux - A Fast and Robust Solver," [Online]. Available: https://altairhyperworks.com/product/flux/Capabilities---Robust-Solver.

[66] R. Brambilla, F. Grilli, L. Martini, M. Bocchi and G. Angeli, "A Finite-Element Method Framework for Modeling Rotating Machines With

Superconducting Windings," *IEEE Transactions on Applied Superconductivity,* vol. 28, no. 5, 2018.

[67] R. Brambilla, F. Grilli and L. Martini, "Development of an edge-element model for AC loss computation of high-temperature superconductors," *Superconductor Science and Technology,* vol. 20, no. 1, pp. 16-24, 2006.

[68] M. Ainslie, Transport AC loss in high temperature, Cambridge: University of Cambridge, 2012.

[69] D. Miyagi, T. Wakatsuki, N. Takahashi, S. Torii and K. Ueda, "3-D finite element analysis of current distribution in HTS power cable taking account of E-J power law characteristic," *IEEE Transactions on Magnetics,* vol. 40, no. 2, pp. 908-911, 2004.

[70] Z. Hong, L. Ye, M. Majoros, A. M. Campbell and T. A. Coombs, "Numerical Estimation of AC Loss in MgB2 Wires in Self-field Condition," *Journal of Superconductivity and Novel Magnetism,* vol. 21, no. 3, pp. 205-211, 2008.

[71] K. Takeuchi, N. Amemiya, T. Nakamura, O. Maruyama and T. Ohkuma, "Model for electromagnetic field analysis of superconducting power transmission cable comprising spiraled coated conductors," *Superconductor Science and Technology,* vol. 24, no. 8, p. 119501, 2011.

[72] Y. B. Kim, C. F. Hempstead and A. R. Strnad, "Flux-flow resistance in type-II superconductors," *Physical Review,* vol. 139, no. 4A, pp. 1163 - 1172, 1965.

[73] D. Shantsev, Y. Galperin and T. Johansen, "Thin superconducting disk with field-dependent critical current: Magnetization and ac susceptibilities," *Physical Review B,* vol. 61, no. 14, pp. 9699-9706, 2000.

[74] W. T. Norris, "Calculation of hysteresis losses in hard superconductors carrying ac: isolated conductors and edges of thin sheets," *Journal of Physics D: Applied Physics,* vol. 3, no. 4, pp. 489 - 507, 1970.

[75] V.A.Altov, V.V.Kurguzov and V.V.Sytchev, "Superconducting materials in oscillating and rotating magnetic fields," *Cryogenics,* vol. 25, no. 5, pp. 266-270, 1985.

[76] T.Ogasawara, K.Yasuköchi, S.Nose and H.Sekizawa, "Effective resistance of current-carring superconducting wire in oscillating magnetic fields 1: Single core composite conductor," *Cryogenics,* vol. 16, no. 1, pp. 33-38, 1976.

[77] M. P. Oomen, J. Rieger, M. L. B. t. Haken and H. H. J. t. Kate, "Dynamic resistance in a slab-like superconductor with Jc(B) dependence," *Superconductor Science and Technology,* vol. 12, no. 6, pp. 382-387, 1999.

[78] A. González-Parada, F. Trillaud, R. Guzmán-Cabrera and M. Abatal, "Torque Ripple Reduction in an Axial Flux High Temperature Superconducting Motor," *IEEE Transactions on Applied Superconductivity,* vol. 25, no. 3, p. 5202805, 2015.

[79] T. Nishimura, T. Nakamura, Q. Li, N. Amemiya and Y. Itoh, "Potential for Torque Density Maximization of HTS Induction/Synchronous Motor by Use of Superconducting Reluctance Torque," *IEEE Transactions on Applied Superconductivity,* vol. 24, no. 3, p. 5200504, 2014.

[80] S. Baik, Y. Kwon, S. Park and H. Kim, "Performance analysis of a superconducting motor for higher efficiency design," *IEEE Transactions on Applied Superconductivity,* vol. 23, no. 3, p. 5202004, 2013.

[81] Z. Wei, Y. Xin, J. Jin and Q. Li, "Optimized design of coils and iron cores for a saturated iron core superconducting fault current limiter," *IEEE Transactions on Applied Superconductivity,* vol. 26, no. 7, p. 5603904, 2016.

[82] P. T. Pascal, A. Badel, G. Auran and G. S. Pereira, "Superconducting fault current limiter for ship grid simulation and demonstration," *IEEE Transactions on Applied Superconductivity,* vol. 27, no. 4, p. 5601705, 2017.

[83] J. Kozak, M. Majka and S. Kozak, "Experimental results of a 15 kV, 140 A superconducting fault current limiter," *IEEE Transactions on Applied Superconductivity,* vol. 27, no. 4, p. 5600504, 2017.

[84] Q. Li, N. Amemiya, K. Takeuchi, T. Nakamura and N. Fujiwara, "AC loss characteristics of superconducting power transmission cables: gap effect and Jc distribution effect," *Superconductor Science and Technology,* vol. 23, no. 11, p. 115003, 2010.

[85] Q.Li, N.Amemiya, R.Nishino, T.Nakamura and T.Okuma, "AC loss reduction of outer-diameter-fixed superconducting power transmission cables using narrow coated conductors," *Physica C: Superconductivity,* vol. 484, no. 15, pp. 217-222, 2013.

[86] N. Amemiya, Q. Li, I. Kaoru, K. Takeuchi, T. Nakamura and T. Okuma, "AC Loss Reduction of Multilayer Superconducting Power Transmission Cables by Using Narrow Coated Conductors," *Superconductor Science and Technology,* vol. 24, no. 6, p. 065013, 2011.

[87] Q. Li, M. Yao, Z. Jiang, C. W. Bumby and N. Amemiya, "Numerical Modelling of Dynamic Loss in HTS Coated Conductors under Perpendicular Magnetic Fields," *IEEE Transactions on Applied Superconductivity* , vol. 28, no. 2, p. 6600106, 2018.

[88] S. Fu, M. Qiu, J. Zhu and H. Zhang, "Numerical Study on AC Loss Properties of HTS Cable Consisting of YBCO Coated Conductor for HTS Power Devices," *IEEE Transactions on Applied Superconductivity,* vol. 28, no. 4, p. 4802005, 2018.

[89] Q. Li, N. Amemiya, K. Takeuchi, T. Nakamura and N. Fujiwara, "Effects of Unevenly Distributed Critical Currents and Damaged Coated Conductors to AC Losses of Superconducting Power Transmission Cables," *IEEE Transactions on Applied Superconductivity,* vol. 21, no. 3, pp. 953-956, 2010.

[90] F. Grilli, R. Brambilla, F. Sirois, A. Stenvall and S. Memiaghe, "Development of a three-dimensional finite-element model for high-temperature superconductors based on the H-formulation," *Cryogenics,* vol. 53, pp. 142-147, 2013.

[91] R. V. Sabariego, C. Geuzaine, P. Dular and J. Gyselinck, "Nonlinear Time-Domain Finite-Element Modeling of Thin Electromagnetic Shells," *IEEE Transactions on Magnetics,* vol. 45, no. 3, pp. 976-979, 2009.

[92] R. Sabariego, C. Geuzaine, P. Dular and J. Gyselinck, "h- and a-formulations for the time-domainmodelling of thin electromagnetic shells," *IET Science, Measurement & Technology,* vol. 2, no. 6, pp. 402-408, 2008.

[93] R.Rannacher, "Adaptive Galerkin finite element methods for partial differential equations," *Journal of Computational and Applied Mathematics,* vol. 128, no. 1-2, pp. 205-233, 2001.

[94] J. Rodriguez, "Galerkin's method for ordinary differential equations subject to generalized nonlinear boundary conditions," *Journal of Differential Equations,* vol. 97, no. 1, pp. 112-126, 1992.

[95] J. Yan and C.-W. Shu, "Local Discontinuous Galerkin Methods for Partial Differential Equations with Higher Order Derivatives," *Journal of Scientific Computing,* vol. 17, no. 1-4, pp. 27-47, 2002.

[96] A. Gokhman, "NEW METHOD FOR SOLVING PARTIAL AND ORDINARY DIFFERENTIAL EQUATIONS USING FINITE-ELEMENT TECHNIQUE," *Numerical Heat Transfer,* vol. 18, no. 1, pp. 1-22, 1990.

[97] V. M. Zermenoa, A. B. Abrahamsenb, N. Mijatovicc, M. P. Sorensena, Pedersena, B. B. Jensenc and N. F.Pedersen, "Simulation of an HTS Synchronous Superconducting Generator," *Physics Procedia*, vol. 36, pp. 786-790, 2012.

[98] V. M. R. Zermeno, A. B. Abrahamsen, N. Mijatovic, B. B. Jensen and M. P. Soerensen, "Calculation of alternating current losses in stacks and coils made of second generation high temperature superconducting tapes for large scale applications," *Journal of Applied Physics*, vol. 114, no. 17, p. 173901, 2013.

[99] V. M. R. Zermeño and F. Grilli, "3D modeling and simulation of 2G HTS stacks and coils," *Superconductor Science and Technology*, vol. 27, no. 4, p. 044025, 2014.

[100] H. Moghnieh and D. A. Lowther, "The Solution of Electromagnetic Field Problems Using a Sliding Window Gauss-Seidel Algorithm on a Multicore Processor," *IEEE Transactions on Magnetics*, vol. 46, no. 8, pp. 3081-3084, 2010.

[101] X.-P. Wang, C. J. García-Cervera and E. Weinan, "A Gauss–Seidel Projection Method for Micromagnetics Simulations," *Journal of Computational Physics*, vol. 171, no. 1, pp. 357-372, 2001.

[102] L.-Y. Sun, "A comparison theorem of the improving Gauss-Seidel method for H-matrix and its comparison matrix," *Applied Mathematics and Computation*, vol. 183, no. 1, pp. 390-393, 2006.

[103] L. J. Lorence Jr., W. R. Martin and M. Luskin, "Analysis of a block Gauss-Seidel iterative method for a finite element discretization of the neutron transport equation," *Transport Theory and Statistical Physics* , vol. 14, no. 1, pp. 35-62, 2006.

[104] A. Chama, S. Gerber and R.-J. Wang, "Newton–Raphson Solver for Finite Element Methods Featuring Nonlinear Hysteresis Models," *IEEE Transactions on Magnetics,* vol. 54, no. 1, p. 7400108, 2018.

[105] S. Stark, S. Roth, P. Neumeister and H. Balke, "Modifications of the Newton–Raphson method for finite element simulations in ferroelectroelasticity," *International Journal of Solids and Structures,* vol. 50, no. 5, pp. 773-780, 2013.

[106] S. Hartmann, "A remark on the application of the Newton-Raphson method in non-linear finite element analysis," *Computational Mechanics,* vol. 36, no. 2, pp. 100-116, 2005.

[107] W. Fu, S. Ho, H. Li and H. Wong, "An effective method to reduce the computing time of nonlinear time-stepping finite-element magnetic field computation," *IEEE Transactions on Magnetics,* vol. 38, no. 2, pp. 441-444, 2002.

[108] J. Saitz, "Newton-Raphson method and fixed-point technique in finite element computation of magnetic field problems in media with hysteresis," *IEEE Transactions on Magnetics,* vol. 35, no. 3, pp. 1398 - 1401, 1999.

[109] J. Šouc, E. Pardo, M. Vojenčiak and F. Gömöry, "Theoretical and experimental study of AC loss in high temperature superconductor single pancake coils," *Superconductor Science and Technology,* vol. 22, no. 1, p. 015006, 2008.

[110] J. R. Clem, J. H. Claassen and Y. Mawatari, "AC losses in a finite Z stack using an anisotropic homogeneous-medium approximation," *Superconductor Science and Technology,* vol. 20, no. 12, pp. 1130-1139, 2007.

[111] G. P. Mikitik and E. H. Brandt, "Generation of a dc voltage by an ac magnetic field in type-II superconductors," *PHYSICAL REVIEW B,* vol. 64, no. 9, p. 092502, 2001.

[112] M. Oomen, J. Rieger, M. Leghissa, B. t. Haken and H. H. J. t. Kate, "Dynamic resistance in a slab-like superconductor with Jc(B) dependence," *Superconductor Science and Technology,* vol. 12, no. 6, pp. 382-387, 1999.

[113] Z. Jiang, R. Toyomoto, N. Amemiya, C. W. Bumby, R. A. Badcock and N. J. Long, "Dynamic resistance measurements in a GdBCO-coated conductor," *IEEE Transactions on Applied Superconductivity,* vol. 27, no. 4, p. 5900205, 2016.

[114] T.Matsushita, "Electromagnetic phenomena and hysteresis losses in superconductors," *Cryogenics,* vol. 30, no. 4, pp. 314-323, 1990.

[115] T. Matsushita, "Flux pinning and electromagnetic phenomenon," Sangyo Tosho Inc,, Tokyo, 1994.

[116] Z. Jiang, R. Toyomoto, N. Amemiya, X. Zhang and C. W. Bumby, "Dynamic resistance of a high-T c coated conductor wire in a perpendicular magnetic field at 77 K," *Superconductor Science and Technology,* vol. 30, no. 3, p. 03LT01, 2017.

[117] E. H. Brandt and M. Indenbom, "Type-II superconductor strip with current in a perpendicular magnetic field," *PHYSICAL REVIEW B,* vol. 48, no. 17, pp. 895-906, 1993.

[118] M. Ciszek, O. Tsukamoto, J. Ogawa and D. Miyagi, "Energy losses in YBCO-123 coated conductors carrying transport current in perpendicular external magnetic field," in *AIP Conference Proceedings 614,* 2002.

[119] M. Ciszek, H. G. Knoopers, J. J. Rabbers, B. t. Haken and H. H. J. t. Kate, "Angular dependence of the dynamic resistance and its relation to the AC transport current loss in Bi-2223/Ag tape superconductors," *Superconductor Science and Technology,* vol. 15, no. 8, pp. 1275-1280, 2002.

[120] Q. Li, M. Yao, Z. Jiang, C. W. Bumby and N. Amemiya, "Numerical Modelling of Dynamic Loss in HTS Coated Conductors under Perpendicular Magnetic Fields," *IEEE Transactions on Applied Superconductivity,* vol. 28, no. 2, p. 6600106, 2018.

[121] M. Iwakuma, M. Nigo, D. Inoue, T. Kiss, K. Funaki, Y. Iijima, T. Saitoh, Y. Yamada and Y. Shiohara, "AC loss properties of YBCO superconducting tapes exposed to external AC magnetic field," *IEEE Transactions on Applied Superconductivity,* vol. 15, no. 2, pp. 1562-1565, 2005.

[122] K. Kajikawa, A. Takenaka, K. Kawasaki, M. Iwakuma and K. Funaki, "Numerical simulation for AC losses of HTS tapes in combined alternating transport current and external AC magnetic field with phase shift," *IEEE Transactions on Applied Superconductivity,* vol. 11, no. 1, pp. 2240-2243, 2001.

[123] Y. Ichiki and H. Ohsaki, "Numerical analysis of AC losses in YBCO coated conductor in external magnetic field," *Physica C: Superconductivity,* Vols. 412-414, no. 2, pp. 1015-1020, 2004.

[124] R. Inoue, D. Miyagi, M. Tsuda and H. i. Matsuki, "Magnetization Loss Characteristics of a GdBCO Tape in kHz Frequency Band," *IEEE Transactions on Applied Superconductivity,* vol. 28, no. 4, p. 8201405, 2018.

[125] N. Amemiya, Z. Jiang, M. Nakahata, M. Yagi and e. al, "AC Loss Reduction of Superconducting Power Transmission Cables Composed of Coated Conductors," *IEEE Transactions on Applied Superconductivity,* vol. 17, no. 2, pp. 1712-1717, 2007.

[126] M. Tsuda, J. Fujimoto, N. Harada and T. Hamajima, "AC loss reduction of coaxial multi-layer HTS cable," *IEEE Transactions on Applied Superconductivity,* vol. 14, no. 2, pp. 642-645, 2004.

[127] S. Mukoyama, K. Miyoshi, H. Tsubouti, T. Yoshida, M. Mimura, N. Uno, M. Ikeda, H. Ishii, S. Honjo and Y. Iwata, "Uniform current distribution conductor of HTS power cable with variable tape-winding pitches," *IEEE Transactions on Applied Superconductivity,* vol. 9, no. 2, pp. 1269 - 1272, 1999.

[128] H. Zhang, J. Zhu, W. Yuan, M. Qiu, S. Fu, S. Rao, W. Yang and a. M. Zhang, "Electromagnetic Analysis of YBCO Superconducting Cables With High Current Transporting for Electric Devices," *IEEE Transactions on Applied Superconductivity,* vol. 26, no. 7, p. 4804604, 2016.

[129] S.-W. Kim, H. J. Kim, J.-H. Joo and K. J. Song, "Transport current loss and I/sub c/ degradation of HTS tapes under mechanical load," *IEEE Transactions on Applied Superconductivity,* vol. 14, no. 2, pp. 1110-1113, 2004.

[130] M. Breschi, E. Berrospe-Juarez, P. Dolgosheev, A. González-Parada, P. L. Ribani and F. Trillaud, "Impact of Twisting on Critical Current and n-value of BSCCO and (Re)BCO Tapes for DC Power Cables," *IEEE Transactions on Applied Superconductivity*, vol. 27, no. 4, p. 5401404, 2017.

[131] C. W. Bumby, R. A. Badcock and N. J. Long, "Critical Current Behavior of HTS Roebel Cable Under Tensile Stress," *IEEE Transactions on Applied Superconductivity,* vol. 23, no. 3, p. 4801805, 2013.

[132] Y. Yang, T. Hughes, E. Martinez, C. Beduz and F. Darmann, "Reduction of AC loss in Ag sheathed PbBi2223 tapes with twisted filaments in external and self-fields," *IEEE Transactions on Applied Superconductivity,* vol. 9, no. 2, pp. 1177-1180, 1999.

[133] M. Takayasu, J. V. Minervini, M. K. Rudziakmrudziak and T. Wong, "Investigation of twisted stacked-tape cable conductor," in *AIP Conference Proceedings*, 2012.

[134] Q. Li, Y. Xin and S. Wang, "Dependence of AC Loss on Structural Compactness of Superconducting Power Cables With Narrow Coated Conductors," *IEEE Transactions on Applied Superconductivity*, vol. 26, no. 7, p. 5900705, 2016.

[135] N. Amemiya, M. Nakahata, N. Fujiwara and Y. Shiohara, "Ac losses in two-layer superconducting power transmission cables consisting of coated conductors with a magnetic substrate," *Superconductor Science and Technology*, vol. 23, no. 1, p. 014022, 2009.

[136] J. Ogawa, S. Fukui, T. Oka, T. Ogawa and M. Sugai, "AC Loss Distribution in Two-Layer HTS Cable," *IEEE Transactions on Applied Superconductivity*, vol. 28, no. 3, p. 5900104, 2018.

[137] Z. Hong, A. M. Campbell and T. A. Coombs, "Computer Modeling of Magnetisation in High Temperature Bulk Superconductors," *IEEE Transactions on Applied Superconductivity*, vol. 17, no. 2, pp. 3761 - 3764, 2007.